

EFFECTS OF OXYGENATED SPECIES ON REFORMING GASOLINE RANGE HYDROCARBONS

John P. Kopasz, Laura Miller, Daniel Applegate, and Shabbir Ahmed

Chemical Engineering Division
Argonne National Laboratory
9700 S. Cass Ave
Argonne, IL 60439

Introduction

High octane rating and good reformability are important characteristics for a gasoline-type fuel that could be marketed to both internal combustion engine (ICE) and fuel cell (FC) vehicle owners. Aromatic components contribute to a high octane rating in the gasoline formulations currently produced for internal combustion engines. Unfortunately, aromatic components are difficult to reform because they require longer residence times in the reformer and, as a result, lower the kinetic rate of paraffin reforming.¹⁻³ An ideal solution would be an inexpensive, low toxicity, easily reformed component that could replace the aromatics, yet maintain a high octane rating in the fuel. The pump octane number (PON), which is an average of the research octane number (RON) and motor octane number (MON), is high for aromatics like toluene as well as for oxygenates like dimethylcarbonate (DMC), ethanol, and methyl *tert*-butyl ether (MTBE).⁴ These oxygenates may improve reforming while maintaining high octane ratings, allowing a fuel with lower aromatic content to be used. This would also make desulfurization easier, since requirements for maintaining high octane aromatic components during hydrodesulfurization would be removed.

Experimental

The experiments were conducted using approximately 2 grams of 0.5 wt% Pt on Ce_{0.8}Gd_{0.2}O_{2-δ}, packed as +25/-35 mesh granules. The reactor tube ID was 0.422 cm and the bed length 5 cm for a bed volume of 0.698 cm³. The furnace settings used in these experiments ranged from 650-800°C, in 50° increments. GHSV's of 15000-150000 h⁻¹ were achieved by using two flow settings (0.04 and 0.08 mL/min fuel) and sample ports at multiple locations in the bed. The fuels tested were binary mixtures of isooctane-xylene and isooctane-oxygenate, and ternary mixtures of isooctane-xylene-oxygenate. The H₂O:C molar ratio was fixed at 1.43. The O₂:C molar ratio was 0.4225 for the isooctane-xylene mixture. For dimethylcarbonate (DMC), the ternary mixture was run such that the overall O:C ratio (accounting for the oxygen in the DMC and water) was the same as that for the isooctane-xylene mixture (2.275). The binary isooctane-DMC mixture was run such that the O₂:C ratio (not accounting for the oxygen in the DMC) was 0.4225. Consequently, the oxygen potential in the reactor was higher for the binary isooctane-DMC mixture than for the other two fuels. The product gas was monitored with a residual gas analyzer (RGA) and the bed temperature was monitored with four thermocouples located at various points in the bed.

Results and Discussion

The ternary blend of 75% isooctane, 5% DMC, and 20% xylene showed improved hydrogen production after accounting for hydrogen which would be produced from the water-gas shift reaction compared to isooctane + 20% xylene over most of the parameter space investigated. A percent difference plot is shown in figure 1. The difference in the percent theoretical hydrogen (% theoretical H₂ = (moles H_{2out} + moles CO_{out})/[(total moles H in)/2-moles excess H₂O] where moles excess H₂O is the water excess or water formed from excess oxygen, and is calculated as (moles excess H₂O) = (total

moles O)/2-(moles C). In this figure as well as the next, positive differences reflect an improvement due to DMC, while negative differences indicate better performance without DMC.

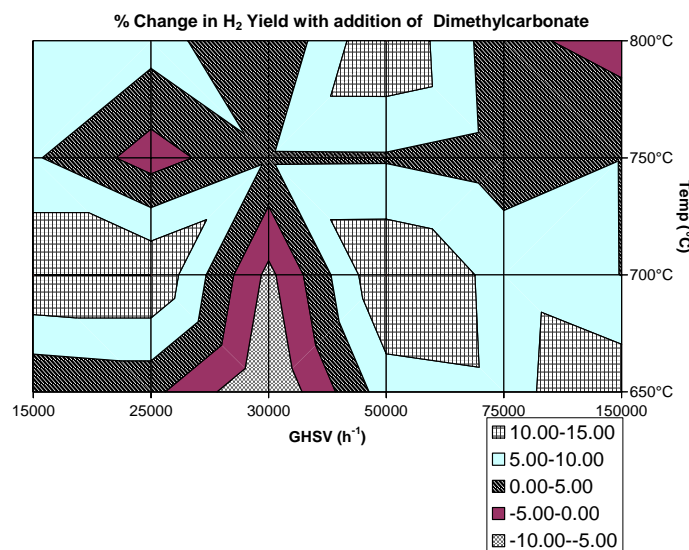


Figure 1. %Change in H₂ yield when adding dimethyl-carbonate to isooctane-xylene mixture.

A large portion of the parameter space investigated showed differences of $\pm 5\%$, which are believed to be in the range of the error of the measurements. However, improvements in H₂ yield of greater than 5% were observed over a substantial portion of the parameter space. At 650°C, improvements in H₂ yield upon addition of DMC generally increased with increasing GHSV. At 700°C hydrogen yield was improved over almost the entire range of space velocities. At 800°C, where reforming is most efficient, DMC's effect is greatest at a GHSV of 50,000h⁻¹. Looking at GHSV variations, DMC addition improves reforming most at a GHSV of 50,000h⁻¹. The largest absolute difference was at 700°C and a space velocity of 15000 h⁻¹, where the ternary mixture (with DMC) produced an additional 13% hydrogen over the binary mixture (no DMC).

Replacing all the xylene in an isooctane + 20% xylene solution with DMC provided mixed results. DMC increased the hydrogen yield over about half of the operating space, but decreased yields over about half the space. Increases were observed for GHSV in the range of 30,000 to 50,000 h⁻¹ at lower temperatures, and shifted to higher GHSV at higher temperatures. To determine how DMC affected reforming kinetics, we looked at how DMC affected the concentration of butyl species, a major product from isooctane cracking, and methane. Methyl species generally decreased in concentration with increasing reaction time, while the butyl species increased with increasing reaction time for both isooctane + 20% xylene and isooctane + 20% DMC. In general, the reformate produced from the solution with DMC contained slightly higher methane content, but larger hydrocarbons, such as butyl species, were reduced. Data for the concentrations as a function of residence time were fit to pseudo-first order rate laws, and the natural log of the rate constants plotted versus the inverse temperature (see fig. 2).

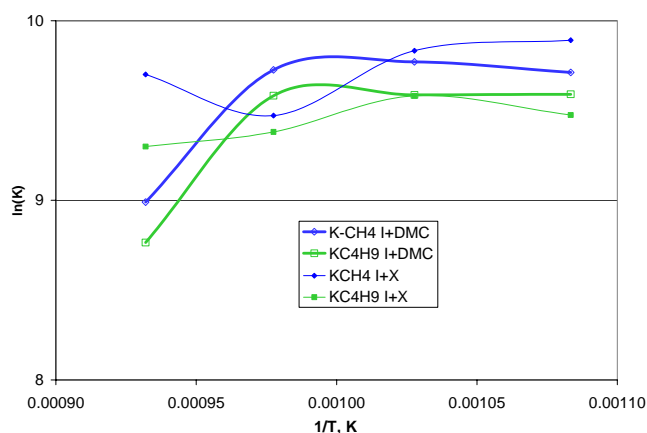


Figure 2. Effect of fuel composition on kinetics of methane decomposition and butyl formation during reforming

The first-order rate constants for methane decay and the net formation of butyl species from isooctane are practically independent of temperature from 650 to 750°C when reforming isooctane + DMC, but drop sharply when the temperature is increased to 800°C, suggesting a change in the rate controlling step between 750 and 800°C. For isooctane + xylene, the rate constants decrease slightly with temperature from 650 to 750°C, with a slight increase in the rate of methane decay at 800°C. This suggests different mechanisms are responsible for fractionation and reforming of isooctane in isooctane + 20% xylene and isooctane + 20% DMC. The mass spectra for the DMC-containing mixtures showed no evidence of DMC remaining in the product. The product gas from all three mixtures produced mass spectra with very similar fragmentation patterns for unreformed isooctane.

Discussion

Dimethylcarbonate holds potential for replacing aromatic components of gasoline to improve reformability while maintaining high octane rating and low toxicity. As an oxygenate, DMC can also raise the P_{O_2} in the reactor, which could further enhance reformability of the fuel. The results showed that there is a slight improvement to autothermal reforming when DMC is added at a 5 vol% level to a mixture of isooctane and xylene. The effect was largest at 700°C. Results were mixed when the entire 20 vol% aromatic component was replaced with DMC in an 80:20 mixture with isooctane. Some combinations of temperature/GHSV showed improvement with DMC, while other combinations showed a drop in performance. Replacement of the xylene component with DMC did not significantly improve autothermal reforming as had been hoped. The increase in P_{O_2} in the reactor did not have a major impact on hydrogen production or reforming products. The mass fragments observed in the RGA were similar for all three fuels, demonstrating that the DMC was being reformed, but suggesting that it did not substantially enhance the reforming of isooctane over the range of conditions investigated. Future experiments will pursue other fuel additives with the potential to enhance autothermal reforming.

Acknowledgement. This work was supported by the U.S. Department of Energy, Office of Hydrogen, Fuel Cells, and Infrastructure Technologies.

References

- (1) Kopasz, J.P.; Miller, L. E.; Ahmed, S.; Devlin, P.; Pacheco, M. Society of Automotive Engineers Technical Paper Series, **2002**, 2002-01-1885.

- (2) Kopasz, J.P.; Krause, T.R.; Ahmed, S.; Krumpelt, M. *Prepr. Pap. - Am. Chem. Soc., Fuel Chem. Div.* **2002**, 47(2), 489-491.
- (3) Borup, R.; Inbody, M.A.; Tafoya, J. I.; Vigil, W. I.; Guidry, D. *Prepr. Pap. - Am. Chem. Soc., Fuel Chem. Div.* **2001**, 46(2), 547-548.
- (4) Pacheco, M. A.; Marshall, C. L. *Energy & Fuels*, **1997**, 11, 2-29.

HIGH CONTACTING EFFICIENCY MICROFIBROUS ENTRAPPED PROX CATALYSTS FOR REFORMATE CLEANUP AND PEM FUEL CELL APPLICATIONS

Bong-Kyu Chang and Bruce J. Tatarchuk

Center for Microfibrous Materials Manufacturing (CM³)
Department of Chemical Engineering
Auburn University, Auburn, AL 36849

Introduction

Preferential oxidation (PROX) of CO in H₂ is believed to be the most efficient way to remove CO from practical reformat for PEM fuel cells.¹ Pt/Al₂O₃ has long been known as a suitable catalyst for this purpose. However, preferential oxidation of CO in H₂ over Pt/Al₂O₃ occurs at temperatures above 150°C, and the maximum CO conversion takes place at around 200°C. The overall objective of this study is to develop a novel catalyst material for effective removal, particularly at low temperatures, of small amounts (1-2%) of CO present in H₂-rich gas such as practical reformat produced by partial oxidation or steam reforming of hydrocarbons for PEM fuel cells.

Conventional Pt/Al₂O₃ was promoted by cobalt (Pt-Co/Al₂O₃) in this study and the promoted catalysts demonstrate enhanced activity and selectivity compared with the un-promoted catalysts. In particular, CO conversion takes place at significantly lower temperature over Pt-Co/Al₂O₃ catalysts and the active reaction temperature window is enlarged to 25-200°C compared with a narrow window around 200°C over conventional Pt/Al₂O₃.

A high void and tailorable sintered microfibrous carrier consisting of 5vol% 4 and 8µm diameter Ni fibers is used to entrap 15vol% 150-250µm Al₂O₃ particulates. SEM images show the microstructures of the thin microfibrous entrapped alumina support particles. The alumina support particulates are uniformly entrapped into a well sinter-locked three-dimensional network of 4 and 8µm Ni fibers. Cobalt and platinum are then dispersed onto the microfibrous entrapped alumina support particles by impregnation method so as to prepare microfibrous entrapped Pt-Co/Al₂O₃ catalysts. The composite catalysts possess 80vol% voidage. A thin bed of microfibrous entrapped small catalyst (150-250µm) was investigated for preferential oxidation (PROX) of CO from practical reformat for PEM fuel cells. At equivalent bed volumes, microfibrous entrapped catalysts demonstrate superior catalytic activity compared to conventional packed beds of same and larger particles demonstrating ultra-high contacting efficiency provided by the microfibrous entrapped catalysts. A microfibrous entrapped H₂S sorbent layer was, then, placed upstream of a microfibrous entrapped PROX catalyst layer to remove both H₂S and CO from a sulfur-contaminated practical reformat stream. Operating in this fashion, an outermost H₂S sorbent layer promotes the activity maintenance of a secondary non-poison tolerant PROX CO catalyst, which ultimately serves to provide activity maintenance to CO-intolerant precious metal based MEA assemblies in PEM fuel cells.

Experimental

Preparation of Microfibrous Entrapped Catalyst.

Traditional high speed and low cost paper making equipment and technique were used in this study to prepare microfibrous composite materials. In this process, 4 and 8µm diameter metal (Ni) fibers in a variety of compositions and alloys are slurried in an aqueous suspension with cellulose fibers and other selected particulates such as alumina support particles. The particle size of alumina support was 150-250µm (60-100 mesh). The resulting mixture is then cast into a preform sheet using a wetlay process and dried to create a sheet of

preform material. Subsequent pre-oxidation in O₂ flow at 500°C for 1hr and sintering of the preform in H₂ flow at elevated temperature (900°C) for 30mins remove the cellulosic binder/pore former and entraps the selected support particulates within a sinter-locked network of conductive metal fibers. The resulting preform generally consists of 10-15vol% support particles, 5vol% metal (Ni) fibers, and 80-85vol% voidage. Finally, the microfibrous entrapped support particles such as alumina are impregnated with the metal salt precursor solutions as in the preparation of powder catalysts. Then, microfibrous entrapped catalysts are dried and calcined at desired temperatures.

Catalytic Activity and Selectivity Investigation. Practical reformat consists of 1% CO, 20% CO₂, 40% H₂, and balance N₂. Reaction products were analyzed using a HP6890 gas chromatograph equipped with a TCD detector. Water condenser was used to prevent water vapor from entering the gas chromatograph. Empty reactor without catalyst showed no CO conversion.

Catalyst Characterization Methods. For SEM (scanning electron microscopy), the samples were coated with carbon using SPI module carbon coater to avoid charge building inside the sample while performing SEM. The SEM images of microfibrous materials were obtained using a JEOL JSM 840 (20KV) SEM. The SEM images were recorded at magnification levels of 37 and 200 using an in-built digital camera. For XRD (X-ray diffraction) analysis, structural phases were determined for catalysts in an X-ray diffractometer using Cu Kα radiation. A continuous scan mode was used to collect 2θ data from 10° to 80° with a 0.02 sampling pitch and a 4°/min scan speed. X-ray tube voltage and current were set at 40kV and 40mA, respectively. For EDX (energy dispersive X-ray spectroscopy) analysis, catalyst sample was coated with carbon using SPI module carbon coater to avoid charge building inside the sample while doing EDX. EDX data for the catalyst was obtained using a JEOL JSM 840 (20KV) SEM/EDX.

Results and Discussion

Effect of Various Transition Metal Promoters. Figure 1 shows the effect of various transition metal promoters on the CO oxidizing activity and O₂ selectivity over 4.0wt%Pt-X/Al₂O₃ catalysts (X is a transition metal promoter) as a function of reaction temperature. All of these modified catalysts show enhanced low-temperature activity for CO oxidation versus un-promoted conventional Pt/Al₂O₃ catalyst. Fe, Co, and Mn are found to be effective promoters for conventional Pt/Al₂O₃ catalyst for enhanced CO oxidizing activity and O₂ selectivity at low temperatures. Fe- and Co-modified catalysts achieve complete CO conversion at room temperature to 50°C. Complete CO conversion means that no CO is detected from the outlet stream by the TCD used in this study and it indicates that CO conversion is 99.5 to 100% since CO sensitivity of the TCD used in this study is 50ppm. It is observed that cobalt (Co) is the best promoter for Pt/Al₂O₃ catalyst to achieve complete removal of trace amount of CO in H₂ gas at low temperatures.

Microfibrous Entrapped PROX Catalyst. Figure 2 shows a SEM image of the microstructures of the thin microfibrous entrapped Al₂O₃ support particulates, i.e., alumina support particles entrapped in the microfibrous metal (Ni) mesh after sintering at magnification level of 200, respectively. As shown in the Figure 2, the alumina support particles are uniformly entrapped into a well sinter-locked three-dimensional network of 4 and 8µm diameter Ni fibers. Approximately 80-85vol%, 5vol%, and 10-15vol% of the microfibrous materials are voidage, nickel fibers, and alumina support particles entrapped, respectively.

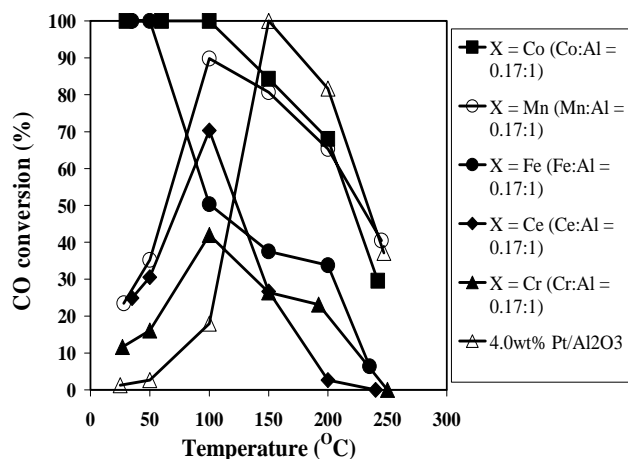


Figure 1. Effect of various transition metal promoters on CO oxidizing activity over 4.0wt%Pt-X/Al₂O₃ catalyst (X is a transition metal promoter) as a function of reaction temperature.

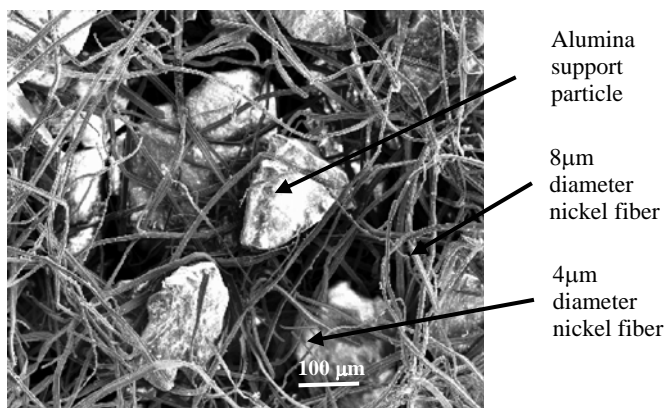


Figure 2. SEM image of 150-250µm γ -Al₂O₃ support particles entrapped in a microfiber matrix of 4 and 8µm nickel fibers at magnification level of 200.

Figure 3 shows stability of microfibrillar entrapped Pt-Co/Al₂O₃ catalysts at 70°C (PEMFC stack temperature) with effect of H₂O on the stability. Stability of PROX unit at PEM fuel cell stack temperature is important considering that PROX unit would be integrated into PEMFC stack if it is stable at stack temperature. 30% H₂O in the feed stream is the maximum amount of water which can be maintained in the vapor phase at 70°C which is the PEMFC stack temperature. As shown in **Figure 3**, at 70°C, 0% (no H₂O added), 10%, 20%, and 30% H₂O which are added in the dry practical reformates - which also correspond to 0%, 33%, 67%, and 100% of the saturation amount at 70°C, respectively - do not cause any negative effects on the stability of the microfibrillar entrapped Pt-Co/Al₂O₃ catalysts mainly since none of the water vapor added in the feed stream does condense at 70°C. In other words, complete CO conversion activity over the microfibrillar entrapped Pt-Co/Al₂O₃ catalysts is maintained for approximately a week without any catalytic deactivation in the presence of 0%, 10%, 20%, and 30% H₂O added in the dry feed stream at 70°C.

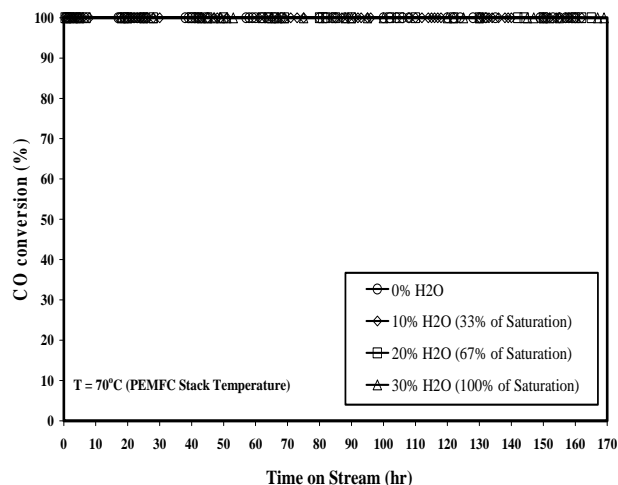


Figure 3. Stability of microfibrillar entrapped Pt-Co/Al₂O₃ catalysts at 70°C (PEM fuel cell stack temperature) – Effect of H₂O.

Layering of Microfibrillar Entrapped Reactive Media to Achieve Multiple Staged Chemical Reactions/Processes in Flow through Geometries of Millimeter Thickness. High contacting efficiency microfibrillar media are used to entrap various reactive materials including; heterogeneous catalysts, electrocatalysts, sorbents, and various solid reactants. These media are then layered so as to permit multiple staged chemical reactions to be achieved within the space of a few millimeters of thickness. Layered media may be used alone or in combination with more traditional contacting schemes (i.e., packed beds, monoliths, etc) so as to be employed as polishing sorbents, polishing catalysts, or both. As a demonstrated example of this generic approach, a microfibrillar entrapped polishing H₂S sorbent was placed upstream of a microfibrillar entrapped polishing PROX CO catalyst to remove both H₂S and CO from a sulfur-contaminated practical reformat stream. Operating in this fashion, an outermost H₂S sorbent layer promotes the activity maintenance of a secondary non-poison tolerant PROX CO catalyst, which ultimately serves to provide activity maintenance to CO-intolerant precious metal based MEA assemblies.

The benefits and attributes of the above approach may be extended to a variety of entrapped materials and chemical processes. The enabling attribute is the high contacting efficiency afforded by microfibrillar entrapment, and the thin layer design of these materials that permit facile and effective layering, packaging and sealing.

Figure 4 shows performance of the integrated bed of microfibrillar entrapped ZnO/SiO₂ H₂S sorbent layer and Pt-Co/Al₂O₃ PROX CO catalyst layer at 25°C in the presence of 50ppmv H₂S in the feed. Total flow rate of the feed stream was 100ml/min and cross-sectional area of the microfibrillar bed was 0.7854cm² making the face velocity 2.12cm/s. Complete CO conversion activity is maintained at least 35hrs without any catalytic deactivation over the microfibrillar entrapped Pt-Co/Al₂O₃ PROX CO catalyst when H₂S does not present in the feed stream. CO conversion activity, however, starts dropping dramatically around 4hrs after 50ppmv H₂S is introduced in the feed stream together with CO mainly due to irreversible and permanent H₂S poisoning on the entrapped PROX catalysts. Finally, a microfibrillar entrapped H₂S sorbent layer was placed upstream of a microfibrillar entrapped PROX CO catalyst layer and the integrated H₂S and PROX CO removal units was investigated at 25°C in the presence of both 1% CO and 50ppmv H₂S in the feed stream. Thickness of the microfibrillar entrapped H₂S sorbent layer and the microfibrillar entrapped PROX catalyst layer

was approximately 2mm each making the total bed thickness 4mm. As it can be seen clearly in Fig. 30, complete CO conversion activity is recovered for approximately 27hrs before CO is detected in the outlet. H₂S is detected approximately 29hrs after introduction of 50ppmv H₂S in the feed stream, and it is the breakthrough time for the H₂S over the integrated system.

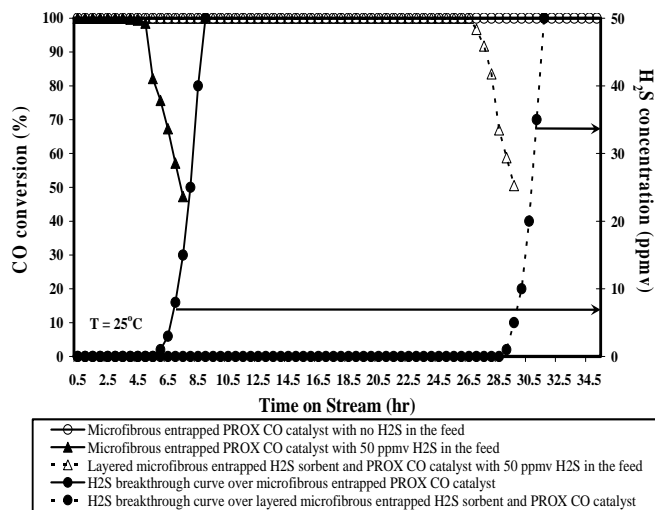


Figure 4. Performance of integrated bed of microfibrous entrapped ZnO/SiO₂ H₂S sorbent and Pt-Co/Al₂O₃ PROX CO catalyst at 25°C in the presence of 50ppmv H₂S in the feed stream.

Catalyst Characterization. Figure 5 shows the XRD patterns of Pt catalyst supported on alumina (4.7wt%Pt-Co/Al₂O₃) compared with those of mixtures of Pt (4.7wt%) and alumina powder. The strongest peak of Pt (111) which is not detected from the catalyst samples is detected at 2θ angle of 39.763° in standard sample of 4.7wt% Pt mixed with alumina powder. Pt (311) peak is also detected at 2θ angle of 81.286° in standard samples. XRD analysis indicates that nano-sized Pt and Co particles are highly dispersed on the alumina support.

Figure 6 shows the EDX spectrum of Pt-Co/Al₂O₃ (4.7wt% Pt, Co:Al = 0.04:1) catalyst. As seen in the figure, there are two peaks corresponding to Pt, two peaks to Co, one peak to Al, and one peak to O in the alumina support. The weight % of Pt obtained by EDS (4.1wt% Pt) is in good agreement with the calculated value (4.7wt% Pt) during the incipient-wetness impregnation process. The atomic ratio of Co:Al measured by EDX (0.034:1) is also in good agreement with the calculated atomic ratio (0.04:1).

Conclusions

Cobalt-promoted Pt/Al₂O₃ (Pt-Co/Al₂O₃) catalyst is significantly superior to un-promoted catalyst for preferential oxidation of CO in excess H₂. XRD patterns for Pt-Co/Al₂O₃ catalysts with different Pt and Co content verify the fact that nano-sized small Pt and Co particles are highly dispersed on the surface of alumina support. All the peaks observed in XRD experiments are from alumina supports. With the attachment of the energy dispersive X-ray spectrometer (EDX), however, the presence of Pt and Co particles is repeatedly verified and the precise elemental composition of catalysts can be obtained with high spatial resolution by scanning electron microscopy (SEM) and the values obtained by EDX show

good agreement with the calculated values during the catalyst preparation.

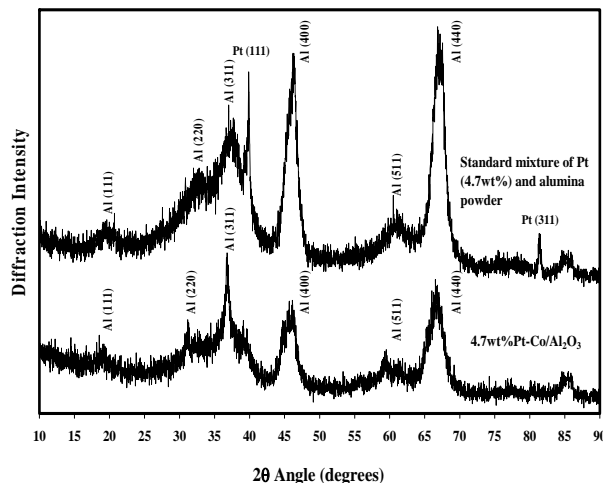


Figure 5. Comparison of XRD patterns of Pt catalyst supported on alumina (Pt-Co/Al₂O₃) with those of mixture of Pt and alumina powder: 4.7wt% Pt.

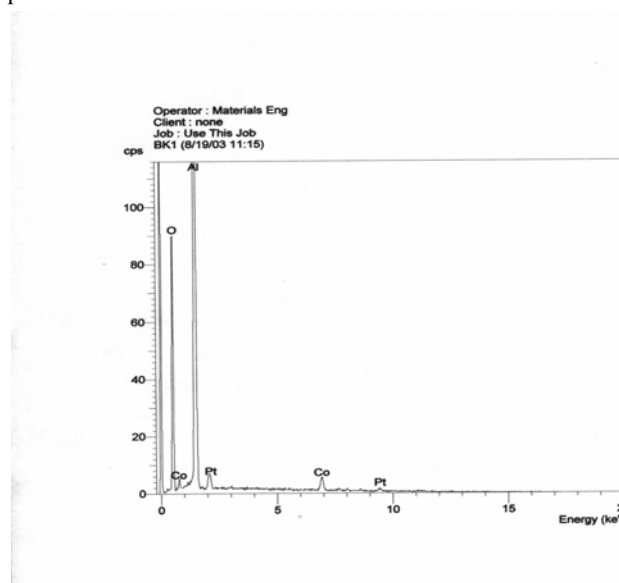


Figure 6. EDX spectrum of Pt-Co/Al₂O₃ catalyst.

High contacting efficiency microfibrous media can be used to entrap various reactive materials including heterogeneous catalysts, sorbents, and various solid reactants. Small particles of Pt-Co/Al₂O₃ catalysts (150-250μm) were entrapped in this study into the microfiber composite materials and investigated for preferential CO oxidation (PROX) reaction for PEM fuel cells. The microfibrous entrapped PROX catalysts demonstrate a long-term stability and high activity at temperature range of 25 (room temperature) to 150°C (PROX unit operating temperature). the nano-dispersed nature of Pt and Co particles combined with packaging of metal fibers and small support particles promotes high contacting efficiency in the microfibrous entrapped catalysts compared with conventional packaging of catalysts in packed bed of even same particle size.

These microfibrous media then could be layered so as to permit multiple staged chemical reactions to be achieved within the space of a few millimeters of thickness. As a demonstrated example

of this generic approach, a microfibrinous entrapped polishing ZnO/SiO₂ H₂S sorbent was placed upstream of a microfibrinous entrapped polishing Pt-Co/Al₂O₃ PROX catalyst to remove both H₂S and CO from a sulfur-contaminated practical reformat stream. Operating in this fashion, an outermost H₂S sorbent layer promoted the activity maintenance of a secondary non-poison tolerant PROX catalyst, which ultimately served to provide activity maintenance to CO-intolerant precious metal based MEA assemblies.

Acknowledgement. This work was performed under a U.S. Army contract at Auburn University (DASG 60-00-C-0070) administered through the U.S. Army Space & Missile Defense Command (SMDC).

Reference

- (1) Sanchez, P. M. T., Ueda, A., Tanaka, K., and Haruta, M., *J. Catal.* **1997**, 168, 125.

MULTIFUEL CLEAN-UP CONSIDERATIONS FOR HIGH TEMPERATURE FUEL CELLS

Sai P. Katikaneni, Mohammad Farooque

FuelCell Energy, Inc.
3 Great Pasture Road
Danbury, CT 06813, USA
skatikaneni@fce.com
(203) 825-6067
Fax: (203) 825-6273

Carbonate fuel cells are new generation of power plants that provide electricity at very high efficiency and low environmental emissions. FCE's "direct carbonate fuel cell" operates on a variety of hydrocarbon fuels such as natural gas, digester gas, coal gas, diesel and HD-5. Conventionally, an external reformer is used to supply hydrogen rich gas to fuel cell. FuelCell Energy's DFCTM technology has adopted an internal reforming approach that eliminates the need for an external reformer, resulting in increased efficiency, compactness, better thermal management and lower cost.

DFC operation on natural gas, peak shaving gas, HD-5, LPG/propane, digester gas, syngas, coal bed methane, and liquid fuels such as diesel, methanol and ethanol has been already demonstrated. Fuel clean-up and fuel processing operation varies based on the nature of fuel. However, the fuel thus supplied to the fuel cell has a two-step refinement approach. Step 1 involves fuel clean up system to remove impurities such as sulfur, halides, solid particulates, aromatic hydrocarbons, and oxygen. The second step is pre-reforming desulfurized fuel to knock out higher hydrocarbons in order to eliminate coke formation during reforming inside the fuel cell. Methane-rich gas obtained from pre-reformer is thus fed into fuel cell for internal reforming to produce hydrogen in DFC stacks which in turn is electrochemically converted to water, thereby producing DC power. At each stage of this operation, catalysts are used to facilitate production of desirable fuel cell fuel.

Fuel clean-up considerations vary with type of fuel and its constituents. The nature of impurities and their concentration will be considered to design suitable clean-up processor for each type of fuel for DFC applications. Table 1 indicates various fuels specification including type of impurities and their levels for designing clean-up processor. The impurities present in fuels will impact the performance of reforming catalysts, cell performance and overall life of fuel cell. Ni-based catalysts are used for internal reforming and prereforming of higher hydrocarbons. Nickel catalysts are sensitive for sulfur, chloride and particulate poisoning, thus, require impurity-free fuel for fuel cell applications. The tolerance level of these impurities on both catalyst and fuel cell components are significantly lower than conventional fuel processing operations. Also, the tolerance level is based on the type of impurity. Although worldwide standards favor a gradually lowering sulfur and other impurity levels in transportation fuels, it is necessary to further reduce the sulfur levels in fuel cells to sub-ppm levels prior to use in fuel cell power plants. Depending on the nature of fuel and impurity levels, an appropriate fuel clean-up process with suitable adsorbents/catalysts is required in DFC balance of power plant operation.

FCE has designed multi-fuel clean-up processor to meet DFC power plant tolerances for each type of impurities present in the fuel. These designs were based on either catalytic or adsorbent and selected based on type of fuel and impurity. Multi-fuels processed at FCE's tests have been able to reduce impurity levels (sulfur, halides, particulates and metals) to less than sub ppm levels. This presentation will discuss FCE's experience with multi-fuel clean-up considerations and primarily focusing on desulfurization of multi-fuels.

NANOSIZED CERIA BASED WATER-GAS SHIFT (WGS) CATALYST FOR FUEL CELL APPLICATIONS

Ranjan K. Pati¹, Ivan C. Lee², Deryn Chu², Sicong Hou¹, and Sheryl H. Ehrman¹

¹Department of Chemical Engineering, University of Maryland, College Park, MD 20770

²Sensors and Electron Devices Directorate, US Army Research Lab, Adelphi, MD 20783

Introduction

Cerium oxide (CeO_2) / ceria is an important inorganic material having the cubic fluorite type crystal structure (1). Ceria either in the pure form or doped with other metals (Cu, Ni, etc) / metal ions (Mg^{2+} , La^{2+} , Sc^{2+} , Gd^{3+} , Y^{3+} , Zr^{4+} etc.), potentially has a wide range of vast applications including gas sensors (2), electrode materials for solid oxide fuel cells (3) oxygen pumps, amperometric oxygen monitors and three way catalytic supports for automobile exhaust gas treatment (4).

In recent years, nanocrystalline particles of ceria have attracted much attention because of their improved physical and chemical properties compared to those of bulk ceria materials. Various solution-based techniques have been used for the preparation of pure ceria and transition metals, rare earth metals, or metal ions doped ceria materials, including coprecipitation (5), hydrothermal (6), microemulsion (7), sol-gel (8), solution combustion (9) and electrochemical methods (10). These methods are either multi step and time-consuming or control of the product composition may be difficult.

In the present paper we report a single step alternative route for synthesizing CeO_2 based nanoparticles. The process involves the pyrolysis of aqueous solutions of the metal acetate without addition of any extra fuel in a methane oxygen flame.

Experimental

The precursors used were cerium acetate as the cerium source, copper acetate as the copper source, nickel acetate as the nickel source and iron acetate as the iron source. The precursors were dissolved in deionized water to make 0.3 M solutions of each. For the transition metal supported ceria, a series of solutions have been prepared starting from 5, 10, 20, 30 and 40 mole % of transition metal in ceria. The solutions were filtered through a membrane filter before filling the nebulizer. Liquid precursor feed was then atomized with compressed air resulting in a fine spray. In the reactor the flame was made by methane, oxygen and nitrogen. The gas flow controller controls the flow rate of the gas and precursors. After burning the fine spray, the particles were collected on a water-cooled surface by thermophoresis, which was kept on the top of the flame.

Characterization

The synthesized materials were then characterized by powder X-ray diffraction (XRD) using CuK_α ($\lambda = 1.5408\text{\AA}$) for the phase analysis and crystal structure determination. Thermogravimetric analysis (TGA) was used to determine the amount of unwanted materials such as water and carbonaceous compounds in the sample. Atomic bonding was analyzed using Fourier transformed infrared spectroscopy (FTIR). Brunauer, Emmett and Teller (BET) gas absorption method was applied to investigate the surface area of the sample. Transmission electron microscopy (TEM) was used for the particle size analysis and surface morphology of the material. X-ray photoelectron spectroscopy (XPS)

was utilized to determining the oxidation state of the transition metal used in the ceria system.

Results and Discussion

Thermogravimetric analysis was performed in air at a heating rate of $10^\circ\text{C}/\text{min}$. The TGA curve (Figure 1) for the pure ceria sample indicates that there were two stage of weight loss. The first weight loss (between 20 to 200°C) was due the removal of water molecules, which probably come from the condensation of water molecule on the water-cooled surface. The second stage weight loss (between 300 to 600°C) resulted from the burning and oxidation of carbon compounds (combustion by-product) likely from incomplete combustion of the metal acetate precursor, which is confirmed by FTIR. Similarly, the TGA of the as prepared Cu/CeO_2 showed the same weight loss behavior with the presence of more carbon in the sample.

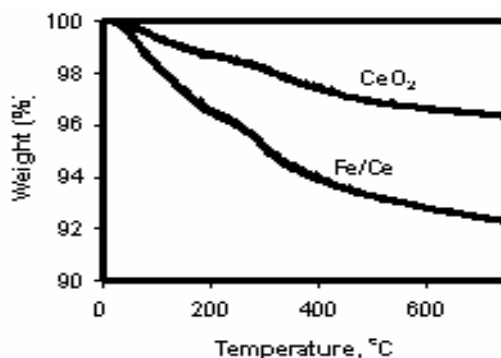


Figure 1. Thermogravimetric analysis (TGA) of as prepared pure CeO_2 and 40% Fe/CeO_2 powder

The X-ray diffraction patterns of transition metal doped CeO_2 are performed. The diffraction lines corresponding to the fluorite type structure and the d values agree well with those expected for CeO_2 . The peaks corresponding to transition metal or oxides could not be detected even with the increase of transition metal content. This suggests that transition metal or its ion may not be substituted for Ce^{4+} in CeO_2 . Increasing the transition metal content increases the line width compared to the pure CeO_2 and the absence of transition metal or its oxide phase suggest that the transition metal or its ions are dispersed on the surface of CeO_2 .

X-ray photoelectron spectra of 40% Ni/CeO_2 in the $\text{Ce}(3d)$ and $\text{Ni}(2p)$ regions have been performed. The $\text{Ce}(3d)$ spectrum with intense satellites identifies with Ce^{4+} in CeO_2 (9). No significant peak is observed in the $\text{Ce}(3d)$ spectrum corresponding to Ce^{3+} . The XPS of as prepared $\text{Ni}(2p_{3/2})$ shows that Ni is in the +2 oxidation state as seen from the Ni^{2+} ($2p_{3/2}$) binding energy as well as the satellite peaks. The Ni/CeO_2 catalyst after the water-gas shift treatment shows the zero oxidation state of Ni, which indicates the reduction of Ni^{2+} to Ni happens in the reducing atmosphere.

Transmission electron microscopic image of 40% Cu/CeO_2 is shown in Figure 2. The particles are spherical in size with particle size in the range of 3-5 nm. The absence of big particle suggests that the precursor droplets are vaporized completely in the flame. The selected area electron diffraction (SAED) pattern is indexed to polycrystalline CeO_2 in the fluorite structure and no line corresponding to Cu or any of the oxides of Cu is detected. This again suggests the dispersion of Cu^{2+} on the CeO_2 surface. A particle sizes obtained from Ni/CeO_2 and

Fe/CeO₂ are in the range of 3-10 nm. The BET surface area for the prepared sample is in the range of 127-163 m²/g.

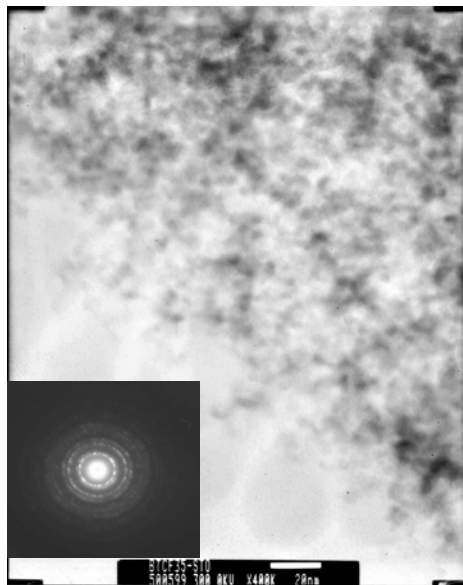


Figure 2. Transmission electron micrograph and the selected area electron diffraction pattern of the as prepared Cu/CeO₂ powder

WGS reaction has been done in a differential reactor with 5% CO, 5% H₂ in Ar and CO/H₂O=5. Figure 3 shows the comparative study of WGS activity of different catalysts. From the graph it is clear that pure ceria is not active because of the absence of any active site. 40% Cu/CeO₂ and annealed 40% Cu/CeO₂ show better activity compared to the other. The reason of the better activity for annealed 40% Cu/CeO₂ is probably the absence of carbon in the sample

Conclusion

Flame synthesis is an easy, single step method for the preparation of pure CeO₂ and the transition metal doped CeO₂ materials starting from aqueous solution of metal salts. From XPS it is clear that the transition metals in the CeO₂ are in an oxidized state and the metal ions may be on the surface of the CeO₂ lattice. The particle sizes of the synthesized materials are in the range of 3-10 nm and the BET surface area are in the range of 127-163 m²/g. Catalysts prepared in the flame synthesis method are WGS active and Cu/CeO₂ is better so far.

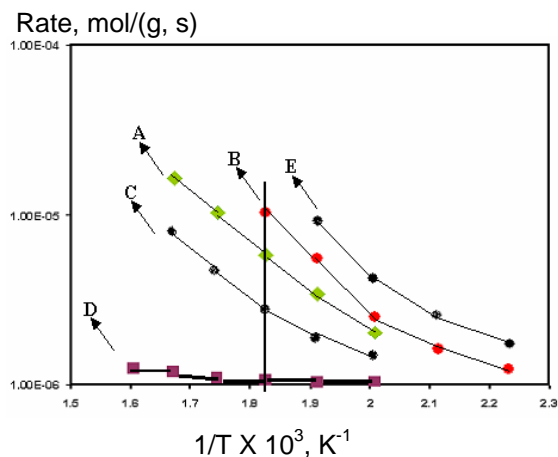


Figure 3. WGS activity of the prepared sample, (A) 15% Cu/CeO₂, (B) 40% Cu/CeO₂, (C) 40% Ni/CeO₂, (D) pure CeO₂, and (E) 700°C annealed 40% Cu/CeO₂.

Acknowledgement

We thank Amy Wingfield, Jason Repac, and Radhika Char for the help in making the materials, and Dr. Bindhu Varughese for the XPS measurements. Ranjan K. Pati and Sheryl H. Ehrman would like to thank U.S. Army Research Laboratory (ARL) for the financial and instrumental support through PEER program.

References

- Hirano, M.; Inagaki, M. *J. Mater. Chem.*, **2000**, 10, 473
- Steele, B.C.H. *Solid State Ionics*, **2000**, 129, 95
- Kubo, T.; Obayasi, H. *J. Electrochem. Soc.* **1975**, 122, 42
- Fornasiero, P.; Balducci, G.; DiMonte, R.; Kaspar, J.; Sergio, V.; Gubitosa, G.; Ferrero, A.; Maziani, G.; *J. Catal.*, **1996**, 164, 173
- Vanherle, J.; Horita, T.; Kawada, T.; Sakai, N.; Yokokawa, H.; Dokiya, M., *J. Am. Ceram. Soc.*, **1997** 80, 933
- Hirano, M.; Kato, E., *J. Am. Ceram. Soc.*, **1999**, 82, 786
- Martinez-Arias, A.; Fernandez-Garcia, M.; Ballesteros, V.; Salamanca, L.N.; Conesa, J.C.; Otero, C.; Soria, J., *Langmuir*, **1999**, 15, 4796
- Li, L.; Lin, X.; Li, G.; Inomata, H., *J. Mater. Res.*, **2001**, 16, 3207
- Bera, P.; Aruna, S.T.; Patil, K.C.; Hegde, M. S., *J. Catal.*, **1999**, 186, 36
- Zhou, Y.; Phillips, R.; Switzer, J.A., *J. Am. Ceram. Soc.*, **1995**, 78, 981

ENERGETIC CATALYST-HYDROGEN PLASMA REACTION AS A POTENTIAL NEW ENERGY SOURCE

R. L. Mills, Y. Lu, M. Nansteel, J. He, A. Voigt, W. Good, B. Dhandapani

BlackLight Power, Inc., 493 Old Trenton Road, Cranbury, NJ 08512

Introduction

Theoretical Predictions. The basic spectral emission of pure helium and hydrogen light sources have been well known for about a century. Recently, however, unique vacuum ultraviolet (VUV) emission lines were found at predicted wavelengths and reported in numerous publications [1-5]. For example, extreme ultraviolet (EUV) spectroscopy was recorded on microwave discharges of helium with 2% hydrogen. Novel emission lines were observed with energies of $q \cdot 13.6 \text{ eV}$, $q = 1, 2, 3, 7, 9, 11$. or $q \cdot 13.6 \text{ eV}$, $q = 4, 6, 8$ less 21.2 eV corresponding to inelastic scattering of these photons by helium atoms due to excitation of $\text{He}(1s^2)$ to $\text{He}(1s^1 2p^1)$. These strong emissions are not found in any single gas plasma, and cannot be assigned to the known emission of any species of the single gases studied such as H , H^- , H_2 , H_2^+ , H_3^+ , He , He_2^+ , and He^+ , known species of the mixture such as He_2^+ , HeH^+ , HeH , HHe_2^+ , and HHe_n^+ and possible contaminants [1], or doubly excited states [6]. However the results can be explained by a novel catalytic reaction of atomic hydrogen [1-5] to lower-energy states given by Rydberg's equation

$$E_n = -\frac{e^2}{n^2 8\pi\epsilon_0 a_H} = -\frac{13.598 \text{ eV}}{n^2} \quad (1a)$$

where

$$n = \frac{1}{2}, \frac{1}{3}, \frac{1}{4}, \dots, \frac{1}{p}; \quad p \leq 137 \text{ is an integer} \quad (1b)$$

replaces the well known parameter

$$n = 1, 2, 3, \dots \quad (1c)$$

for hydrogen excited states.

The theory reported previously [1-5, 7-12] predicts that atomic hydrogen may undergo a catalytic reaction with certain atoms, excimers, and ions which provide a reaction with a net enthalpy of an integer multiple of the potential energy of atomic hydrogen, $E_h = 27.2 \text{ eV}$ where E_h is one hartree. Specific species (e.g.

He^+ , Ar^+ , Sr^+ , and K) identifiable on the basis of their known electron energy levels are required to be present in plasmas with atomic hydrogen to catalyze the process. In contrast, species such as atoms or ions of Kr , Xe , Na , or Mg do not fulfill the catalyst criterion—a chemical or physical process with an enthalpy change equal to an integer multiple of E_h that is sufficiently reactive with atomic hydrogen under reaction conditions. The highly exothermic reaction involves a nonradiative energy transfer followed by $q \cdot 13.6 \text{ eV}$ emission or $q \cdot 13.6 \text{ eV}$ transfer to H to form extraordinarily hot H [1, 10-16] and a hydrogen atom that is lower in energy than unreacted atomic hydrogen that corresponds to a fractional principal quantum number given by Eq. (1b). That is, the

$n = 1$ state of hydrogen and the $n = \frac{1}{\text{integer}}$ states of hydrogen are nonradiative, but a transition between two nonradiative states, say

$n = 1$ to $n = 1/2$, is possible via a nonradiative energy transfer. A catalyst provides a net positive enthalpy of reaction of $m \cdot 27.2 \text{ eV}$ (i.e. it resonantly accepts the nonradiative energy transfer from hydrogen atoms and releases the energy to the surroundings to affect electronic transitions to fractional quantum energy levels). As a consequence of the nonradiative energy transfer, the hydrogen atom becomes unstable and emits further energy until it achieves a lower-energy nonradiative state having a principal energy level given by Eqs. (1a) and (1b).

Prior related studies that support the possibility of a novel reaction of atomic hydrogen which produces hydrogen in fractional quantum states that are at lower energies than the traditional “ground” ($n = 1$) state include extreme ultraviolet (EUV) spectroscopy [1-5, 9-12, 15, 17-24, 26-28], characteristic emission from catalysts and the hydride ion products [11-12, 17-20, 23-24], lower-energy hydrogen emission [1-5], chemically formed plasmas [9-12, 17-24], Balmer α line broadening [1, 2, 10-17, 20, 23-24, 26-27], population inversion of H lines [23-26], elevated electron temperature [13-15, 27], anomalous plasma afterglow duration [21-22], power generation [2, 4, 15, 20, 27, 29], and analysis of novel chemical compounds [20, 30-33].

$\text{H}(1/p)$ may react with a proton, and two $\text{H}(1/p)$ may react to form $\text{H}_2(1/p)^+$ and $\text{H}_2(1/p)$, respectively. The hydrogen molecular ion and molecular charge and current density functions, bond distances, and energies were solved previously [8] from the Laplacian in ellipsoidal coordinates with the constraint of nonradiation. The bond dissociation energy, E_D , of hydrogen molecular ion $\text{H}_2(1/p)^+$ was given as

$$E_D = p^2 2.535 \text{ eV} + p^3 0.118755 \text{ eV} \quad (2)$$

where p is an integer. The bond dissociation energy, E_D , of hydrogen molecule $\text{H}_2(1/p)$ E_D was given previously as

$$E_D = p^2 4.151 \text{ eV} + p^3 0.326469 \text{ eV} \quad (3)$$

The vibrational and rotational energies of fractional-Rydberg-state hydrogen molecular ion $\text{H}_2(1/p)^+$ and molecular hydrogen $\text{H}_2(1/p)$ are p^2 those of H_2^+ and H_2 , respectively. Thus, the vibrational energies, E_{vib} , for the $v = 0$ to $v = 1$ transition of hydrogen-type molecular ions $\text{H}_2(1/p)^+$ are [8]

$$E_{vib} = p^2 0.271 \text{ eV} \quad (4)$$

where p is an integer and the experimental vibrational energy for the $v = 0$ to $v = 1$ transition of H_2^+ , $E_{\text{H}_2^+}(v=0 \rightarrow v=1)$, is given by Karplus and Porter [34] and NIST [35]. Similarly, the vibrational energies, E_{vib} , for the $v = 0$ to $v = 1$ transition of hydrogen-type molecules $\text{H}_2(1/p)$ are [8]

$$E_{vib} = p^2 0.515902 \text{ eV} \quad (5)$$

where p is an integer and the experimental vibrational energy for the $v = 0$ to $v = 1$ transition of H_2 , $E_{\text{H}_2}(v=0 \rightarrow v=1)$, is given by Beutler [36] and Herzberg [37]. The rotational energies, E_{rot} , for the J to $J + 1$ transition of hydrogen-type molecules $\text{H}_2(1/p)$ are [8]

$$E_{rot} = E_{J+1} - E_J = \frac{\hbar^2}{I} [J + 1] = p^2 (J + 1) 0.01509 \text{ eV} \quad (6)$$

where p is an integer, I is the moment of inertia, and the experimental rotational energy for the $J=0$ to $J=1$ transition of H_2 is given by Atkins [38]. The p^2 dependence of the rotational energies results from an inverse p dependence of the internuclear distance and the corresponding impact on I . The predicted internuclear distances $2c'$ for $H_2(1/p)$ are

$$2c' = \frac{a_o \sqrt{2}}{p} \quad (7)$$

Experiments to Test the Theoretical Predictions. The reaction Ar^+ to Ar^{2+} has a net enthalpy of reaction of 27.63 eV; thus, it may serve as a catalyst to form $H(1/2)$. The product of the catalysis reaction, $H(1/2)$, may further serve as both a catalyst and a reactant to form $H(1/4)$ [2-3]. Also, the second ionization energy of helium is 54.4 eV; thus, the ionization reaction of He^+ to He^{2+} has a net enthalpy of reaction of 54.4 eV which is equivalent to $2 \cdot 27.2$ eV. The product of the catalysis reaction, $H(1/3)$, may further serve as both a catalyst and a reactant to form $H(1/4)$ and $H(1/2)$ [2-3].

Since $H_2(1/2)^+$ is a resonant state of $H_2(1/4)^+$, the reaction designated



wherein $H(1/4)$ reacts with a proton to form $H_2(1/4)^+$ is possible with strong emission through vibronic coupling with the resonant state $H_2(1/2)^+$. The energies, E_{D+vib} , of this series due to vibration in the transition state given previously [28] are

$$E_{D+vib} = E_D(H_2(1/4)^+) - \left(\nu^* + \frac{1}{2} \right) 2^2 E_{vib H_2^+} \quad (9)$$

$$= 48.16 - \left(\nu^* + \frac{1}{2} \right) 1.172 \text{ eV} \quad , \quad \nu^* = 0, 1, 2, 3, \dots$$

where $E_D(H_2(1/4)^+)$ is the bond energy of $H_2(1/4)^+$ given by Eq. (2) and $E_{vib H_2^+}$ is the transition-state vibrational energy of H_2^+ given by Eq. (108) of Ref. [8]. In Eq. (9), ν^* refers to vibrational energies of the transition state which must have equal energy separation as a requirement for resonant emission [8, 28]. Thus, anharmonicity is not predicted. The series is predicted to end at 25.74 nm corresponding to the predicted $H_2(1/4)^+$ bond energy of 48.16 eV given by Eq. (2).

The present paper tests theoretical predictions [1-5, 7-12] that atomic and molecular hydrogen form stable states of lower energy than traditionally thought possible. Substantial spectroscopic and physical differences are anticipated. For example, novel EUV atomic, molecular ion, and molecular spectral emission lines from transitions corresponding to energy levels given by Eqs. (1a) and (1b), Eqs. (2) and (4), and Eqs. (3) and (5-7), respectively, are predicted. The atomic lines have been shown previously [1-4, 27] as well as a series of unique EUV lines assigned to $H_2(1/2)$ [4]. To test additional predictions, EUV spectroscopy was performed to search for emission that was characteristic of and identified $H_2(1/4)^+$ and $H_2(1/4)$. Low pressure plasmas are more highly ionized. Thus, we further investigated the emission of the

$H_2(1/4)^+$ vibrational series given by Eq. (9) from microwave discharges of helium-hydrogen and argon-hydrogen mixtures.

The rotational energies provide a very precise measure of I and the internuclear distance using well established theory [34]. Neutral molecular emission was anticipated for high pressure argon-hydrogen plasmas excited by a 15 keV electron beam. Rotational lines for $H_2(1/4)$ were anticipated and sought in the 150-250 nm region. The spectral lines were compared to those predicted by Eqs. (5-6) corresponding to the internuclear distance of $1/4$ that of H_2 given by Eq. (7). The predicted energies for the $\nu=1 \rightarrow \nu=0$ vibration-rotational series of $H_2(1/4)$ (Eqs. (5-6)) are

$$E_{vib-rot} = p^2 E_{vib H_2(\nu=0 \rightarrow \nu=1)} \pm p^2 (J+1) E_{rot H_2}$$

$$= 4^2 E_{vib H_2(\nu=0 \rightarrow \nu=1)} \pm 4^2 (J+1) E_{rot H_2} \quad , \quad J = 0, 1, 2, 3, \dots \quad (10)$$

$$= 8.254432 \text{ eV} \pm (J+1) 0.24144 \text{ eV}$$

for $p = 4$.

The product $H_2(1/p)$ gas predicted to liquefaction at a higher temperature than H_2 [28]. Helium-hydrogen (90/10%) plasma gases were flowed through a high-vacuum (10^{-6} Torr) capable, liquid nitrogen (LN) cryotrap, and the condensed gas was characterized by 1H nuclear magnetic resonance (NMR) of the LN-condensable gas dissolved in $CDCl_3$. Other sources of hydrogen such as hydrocarbons were eliminated by mass spectroscopy (MS) and Fourier transform infrared spectroscopy (FTIR). The 1H NMR resonance of $H_2(1/p)$ is predicted to be upfield from that of H_2 due to the fractional radius in elliptic coordinates [7-8] wherein the electrons are significantly closer to the nuclei. The predicted shift, $\frac{\Delta B_T}{B}$, for $H_2(1/p)$ derived previously [7-8] is given by the sum of that of H_2 and a relativistic term that depends on $p > 1$:

$$\frac{\Delta B_T}{B} = -\mu_0 \left(4 - \sqrt{2} \ln \frac{\sqrt{2}+1}{\sqrt{2}-1} \right) \frac{e^2}{36a_0 m_e} (1 + \pi \alpha (p-1)) \quad (11)$$

$$\frac{\Delta B_T}{B} = -(28.01 + 0.64(p-1)) \text{ ppm} \quad (12)$$

where for H_2 there is no relativistic effect and $p = \text{integer} > 1$ for $H_2(1/p)$.

The exothermic helium plasma catalysis of atomic hydrogen was shown previously [13-14] by the observation of an average hydrogen atom temperature of 180-210 eV for helium-hydrogen mixed plasmas versus ≈ 3 eV for hydrogen alone. Since the electronic transitions are very energetic, power balances of helium-hydrogen plasmas compared to control krypton plasmas were measured using water bath calorimetry to determine whether this reaction has sufficient kinetics to merit its consideration as a practical power source.

$2K^+$ to $K + K^{2+}$ and K to K^{3+} also provide a reaction with a net enthalpy equal to one and three times the potential energy of atomic hydrogen, respectively. The presence of these gaseous ions or atoms with thermally dissociated hydrogen formed a so-called resonance transfer (rt)-plasma having strong VUV emission with a stationary inverted Lyman population [9, 17, 19-24]. Significant line broadening of the Balmer α , β , and γ lines of 18 eV was observed, compared to 3-4 eV from a hydrogen microwave plasma

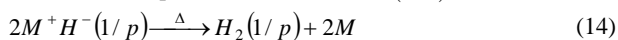
[17, 23-24]. Emission from rt-plasmas occurred even when the electric field applied to the plasma was zero [21-22]. Light output per unit power input up to 8600 times that of the control standard light sources as also observed from certain rt-plasmas [10-12]. The reaction was exothermic since excess power of $20 \text{ mW} \cdot \text{cm}^{-3}$ was measured by Calvet calorimetry [20]. An energetic catalytic reaction was proposed involving a resonant energy transfer between hydrogen atoms and $2K^+$ or K to form very stable novel hydride ions $H^-(1/p)$ called hydrino hydrides having a fractional principal quantum numbers $p=2$ and $p=4$, respectively. Characteristic emission was observed from K^{2+} and K^{3+} that confirmed the resonant nonradiative energy transfer of 27.2 eV and $3 \cdot 27.2 \text{ eV}$ from atomic hydrogen to $2K^+$ and K , respectively. The product hydride ion $H^-(1/4)$ was observed spectroscopically at 110 nm corresponding to its predicted binding energy of 11.2 eV [17, 19, 20].

In addition to liquefaction at liquid nitrogen temperature, $H_2(1/p)$ gas was also isolated by decomposition of compounds found to contain the corresponding hydride ions $H^-(1/p)$. The total shift, $\frac{\Delta B_T}{B}$, was calculated previously [6, 20] for the hydride ions $H^-(1/p)$ having a fractional principal quantum number. The shift was given by the sum of that of ordinary hydride ion H^- and a component due to a relativistic effect:

$$\frac{\Delta B_T}{B} = -\mu_0 \frac{e^2}{12m_e a_0 (1 + \sqrt{s(s+1)})} (1 + \alpha 2\pi(p-1)) = -(29.9 + 1.37(p-1)) \text{ ppm} \quad (13)$$

where for H^- there is no relativistic effect and $p = \text{integer} > 1$ for $H^-(1/p)$. The experimental absolute resonance shift of tetramethylsilane (TMS) is -31.5 ppm relative to the proton's gyromagnetic frequency [39, 40]. The results of ^1H MAS NMR spectroscopy were given previously [20, 31-32] on control and novel hydrides synthesized using atomic potassium as a hydrogen catalyst wherein the triple ionization reaction of K to K^{3+} , has a net enthalpy of reaction of 81.7766 eV , which is equivalent to $3 \cdot 27.2 \text{ eV}$. The KH experimental shift of $+1.3 \text{ ppm}$ relative to TMS corresponding to absolute resonance shift of -30.2 ppm matched very well the predicted shift of H^- of -30 ppm given by Eq. (13). The ^1H MAS NMR spectrum of novel compound $KH * Cl$ relative to external tetramethylsilane (TMS) showed a large distinct upfield resonance at -4.4 ppm corresponding to an absolute resonance shift of -35.9 ppm that matched the theoretical prediction of $p = 4$. A novel peak of $KH * I$ at -1.5 ppm relative to TMS corresponding to an absolute resonance shift of -33.0 ppm matched the theoretical prediction of $p = 2$. The predicted catalyst reactions, position of the upfield-shifted NMR peaks, and spectroscopic data for $H^-(1/2)$ and $H^-(1/4)$ were found to be in agreement [7, 20].

The decomposition reaction of $H^-(1/p)$ is

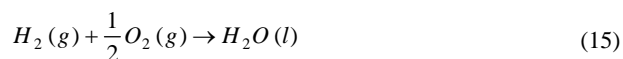


where M^+ is a metal ion. NMR peaks of $H_2(1/p)$ given by Eqs. (11-12) provide a direct test of whether compounds such as $KH * I$

contain hydride ions in the same fractional quantum state p . Furthermore, the observation of a series of singlet peaks upfield of H_2 with a predicted integer spacing of 0.64 ppm provides a powerful means to confirm the existence of $H_2(1/p)$.

Since atomic hydrogen and K atoms are formed by reduction at the cathode of an aqueous K_2CO_3 electrolysis cell and K^+ ions present in the electrolyte as well as the K atoms contact the atomic hydrogen at the cathode, the catalysis of atomic hydrogen to fractional Rydberg states was also predicted to occur in these cells. The electrolysis reaction is supported by the observation of novel hydride compounds that were reported previously [33]. For example, after 10^4 hours of continuous aqueous electrolysis with K_2CO_3 as the electrolyte, highly stable novel inorganic hydride compounds such as $KH KHCO_3$ and KH were isolated and identified by time of flight secondary ion mass spectroscopy (ToF-SIMS). The existence of novel hydride ions was determined using X-ray photoelectron spectroscopy (XPS) and ^1H MAS NMR.

The energy given off during catalysis is much greater than the energy initially transferred to the catalyst, and the energy released is large as compared to conventional chemical reactions. For example, when hydrogen and oxygen gases undergo combustion to form water



the known enthalpy of formation of water is $\Delta H_f = -286 \text{ kJ/mole}$ or 1.48 eV per hydrogen atom. By contrast, each ($n=1$) ordinary hydrogen atom undergoing a catalysis step to $n = \frac{1}{2}$ releases a net of 40.8 eV . Moreover, further catalytic transitions may occur: $n = \frac{1}{2} \rightarrow \frac{1}{3}, \frac{1}{3} \rightarrow \frac{1}{4}, \frac{1}{4} \rightarrow \frac{1}{5}$, and so on. Once catalysis begins, $H(1/p)$ atoms autocatalyze further in a process called disproportionation discussed previously [2-3, 7].

The power corresponding to the exothermic reaction to form H states given by Eqs. (1a) and (1b) was studied by measuring the temperature of the electrolyte of a K_2CO_3 electrolytic cell for a given input electrolysis power compared to the heat loss of the electrolyte using a resistive heater. For sodium, no electrocatalytic reaction of approximately 27.2 eV is possible by the transfer of an electron between two Na^+ ions as is the case with K^+ . Thus, Na_2CO_3 served as a control electrolyte. $H_2(1/p)$ formed from the product $H(1/p)$ has an internuclear distance of $1/p$ times that of H_2 ; thus, it is predicted to have a higher mobility through metals than H_2 . This provided a means to enrich and isolate $H_2(1/p)$ by differential diffusion through a hollow nickel cathode. The collected gas was dissolved in dissolved in $CDCl_3$ and characterized by ^1H NMR which has the capability to measure the energy state of hydrogen according to Eqs. (11-12) with the elimination of hydrocarbons as the source of the peaks by FTIR. Since the ionization energy of $H_2(1/2)$ is about a factor of four times that of H_2 ($IP_1(H_2(1/2)) = 62.53 \text{ eV}$ versus $IP_1(H_2) = 15.426 \text{ eV}$) [7-8, 28], the mass spectral $m/e = 2$ ion current as a function of time was recorded while changing the

electron gun energy from 30 to 70 eV for ultrapure hydrogen and the gas collected electrolysis gases.

Experimental

To investigate the vibrational series of $H_2(1/4)^+$, EUV spectra (20–65 nm) were recorded on light emitted from microwave discharge plasmas of helium, argon, krypton, or xenon or a mixture of 10% hydrogen with each noble gas. Each ultrapure (99.999+%) test gas or mixture was flowed through a half inch diameter quartz tube at 100 mTorr maintained with a total gas flow rate of 10 sccm. The tube was fitted with an Ophos coaxial microwave cavity (Evenson cavity). The microwave generator was an Ophos Model MPG-4M generator (Frequency: 2450 MHz). The input power to the plasma was set at 40 W.

The spectrometer was a McPherson 4° grazing incidence EUV spectrometer (Model 248/310G) equipped with a grating having 600 G/mm with a radius of curvature of ≈ 1 m that covered the region 5–65 nm. The angle of incidence was 87°. The wavelength resolution was about 0.1 nm (FWHM) with an entrance and exit slit width of 40 μ m. A CEM was used to detect the EUV light. The increment was 0.01 nm and the dwell time was 1 s.

Vibration-rotational emission of $H_2(1/4)$ was investigated using an electron gun described previously [41, 42] to initiate argon plasmas with 1% hydrogen in the pressure range of 450–1000 Torr. The plasma cell was flushed with oxygen, then pumped down, flushed with argon-hydrogen (99/1%), and filled with argon-hydrogen (99/1%). Krypton replaced argon in the controls, and argon, hydrogen, oxygen, nitrogen, water vapor, nitrogen-oxygen (50/50%), and argon or krypton with oxygen addition up to 100% oxygen served as further controls. The Ar^+ catalyst mechanism was tested by atmospheric-pressure-plasma-gas flow at 75 sccm and nonflow conditions. The electrons were accelerated with a high voltage of 12.5 keV at a beam current of 10 μ A. The electron gun was sealed with a thin (300 nm thickness) SiN_x foil that served as a 1 mm² electron window to the cell at high gas pressure (760 Torr). The beam energy was deposited by hitting the target gases, and the light emitted by beam excitation exited the cell through a MgF_2 window mounted at the entrance of a normal incidence McPherson 0.2 meter monochromator (Model 302) equipped with a 1200 lines/mm holographic grating with a platinum coating. The resolution was 0.5 nm (FWHM) at an entrance and exit slit width of 100 μ m. The increment was 0.1 nm and the dwell time was 1 s. The PMT (Model R8486, Hamamatsu) used has a spectral response in the range of 115–320 nm with a peak efficiency at about 225 nm. The emission was essentially flat for $200 < \lambda < 275$ nm, but a notch in the response of about 20% existed in the short wavelength range with a minimum at 150 nm. Peak assignments were determined by an external calibration against standard line emissions.

Condensable gas from helium-hydrogen (90/10%) microwave plasmas maintained in the Evenson cavity was collected in a high-vacuum (10^{-6} Torr) capable, LN cryotrap described previously [28]. After each plasma run the cryotrap was pumped down to 10^{-5} Torr to remove any non-condensable gases in the system. The pressure was recorded as a function of time as the cryotrap was warmed to room temperature. Typically, about 45 μ moles of condensed gas was collected in a 2 hr plasma run. Controls were hydrogen and helium alone.

The mass spectra ($m/e = 1$ to $m/e = 200$) of ultrahigh purity (99.999+%) hydrogen (Praxair) control samples and samples of the condensable gas from the helium-hydrogen microwave plasmas were recorded with a residual gas analyzer.

Premixed He/H_2 (90/10%) was flowed from a supply bottle through a metering valve and a LN trap just upstream of a 700 mTorr Evenson microwave plasma. A second LN trap downstream of the plasma tube was used to remove any water vapor generated by the plasma. The plasma gas, devoid of impurities due to the LN traps, was flowed through a long capillary tube which was maintained in the temperature range ~ 12 –17 K by a cryo-cooler described previously [28]. Residual gas was pumped from the capillary, condensable gas was collected over a period of several hours, and the system was evacuated to 10^{-5} Torr to remove any non-condensable gases in the system. Controls were hydrogen and helium alone. Two capillary valves were closed to trap any vaporizing gas as the cryo-cooler was stopped, and the tube was warmed to room temperature. Typically about 100 mTorr of gas was collected over a 24 to 48 hour period and then analyzed by mass spectroscopy and compared with the results for a control sample collected in the same way, except that no plasma was present.

Sealed 1H NMR samples were prepared by collecting the condensed gas from the cryotrap in $CDCl_3$ solvent (99.99% Cambridge isotopes) in an NMR tube (5 mm OD, 23 cm length, Wilmad) maintained at LN-temperature which was then sealed as described previously [28]. Control NMR samples comprised ultrahigh purity hydrogen (Praxair) and the helium-hydrogen (90/10%) mixture with $CDCl_3$ solvent. The NMR spectra were recorded with a 300 MHz Bruker NMR spectrometer that was deuterium locked. The chemical shifts were referenced to the frequency of tetramethylsilane (TMS) at 0.00 ppm.

KH^*I that was prepared under long duration (two weeks) synthesis according to methods given previously [30–32], and about a one gram sample was placed in a thermal decomposition reactor under an argon atmosphere. The reactor comprised a 1/4" OD by 3" long quartz tube that was sealed at one end and connected at the open end with Swagelok™ fittings to a T. One end of the T was connected to the NMR tube containing $CDCl_3$ solvent, and the other end was attached to a turbo pump. The apparatus was evacuated to less than 1 milliTorr with the $CDCl_3$ maintained at LN temperature. The sample was heated to 200 °C under vacuum. A valve to the pump was closed, and the sample was heated in the evacuated quartz chamber containing the sample to above 600 °C until the sample melted. Gas released from the sample was collected in the $CDCl_3$ solvent, the NMR tube was sealed and warmed to room temperature, and the NMR spectrum was recorded. Using identical samples, the NMR-tube end of the collection apparatus was connected directly to the sampling port of a quadrupole mass spectrometer to test for hydrocarbon contamination. FTIR was also performed on the released gas for this purpose.

An NMR sample from KH^*I provided by BlackLight Power, Inc. was also prepared and analyzed at the Naval Air Warfare Center Weapons Division, Naval Air Warfare Center, China Lake, CA under the same procedure except that the $CDCl_3$ solvent was maintained at ice temperature during hydrogen gas collection, and the NMR spectrum was recorded with a 400 MHz instrument at China Lake. Control NMR samples of ultrapure hydrogen dissolved in $CDCl_3$ solvent were also prepared, and NMR spectra were

obtained under conditions matching those of the KH^*I -derived samples.

The excess power was measured by water bath calorimetry on helium-hydrogen (95/5%) plasmas maintained in a microwave discharge cell compared to control plasmas with the same input power as described previously [27]. The water bath was calibrated by a high precision heater and power supply. A high precision linear response thermistor probe (Omega OL-703) recorded the temperature of the 45 L water bath as a function of time for the stirrer alone to establish the baseline. The heat capacity was determined for several input powers, 30, 40, and 50 W \pm 0.01 W, and was found to be independent of input power over this power range within \pm 0.05%. The temperature rise of the reservoir as a function of time gave a slope in $^{\circ}\text{C/s}$. This slope was baseline corrected for the negligible stirrer power and loss to ambient. The constant known input power (J/s), was divided by this slope to give the heat capacity in J/ $^{\circ}\text{C}$. Then, in general, the total power output from the cell to the reservoir was determined by multiplying the heat capacity by the rate of temperature rise ($^{\circ}\text{C/s}$) to give J/s.

Since the cell and water bath system were adiabatic, the general form of the power balance equation with the possibility of excess power is:

$$P_{in} + P_{ex} - P_{out} = 0 \quad (16)$$

where P_{in} is the microwave input power, P_{ex} is the excess power generated from the hydrogen catalysis reaction, and P_{out} is the thermal power loss from the cell to the water bath. Since the cell was surrounded by water that was contained in an insulated reservoir with negligible thermal losses, the temperature response of the thermistor T as a function of time t was determined to be

$$\dot{T}(t) = (1.940 \times 10^5 \text{ J}/^{\circ}\text{C})^{-1} \times P_{out} \quad (17)$$

where $1.940 \times 10^5 \text{ J}/^{\circ}\text{C}$ is the heat capacity for the least square curve fit of the response to power input for the control experiments ($P_{ex} = 0$). The slope was recorded for about 2 hours after the cell had reached a thermal steady state, to achieve an accuracy of \pm 1%.

The power balance of the electrolysis of aqueous potassium carbonate (K^+ / K^+ and K catalysts) was determined using single cell 350 ml silvered vacuum jacketed dewars and compared with the results with the replacement of K_2CO_3 with Na_2CO_3 as described previously [29]. A linear calibration curve was obtained. Two methods of differential calorimetry were used to determine the cell constant which was used to calculate the excess enthalpy. First, the cell constant was calculated during the experiment (on-the-fly-calibration) by turning an internal resistance heater off and on, and inferring the cell constant from the difference between the losses with and without the heater. Second, the cell constant was determined with no electrolysis processes occurring by turning an internal resistance heater off and on for a well stirred matched dewar cell, and inferring the cell constant from the difference between the losses with and without the heater.

The general form of the energy balance equation for the cell in steady state is:

$$0 = P_{appl} + Q_{htr} + Q_{xs} - P_{gas} - Q_{loss} \quad (18)$$

where P_{appl} is the electrolysis power; Q_{htr} is the power input to the heater; Q_{xs} is the excess heat power generated by the hydrogen catalysis reaction; P_{gas} is the power removed as a result of evolution of H_2 and O_2 gases; and Q_{loss} is the thermal power loss from the cell. When an aqueous solution is electrolyzed to liberate

hydrogen and oxygen gasses, the electrolysis power $P_{appl} (= E_{appl}I)$ can be partitioned into two terms:

$$P_{appl} = E_{appl}I = P_{cell} + P_{gas} \quad (19)$$

An expression for $P_{gas} (= E_{gas}I)$ is readily obtained from the known enthalpy of formation of water from its elements:

$$E_{gas} = \frac{-\Delta H_{form}}{\alpha F} \quad (20)$$

(F is Faraday's constant), which yields $E_{gas} = 1.48V$ for the reaction



The net Faradaic efficiency of gas evolution is assumed to be unity; thus, Eq. (19) becomes

$$P_{cell} = (E_{appl} - 1.48V)I \quad (22)$$

The cell was calibrated for heat losses by turning an internal resistance heater off and on while maintaining constant electrolysis and by inferring the cell conductive constant from the difference between the losses with and without the heater where heat losses were primarily conductive losses through the cap of the dewar. When the heater was off, the losses were given by

$$c(T_c - T_b) = P_{appl} + 0 + Q_{xs} - P_{gas} \quad (23)$$

where c is the conductive heat loss coefficient; T_b is ambient temperature and T_c is the cell temperature. When a new steady state is established with the heater on, the losses change to:

$$c(T_c' - T_b) = P'_{appl} + Q_{htr} + Q'_{xs} - P'_{gas} \quad (24)$$

where a prime superscript indicates a changed value when the heater was on. When the following assumptions apply

$$Q_{xs} = Q'_{xs}; P_{appl} = P'_{appl}; P_{gas} = P'_{gas} \quad (25)$$

the cell constant or heating coefficient a , the reciprocal of the conductive loss coefficient (c), is given by the result

$$a = \frac{T_c' - T_c}{Q_{htr}} \quad (26)$$

In all heater power calculations, the following equation was used

$$Q_{htr} = E_{htr}I_{htr} \quad (27)$$

The experiments were carried out by observing and comparing the temperature difference ($\Delta T_1 = T(\text{electrolysis only}) - T(\text{blank})$) and ($\Delta T_2 = T(\text{resistor heating only}) - T(\text{blank})$) referred to unit input power, between two identical dewars. The heating coefficients were calculated from

$$a_1 = \frac{\Delta T_1}{P_{cell}} \quad (28)$$

$$a_2 = \frac{\Delta T_2}{Q_{htr}} \quad (29)$$

Then, the excess power is given by

$$Q_{xs} = \frac{\Delta T_1}{a_2} - P_{cell} \quad (30)$$

or

$$Q_{xs} = P_{cell} \left(\frac{a_1}{a_2} - 1 \right) \quad (31)$$

The heating coefficient was also determined "on the fly" by the addition of increments of ~ 0.1 W of heater power to the electrolytic cell where 24 hours was allowed for steady state to be achieved.

The temperature rise above ambient ($\Delta T_3 = T(\text{electrolysis} + \text{heater}) - T(\text{blank})$) was recorded as well as the electrolysis power and heater power. The heating coefficient, a_3 , in this case was given by the slope of the plot of ΔT_3 versus total input power ($P_{\text{cell}} + Q_{\text{htr}}$):

$$a_3 = \frac{\Delta T_3}{P_{\text{cell}} + Q_{\text{htr}}} \quad (32)$$

wherein the electrolysis heating power, P_{cell} , was kept constant. The heating coefficient a_3 and the temperature rise of the cell with electrolysis power only, ΔT_1 , were used to determine the total cell power comprising $P_{\text{cell}} + Q_{\text{xs}}$. Then, Q_{xs} was determined by subtracting P_{cell} :

$$Q_{\text{xs}} = \frac{\Delta T_1}{a_3} - P_{\text{cell}} \quad (33)$$

The electrolyte solution was 200 ml of 0.57 M aqueous K_2CO_3 (Aldrich $K_2CO_3 \cdot 3/2H_2O$ 99±%) or 200 ml of 0.57 M aqueous Na_2CO_3 (Aldrich Na_2CO_3 A.C.S. primary standard 99.95 ±%).

The cathode and anode comprised 24 meters of 0.38 mm diameter coiled nickel wire (99.8 % Alfa, cold drawn, clean Ni wire). The electrodes were cleaned by placing them in a beaker of 0.57 M $K_2CO_3/3\%$ H_2O_2 for 30 minutes and then rinsing it with distilled water. The leads were inserted into Teflon tubes to insure that no recombination of the evolving gases occurred. The Faraday efficiency was determined by measuring the volume of the evolved electrolysis gases. The power was applied as 83.0 mA constant current at a measured 1.95 V. When Na_2CO_3 replaced K_2CO_3 the power was applied as 83.0 mA constant current at a measured 3.26 V.

For heat measurement and electrolysis gas collection, the cathode comprised a 170 cm long nickel tubing cathode (Ni 200 tubing, 0.159 cm O.D., 0.107 cm I.D., with a nominal wall thickness of 0.0254 cm, MicroGroup, Inc., Medway, MA). The cathode was coiled into a 3.0 cm long helix with a 2.0 cm diameter about the central Pt anode. The cathode was cleaned by placing it in a beaker of 0.57 M $K_2CO_3/3\%$ H_2O_2 for 30 minutes and then rinsing it with distilled water. The power was applied as 101 mA constant current at a measured 1.86 V. The anode was a platinum basket (Johnson Matthey) with a 0.38 mm Ni lead wire. The leads were inserted into Teflon tubes to prevent recombination, if any, of the evolving gases. The cathode-anode separation distance was 1 cm.

An ultrahigh-vacuum system was used to collect sealed 1H NMR samples of the electrolysis gases from the hollow as described previously [29]. The NMR spectra were recorded with the 300 MHz Bruker NMR spectrometer that was deuterium locked. The chemical shifts were referenced to the frequency of tetramethylsilane (TMS) at 0.00 ppm. Hydrocarbon contamination in the samples was eliminated by mass spectroscopic analysis and by FTIR spectral analysis.

The mass spectra ($m/e = 1$ to $m/e = 200$) of ultrahigh purity hydrogen (Praxair) control samples and samples of the electrolysis gases collected in the hollow nickel cathode from K_2CO_3 and Na_2CO_3 cells were recorded with a residual gas analyzer. In addition, the ion current as a function of time of the mass to charge ratio of two ($m/e = 2$) was recorded while changing the electron gun energy from 30 to 70 eV for ultrapure hydrogen and the

electrolysis gas from the hollow cathode connected directly to a needle valve on the sampling port mass spectrometer. The pressure of the sample gas in the mass spectrometer was kept the same for each experiment by adjusting the needle value of the mass spectrometer. The entire range of masses through $m/e = 200$ was measured before and after the determinations at $m/e = 1$ and $m/e = 2$.

Results and Discussion

EUV spectroscopy of Helium-Hydrogen and Argon-Hydrogen Plasmas. *Detection of Fractional Rydberg State Hydrogen Molecular Ion $H_2(1/4)^+$.* In the case of the EUV spectra of helium, krypton, xenon, krypton-hydrogen (90/10%), or xenon-hydrogen (90/10%), no peaks were observed below 65 nm, and no spurious peaks or artifacts due to the grating or the spectrometer were observed. No changes in the emission spectra were observed by the addition of hydrogen to noncatalysts krypton or xenon. Only known atom and ion peaks were observed in the EUV spectrum of the helium and argon microwave discharge emission.

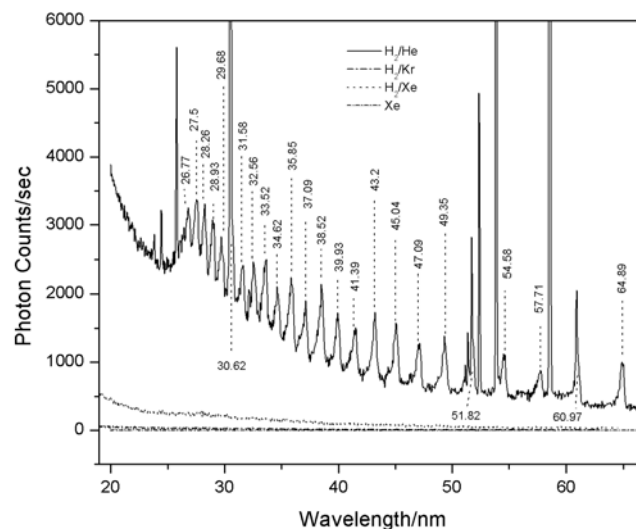


Figure 1. The EUV spectra (20-65 nm) of microwave plasmas of xenon and 10% hydrogen mixed with helium, krypton, and xenon. A vibrational pattern of peaks with an energy spacing of 1.18 eV was observed from the helium-hydrogen plasma having He^+ catalyst. The peaks matched Eq. (9) for $\nu^* = 0, 1, 2, 3, \dots, 24$. The series terminated at about 25.7 nm corresponding to the predicted bond energy of $H_2(1/4)^+$ of 48.16 eV given by Eq. (2). No emission was observed from the noncatalyst controls, krypton and xenon alone or with hydrogen. The sharp peaks in the spectrum were assigned to He I and He II.

The EUV spectra (20-65 nm) of the microwave plasmas of xenon and 10% hydrogen mixed with helium, krypton, and xenon are shown in Figure 1. No emission was observed from the noncatalyst controls, krypton and xenon. A characteristic vibrational series was observed for helium-hydrogen (90/10%), but at higher energies than any known molecule by about an order of magnitude. The series was not observed with helium alone as shown in Figure 2. The energies of the peaks observed in Figures 1 and 2 are plotted in Figure 3 as a function of peak number or integer ν^* . The slope of the linear curve fit in Figure 3 is 1.18 eV, and the intercept is 47.6 eV which matches the predicted series given by Eq.

(9) to within the spectrometer resolution of 1%. This energy separation matches the transition-state vibrational energy of the resonant state $H_2(1/2)^+$, and the series terminates at about 25.7 nm corresponding to the predicted bond energy of $H_2(1/4)^+$ of 48.16 eV given by Eq. (2). Thus, emission in this region was due to the reaction $H(1/4)+H^+ \rightarrow H_2(1/4)^+$ with vibronic coupling with the resonant state $H_2(1/2)^+$ within the transition state. The predicted emission at $E_{D+vib} = E_D(H_2(1/4)^+) - \left(\nu^* + \frac{1}{2}\right)2^2 E_{vib H_2^+}$ was observed for $\nu^* = 0, 1, 2, 3, \dots, 24$. All other peaks in the spectra were assigned to He I and He II.

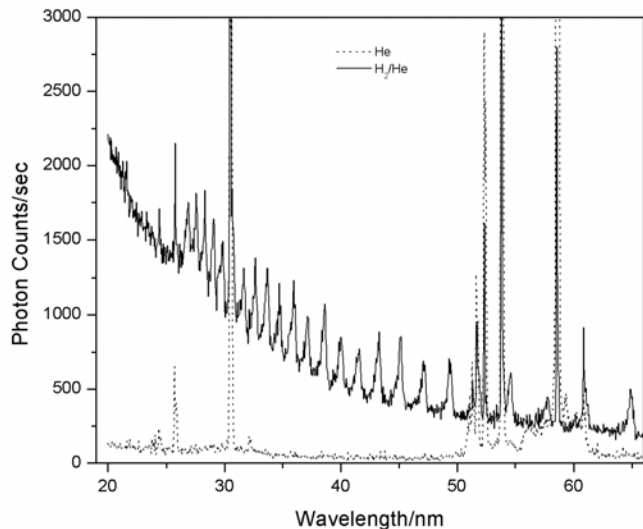


Figure 2. The EUV spectra (20-65 nm) of microwave plasmas of helium-hydrogen (90/10%) (solid) and helium alone (dashed). The vibrational series of peaks assigned to the reaction $H(1/4)+H^+ \rightarrow H_2(1/4)^+$ was observed from the helium-hydrogen plasma having He^+ catalyst and hydrogen, but not from helium alone. The sharp peaks in the spectrum were assigned to He I and He II.

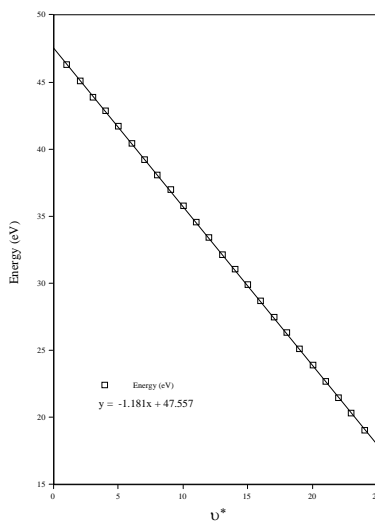


Figure 3. The plot of the energies of the peaks shown in Figures 1 and 2. The slope of the linear curve fit is 1.18 eV, and the intercept is 47.6 eV which matches the predicted emission given by Eq. (9) to within the spectrometer resolution of about 1%.

The EUV spectra (20-65 nm) of microwave plasmas of argon-hydrogen (90/10%) compared with argon alone are shown in Figure 4. The vibrational series of peaks with an energy spacing of 1.18 eV was observed from the argon-hydrogen plasma having Ar^+ catalyst with hydrogen. In contrast, the series was not observed without hydrogen. The peaks matched Eq. (9) for $\nu^* = 0, 1, 2, 3, \dots, 24$.

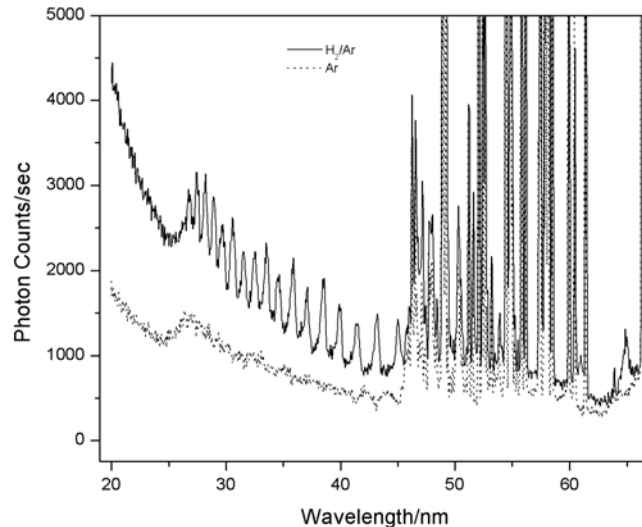


Figure 4. The EUV spectra (20-65 nm) of microwave plasmas of argon-hydrogen (90/10%) (solid) and argon alone (dashed). The vibrational series of peaks assigned to the reaction $H(1/4)+H^+ \rightarrow H_2(1/4)^+$ was observed from the argon-hydrogen plasma having Ar^+ catalyst and hydrogen, but not from argon alone. The sharp peaks in the spectrum were assigned to Ar II.

Detection of Fractional Rydberg State Molecular Hydrogen $H_2(1/4)$. The observation of emission due to the reaction $H(1/4)+H^+ \rightarrow H_2(1/4)^+$ at low pressure (< 1 Torr) shown in Figures 1 and 2 indicates that $H(1/4)$ formed in the argon-hydrogen plasma. Molecular formation was anticipated under high-pressure conditions (~760 Torr). Thus, EUV spectroscopy of argon-hydrogen plasmas was performed to search for $H_2(1/4)$ from $H(1/4)$ formed by Ar^+ as a catalyst using a 15 keV electron beam to maintain the plasma and to collisionally excite vibration-rotational states of $H_2(1/4)$. The corresponding emission provides a direct measure of the internuclear distance; thus, this method provides the possibility of direct confirmation of $H_2(1/4)$.

The 100-350 nm spectrum of a 450 Torr plasma of argon containing about 1% hydrogen is shown in Figure 5. Lyman α was observed at 121.6 nm with an adjoining H_2 band, the third continuum of Ar was observed at 200 nm, O I was observed at 130.6 nm, and the $OH(A-X)$ band was observed at 309.7 nm. A series of sharp, evenly-spaced lines was observed in the region 145-185 nm. The only possibilities for peaks of the instrument width are those due to rotation or electronic emission from atoms or ions. The

series was not observed when krypton replaced argon or with any of the controls and could not be assigned to any known species [28].

The series matched the P branch of $H_2(1/4)$ for the vibrational transition $\nu = 1 \rightarrow \nu = 0$. P(1), P(2), P(3), P(4), P(5), and P(6) were observed at 155.0 nm, 160.2 nm, 165.8 nm, 171.1 nm, 178.0 nm, and 183.2 nm, respectively. The sharp peak at 147.3 nm may be the first member of the R branch, R(0). Since the vibration-rotational transitions of $H_2(1/4)$ are allowed with nuclear spin-rotational coupling, the vibrational rotational spectrum of $H_2(1/4)$ was predicted to comprise only the R(0) line and the P branch [28] in agreement with observations. The slope of a linear curve fit was 0.241 eV with an intercept of 8.21 eV which matches Eq. (10) very well for $p = 4$. Using Eqs. (6) and (7) with the measured rotational energy spacing of 0.24 eV establishes an internuclear distance of $1/4$ that of the ordinary hydrogen species for $H_2(1/4)$. This technique which is the best measure of the bond distance of any diatomic molecule identifies and unequivocally confirms $H_2(1/4)$.

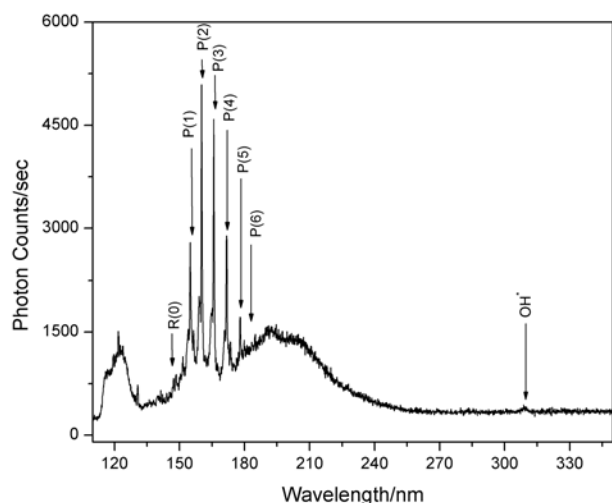


Figure 5. The 100-350 nm spectrum of a 450 Torr plasma of argon containing about 1% hydrogen and trace oxygen using a 15 keV electron gun. Lyman α was observed at 121.6 nm with an adjoining H_2 band, the third continuum of Ar was observed at 200 nm, O I was observed at 130.6 nm, and the $OH(A-X)$ band was observed at 309.7 nm. A series of sharp, evenly-spaced lines was observed in the region 145-185 nm. The series matched the P branch of $H_2(1/4)$ for the vibrational transition $\nu = 1 \rightarrow \nu = 0$. P(1), P(2), P(3), P(4), P(5), and P(6) were observed at 155.0 nm, 160.2 nm, 165.8 nm, 171.1 nm, 178.0 nm, and 183.2 nm, respectively. The sharp peak at 147.3 nm may be the first member of the R branch, R(0). The slope of a linear curve fit is 0.241 eV with an intercept of 8.21 eV which matches Eq. (10) very well for $p = 4$.

The Ar^+ catalyst mechanism was confirmed by atmospheric-pressure-plasma-gas flow at 75 sccm and nonflow conditions. Flow does not change known atomic and ionic line emission such as the O I line at 130.6 nm. In contrast, the series assigned to vibration-rotation of $H_2(1/4)$ was observed under static conditions; whereas, the series decreased to about 10% with flow indicating a reaction involving the formation of intermediates as predicted.

A possible confirmation of the lines identified in this study has been published previously. Ulrich, Wieser, and Murnick [42] compared the third continuum of argon gas with a very pure gas and a spectrum in which the gas was slightly contaminated by oxygen as evidenced by the second order of the 130 nm resonance lines at 160 nm. A series of very narrow lines at the instrument width having an intensity profile that was characteristic of that of a P-branch were observed in the 145-185 nm region. These lines shown in Figure 6 of Ref. [42] matched those in Figure 5. The slope of the linear curve fit was 0.24 eV with an intercept of 8.24 eV which matches Eq. (10) very well for $p = 4$. The series matches the predicted $\nu = 1 \rightarrow \nu = 0$ vibrational energy of $H_2(1/4)$ of 8.25 eV (Eq. (5)) and its predicted rotational energy spacing of 0.24 eV (Eq. (6)) with $\Delta J = +1; J = 1, 2, 3, 4, 5, 6$ and $\Delta J = -1; J = 0$ where J is the rotational quantum number of the final state. With this assignment all of the peaks in Figure 6 of Ref. [42] could be identified; whereas, the evenly-spaced lines could not be unambiguously assigned by Ulrich et al [42]. The series was not observed in krypton and xenon plasmas. The determination of the presence of the common contaminant, hydrogen, in the argon plasmas is warranted in future studies.

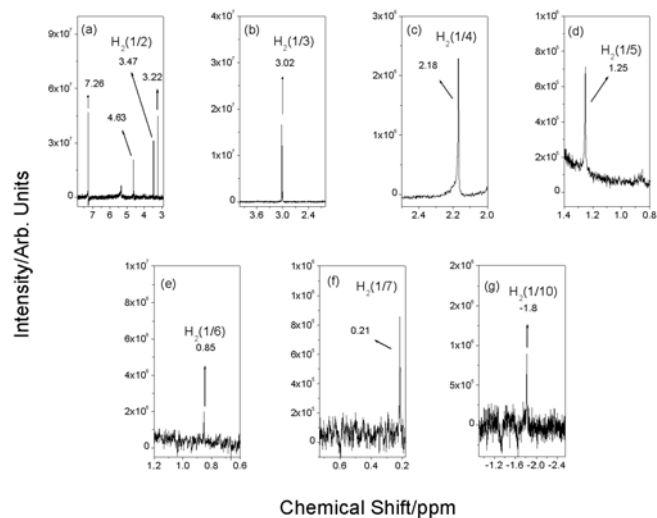


Figure 6 (a)-(g). 1H NMR spectra on sealed samples of liquid-nitrogen-condensable helium-hydrogen plasma gases dissolved in $CDCl_3$ relative to tetramethylsilane (TMS). The solvent peak was observed at 7.26 ppm, the H_2 peak was observed at 4.63 ppm, and a singlet at 3.22 ppm matched silane. Singlet peaks upfield of H_2 were observed at 3.47, 3.02, 2.18, 1.25, 0.85, 0.21, and -1.8 ppm relative to TMS corresponding to solvent-corrected absolute resonance shifts of -29.16, -29.61, -30.45, -31.38, -31.78, -32.42, and -34.43 ppm, respectively. Using Eq. (12), the data indicates that $p = 2, 3, 4, 5, 6, 7$, and 10, respectively. The data matched the series $H_2(1/2)$, $H_2(1/3)$, $H_2(1/4)$, $H_2(1/5)$, $H_2(1/6)$, $H_2(1/7)$, and $H_2(1/10)$.

Isolation and Characterization of $H_2(1/p)$. Cryotrap Pressure Helium-hydrogen (90/10%) gas was flowed through the microwave tube and the cryosystem for 2 hours with the trap cooled to LN temperature. No change in pressure over time was observed when the dewar was removed, and the system was warmed to room temperature. The experiment was repeated under the same

conditions but with a plasma maintained with 60 W forward microwave power and 10 W reflected. In contrast to the control case, a liquid-nitrogen-condensable gas was generated in the helium-hydrogen plasma reaction since the pressure due to the reaction product rose from 10^{-5} Torr to 3 Torr as the cryotrap warmed to room temperature.

Mass Spectroscopy. The mass spectrum for the gases collected in the cryotrap from the He/H_2 (90/10%) plasma over the range $m/e=1$ to $m/e=200$ showed that the LN-condensable gas was highly pure hydrogen. The mass spectrum ($m/e=1$ to $m/e=200$) for the gases collected in the cryo-cooler from the He/H_2 (90/10%) plasma only showed peaks in the ($m/e=1$ to $m/e=50$) region. The $m/e=2$ peak was 40-50 times more intense than the $m/e=28$ (nitrogen), $m/e=32$ (oxygen), and $m/e=40$ (argon) peaks that were assigned to very trace residual air contamination. Whereas, without the plasma, the mass $m/e=2$ peak was present in only trace concentration ($\sim 10^{-10}$ Torr) compared with the air contaminant gases that were also present in low abundance ($\sim 10^{-9}$ Torr). Von Engel [43] gives the efficiency of production of various common ions at 70 eV and shows that the cross section for the formation of H_2^+ is 10% of that of air contaminants at the same partial pressure. Thus, hydrogen was ~ 500 times more abundant in the collected gas than air contaminants which may have originated through back-streaming in the mass spectrometer.

From the phase diagram of helium and hydrogen plotted from data given by Lide [44] and extended to lower pressures and temperatures using the Clausius-Clapeyron equation [45], it is not possible to condense ordinary hydrogen below ~ 50 Torr at 12-17 K. The condensation of a $m/e=2$ gas in the temperature range of 12-17 K at 700 mTorr that was not removed at 10^{-5} Torr indicates that a novel hydrogen gas formed in the plasma reaction between hydrogen and helium. The results are even more dramatic in the case of the condensation of a $m/e=2$ gas in the temperature range of 77 K using the LN cryotrap.

1H NMR. The 1H NMR on $CDCl_3$ showed only a singlet solvent ($CHCl_3$) peak at 7.26 ppm relative to tetramethylsilane (TMS) with small ^{13}C side bands. The 1H NMR on ultrahigh purity hydrogen dissolved in $CDCl_3$ relative to tetramethylsilane (TMS) showed only singlet peaks at 7.26, 4.63, and 1.57 ppm corresponding to $CHCl_3$, H_2 , and H_2O , respectively. The chemical shifts of the $CHCl_3$ and H_2O peaks matched the literature values of 1.56 and 7.26 ppm, respectively [46]. The error in the observed peaks was determined to be ± 0.01 ppm. The 1H NMR spectroscopic results of the control prepared from the reagent helium-hydrogen mixture was the same as that of the high purity hydrogen control.

H_2 has been characterized by gas phase 1H NMR. The experimental absolute resonance shift of gas-phase TMS relative to the proton's gyromagnetic frequency is -28.5 ppm [47]. H_2 was observed at 0.48 ppm compared to gas phase TMS set at 0.00 ppm [48]. Thus, the corresponding absolute H_2 gas-phase resonance shift of -28.0 ppm ($-28.5 + 0.48$) ppm was in excellent agreement

with the predicted absolute gas-phase shift of -28.01 ppm given by Eq. (12).

The absolute H_2 gas-phase shift can be used to determine the solvent shift for H_2 dissolved in $CDCl_3$. The correction for the solvent shift can then be applied to other peaks to determine the gas-phase absolute shifts to compare to Eq. (12). The shifts of all of the peaks were relative to liquid-phase TMS which has an experimental absolute resonance shift of -31.5 ppm relative to the proton's gyromagnetic frequency [39, 40]. Thus, the experimental shift of H_2 in $CDCl_3$ of 4.63 ppm relative to liquid-phase TMS corresponds to an absolute resonance shift of -26.87 ppm (-31.5 ppm + 4.63 ppm). Using the absolute H_2 gas-phase resonance shift of -28.0 ppm corresponding to 3.5 ppm (-28.0 ppm - 31.5 ppm) relative to liquid TMS, the $CDCl_3$ solvent effect is 1.13 ppm (4.63 ppm - 3.5 ppm) which is comparable to that of hydrocarbons [46].

1H NMR spectra on sealed samples of condensable helium-hydrogen plasma gases dissolved in $CDCl_3$ relative to tetramethylsilane (TMS) are shown in Figures 6 (a)-(f). The solvent peak was observed at 7.26 ppm, the H_2 peak was observed at 4.63 ppm, and a singlet at 3.22 ppm matched silane. Small ^{29}Si side bands were observed for the latter. The source was determined to be hydrogen-plasma reduction of the quartz tube. The peak was unchanged after three weeks at room temperature. No other silanes, silane decomposition species, or solvent decomposition species were observed even after one month of repeat NMR analysis. Since the plasma gases were first passed through an LN trap before the plasma cell, and the cryotrap was high-vacuum (10^{-6} Torr) capable, no hydrocarbons were anticipated. This was confirmed by mass spectroscopic and FTIR analysis that showed only water vapor in addition to silane as contaminants. Again, the source was determined to be hydrogen-plasma reduction of the quartz tube.

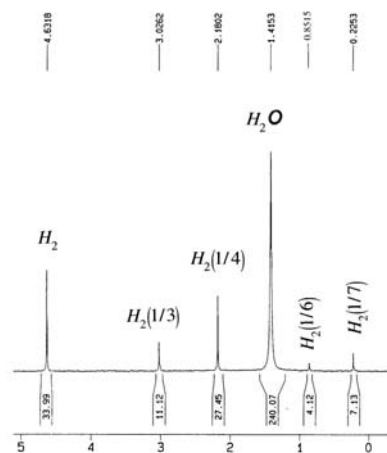


Figure 7. The 1H NMR spectrum recorded at China Lake on gases from the thermal decomposition of KH^*I dissolved in $CDCl_3$ relative to tetramethylsilane (TMS). H_2 and H_2O were observed at 4.63 ppm and 1.42, respectively. Singlet peaks upfield of H_2 were observed at 3.02, 2.18, 0.85, and 0.22 ppm relative to TMS corresponding to solvent-corrected absolute resonance shifts of -29.61, -30.45, -31.78, and -32.41 ppm, respectively. Using Eq. (12),

the data indicates that $p = 3, 4, 6,$ and $7,$ respectively. The data matched the series $H_2(1/3), H_2(1/4), H_2(1/6),$ and $H_2(1/7).$

As further shown in Figures 6 (a)-(g), singlet peaks upfield of H_2 were observed at 3.47, 3.02, 2.18, 1.25, 0.85, 0.21, and -1.8 ppm relative to TMS corresponding to solvent-corrected absolute resonance shifts of -29.16, -29.61, -30.45, -31.38, -31.78, -32.42, and -34.43 ppm, respectively. Using Eq. (12), the data indicates that $p = 2, 3, 4, 5, 6, 7,$ and $10,$ respectively. The data matched the series $H_2(1/2), H_2(1/3), H_2(1/4), H_2(1/5), H_2(1/6), H_2(1/7),$ and $H_2(1/10).$ The molecules corresponding to the reaction product atom $H(1/3)$ with products from further transitions as given in Refs. [2-3] are in agreement with the observed molecules.

1H NMR spectra were recorded at China Lake and at BlackLight Power, Inc. on ultrahigh purity hydrogen and gases from the thermal decomposition of KH^*I dissolved in $CDCl_3$ relative to tetramethylsilane (TMS). These samples were determined not to contain hydrocarbons by mass spectroscopy and FTIR analysis. Only the $CDCl_3, H_2,$ and H_2O peaks were observed from the controls. As shown in Figure 7, novel singlet peaks upfield of H_2 were observed from a KH^*I -derived sample run at China Lake. The peaks at 3.02, 2.18, 0.85, and 0.22 ppm relative to TMS corresponded to solvent-corrected absolute resonance shifts of -29.61, -30.45, -31.78, and -32.41 ppm, respectively. Using Eq. (12), the data indicates that $p = 3, 4, 6,$ and $7,$ respectively. The data matched the series $H_2(1/3), H_2(1/4), H_2(1/6),$ and $H_2(1/7).$ The observed products were consistent with those anticipated with the catalysis of H by K to form $H(1/4)$ and subsequent transition reactions [2-3, 8, 17, 20].

As shown in Figures 6 and 7, the observation of the series of singlet peaks upfield of H_2 with a predicted integer spacing of 0.64 ppm at 3.47, 3.02, 2.18, 1.25, 0.85, and 0.22 ppm identified as the consecutive series $H_2(1/2), H_2(1/3), H_2(1/4), H_2(1/5), H_2(1/6),$ and $H_2(1/7)$ and $H_2(1/10)$ at -1.8 ppm provides powerful confirmation of the existence of $H_2(1/p).$ Furthermore, the 1H NMR spectra of gases from the thermal decomposition of KH^*I matched those of LN-condensable hydrogen. This provides strong support that compounds such as KH^*I contain hydride ions $H^-(1/p)$ in the same fractional quantum state p as the corresponding observed $H_2(1/p).$ Observational agreement with predicted positions of upfield-shifted 1H MAS NMR peaks (Eq. (13)) of the compounds [8, 20, 30-32], catalyst reactions [17, 20, 23-24], and spectroscopic data [17] supports this conclusion.

The existence of novel alkaline and alkaline earth hydride and halido-hydrides were previously identified by large distinct upfield 1H NMR resonances compared to the NMR peaks of the corresponding ordinary hydrides [20, 30-32]. Using a number of analytical techniques such as XPS and time-of-flight-secondary-mass-spectroscopy (ToF-SIMS) as well as NMR, the hydrogen content was assigned to $H^-(1/p),$ novel high-binding-energy hydride ions in stable fractional principal quantum states [8, 20, 30-32]. Upfield shifts of the novel hydride compounds matched those predicted for $H^-(1/2)$ and $H^-(1/4)$ (Eq. (13)). Novel spectral emission from $H^-(1/2)$ and $H^-(1/2),$ the predicted products from

the potassium catalyst reaction and the supporting results of 1.) the formation of a hydrogen plasma with intense extreme ultraviolet (EUV) emission at low temperatures (e.g. $\approx 10^3 K$) and an extraordinary low field strength of about 1-2 V/cm [9-12, 17-24] or without an electric field or power input other than thermal [21-22] from atomic hydrogen and certain atomized elements or certain gaseous ions that serve as catalysts, 2.) a high positive net enthalpy of reaction [20], 3.) characteristic predicted catalyst emission [17, 23-24], 4.) ~ 15 eV Doppler broadening of the Balmer lines [17, 23-24], and 5.) inversion of the Lyman lines [23-24] have also been reported previously.

Based on their stability characteristics, advanced hydride technologies are indicated. Hydride ions $H^-(1/p)$ having extraordinary binding energies may stabilize a cation M^{x+} in an extraordinarily high oxidation state as the basis of a high voltage battery. And, a rocketry propellant based on $H^-(1/24)$ to $H_2(1/24)$ may be possible with an energy release so large that it may be transformational. Significant applications also exist for the corresponding molecular species $H_2(1/p).$ The results of this study indicate that excited vibration-rotational levels of $H_2(1/4)$ could be the basis of a UV laser that could significantly advance photolithography.

Power Balance of the Helium-Hydrogen Microwave Plasma In addition to high energy spectral emission as shown in Sec. IIIA and previously [1-5], other indications of very energetic reactions are observed. For example, population inversion has been observed from plasmas which contain atomic hydrogen with the presence of a catalyst [23-26], and selective H broadening with a microwave plasma having no high DC field present was reported previously [13-15]. Microwave He/H_2 and Ar/H_2 plasmas showed extraordinary broadening corresponding to an average hydrogen atom temperature of 80–120 eV and 110–130 eV, respectively. Whereas, pure hydrogen and Xe/H_2 microwave plasmas showed no excessive broadening corresponding to an average hydrogen atom temperature of <2 eV [13-15]. Only the H lines were Doppler broadened, and this result was shown to be inexplicable by any mechanism based on electric field acceleration of charged species. The observation of excessive Balmer line broadening in microwave driven plasmas as well as other hydrogen-mixed plasmas maintained in glow discharge [10-15] and RF discharge cells [14, 16] as well as unique chemically driven plasmas called resonant-transfer or rt-plasmas [17, 20, 23-24] requires a source of energy other than that provided by the electric field. The formation of fast H only in specific predicted plasmas was explained by a resonant energy transfer between hydrogen atoms and catalysts such as Ar^+ or He^+ of an integer multiple of the potential energy of atomic hydrogen, 27.2 eV [13-15]. Consistent with predictions, noncatalyst plasma mixtures such as Kr/H_2 and Xe/H_2 show no unique features. The observation of the $H_2(1/4)$ rotational lines reported in Sec. IIIAb from Ar/H_2 plasmas but not from Kr/H_2 and Xe/H_2 plasmas also matches predictions.

The excess power of the catalytic reaction was measured by water bath calorimetry. The water bath calorimeter is an absolute standard and indicated $P_{in} = 41.9 \pm 1W$ input power at the selected diode settings for all control plasmas. From these results, power input to the helium-hydrogen plasma was confidently known as the diode readings were identically matched for the controls. For

example, the $T(t)$ water bath response to stirring and then with selected panel meter readings of the constant forward and reflected microwave input power to krypton was recorded. Using the corresponding $\dot{T}(t)$ in Eq. (17), the microwave input power was determined to be 41.9 ± 1 W. The $T(t)$ response was significantly increased for helium-hydrogen (95/5%). From the difference in the $T(t)$ water bath response, the output and excess power of the helium-hydrogen plasma reaction was determined to be 62.1 ± 1 W and 20.2 ± 1 W using Eq. (17) and Eq. (16) with the measured $P_{in} = 41.9 \pm 1$ W. The sources of error were the error in the calibration curve (± 0.05 W) and the measured microwave input power (± 1 W). The propagated error of the calibration and power measurements was ± 1 W. Given an excess power of 20.2 W in 3 cm³ and a helium-hydrogen (95/5%) flow rate of 10.0 sccm, the excess power density and energy balance were high, 6.7 W/cm³ and -5.4×10^4 kJ/mole H_2 (280 eV / H atom), respectively.

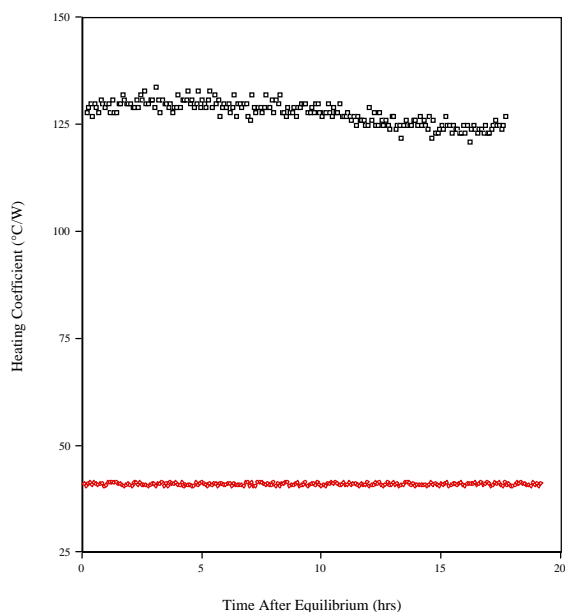


Figure 8. Plot of the heating coefficients versus time. (top) - K_2CO_3 electrolysis with a nickel wire cathode at 83.0 mA and 1.95 V, (bottom) - resistor working in K_2CO_3 . The heating coefficient of the heater run (calibration) was 41°C/W.; whereas, the heating coefficient of the electrolysis run was 127 °C/W. The production of excess power of 81.8 mW was observed that was 3.1 times P_{cell} and 75% of P_{appl} .

Isolation and Characterization of $H_2(1/p)$ from Electrolysis Cells. Power Balance of the Electrolysis Cells.

The temperature versus time results of the electrolysis of K_2CO_3 with a nickel wire cathode at 83.0 mA constant current and 1.95 V corresponding to an electrolysis resistive input power, P_{cell} , of 39.0 mW (Eq. (22)) and heater run of K_2CO_3 with 50 mW appear in Figure 8. The heating coefficient of the heater run (calibration) was 41°C/W.; whereas, the heating coefficient of the electrolysis run was 127°C/W. The production of excess enthalpy is observed. The higher the heating coefficient, the more heat released

in the process. Using Eq. (31), the excess power, Q_{xs} , was determined to be

$$Q_{xs} = P_{cell} \left(\frac{a_1}{a_2} - 1 \right) = 39.0 \text{ mW} \left(\frac{127}{41} - 1 \right) = 81.8 \text{ mW} \quad (34)$$

Thus, the experiment developed an extra 81.8 mW over the input power, P_{cell} , which corresponded to a total thermal power of 3.1 times P_{cell} and 75% of P_{appl} . The Faradaic efficiency of the production of gas by a K_2CO_3 cell and a control Na_2CO_3 cell was 100% within experimental error. The results of excess heat observed only from the K_2CO_3 cell could not be explained by recombination of electrolysis gases as shown previously [49, 50]. The observed heating coefficient of the electrolysis run when Na_2CO_3 replaced K_2CO_3 was 45 °C/W; whereas, the heating coefficient of the heater run (calibration) was 46 °C/W. The production of excess heat was not observed for the control as predicted. Similar excess heat results from K_2CO_3 electrolysis have been reported by Mills [49-51] and others [50, 52].

Neglect, for the moment that $H(1/2)$ can form a diatomic molecule $H_2(1/2)$ and subsequent transitions to lower energy states occur to a substantial extent. From Eqs. (1a) and (1b), 40.8 eV is released per H atom transition to the $n = 1/2$ quantum state due to catalysis by potassium ions which corresponds to 8 MJ/mole of H_2 [9, 17, 19-20]. In contrast, only 286 kJ is consumed by electrolyzing one mole of H_2O to produce one mole of H_2 (Eq. (15)). Thus, the excess power of 82 mW produced by the K_2CO_3 electrolytic cell as shown in Figure 8 (which also produces 0.43 μ moles of H_2 per second) could be accounted for by the conversion of at most 3.5% of the hydrogen atoms from the $n = 1$ state to the $n = 1/2$ state.

¹H NMR of Electrolysis Gases. ¹H NMR spectra on sealed samples of K_2CO_3 electrolytic gases dissolved in $CDCl_3$ relative to tetramethylsilane (TMS) are shown in Figures 9 (a)-(d). The solvent peak was observed at 7.26 ppm, the H_2 peak was observed at 4.63 ppm. No hydrocarbons were anticipated to permeate the nickel tube. This was confirmed by mass spectroscopic and FTIR analysis. For example, the FTIR spectra of the electrolysis gases in the region of the C-H stretching showed no evidence for hydrocarbons. As further shown in Figures 9 (a)-(d), singlet peaks upfield of H_2 were observed at 3.49¹, 2.17, 1.25, 0.86, and 0.21 ppm relative to TMS corresponding to solvent-corrected absolute resonance shifts of -29.14, -30.46, -31.38, -31.77, -and -32.42 ppm, respectively. Using Eq. (12), the data indicates that $p = 2, 4, 5, 6$, and 7, respectively.

The observed series has implications for the catalysis reactions and the corresponding rates of the formation of atoms $H(1/p)$ and the corresponding molecules $H_2(1/p)$ and their diffusion through the nickel tubing. The product of the catalysis of H by potassium ions is $H(1/2)$ corresponding to the peak at 3.49 ppm shown in Figure 9. Similarly, the product of catalysis of H by K is $H(1/4)$ corresponding to the peak at 2.17 ppm shown in Figure 9 which was the dominant peak. K as the principle catalyst with K_2CO_3 or

¹ The broad increase in the baseline in the region 3.25-3.75 ppm was an instrument artifact.

$K(m)$ as the source was also supported by the observation of characteristic catalyst emission and EUV emission from the corresponding hydride ion having an upfield-shifted 1H MAS NMR peak at -4.4 ppm as discussed in Sec. IB. Since the products of the catalysis reaction have binding energies of $m \cdot 27.2\text{eV}$, they may further serve as catalysts by so called exothermic disproportionation reactions where one atom goes to a lower state (e.g. $n = \frac{1}{2} \rightarrow \frac{1}{3}, \frac{1}{3} \rightarrow \frac{1}{4}, \frac{1}{4} \rightarrow \frac{1}{5}$.) while another goes to a higher state [2, 3, 7]. Thus, $H_2(1/p)$ molecules corresponding to the product atoms $H(1/p)$ from further transitions having $p > 2$ or $p > 4$ as given in Refs. [2-3] are anticipated as the reaction products.

As shown in Figures 9 (a)-(d), the observation of the series of singlet peaks upfield at 3.49, 2.17, 1.25, 0.86, and 0.21 ppm with an integer spacing of 0.64 ppm (except for the previously observed 3.02 peak shown in Figure 6) identified as the consecutive series $H_2(1/2)$, $H_2(1/4)$, $H_2(1/5)$, $H_2(1/6)$, and $H_2(1/7)$ provides powerful confirmation of the existence of $H_2(1/p)$.

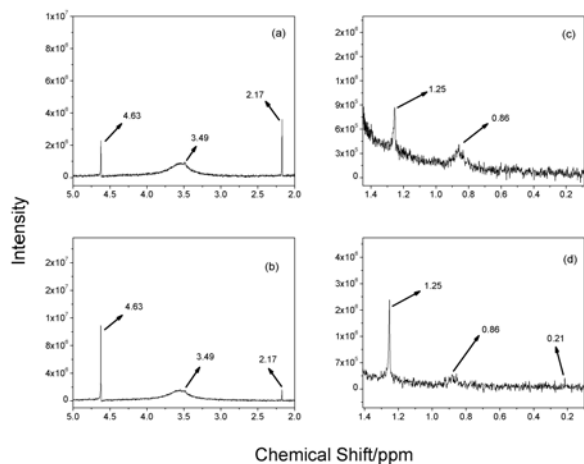


Figure 9. (a)-(d). 1H NMR spectra on sealed samples of K_2CO_3 electrolytic gases dissolved in $CDCl_3$ relative to tetramethylsilane (TMS). The solvent peak was observed at 7.26 ppm, and the H_2 peak was observed at 4.63 ppm. Singlet peaks upfield of H_2 were observed at 3.49, 2.17, 1.25, 0.86, and 0.21 ppm relative to TMS corresponding to solvent-corrected absolute resonance shifts of -29.14, -30.46, -31.38, -31.77, and -32.42 ppm, respectively. Using Eq. (12), the data indicates that $p = 2, 4, 5, 6$, and 7 , respectively. The data matched the series $H_2(1/2)$, $H_2(1/4)$, $H_2(1/5)$, $H_2(1/6)$, and $H_2(1/7)$.

Mass Spectroscopy of Electrolysis Gases. $H_2(1/2)$ was identified by mass spectroscopy as a species with a mass to charge ratio of two ($m/e = 2$) that has a higher ionization potential than that of normal hydrogen by recording the ion current as a function of the electron gun energy. The mass spectra of the K_2CO_3 and

Na_2CO_3 electrolysis gases was obtained over the range $m/e = 1$ to $m/e = 200$. In both cases, the sample contained only hydrogen.

The relative changes in the $m/e = 2$ ion current while changing the electron gun energy from 30 to 70 eV indicated that the K_2CO_3 electrolysis gases has a higher ionization potential than ultrapure hydrogen and Na_2CO_3 electrolysis gases. Upon increasing the ionization potential from 30 eV to 70 eV, the $m/e = 2$ ion current for the controls increased by a factor of about 30%; whereas, the current for K_2CO_3 electrolysis gases collected under liquid nitrogen increased by a factor of about 10 under the same pressure condition as that of the controls.

Conclusion

In this study we made specific theoretical predictions regarding the exothermic reaction to form $H_2(1/p)$ and its characterization and tested them with standard, easily interpretable experiments. The results show that new states of hydrogen are formed by reaction of hydrogen atoms with He^+ , Ar^+ , and potassium ions and atoms that serve as catalysts but not with control atoms and ions as predicted. The observation of excess enthalpy and the same states of hydrogen, $H_2(1/p)$, from chemicals compound, plasma gases, and electrolysis cells demonstrates the hydrogen catalysis reaction occurs in liquid-solid interfacial environments as well as in the gas phase under a range of reaction conditions. The power results indicate that a new power source based on the catalysis of atomic hydrogen is not only possible, but it may be competitive with gas-turbine combustion. Furthermore, since the identified $H_2(1/p)$ byproduct is stable and lighter-than-air, it can not accumulate in the Earth's atmosphere. The environmental impact of handling fossil fuels and managing the pollution of air, water, and ground caused by the ash generated by fossil fuels or the radioactive waste from a nuclear plant may be eliminated.

Acknowledgments. Special thanks to D. E. Murnick and M. Salvermoser of Rutgers University for providing the 15 keV electron gun. D. C. Harris, Naval Air Warfare Center Weapons Division, Naval Air Warfare Center, China Lake, CA, is acknowledged for suggesting the method of identifying $H_2(1/p)$ by 1H NMR using $CDCl_3$ solvent. D. C. Harris and L. Merwin are acknowledged for preparing and analyzing a $KH * I$ NMR sample.

References

- (1) R. L. Mills, P. Ray, *J. Phys. D: Appl. Phys.*, **2003**, 36, 1535.
- (2) R. L. Mills, P. Ray, B. Dhandapani, M. Nansteel, X. Chen, J. He, *J. Mol. Struct.*, **2002**, 643 (1-3), 43.
- (3) R. Mills, P. Ray, *Int. J. Hydrogen Energy*, **2002**, 27, 301.
- (4) R. L. Mills, P. Ray, J. Dong, M. Nansteel, B. Dhandapani, J. He, *Vib. Spectrosc.*, **2003**, 31, 195.
- (5) R. Mills, P. Ray, *Int. J. Hydrogen Energy*, **2002**, 27, 533.
- (6) R. Brunch, P. L. Altick, E. Trabert, P. H. Heckmann, *J. Phys. B: At. Mol. Phys.*, **1984**, 17, L655.
- (7) R. Mills, *The Grand Unified Theory of Classical Quantum Mechanics*, September 2001 Edition, BlackLight Power, Inc., Cranbury, New Jersey, Distributed by Amazon.com; January (2003) Edition posted at www.blacklightpower.com.
- (8) R. L. Mills, "The Nature of the Chemical Bond Revisited and an Alternative Maxwellian Approach," submitted.
- (9) R. Mills, J. Dong, Y. Lu, *Int. J. Hydrogen Energy*, **2000**, 25, 919.

- (10) R. Mills, M. Nansteel, P. Ray, *IEEE Transactions on Plasma Science*, **2002**, 30, 639.
- (11) R. Mills, M. Nansteel, P. Ray, *New J. Phys.*, **2002**, 4, 70.1.
- (12) R. Mills, M. Nansteel, P. Ray, *J. Plasma Phys.*, **2003**, 69, 131.
- (13) R. L. Mills, P. Ray, B. Dhandapani, R. M. Mayo, J. He, *J. Appl. Phys.*, **2002**, 92, 7008.
- (14) R. L. Mills, P. Ray, B. Dhandapani, J. He, *IEEE Trans. Plasma Sci.*, **2003**, 31(3), (2003), 338.
- (15) R. L. Mills, P. Ray, *New J. Phys.*, www.njp.org, **2002**, 4, 22.1.
- (16) J. Phillips, C. Chen, "Evidence of Energetic Reaction Between Helium and Hydrogen Species in RF Generated Plasmas," submitted.
- (17) R. L. Mills, P. Ray, *Int. J. Hydrogen Energy*, **2003**, 28, 825.
- (18) R. Mills, *Int. J. Hydrogen Energy*, **2001**, 26, 1041.
- (19) R. Mills, P. Ray, *Int. J. Hydrogen Energy*, **2002**, 27, 183.
- (20) R. Mills, P. Ray, B. Dhandapani, W. Good, P. Jansson, M. Nansteel, J. He, A. Voigt, "Spectroscopic and NMR Identification of Novel Hydride Ions in Fractional Quantum Energy States Formed by an Exothermic Reaction of Atomic Hydrogen with Certain Catalysts," in press.
- (21) H. Conrads, R. Mills, Th. Wrubel, *Plasma Sources Sci. Technol.*, **2003**, 12, 389.
- (22) R. Mills, T. Onuma, Y. Lu, *Int. J. Hydrogen Energy*, **2001**, 26, 749.
- (23) R. Mills, P. Ray, R. M. Mayo, *IEEE Trans. Plasma Sci.*, **2003**, 31 (2), 236.
- (24) R. L. Mills, P. Ray, *J. Phys. D: Appl. Phys.*, **2003**, 36, 1504.
- (25) R. Mills, P. Ray, R. M. Mayo, *Appl. Phys. Lett.*, **2003**, 82 (11), 1679.
- (26) R. L. Mills, P. C. Ray, R. M. Mayo, M. Nansteel, B. Dhandapani, J. Phillips, "Spectroscopic Study of Unique Line Broadening and Inversion in Low Pressure Microwave Generated Water Plasmas," submitted.
- (27) R. L. Mills, X. Chen, P. Ray, J. He, B. Dhandapani, *Thermochim. Acta*, **2003**, 406 (1-2) 35.
- (28) R. L. Mills, Y. Lu, J. He, M. Nansteel, P. Ray, X. Chen, A. Voigt, B. Dhandapani, "Spectral Identification of New States of Hydrogen," submitted.
- (29) R. Mills, B. Dhandapani, W. Good, J. He, "New States of Hydrogen Isolated from K_2CO_3 Electrolysis Gases," submitted.
- (30) R. Mills, B. Dhandapani, M. Nansteel, J. He, T. Shannon, A. Echezuria, *Int. J. Hydrogen Energy*, **2001**, 26, 339.
- (31) R. Mills, B. Dhandapani, N. Greenig, J. He, *Int. J. Hydrogen Energy*, **2000**, 25, 1185.
- (32) R. Mills, B. Dhandapani, M. Nansteel, J. He, A. Voigt, *Int. J. Hydrogen Energy*, **2001**, 26, 965.
- (33) R. Mills, E. Dayalan, P. Ray, B. Dhandapani, J. He, *Electrochim. Acta*, **2002**, 47, 3909.
- (34) M. Karplus, R. N. Porter, *Atoms and Molecules an Introduction for Students of Physical Chemistry*, The Benjamin/Cummings Publishing Company, Menlo Park, California, (1970), pp. 447-484.
- (35) NIST Atomic Spectra Database, www.physics.nist.gov/cgi-bin/AtData/display.ksh.
- (36) H. Beutler, *Z. Phys. Chem.*, **1934**, 27B, 287.
- (37) G. Herzberg, L. L. Howe, *Can. J. Phys.*, **1959**, 37, 636.
- (38) P. W. Atkins, *Physical Chemistry*, Second Edition, W. H. Freeman, San Francisco, (1982), p. 589.
- (39) K. K. Baldrige, J. S. Siegel, *J. Phys. Chem. A*, **1999**, 103, 4038.
- (40) J. Mason, Editor, *Multinuclear NMR*, Plenum Press, New York, (1987), Chp. 3.
- (41) J. Wieser, D. E. Murnick, A. Ulrich, H. A Higgins, A. Liddle, W. L. Brown, *Rev. Sci. Instrum.*, **1997**, 6 (3), 1360.
- (42) A. Ulrich, J. Wieser, D. E. Murnick, Second International Conference on Atomic and Molecular Pulsed Lasers, *Proc. SPIE*, **1998**, 3403, 300.
- (43) A. von Engel, *Ionized Gases*, American Institute of Physics Press, New York, (1965), pp. 62-64.
- (44) D. R. Lide, *CRC Handbook of Chemistry and Physics*, 76 th Edition, CRC Press, Boca Raton, Florida, (1995-6), p. 6-66 and p. 6-140.
- (45) I. N. Levine, *Physical Chemistry*, McGraw-Hill Book Company, New York, (1978), pp. 174-175.
- (46) H. E. Gottlieb, V. Kotlyar, A. Nudelman, *J. Org. Chem.*, **1997**, 62, 7512.
- (47) C. Suarez, E. J. Nicholas, M. R. Bowman, *J. Phys. Chem. A*, **2003**, 107, 3024.
- (48) C. Suarez, "Gas-phase NMR spectroscopy," *The Chem. Educator*, 1998, 3 (2).
- (49) R. Mills, W. Good, *Fusion Technol.*, **1995**, 28, 1697.
- (50) R. Mills, W. Good, R. Shaubach, *Fusion Technol.*, **1994**, 25, 103.
- (51) R. Mills, S. Kneizys, *Fusion Technol.*, **1991**, 20, 65.
- (52) J. Niedra, I. Meyers, G. C. Fralick, R. Baldwin, "Replication of the Apparent Excess Heat Effect in a Light Water-Potassium Carbonate-Nickel Electrolytic Cell," NASA Technical Memorandum 107167, February, (1996). pp. 1-20.; Niedra, J., Baldwin, R., Meyers, I., NASA Presentation of Light Water Electrolytic Tests, May 15, 1994.

PROTECTIVE COATINGS FOR Pd-BASED HYDROGEN SENSORS

Rodney D. Smith II, Roland Pitts, Se-Hee Lee and Edwin Tracy

National Renewable Energy Laboratory, 1617 Cole Blvd., Golden, CO 80401

Introduction

The ability to detect hydrogen gas leaks economically and with inherent safety is an important technology that will help facilitate commercial acceptance of hydrogen as a fuel source in various applications. The sensors used in these applications must be inexpensive enough for liberal deployment on a hydrogen powered vehicle, and they must be adequately responsive to provide early leak detection so that appropriate action can be taken before the explosive limit in air is reached. NREL has chosen to work on a fiber-optic sensor configuration that represents the best chance of meeting all of these goals (1-4). The fiber-optic approach is the only proposed sensor configuration that meets the criterion of being inherently safe and does not represent a possible ignition source as in other conventional sensor designs powered by electrical means.

The sensor consists of a hydrogen sensitive chemochromic coating at the end of an optical fiber. Chemochromic materials such as tungsten oxide (WO_3) can reversibly react with hydrogen and exhibit significant changes in their optical properties. A thin catalytic over-layer of palladium (Pd) acts as a dissociation catalyst forming atomic hydrogen, which subsequently reacts with the WO_3 . Light from a central electro-optic control unit is projected down the optical fiber where it is either reflected from the sensor coating or is transmitted to another fiber leading to a remote optical detector. A change in the reflected or transmitted light intensity indicates the presence of hydrogen. A conceptual schematic of such a sensor is presented in Fig. 1.

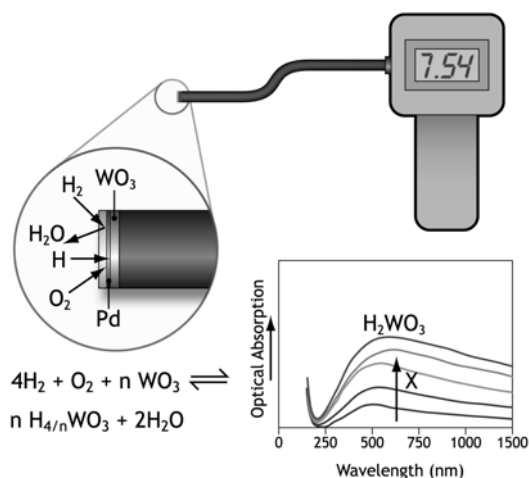


Figure 1. Schematic of fiber optic hydrogen sensor.

Efforts at NREL have been focused on developing a better understanding of the service lifetime and performance issues that will enable thin film hydrogen sensors to be commercialized. These issues have been addressed through real time reliability testing of

sensor films as well as sensor fabrication with advanced materials to achieve improved durability in the presence of contaminants.

The main mode of degradation in thin film chemochromic hydrogen sensors is poisoning of the palladium (Pd) catalyst layer by airborne contaminants. Fouling of the Pd surface inhibits the dissociation of hydrogen on the catalyst surface, severely degrading the device. Several protective layers for the Pd film have been investigated, with varying degrees of success. These include films of amorphous carbon deposited by plasma enhanced chemical vapor deposition (PECVD) and spin coated nano-phase anatase titanium dioxide (TiO_2).

Of these, a colloidal suspension of nano- TiO_2 applied as a spin coating offers the best protection. Spin coating produces a thick (approximately 300 nanometers [nm]) porous film that does not impede the diffusion of hydrogen or oxygen to the underlying thin film stack.

The main function of the coating is to maintain the activity of the Pd catalyst surface by a photocatalytic cleaning mechanism. The coating is continuously exposed to ultraviolet (UV) radiation at 365 nm from a UV source. Interaction with UV light causes the TiO_2 particles to form hydroxide radicals on their surfaces from water vapor in the atmosphere. These radicals will subsequently oxidize any contaminants that are adsorbed on the TiO_2 surface. Any contaminants that may diffuse through the coating and occupy sites on the metal surface are also eventually oxidized, converted to a volatile species and escape from the film. Sensor operational lifetimes have been extended to 3 years with this photocatalytic coating. Unprotected sensors will degrade in days or weeks, depending upon the concentration of pollutants in the air.

The photocatalytic properties of TiO_2 have been studied extensively (5-8). TiO_2 has been used for many applications including organic and inorganic catalysis, self-cleaning coatings, and as semiconductor layers in dye sensitized solar cells. However, to the best of our knowledge this material has never been used to maintain the functionality of noble metal-based catalysts or other metal surfaces.

Experimental

Methods for fabrication and the apparatus for testing the sensor films have been described previously (4). Sensor films were deposited by thermal evaporation and all depositions were monitored with a quartz crystal deposition rate monitor. To calibrate the deposition rate monitor, film thicknesses were measured with a stylus profilometer.

Colloidal Anatase TiO_2 Films. TiO_2 colloids were synthesized by a hydrothermal process from an alkoxide precursor such as titanium isopropoxide. The resulting particle size was typically in the range of 15-30 nm. The TiO_2 suspension was then diluted in ethanol to obtain the proper consistency and spin coated at 2000 rpm on the evaporated thin film sensor stacks. The sensors were continuously exposed to 365 nm radiation from a UV pencil lamp under ambient air. Performance was measured periodically using a diode array fiber optic UV/VIS spectrophotometer (Ocean Optics model S2000).

Results and Discussion

TEM/SEM images of the TiO_2 particles and resulting spin coated thin film are presented in Figures 2 and 3. Experiments at NREL have indicated that variations in synthesis temperature, particle size or precursor purity do not significantly alter the effectiveness of the film for this application.

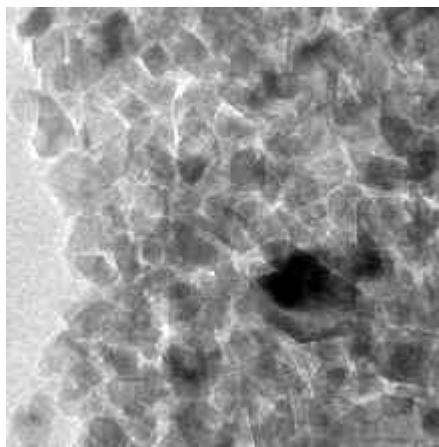


Figure 2. TEM image of colloidal TiO₂ synthesized at 230°C.

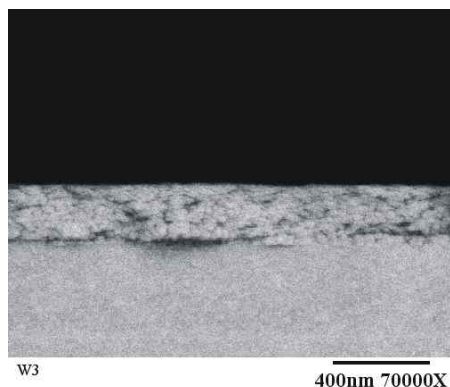


Figure 3. SEM image of spin coated colloidal TiO₂ thin film.

Figure 4 shows typical optical response data for a sensor with the TiO₂ coating. The sensor is still operational at the working detection limit of 0.1% hydrogen after almost 3 years. Figure 5 shows more recent response data for a similar sensor after 1 year of testing.

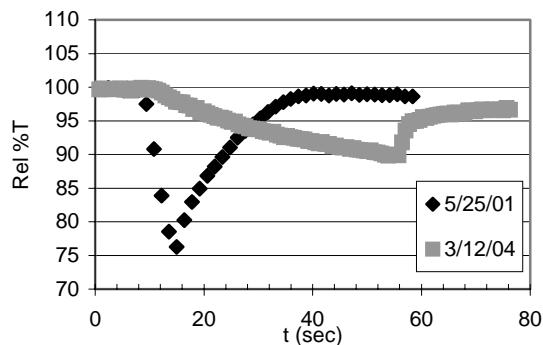


Figure 4. Optical response of thin film WO₃/Pd/TiO₂ sensor stack after 3 years of storage in ambient air (0.1% H₂/N₂).

This method of using a photocatalytic TiO₂ layer for prolonging catalyst lifetime could conceivably be carried out with other systems as well (patent filed). While the results presented here describe a continuous thin film of Pd that is protected from contamination,

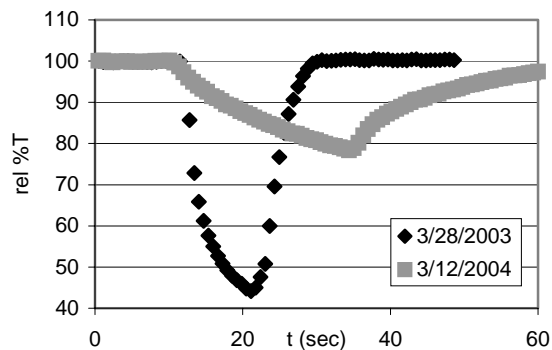


Figure 5. Optical response of thin film WO₃/Pd/TiO₂ sensor stack after 1 year of storage in ambient air (0.1% H₂/N₂).

protection could also be obtained on discontinuous metal films as well as metal islands on supported catalysts.

The TiO₂ coating should be equally effective at protecting Pd or other noble metal based catalysts used for hydrogen sensors, maintaining functionality of metal membranes used for hydrogen purification, and preventing poisoning or cleaning fouled supported catalysts used in fluidized beds.

Conclusions

Chemochromic hydrogen sensors have been developed at NREL to indicate the presence of hydrogen by a change in optical properties. Thin film stacks deposited on the end of fiber optic cables can be used to detect hydrogen economically and with inherent safety. The response of these and other Pd-based sensors tends to degrade over time due to the exposure of the catalyst surface to airborne contaminants. A photocatalytic TiO₂ coating has been developed for protection of the Pd catalyst that can prolong the working life of the Pd from days or weeks up to 3 years. This protective coating may have other possible applications where noble metal catalysts are used (fuel cell membrane assemblies, hydrogen separation membranes and industrial catalysts).

This advancement provides the opportunity to greatly simplify the sensor design and to further reduce cost. Future work will concentrate on optimization of the TiO₂ and modification of the technology for use with other systems.

Acknowledgement. This work was supported by the Hydrogen Program of the U.S. Department of Energy under Contract No. DE-AC-36-99-G010337.

References

- (1) Benson, D. K., Tracy, C. E. and Bechinger, C. *Proceedings of the DOE Hydrogen Program Meeting Vol. II, Miami, FL, 1996*, pp. 605-624.
- (2) Benson, D. K., Tracy, C. E., Hishmeh, G. A., Ciszek, P. A., Lee, S. and Haberman, D. P. *Proceedings of the SPIE International Symposium on Industrial and Environmental Monitors and Biosensors, Boston, MA, 1998*, pp. 185-202.
- (3) Benson, D. K., Tracy, C. E. and Bechinger, C. U. S. Patent 5,708,735, **1998**.
- (4) Smith II, R. D., Liu, P., Lee, S-H., Tracy, C. E. and Pitts, J. R. *Am. Chem. Soc., Div. Fuel Chem.*, **2002**, 47 (2), pp. 825-827.
- (5) *Photocatalysis Fundamentals and Applications*, Serpone, N. and Pellizzetti, E., ed. John Wiley and Sons, New York, **1989**.
- (6) Fujishima, A., Watanabe T. and Hashimoto, K., *TiO₂ Photocatalysis: Fundamentals and Applications*, **1999**.
- (7) Fox, M. A. and Dulay, M. T. *Chem. Rev.* **1993**, 93, pp. 341-357.
- (8) M. Lisebigler, G. Lu and J. T. Yates Jr., *Chem. Rev.*, **1995**, 95, pp. 735-758.

PLASMATRON NATURAL GAS REFORMING

L. Bromberg, D.R. Cohn, K. Hadidi, A. Rabinovich, N. Margarit, N. Alexeev, A. Samokhin

MIT Plasma Science and Fusion Center
Cambridge MA 02139

Introduction

Low-current plasma discharges have been tested for reformation of natural gas. Experiments were carried out using both homogeneous (non-catalytic) and heterogeneous (catalytic) conditions at power levels of 200 and 700 W. Byproducts of the reforming process were hydrogen, CO, and light hydrocarbons. Hydrogen yields were around 40% for homogeneous conditions with 40% energy efficiency whereas for catalytic reforming it was 70% with an energy efficiency of 90%. In addition, the effect of stratification (inhomogeneous air/fuel mixtures) were investigated. This paper presents comparison between models and experiments carried out with air. Future papers will present results using oxygen-enriched air, and CO₂ enriched-air. Results of modeling that involves simple CFD simulations without combustion have been used to calculate the mixing time. The chemistry is modeled using the Partially Stirred Reactor and Perfectly Stirred Reactor options of Chemkin.

Plasma Reforming. Experimental results of plasma reformation and the reformation setup have been described before^{1,2}. The experiments that were modeled were carried with commercial grade natural gas with a power of 250 W, and a flow rate of 0.3 g/s, with O/C ratio ~ 1.1. Although some of the experiments were carried out with a catalyst downstream from the plasma, the results commented in this paper were for homogeneous reforming.

Experimentally it was determined that strong stratification of the air fuel mixture in the plasma zone was required for reaction initiation. Premixed air/methane mixtures could not be started under the conditions tested.

Models for plasmatron methane reforming. To understand the plasmatron reformer several models were developed. They included PFR as well as Partially Stirred Reactor (PaSR).

Ignition delay in the presence of radicals

In order to determine the effect of radicals that are produced by the nonthermal plasma, calculations were performed using CHEMKIN 3.7 Plug Flow Reactor. Multiple radical concentrations were used, with the rest of the well-mixed air/methane mixture. Multiple temperatures were considered. The results from the calculations are shown in Table 1.

Three radical types were used: atomic oxygen (O), hydroxyl (OH) radical, and atomic hydrogen (H) radicals, for initial temperatures from 600 to 1000 K. Shown in table 1 is the ignition delay, defined as the time for consumption of 10% of the fuel. However, the reaction, once it starts, is so fast (stiff chemistry) that the 10% assumption is not important.

The results in Table 1 indicate that even very large concentrations of radicals at low temperature do not substantially change the ignition delay. The radical concentration assumed in table 1 is very large, much larger than what could be expected for the conditions of the experiment. From the simulations it is clear the radicals recombine, raising slightly the air/methane temperature. This increase in temperature occurs very quickly (on the order of 10's of microseconds). The slightly increase in temperature is responsible for the relatively small effect in the ignition delay.

Table 1. Ignition Delay Time (In Seconds) For Various Radicals For Multiple Air/Methane Temperatures.

Methane homogeneous ignition delay time (s)

Initial Temperature	600 K	700 K	800 K	1000 K
No radicals	>1000	920	12.5	0.31
[O]=3e-4	>1000	195	4.3	0.23
[O]=3e-5	>1000	515	8.1	0.30
[OH]=3e-4	>1000	290	5.7	0.29
[H]=3e-4	>1000	240	4.9	0.25
[O]=[H]=3e-4	>1000	140	3.5	0.23

Model Using Partial Stirred Reactor

The plasma was modeled by using a high temperature zone that started local reaction and then through mixing carried the reactions to the rest of the air/fuel mixture.

To simulate the inhomogeneities, the PASR model³ was used. The model allows for control of the mixing time. However, the code has limitation with respect to the number of input streams (two). This places a severe constrain in the capabilities of the model.

It is thought that the effect of the plasma is to raise the local temperature of the air/methane mixture in order to locally ignite the air/fuel mixture. The actual temperature of the local regions is not known. Possible energy distribution are shown in Figure 1. The plasma power requirement is shown in this Figure as a function of the temperature of the hot zone, with the fraction of the hot zone as a parameter. Different fractions of hot-zones (with respect to the total gas flow) are assumed: 1%, 5%, and 10%. As the temperature of the hot zone increases for a given hot-zone fraction, the power required increases. Because of changes of the heat capacity as a function of temperature, the lines are not quite linear (although approximately linear). When the fraction of hot particles increases, the power increases. Figure 1 was calculated for flow rates typical of the plasmatron operation, about 0.4 g/s methane and O/C = 1.

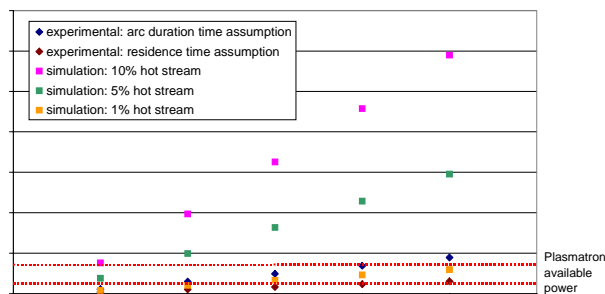


Figure 1. Power requirement as a function of the temperature of the hot zone, for several hot zone fractions.

Calculation of the PASR for the type of hot zone fraction and hot zone temperature shown in Figure 1 are given in Figure 2. These are the results of homogeneous mixture of methane and air, with a fraction of the zones at high temperature, for different ratios of mixing time to residence time, for different values of the hot zone temperature. It is assumed that 10% of the air/methane mixture is in the hot zone.

There is a maximum of the hydrogen production as a function of the ratio between the mixing time and the residence time. This can be understood by realizing that if the mixing is too fast, the hot zone enthalpy is divided with the rest of air/methane, with an increase in temperature but with little reaction. On the other hand, if the mixing time is too long, too many cold zones never get the energy required for reaction initiation, and conversion is poor.

The residence time in the plasmatron region is on the order of 1 ms. Calculations of the mixing time, by both back-of-the-envelope and CFD calculations (in the absence of chemistry), indicate that the mixing time in the plasmatron is on the order of 100 microseconds.

The results are in relatively good agreement with the experiments. However, the power required by the calculations is substantially larger than the one that is determined experimentally. While the calculations assumed about 2.5 kW power (10% as hot zone fraction with a temperature of about 5000 K), the experimental results are obtained at about one order of magnitude smaller powers.

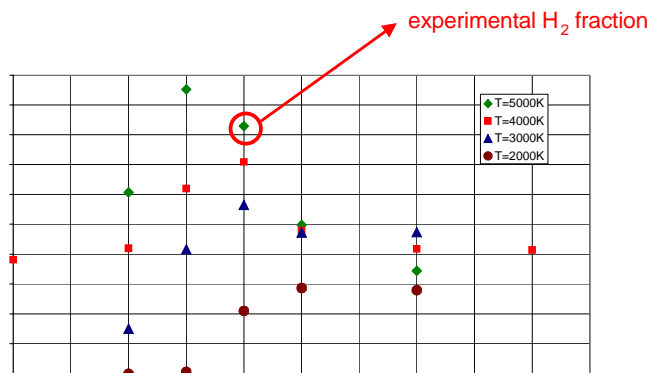


Figure 2. Hydrogen concentration (by mass) as a function of the ratio between the mixing time and the residence time, for residence time of 1 ms. Results are plotted for different temperatures of the hot zone.

Table 2 shows the results from the experiments as well as from the calculations. Because the PASR model in Chemkin does not calculate volume fractions, Table 2 shows mass concentrations. The first row shows the experimentally determined H_2 , CO, H_2O and CO_2 mass fractions. The last three rows show the results for the PASR model assuming that a fraction of the particles in the PASR model are at 5000K. The fraction of particles at this temperature is varied from 1% to 10%.

The hydrogen mass concentration is comparable to those in the experiment. However, the measured concentrations of water (experimentally derived from mass balance) CO_2 are substantially higher than in the model.

In addition, the power required for good comparison in the experimentally and calculated values of the hydrogen mass balance (about 5% particles at 5000K) is substantially higher (~1500 W from Figure 1) than the power in the experiment.

We assume that the reason for the difference in the results is due to the limited capabilities of the PaSR model to handle non-uniform air/fuel mixtures,

A recently released version of CHEMKIN 4.0 has substantially enhanced PaSR modeling capabilities. Calculations will be carried out to determine whether better agreement between experiment and the model can be obtained. The greater flexibility in establishing particle distribution functions (PDF's) at user-defined temperatures allows the model to represent closer the experiment. Presently, our understanding of the process is that in a non-uniform air/natural gas

mixture the plasma starts the reaction in zones that have O/C ratios that are favorable for reaction (i.e., near stoichiometric combustion). The heat generated in these zones increase the temperature, through mixing, of the other zones. Once hot, reaction in these zones can take place.

Summary

In order to understand the natural gas plasma reformation process, modeling has been undertaken. At the present time we believe that processing requires air/fuel stratification, combustion of a fraction of the fuel in regions of appropriated O/C ratios, mixing with the unreacted mixture. This process generates combustion products with energy and fuel loss that may not be recoverable.

The nonthermal plasma processing is good, however, for initial processing of hydrocarbons fuels. Controlled preprocessing with the use of nonthermal plasmas could lead to a decrease in the amount of catalyst required for initial gas preheating, decreasing the problems with hot-spots in the catalyst bed (having the hot spot in the homogeneous zone), and decreasing the amount of carbon formation and decreased methane concentration and free oxygen in the reagents at the location of the catalyst.

Acknowledgement. Support for this work came from ChevronTexaco and ArvinMeritor.

References

- (1) *Plasma Catalytic Reforming of Methane*, L. Bromberg, D.R. Cohn, A. Rabinovich and N. Alexeev, *Int. J. Hydrogen Energy* **1999** 24, 1131
- (2) *Plasma Reforming of Natural Gas*, L. Bromberg et al., submitted for publication, *Int Journal Hydrogen Energy*.
- (3) Reaction Design, PASR Application User Manual, CHEMKIN Collection 3.7.1, 2003.

Table 2. Comparison of Mass Concentratatino of H_2 , CO, H_2O and CO_2 Between Experiment and Calculations, For 250 W Plasma Power and O/C ~ 1, with Natural Gas.

O/C=1 $t_{res}=1ms$ $t_{mix}=0.1ms$	Power input [kW]	H_2	CO	H_2O	CO_2
Exper. results	0.6	.60%	5.0%	7.0%	4.0%
10% particles @ 5000K	3	.80%	5.7%	1.8%	0.3%
5% particles @ 5000K	1.5	.45%	3.0%	1.0%	0.2%
1% particles @ 5000K	0.3	.03%	0.3%	0.1%	.05%

IN-SITU SPECTROSCOPIC STUDIES OF RHODIUM CATALYZED PRODUCTION OF HYDROGEN FROM DIMETHYLAMINE BORANE. HOMOGENEOUS OR HETEROGENEOUS CATALYSIS?

Yongsheng Chen, John Fulton, John Linehan & Tom Autrey

Fundamental Science Division
Pacific Northwest National Laboratory

Introduction

The US Department of Energy has recently issued a Grand Challenge in Hydrogen Storage.¹ The ambitious goals for volumetric and gravimetric densities and the controlled release of H₂ from materials at temperatures below 80 °C contained within this Grand Challenge demand the discovery of new materials and catalysts. Our interests in discovery of novel materials for hydrogen storage have led us to examine the chemical and physical properties of amine borane complexes.² In previous work we have discovered that both the kinetics and thermodynamics for the dehydropolymerization of ammonia borane (NH₃BH₃) are perturbed when the material is coated into mesoporous silica.³ These results piqued our interest for catalyst materials which would facilitate N-B bond formation with the concurrent release of hydrogen. Recent work from the Manners group suggested that colloidal rhodium catalyzes the release of hydrogen via dimerization of dimethylaminoborane in solution at room temperature.⁴ However, whether the dehydrocoupling and release of hydrogen occurred by a heterogeneous catalytic or a homogeneous catalytic pathway was not conclusively identified. To help elucidate the mechanistic pathway we undertook an *in-situ* spectroscopy approach (XAFS/XANES) to help identify the active catalyst concurrent with ¹¹B NMR studies to follow the kinetics of the reaction. This study demonstrates the utility of *in-situ* XAFS and XANES to differentiate between heterogeneous and homogeneous reaction pathways.

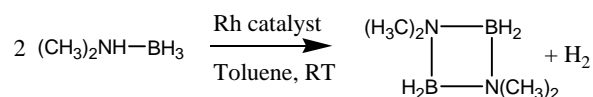
Experimental

The catalyst precursor, [Rh(1,5-cod)(μ-Cl)]₂ (17mM) and Me₂NHBH₃ (1.1M) were prepared in a solution of toluene in an Ar-purged glove box. The reaction solution was immediately transferred into sealed, 4-cm long glass EXAFS (extended x-ray absorption fine structure spectroscopy) sample holders having Kapton windows on both ends or into a 5 mm NMR tube. The reaction was conducted at 25°C for over 3 hrs. The *in situ* Rh K-edge (23222 eV) EXAFS spectra were collected on the bending magnet beamline (PNC-CAT, Sector 20) at the Advanced Photon Source, Argonne National Laboratory. Data were analyzed using AUTOBK and IFEFFIT routines.⁵ The kinetics of Me₂NHBH₃ disappearance were followed using ¹¹B{¹H} NMR spectroscopy run unlocked on a Varian VXR-300 NMR spectrometer operating at 96 MHz. **Caution:** The reactions described release a large amount of H₂ gas and can be exothermic and the gas release can be violent. Proper safety precautions including but not limited to pressure release devices and personal safety equipment should be used.

Results and Discussion

In-situ characterization of the active transition metal catalyst: EXAFS spectroscopy of Rhodium complex. In order to clarify the identity of the active Rh species, a series of *in situ* EXAFS spectra were collected as the solution was evolving hydrogen gas. Upon the initial mixing of the catalyst precursor with the dimethylamine borane solution the initial XAFS spectra shows that the Rh complex rapidly evolves during the first stages of the

reactions, undergoing a complete conversion to a new Rh compound in about 20 min. Further, from the heights of the XAFS absorption edges we determine that, during the first 40 minutes of the reaction, the amount of soluble Rh species remains constant (during which 60% of the reaction has occurred). Thus we conclude that the complex at this point corresponds to the active rhodium complex. The spectrum for the active complex in Figure 1 was acquired after 30 minutes of reaction where all Rh was completely soluble in the toluene. Finally, we observe that as the reaction proceeds beyond 40 min, the amount of soluble Rh then steadily decreases until it reaches about 20% of the starting concentration after about 3 hrs of reaction time.



The EXAFS radial structure plot (RSP) for the active rhodium complex is shown in Figure 1, together with that for Rh(0) metal for comparison. The RSP is related to the probability of finding an atom at some radial distance from the central absorbing atom (Rh). The EXAFS backscattering amplitudes for high-Z atoms such as rhodium are uniquely different than those from the low-Z ligands around the rhodium. Hence we can uniquely identify the peak in Figure 1 at about 2.7 Å as belonging to Rh-Rh structures in the active rhodium complex.

As a first approximation, we know that the coordination number is proportional to the peak amplitude in the radial structure plot. The active complex has a Rh-Rh peak amplitude that is about 4 times smaller than that of bulk Rh(0) metal (12 first shell rhodiums). Furthermore, this peak for the active complex, is about 2 times smaller than that for a Rh(0)₆ metal cluster.⁶ Preliminary EXAFS peak fitting to theoretical standards shows that the active metal contains no more than 4-6 metal atoms in a core cluster surrounded by ligands. As shown in Figure 1 the Rh-Rh distance for the Rh(0)₆ metal cluster is the same as for the bulk metal, whereas the one for the active complex is significantly longer by about 0.06 Å. This is evidence that the strong ligand-rhodium interactions in the complex decrease the Rh-Rh interaction and thereby increase the Rh-Rh

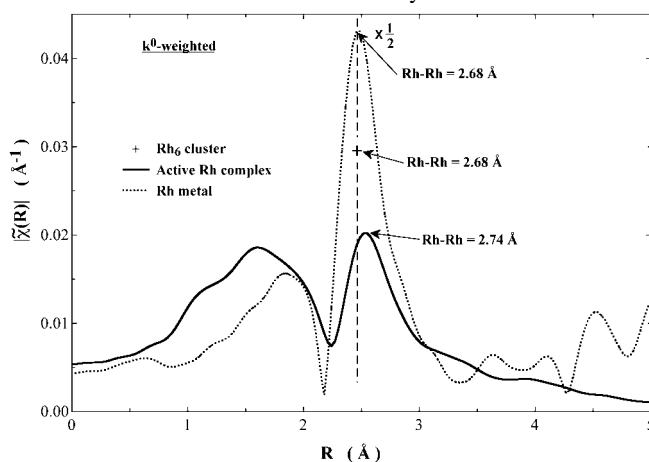


Figure 1. The radial structure plot for the active Rh complex at t=30 min (solid), and for Rh metal (dashed), both without phase corrections. The phase-corrected Rh-Rh distances are listed next to their respective peaks. The (---) vertical line and the (+) symbol locates the distance and amplitude respectively for a Rh(0)₆ cluster (from Ref. 6).

distances. The same effect is observed for the $\text{Rh}_6(\text{CO})_{16}$ complex.⁶ This EXAFS study concludes that the active Rh complex for $[\text{Rh}(\text{cod})\text{Cl}]_2$ catalyzed Me_2NHBH_3 dehydrocoupling is most likely a Rh (0) cluster with no more than 4-6 core Rh atoms with strongly-bound external ligands. This cluster size is significantly smaller than the 2 nm Rh(0) particles suggested in previous studies.⁴

Kinetics of hydrogen formation in the Rh catalyzed coupling of dimethylamine borane. Solution phase ^{11}B NMR spectroscopy was used to follow the reaction kinetics of the catalyzed dehydrocoupling reaction of Me_2NHBH_3 in toluene to yield the cyclic dimer and hydrogen. In the NMR experiment the solid catalyst precursor and the solid amine borane complex were weighed into the same vial and the mixture taken into the glove box. When toluene was added to the $[\text{Rh}(1,5\text{-cod})(\mu\text{-Cl})_2]/\text{amine borane}$ mixture the solution began to bubble immediately. As shown in Figure 2b the $^{11}\text{B}\{^1\text{H}\}$ NMR spectra at ca. 50% conversion shows the starting material and the product are the predominate species. The reaction does not appear to generate any significant amount of side products.

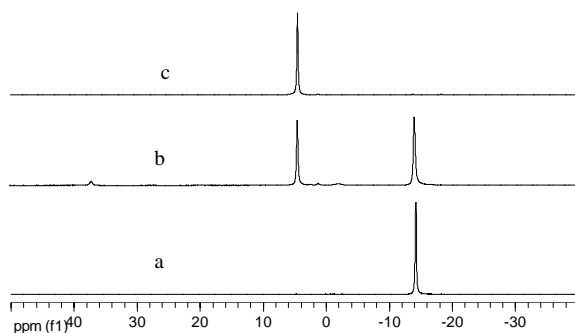


Figure 2. a) The $^{11}\text{B}\{^1\text{H}\}$ toluene solution NMR spectra of Me_2NHBH_3 (-14.2 ppm) b) at ca. 50% conversion, 30 minutes, c) complete conversion, 200 minutes. The product $[\text{Me}_2\text{NBH}_2]_2$ (4.4 ppm) grows in over time.

For the kinetic analysis, the area under each peaks was integrated at various times and provides the rates of disappearance of the starting material Me_2NHBH_3 and the appearance of the product dimer $[\text{Me}_2\text{NBH}_2]_2$. These results are shown in Figure 3.

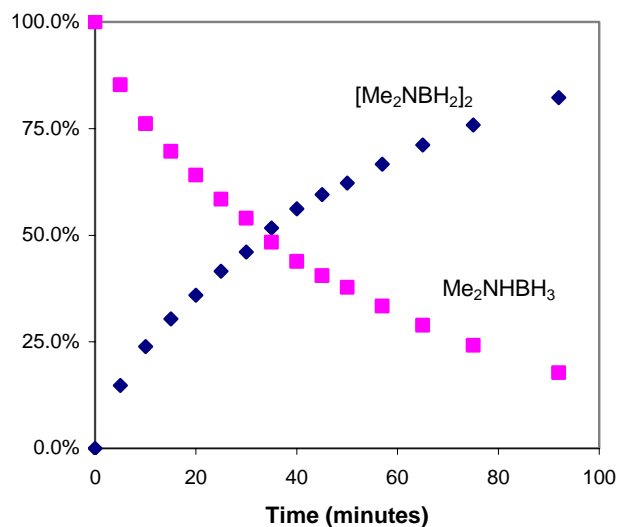


Figure 3. Time evolution of Me_2NHBH_3 disappearance/ $[\text{Me}_2\text{NBH}_2]_2$ appearance in toluene in the presence of rhodium at room temperature as determined by $^{11}\text{B}\{^1\text{H}\}$ NMR.

Conclusions

The *in-situ* EXAFS experiments permit the observation of the transition metal species during the progression of the reaction. The predominant species observed during H_2 evolution does not appear to be colloidal but most likely is composed of 2 to 6 Rh atoms surrounded by tightly bound external ligands. This result is in contrast to previous conclusions that suggest the mechanism involves a heterogeneous catalyst.

We believe the combination of *in-situ* EXAFS spectroscopy to identify the active catalyst species and *in-situ* NMR spectroscopy to monitor kinetics provides a unique approach to answering the elusive question for many reported ambiguities, “Is it homogeneous or heterogeneous catalysis?”⁷

Acknowledgement. The authors wish to acknowledge support from the Laboratory Directed Research and Development Program at the PNNL and the Nano Science and Technology Initiative. Pacific Northwest is operated for the Department of Energy by Battelle. Use of the Advanced Photon Source was supported by the U. S. Department of Energy, Office of Science, Office of Basic Energy Sciences, under Contract No. W-31-109-ENG-38.

References

- 1 Hydrogen, Fuel Cells & Infrastructure Technologies Program, 2003 Merit Review and Peer Evaluation Meeting, May 19-22, 2003, Berkeley, CA.
- 2 Gutowski, M., Autrey, T., Prepr. Pap. - *Am. Chem. Soc., Div. Fuel Chem.*, **2004**, 49 (1), 275.
- 3 Autrey, T., Gutowska, A., Li, L., Linehan, J.C., Gutowski, M., Prepr. Pap. - *Am. Chem. Soc., Div. Fuel Chem.*, **2004**, 49 (1), 150.
- 4 Jaska, C. A.; Mannors, I., *J. Am. Chem. Soc.* **2004**, 126, 1334. and references cited therein.
- 5 Newville M. *J. Synchrotron Rad.* **2001**, 8, 322.
- 6 Alexeev, O. S.; Panjabi, G.; Phillips, B. L.; and Gates, B. C. *Langmuir* **2003**, 19, 9494.
- 7 (a) Dyson, P. J., *Dalton Trans.* **2003**, 2964. (b) Weddle, K. S.; Aiken III, J. D.; Finke, R. G. *J. Am. Chem. Soc.* **1998**, 120, 5653.

NEW OXYGEN-EVOLVING COMPLEXES IN ARTIFICIAL PHOTOSYNTHESIS SYSTEM SPLITTING WATER INTO OXYGEN AND HYDROGEN

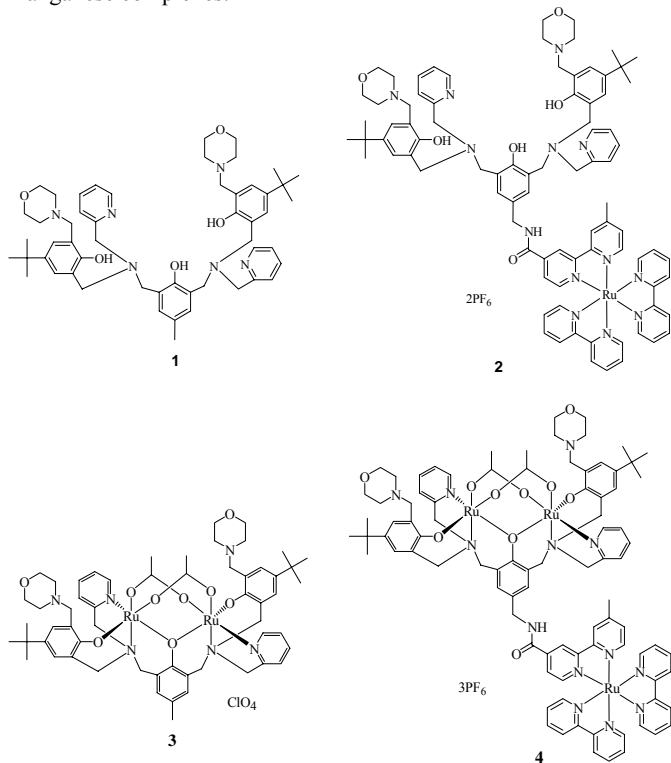
Xiaojun Peng,^{1*} Feng Shi,¹ Hongyang Li,¹ Rong Zhang,¹ Xiaoqiang Chen,¹ Licheng Sun,^{2*} and Björn Åkermark²

¹State Key Laboratory of Fine Chemicals, Dalian University of Technology, 116012 Dalian, China.

²Department of Organic Chemistry, Arrhenius Laboratories, Stockholm University, 106 91 Stockholm, Sweden.

Introduction

Photosynthesis oxygen evolving through water oxidation performed in photosystem II (PSII) of plants and cyanobacteria. The key player in water oxidation is a triad composed of a multimer of chlorophylls (named P₆₈₀), a redox active amino-acid (named Tyrosine_z), and a Mn-cluster composed of 4 Mn ions of high valence (oxygen-evolving complex, OEC).¹ In the past decades, considerable attention has been paid to biomimic the structure of OEC,² which resides on the electron donor side of PSII. P₆₈₀ is excited when it absorbs a photon, and transfer an electron to the acceptor system (pheophytin and two quinines Q_A and Q_B). We use the ruthenium(II) *tris*-bipyridine complex as photosensitizer, that plays the role of the P₆₈₀ chlorophyll in PSII. And our former work³ has been to use the principles of the nature PSII to construct supramolecular complexes in which a photosensitizer is linked to monomeric and dinuclear manganese complexes.



But until now, there are few well-defined molecules which act as catalysts toward water oxidation.⁴ Among the very few water oxidation catalysts, the Ru^{III} dimer and its derivatives are the only materials shown to perform water oxidation function through homogeneous chemical catalysis.⁵ As a good alternative model for the electron donor side of photosystem II in green plants, we have prepared dinuclear ruthenium complex **2** and *tris*-nuclear ruthenium supramolecular complex. Introduction of phenolate groups into the

ligand instead of some of the pyridyl groups in **1** or **2** can make them possible to coordinate two high valent Ru(III) ions. *tert*-Butyl groups in the ligand not only improves the solubility of complex,⁶ but also increases their electron donating effect that may result in lower redox potentials for the Ruthenium. The two “out-standing” arms of morpholine on *tert*-butyl-phenol provide the function of anchoring water via a chain “N---H-O-H---N” by the hydrogen bond function between two nitrogen atoms in morpholine and two hydrogen atoms in H₂O.⁷ It is a very important improvement for the reason that the decreasing distance between anchored water and reactive center Ru(III, III) benefits the following water oxidation with less external influence. They will also increase the solubility of the complex and electron donating effect as the *tert*-butyl groups. According to these ideas, two novel complex **1** and **2** in which {[2-(hydroxy-3-(morpholin-4-ylmethyl)-5-*tert*-butylbenzyl)(pyridyl-2-methyl-amino)-methyl]} arms are linked to the *ortho*-positions of the hydroxyl group have been synthesized. And complex **3** was prepared by refluxing the complex **1** and Ru(DMSO)₄Cl₂ in MeOH in the presence of NaOAc followed by addition of a saturated aqueous solution of NaClO₄.⁸ The complex **4** was synthesized by the similar method. We have also studied the properties of these complexes, including electrochemical and photophysical properties. Moreover, we hope that the simplified and explicit model system may offer mechanistic insight into elucidation of electron transfer coupled with proton transfer involved in photosynthetic water oxidation.

Results and Discussion

Absorption and Emission Properties. For the simple dinuclear ruthenium complex **3**, there is almost no absorption between 400–500 nm in the visible region and there are two weak absorptions at $\lambda_{\text{max}} = 290 \text{ nm}$ ($\epsilon = 9.5 \times 10^3 \text{ M}^{-1} \cdot \text{cm}^{-10}$) and 340 nm ($\epsilon = 4.5 \times 10^3 \text{ M}^{-1} \cdot \text{cm}^{-10}$). The UV-Vis absorption spectrums of complex **2** and **4** essentially have similar features to those of Ru *tris*-bipyridine compounds. The main absorption band between 400–500 nm arises from MLCT (the metal to ligand charge transfer $\text{M} \rightarrow \pi^* \text{L}$). The intense absorption peak at 288 nm is due to LC (a ligand center transition $\pi \rightarrow \pi^*$). In compound **2**, the emission maximum locates at 627 nm, is red-shifted compared to that of Ru(bpy)₃ and the radiative quantum yield (Φ_r) is 0.082 while the Φ_r of Ru(bpy)₃ is 0.062.¹¹ The red-shift of the MLCT band and the higher luminescence quantum yield compared to Ru(bpy)₃ are caused by the different ligands in the compounds. In **2**, the bipyridine ligand with an amide group has a lower energy than the unsubstituted ones, thus the MLCT state may involve this ligand that may result in the small red-shift of the MLCT band. Moreover, in the presence of ruthenium no change was observed in the absorption maximum and only a small red shift (<5 nm) in the emission maximum. However, the emission intensity was much lower for the *tris*-ruthenium compounds than for the corresponding ruthenium complex.

Electron transfer. All the complexes investigated were photooxidized in laser flash photolysis experiments in the presence of the external acceptor methyl viologen [MV(PF₆)₂]. Even the short-lived states of **4** could be effectively photooxidized to Ru^{III} if the concentration of viologen was high as 0.2 M. In complex **2** or **4**, the negative absorption at 400–500 nm is due to the Ru^(II) ground state bleaching. Two positive absorption bands with the maximum at 600 and 398 nm, are assigned to the absorption of MV^{•+}. Formation of the MV^{•+} indicates the oxidative quenching of the Ru(II) ³MLCT excited state by MV²⁺. According to the emission kinetics of Ru(II) ³MLCT at 640 nm, giving a pseudo-first-order quenching rate constant of $2.5 \times 10^7 \text{ s}^{-1}$. The lifetime of 1.27 μs for complex **2**, so 97 % of photoexcited Ru(II) was oxidized to Ru(III) under such condition. And from the Fig. 1(a), we can see no decay of MV^{•+}

absorption when the recovery of Ru(II) complete. This result shows that the regeneration of Ru(II) is due to the intramolecular electron transfer from the substituted phenols to the photooxidized Ru(III), rather than the electron recombination from the MV^{+} . The ET rate constant in complex **2** determined from the 470 nm trace was $2.5 \times 10^6 \text{ s}^{-1}$, which is almost two orders of magnitude faster than the ET rate of $ca. 10^4 \text{ s}^{-1}$ in the compound without substitute on the tyrosine moiety. From the above results, we conclude that the introduction of an amine, morphine and a pyridine would increase the electron-donated ability of Ph-OH.

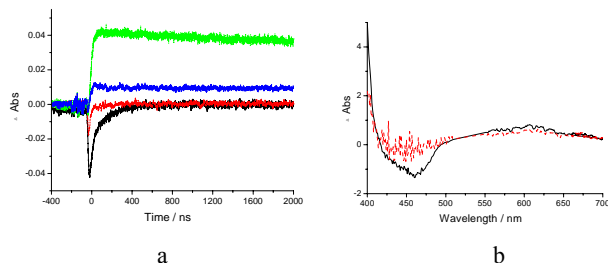


Figure 1. Transient absorption changes after excitation at 532 nm for complex **2** and **4** in the presence of 200 mM methyl viologen (MV^{2+}): (a) increased absorption at 600 nm due to the formation of MV^{+} (upper curves) and bleaching of the Ru(II) ground state at 470 nm (lower curves). (b) Transient absorption spectra at 100 ns after excitation for complex **2** and **4**. The spectra were normalized at 600 nm (the complex **4** spectra was multiplied by 2) to facilitate comparison of the spectra shapes.

In complex **4**, the Ru^{II} recovery was clearly much faster than the MV^{+} decay. From a comparison of the signal amplitude in **Fig. 1(a)**, it is clearly that most of Ru^{II} recovery occurred within the time of $ca. 20$ ns. According to fitting the kinetics of 470 nm trace, 80 % of the Ru^{II} recovery occurred with $k > 5.5 \times 10^7 \text{ s}^{-1}$. We attribute this to intramolecular electron transfer from the $Ru_2^{III,III}$ moiety, probably generating the $Ru_2^{III,IV}$ or $Ru_2^{IV,IV}$ complex. The remaining, slower recovery seen at 470 nm occurred with the same rate as that in complex **2** ($k = 2.5 \times 10^6 \text{ s}^{-1}$) may be the partly dissociation of Ru. It is important to note in **Fig. 1(b)**, the (normalized) transient absorption spectra at 400 ns after excitation for complex **2** and **4**, the very rapid Ru^{II} recovery in **4**, which is not observed in complex **2**, which lacks dinuclear Ru, suggested that electron transfer from the ruthenium complex moiety to the photogenerated Ru^{III} occurs with a rate constant of $k > 5.5 \times 10^7 \text{ s}^{-1}$.

Electrochemistry. Electrochemical properties of **2**, **3**, **4** were studied by cyclic voltammetry (CV) and differential pulse voltammetry (DPV) in acetonitrile. DPV of **2** obtain the typical waves of the metal and the reduction of the three ligands in $Ru(bpy)_3^{2+}$ moiety: an quasi-reversible oxidation wave at $E_{1/2} = 0.986 \text{ V vs } Fc^{+/0}$ ($\Delta E = 80 \text{ mV}$), due to Ru^{3+}/Ru^{2+} for **2**, and three quasi-reversible reductive waves ($E_{pc1} = -1.601 \text{ V}$, $\Delta E_1 = 38 \text{ mV}$; $E_{pc2} = -1.862 \text{ V}$, $\Delta E_2 = 21 \text{ mV}$; $E_{pc3} = -2.142 \text{ V}$, $\Delta E_3 = 38 \text{ mV vs } Fc^{+/0}$ respectively) due to the three bipyridine ligands. In CV, the oxidation peaks of the three bipyridine ligands are smaller than the reduction peaks, but there are also three equal peak heights of redox waves in DPV. In addition to these waves, the peak at $ca. 0.52 \text{ V vs } Fc^{+/0}$ obtained from DPV is probably related to the phenol oxidation since it is close to the reported peaks of phenol oxidation in $Ru(bpy)_3$ -tyrosine compound in acetonitrile.^{3a} The peak at $ca. -1.0 \text{ V vs } Fc^{+/0}$ is due to an impurity present in the electrode which is adsorbed on to the electrode. The CV of complex **3** shows two reversible oxidation waves ($E_{1/2} = 0.554, 0.765 \text{ V vs } Fc^{+/0}$), and two reversible reduction waves ($E_{1/2} = -0.849, -1.099 \text{ V vs } Fc^{+/0}$). DPV

shows these well-resolved peaks. The compound **3** is a dinuclear ruthenium (III,III) complex, so these four voltammetric waves could be assigned to two subsequent oxidations ($Ru_2^{III,III} \rightarrow Ru_2^{III,IV}$ and $Ru_2^{III,IV} \rightarrow Ru_2^{IV,IV}$). In addition to these waves above, there are two small reversible peaks at 0.384 and 0.511 V vs $Fc^{+/0}$. These reactions may involve the oxidation of tertiary amine and phenol groups.

For the mononuclear $[Ru(bpy)_3]^{2+}$ complex **2**, the Ru^{II} to Ru^{III} is 0.906 V. This is decreased to -1.099 V for the $Ru_2^{II,II}$ to $Ru_2^{III,III}$ and -0.853 V for the $Ru_2^{II,III}$ to $Ru_2^{III,III}$. The difference for the redox potential may be due to the introduction of *tris*-phenolate group. And in complex **3**, the $Ru_2^{III,IV}$ can easily performed, the potential is only at 0.765 V. Furthermore, although the redox potentials of dinuclear Ru moiety in CV of complex **4** are not clear, the DPV have these four well-resolved peaks, which are close to the Ru moiety in complex **3**. The result also shows in the complex **4**, the Ru in the photosensitizer could oxide the dinuclear $Ru_2^{III,III}$ to $Ru_2^{III,IV}$ and $Ru_2^{IV,IV}$, which is important for the water oxidation.

Acknowledgment. This work was financially supported by the “973 program” Ministry of Science & Technology of China and National Natural Science Foundation of China (Project 20376010 and 20128005).

References

1. Sun, L.; Hammarström, L.; Åkermark, B.; Styring, S., *Chem. Soc. Rev.*, **2001**, 30, 36-49.
2. a) Pecoraro, V. L.; Baldwin, M.; Gelasco, A.; *Chem. Rev.*, **1994**, 94, 807-826. b) Kitajima, N.; Singh, U. P.; Amagai, H.; Osawa, M.; Moro-oka, Y. J., *J. Am. Chem. Soc.*, **1991**, 113, 7757-7758. c) Chen, C.; Huang, D.; Zhang, X.; Chen, F.; Zhu, H.; Liu, Q.; Zhang, C.; Liao, D.; Li, L.; Sun, L., *Inorg. Chem.*, **2003**, 42, 3540-3548. d) Mukhopadhyay, S.; Armstrong, W. H., *J. Am. Chem. Soc.*, **2003**, 125, 3540-3548. e) Gupta, R.; MacBeth, C. E.; Young, V. G.; Borovik, A. S., *J. Am. Chem. Soc.*, **2002**, 124(7), 1136-1137.
3. a) Sun, L.; Burkitt, M.; Tamm, M.; Raymond, M. K.; Abrahamsson, M.; LeGourriec, B.; Frapart, Y.; Magnuson, A.; Kenez, P. H.; Brandt, P.; Tran, A.; Hammarström, L.; Styring, S.; Åkermark, B., *J. Am. Chem. Soc.*, **1999**, 121, 6834-6842. b) Sun, L.; Raymond, M. K.; Magnuson, A.; LeGourriec, B.; Tamm, M.; Abrahamsson, M.; Kenez, P. H.; Martensson, J.; Stenham, G.; Hammarström, L.; Styring, S.; Åkermark, B., *J. Inorg. Biochem.*, **2000**, 78, 15-22. c) Abrahamsson, M. L. A.; Baudin, H. B.; Tran, A.; Philouze, C.; Berg, K. E.; Raymond-Johansson, M. K.; Sun, L.; Åkermark, B.; Styring, S.; Hammarström, L., *Inorg. Chem.*, **2002**, 41(6), 1534-1544.
4. Yagi, M.; Kaneko, M., *Chem. Rev.*, **2001**, 107, 21-36. b) Ruttinger, W.; Dismukes, G. C., *Chem. Rev.*, **1997**, 97, 1-18.
5. Ramaraj, R.; Kiva, A., *Chem. Lett.*, **1987**, 264, 261-266. b) Binstead, R. A.; Chronister, C. W.; Ni, J.; Hartshorn, C. W.; Meyer, T. J., *J. Am. Chem. Soc.*, **2000**, 122, 8464-8472.
6. Lomoth, R.; Huang, P.; Zheng, J.; Sun, L.; Hammarström, L.; Åkermark, B.; Styring, S., *Eur. J. Inorg. Chem.*, **2002**, 2965-2974.
7. White, D. J.; Laing, N.; Miller, H. A.; Parson, S.; Coles, S.; Tasker, P. A., *Chem. Commun.*, **1999**, 2077-2078.
8. Lomoth, R.; Magnuson, A.; Xu, Y.; Sun, L., *J. Phys. Chem.*, **2003**, 107(22), 4373-4380.
9. Miller, H. A.; Laing, N.; Parsons, S.; Parkin, A.; Tasker, P. A.; White, D. J., *J. Chem. Soc. Dalton Trans.*, **2000**, 3773-3782.
10. Adams, H.; Bailey, N. A.; Fenton, D. E.; Papageorgiou, G. J., *J. Chem. Soc. Dalton Trans.*, **1995**, 1883-1885.
11. Casper, J. V.; Meyer, T. J., *J. Am. Chem. Soc.*, **1983**, 105, 5583-5591.

NON-THERMAL PLASMA CATALYTIC CONVERSION OF METHANE TO SYN-GAS

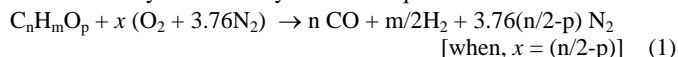
Chiranjeev Kalra¹, Young Cho¹, Alexander Gutsol¹,
Alexander Fridman¹, Teclé S Rufael²

¹ Drexel Plasma Institute, Drexel University, Philadelphia, PA19104

² ChevronTexaco Energy Technology Company, Houston TX 77042

Introduction

Syn-gas, a mixture of hydrogen and carbon monoxide, is used as a major intermediary for the production of hydrogen or other hydrogen based chemical compounds like ammonia, liquid fuels, solvents etc. Commercially syn-gas production from methane or lower hydrocarbons can be carried out in a number of ways: steam reforming, thermo-catalytic reforming, partial oxidation, etc. [1]. Syn-gas formed via endothermic reactions (steam and CO₂ reforming) requires high-energy input. The simplest and most efficient way for the large scale production would be partial oxidation of hydrocarbons [1]. The partial oxidation of hydrocarbons in air is usually described by idealized equation as:



Increase in x from $(n/2-p)$, for rich mixtures, increases heat of reaction but at the same time produces carbon dioxide and water vapor thus reducing the amount of syn-gas generated. The oxygen to fuel ratio (x) determines the heat of the reaction and amount of syn-gas generated. For this process Nickel (Ni) has traditionally been used as catalyst, but problems concerning to bulky catalyst volume, catalyst poisoning and high maintenance costs have limited application to large scale industrial operations.

The use of highly active electrical discharges (plasmas) for this conversion has been experimented with and studied numerically during the last decade, but traditional plasma systems cannot simultaneously provide high power density, for large scale industrial output, and chemically selective conversion process [2]. Broader understanding of electrical discharge physics resulted in development of newer class of discharge systems, which fall in the category of transitional discharges, looks very attractive for the above application [3]. These are discharges with plasma parameters between those of the thermal and cold non-thermal discharges called the transitional non-thermal discharges, where the gas temperature increases considerably (2000 – 3000 K) but the discharges still are not in the thermal regime [4]. Gliding Arc is an example of such transitional discharges can be achieved in Gliding Arc (GA) reactor.

Experiments and Numerical Modeling of the Process

A large-scale laboratory experimental unit for Gliding Arc in Tornado (GAT) assisted syn-gas generation was developed at Drexel Plasma Institute. GAT is an advanced Gliding Arc (GA) system developed by the authors where GA plasma is stabilized inside a Reverse Vortex Flow, and has many advantages over traditional systems as reported in [5] and [6]. This unit had 3 important components: (1) GAT reactor with heat exchanger, (2) Power supply and (3) Instrumentation.

GAT reactor design [3], based on cylindrical geometry, generates transitional plasma in a volumetric continuous flow reactor providing uniform flow treatment. Reverse Vortex Flow (RVF), which is very similar to the natural tornado, is set up inside the reactor. It has a circular disc shaped electrode and a spiral electrode both are arranged such that they are locally parallel to the streamlines thus causing minimum disturbance to the gliding arc. These two electrodes in RVF are in effect diverging electrodes in the “plane” of the flow. Reverse vortex flow provides perfect thermal insulation of

the discharge zone from the reactor walls at the same time intense convective cooling of the arc. Also there is a recirculation zone near the exit. Here the active species from the plasma zone are retained inside the reactor [5]. This recirculation is very important for plasma-catalytic reactions. Heat exchanger is employed for internal heat recuperation, as this conversion process is exothermic for methane. DC power supply from Voltronics (10kV, 1A maximum) is used to generate GA plasma inside the reverse vortex reactor. Inlet flow controllers, thermocouples to measure temperature at heat exchanger, and analyzers for CO, CO₂, H₂, GC/MS for hydrocarbons from C₁ – C₅ and out-flow meter complete the instrumentation of the apparatus.

The modeling was done in ChemKin using zero dimension assumption and GRI 2.11 mechanism of kinetic scheme with 65 species and 200 reactions, including low temperature reactions.



Figure 1. Experimental GAT reactor fired at equivalence ratio 4, in the background syn-gas produced is burned before disposal.

Results and Discussion

Experiments in different regimes were conducted. For same equivalence ratio, different flow rates and flow configurations were tried. The most optimal and stable of the cases is for tangential entry of methane and axial air inlet, with minimum flow rate of methane at about 0.35 L/S for the present system. In fact the Reverse Vortex configuration it self is very effective in flame stabilization and experiments for methane conversion with out any plasma power gave stable combustion zone, but not very good conversion to syn-gas. Temperatures reach as high as 750 K at entry to the plasma reactor. Tangential methane and axial air in reverse vortex form a rotating central column of plasma and flame. The zone is cooled by intense flow around it and is simultaneously insulated from any heat losses to the surrounding by the same reverse vortex. Tangential methane ensures dissociation of methane in plasma and not air thus ensuring no NO_x emissions.

The data collected from experimental tests and analyzed for mass balance. The secondary data thus obtained: the conversion degree (methane conversion to syn-gas) and energy cost analysis were plotted vs. the equivalence ratio.

Conversion Degree is a good measure of the system performance and evaluation as shown in **Figure 2**. Numerical results (curve in fig 2) show that the conversion is best for equivalence ratio 3.0 to 3.6, and not 4.0. This is because of the fact that as we go to lower equivalence ratio we have higher heat in the system.

This heat helps achieve better conversion and reaction rates. Experimental points as shown in **Figure 2** are in good agreement with the numerical results.

Electrical Energy is added to the system in the form of plasma power. Plasma acts as a catalyst and thus this power should be optimized. We should not spend too much power on one hand and lesser power should not restrict the extent of reaction on the other.

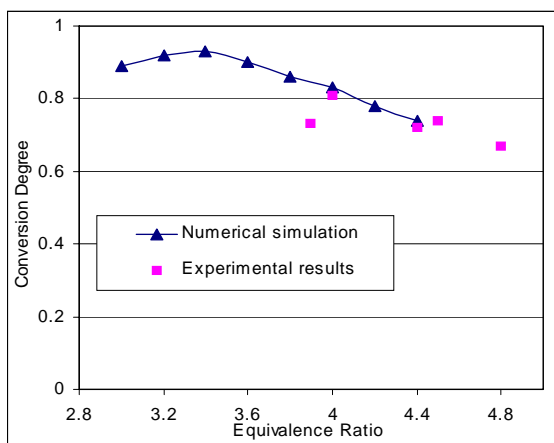


Figure 2. Conversion degree as a function of equivalence ratio

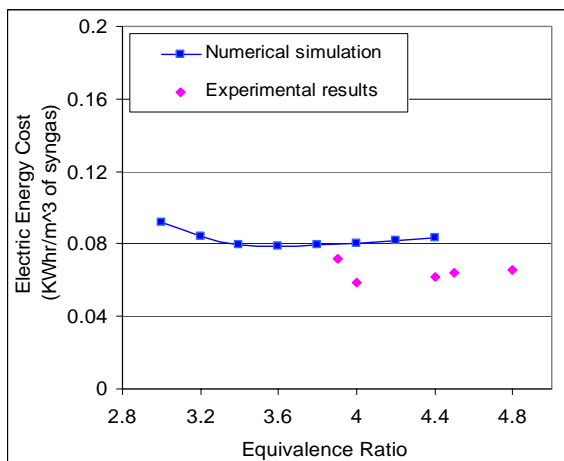


Figure 3. Electric Energy Cost as a function of equivalence ratio

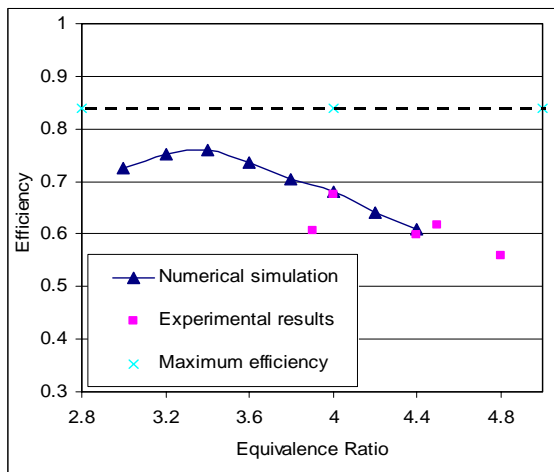


Figure 4. Efficiency as a function of equivalence ratio

As in **Figure 3**, At high equivalence ratio the heat of the system is low so more plasma power is required. But as we decrease the equivalence ratio we need lesser power and we achieve a minimum power level, which again rises as production rates start decreasing rapidly. Comparison with Experimental results reveal similar trend. Experimental values of power required are just lower this signifies

the importance of reverse vortex geometry and positive impact of recirculation.

Total Energy cost: This represents the amount of energy spent to get 1-meter cube of syn gas. This includes electrical energy cost in KW-hr and the energy spent in the form of methane, which is a fuel, so can be interpreted in terms of KW-hr energy equivalent for producing 1 meter cube of syn-gas. Similarly the syn-gas produced is again a fuel so its equivalent in KW-hr is our output. The ratio of these energy equivalents spent and produced gives a very accurate efficiency of the system. Theoretically the maximum efficiency of such a system can never be more than 84%, because syn-gas gas lower heat value than methane. This efficiency as function of equivalence ratio is expressed in **Figure 4**. Energy cost is optimal between equivalence ratio 3.2 and 3.8.

Conclusions

Experimental system built for syn-gas production from hydrocarbon fuel was tested and evaluated based on various production parameters as stated above. Syn-gas was generated in this continuous volumetric flow reactor pilot plant at output of about 1.1 L/S. Electric energy spent in the process was as low as 0.06 KW-hr/m³ of syn-gas. High chemical process selectivity is obtained using GAT. GC/MS analysis of the reactants shows no production of C2 to C5 hydrocarbon species.

The experimental system worked predominantly at higher equivalence ratio. This was due to the fact that since methane flow was driving the arc there was a lower limit to this flow rate. Lower equivalence ratio can be achieved by designing fine nozzle for gas injection. The system can run continuously without the need of any maintenance, as there are no consumables, electrode erosion or cooling requirements. In fact the reverse vortex burner stabilizes flame at very high equivalence ratio without any combustion support. In that case we have very low conversion to syn-gas and high soot formation. This result signifies the importance of selectivity of chemical processes that can be achieved by plasma catalysis.

References

- (1) Jean Marie, Iulian Rusu, 2001 J. Phys. D: Applied Phys. 34, Pg. 2798-2803.
- (2) Sobacchi M.G., Saveliev A.V, Fridman A.A, Kennedy L.A, Ahmed S, Krause T. 2002, International Journal of Hydrogen Energy 27, Pg. 635-642.
- (3) C. S. Kalra, M. Kossitsyn, K. Iskenderova, A. Chirokov, Y. I. Cho, A. Gutsol, A. Fridman, Electronic Proceedings of 16th International Symposium on Plasma Chemistry, Taormina, Italy, June 22-27, 2003. ISPC-565.pdf.
- (4) A. A. Fridman, L. Kennedy "Plasma Physics and Engineering" (Taylor & Francis, accepted for publication in 2003).
- (5) Gutsol A. F. and Kalinnikov V. T. Reverse-Flow Swirl Heat Insulation of Plasma and Gas Flame. (High Temperature, Vol. 37, No. 2, 1999, pp. 172 - 179.)
- (6) Gutsol A. Thermal Insulation of Plasma and Flame in Reverse Vortex. In: Progress in Plasma Processing of Materials 1999. Editors: Pierre Fauchais and Jacques Amouroux. Begell House, Inc., NY, 1999. (Proceedings of the Fifth International Thermal Plasma Processes Conference, St.-Petersburg, July 13-16, 1998) P. 81 - 86.

ACHIEVING SEPARATIONS AND DISTRIBUTED PRODUCTION TECHNICAL TARGETS OF THE PRESIDENT'S HYDROGEN FUEL INITIATIVE

Steven Chalk, Program Manager
Arlene Anderson, Technology Development Manager

Hydrogen, Fuel Cells, and Infrastructure Technologies Program
 Office of Energy Efficiency and Renewable Energy
 U.S. Department of Energy

EE-2H, 1000 Independence Avenue, SW Washington, D.C. 20585

The President's Hydrogen Fuel Initiative

Announced on January 28, 2003 by the President in his State of the Union Address, the Hydrogen Fuel Initiative envisions a hydrogen economy that could have fundamental and dramatic benefits regarding energy security and the environment.

A transition to hydrogen as a major fuel in the next 50 years could fundamentally transform the U.S. energy system, creating opportunities to increase energy security through the use of a variety of domestic energy sources for hydrogen production while reducing environmental impacts, including atmospheric CO₂ emissions and criteria pollutants.

New Hydrogen Separations and Purification Research

With funding from the President's Hydrogen Fuel Initiative, next year DOE's Office of Energy Efficiency and Renewable Energy will cost-share 80% of total R&D expenditures for several new hydrogen separations and purification projects. The total funding for these projects is expected to be up to \$10 million (including 20% cost share) and, the DOE Office of Fossil Energy is providing a portion of the DOE funding for hydrogen to coal related separations research. As a result of this research, within three to four years DOE will verify advanced pilot scale membranes that meet or exceed the membrane separations targets listed in Table 1.

As part of integrated decentralized hydrogen production systems and potentially as part of many possible technologies to be utilized for hydrogen production, DOE received many highly qualified research applications for new hydrogen membrane separation and purification technologies based on membrane systems that cost-effectively optimize different types of membrane characteristics while maintaining key attributes for producing high purity hydrogen.

Desirable membrane system characteristics include: 1) a high flux rate; 2) low cost; 3) improved durability; 4) low parasitic power requirements; and 5) low membrane fabrication costs. This new research will lend itself to membrane systems that integrate the hydrogen separation and purification steps with a shift reactor as a one step operation.

Another key theme of the research includes the development of membranes suitable for use with a wide range of fuels especially in reforming renewable biomass based liquid fuels (e.g. ethanol, methanol, biomass pyrolysis oils, etc.) and in a robust syngas environment, as from natural gas or coal-based applications. The targets shown in Table 1 are based on a palladium membrane that is fuel neutral and that can be used for hydrogen separation and purification from a variety of fuels. Sulfur tolerance and lower cost fabrication techniques are also desirable membrane system characteristics.

Table 1. Membrane Separations Targets

Characteristics	Units	Target
Flux Rate	scfh/ft ²	200
Cost	\$/ft ²	<100
Durability	Hrs	100,000
Operating Temp	°C	300-600
Parasitic Power	kWh/ 1,000 scfh	2.8

New Distributed Reforming Hydrogen Production Research

Also with funding from the President's Hydrogen Fuel Initiative, DOE will cost-share 65% of total R&D expenditures for several new distributed reforming projects. The total funding for these projects will be about \$8 million (including the 35% DOE cost share). As a result of this research, within three to four years DOE will verify pilot scale systems that can meet or exceed the targets specified in Table 2.

Small-scale distributed reforming production (i.e., 1,500 kg/day or less) of hydrogen from natural gas and/or liquid fuels at refueling stations, with an emphasis on fuels produced from renewable biomass resources (e.g. ethanol, methanol, biomass pyrolysis oils, etc.), is a viable approach to hydrogen production, but current small-scale distributed technologies are too expensive to compete with gasoline. Renewable biomass based liquid fuels have the added advantage of near-zero green house gases emissions. DOE is funding this new research to develop low cost, highly efficient distributed hydrogen production technologies from natural gas, other liquid fuels and renewable biomass based liquid fuels aimed at distributed production for refueling stations at capacities of 100-1,500 kg/day of hydrogen.

The hydrogen purity for use in Polymer Electrolyte Membrane fuel cells is critical. Hydrogen purity requirements are:

Hydrogen Purity: 98% minimum on a dry basis;
 Carbon Monoxide <1 ppm;
 Carbon Dioxide <100 ppm;
 Sulfur <10 ppb;
 Ammonia <1 ppm;
 Non-methane hydrocarbons <100ppm;
 Oxygen, Nitrogen, and Argon <2% in total.

Opportunities for cost reductions in distributed hydrogen production systems include better heat integration, improvements in reforming catalysts and purification technology, development of a single-stage shift reactor, and other unit operation integration.

Delivery of hydrogen at 5,000 psi on a cost effective, synergistic approach, integrated with the production step with capacities of up to 1,500 kg/day of hydrogen is also important to this research.

Costs used to develop the targets in Table 2 are based on a hydrogen refueling station serving 138 vehicles per day (690 kg per day) with on-site production assuming a high (90%) utilization factor and relatively low capital recovery factor (11%). Much lower utilization factors would be expected during the early years of fuel cell vehicle introduction. Capital equipment cost targets assume mature production volumes of 100 units per year. Energy costs assume a natural gas price of \$4.40/MMBtu (LHV) and a power

price of \$0.07/kWh. Primary energy efficiency of each step is defined as Hydrogen Output LHV / Energy Input LHV of that process step. Input energy associated with on-site power use assumes a 35% production and transmission efficiency penalty – a typical US grid mix. The total primary energy efficiency is defined as the net Hydrogen Output LHV / Total Energy Input LHV into the process.

Table 2. Distributed Production Targets

Characteristics		Units	Target
Reforming	Natural Gas Cost	\$/kg H ₂	0.58
	Cost	\$/kg H ₂	0.24
	Primary Energy Efficiency	%(LHV)	75
Purification	Cost	\$/kg H ₂	0.03
	Hydrogen Efficiency	%(LHV)	90
Compression	Cost	\$/kg H ₂	0.24
	Primary Energy Efficiency	%(LHV)	88
Storage & Dispensing	Cost	\$/kg H ₂	0.11
	Primary Energy Efficiency	%(LHV)	100
Other	Cost	\$/kg H ₂	0.30
	Primary Energy Efficiency	%(LHV)	100
Total	Cost	\$/kg H ₂	1.50
	Primary Energy Efficiency	%(LHV)	75

New Advanced Electrolysis Systems Research

DOE is also funding new technologies suited for power park and utility size systems including alkaline and solid oxide electrolysis. Key research areas include system cost reduction and efficiency improvement including power conversion, storage, and other components through renewable system integration, and steam electrolysis materials and systems development.

Regarding renewable energy/electrolysis system engineering, new technologies are targeting low-cost electrolysis systems capable of efficient, reliable integration with renewable electricity that may include the use of reversible solid oxide fuel cells. For example, systems are being designed to match utility scale wind turbines in the 500-1,500kW range and that have the modular capability to allow scaling to multi-Megawatt utility applications. These new systems will also have the potential for direct integration with other renewable energy sources. Projects include electrolyzer system design, renewable electric system interface, and grid interface with the focus on lowering capital costs and improving efficiency of system components including storage, power electronics, and other components.

As a result of this research, within three to four years DOE will verify pilot scale 500-1,500kWe electrolysis systems that can be modularly integrated with a utility sized renewable electricity system to verify the potential of producing 10,000 kg per day hydrogen at \$2.00 per kg at the plant gate.

High temperature steam electrolysis research activities will explore solid-oxide technology for low cost hydrogen production and opportunities for co-generation of hydrogen and electricity. This research includes development of electrodes and system designs for reversible electrolysis/fuel cell systems or development of system designs for low cost production of hydrogen using solid oxide technology.

Renewable power park applications and distributed production of hydrogen and electricity are key focus areas where DOE will verify low-cost, reversible electrolysis/fuel cell electrode materials and pilot scale system designs to achieve 70% energy efficiency and hydrogen production cost of \$2.00 per kg at the plant gate when scaled to a 500kW system.

References

- (1) U.S. Department of Energy, Energy Efficiency and Renewable Energy, *Hydrogen, Fuel Cells & Infrastructure Technologies Program, Multi-Year Research Development and Demonstration Plan*, **2003**

FUELING OUR FUTURE: FOUR STEPS TO A NEW RELIABLE, CLEANER, DECENTRALISED ENERGY SUPPLY BASED ON HYDROGEN & FUEL CELLS

Arno A. Evers

Arno A. Evers FAIR-PR
Achheimstr. 3
82319 Starnberg, Germany

Abstract

This presentation demonstrates the possible driving factors and necessary elements needed to move Hydrogen and Fuel Cells (H₂/FC) to worldwide commercialisation. Focusing not only on the technology itself, this presentation looks at the “bigger picture” explaining how certain trends have impacted the progress of new technologies developments in the past. The presentation demonstrates how these models can be applied to our present day situation. Examining different Distributed Generation scenarios, the catalyst to the Hydrogen Economy may be found through distributed generation via fuel cells. One possible step could be the use of Personal Power Cars equipped with Fuel Cells which not only drive on Hydrogen, but also supply (while standing) electricity /heat to residential and commercial buildings. This scenario, as well as, the inter-dependability between supply and consumer-driven demand (or better, demand and supply) will be further explained.

FUEL CELL APPLICATIONS

(STATIONARY/MOBILE/PORTABLE). More than 100 international Fuel Cell companies are supplying their equipment to a number of Utility companies around the globe. Car manufacturers worldwide are working on vehicles with Fuel Cells and electrical motor drives or ICE's, powered by Hydrogen. All computer manufacturers are working on portable fuel cells. A Toshiba H₂/FC notebook powered by Hydrogen will come on the market in 2004 as announced at CeBIT '03, March 2003.

ON PROBATION OR READY FOR TAKE-OFF? Fuel Cell technology has been on worldwide probation for the last 30 years. Billions of US \$ – both from Private finance and Governmental funds - have already been invested. Adoption was announced several times, but often postponed. There are two critical issues to bear in mind. First, how long will it take for H₂/FC to become commercial? Second, will H₂/FC be on probation for another 30 years?

IMPLEMENTATION TIME OF NEW PRODUCTS.

Figure 1. Chart illustrating implementation time of new products. According to Siemens AG, over the years, new appliances have taken different time spans to reach 100 million U.S. customers. The radio, for example, took 90 years to reach 100 million U.S. customers; telephone, 70 years; television, 50 years; cable TV Network, 25 years; computer, 20 years; mobile phones, 15 years; Internet less than 5 years. The speed of implementation continues to grow faster and faster with every new product invented. I am convinced that the introduction of Hydrogen and Fuel Cells applications, products and services will take even less time; maybe just a few years.

Implementation time of new Products

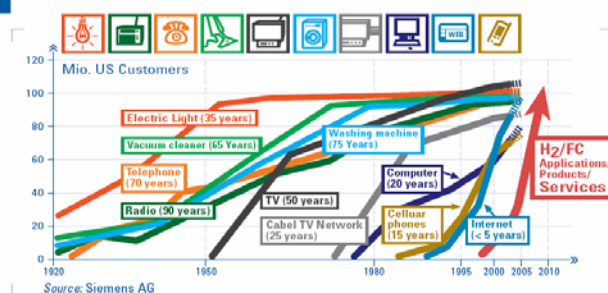


Figure 1. Chart illustrating implementation time of new products

Home appliance ownership in every 100 Shanghai, P.R. China, families. As the Chinese economy grew fast in recent years, the income of Chinese people had increased largely. As China's overall economy is expected to continue its growth over the next years, the income level of Chinese residents will also continue to grow. The reasonable rise of the income will ensure the purchasing power needed for unexpected expansion of daily-use electrical appliance market. This is demonstrated in **Figure 2** by the demand for highly efficient new products bought by the average Shanghai family.

Home appliance ownership in every 100 Shanghai, P.R. China, families

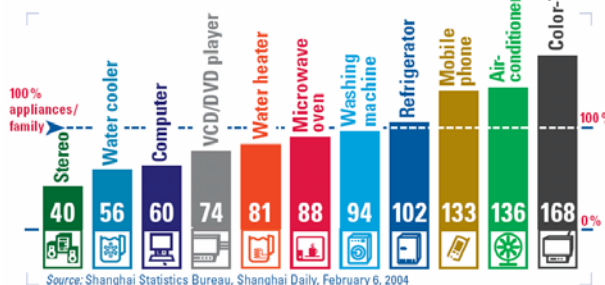


Figure 2. Home appliance ownership in P.R. China

Evolution of Cellular Phone 1983-2004. Figure 3. Evolution of the telecommunications industry is immense; for example, a 3,000 USD Dynetek cellular phone from 1983 with a weight of 3 lbs without display has less performance than a 299 USD Samsung cellular phone from 2004 with a weight of 3,6 oz. with color LCD. Worldwide, this progress is not driven by any governmental subsidy; it is only driven by the demand of the consumer who is looking for added value. The increase of quantities per time of the units leads to a sharp decrease in the price per unit.

> Evolution of the Cellular Phone 1983 – 2004

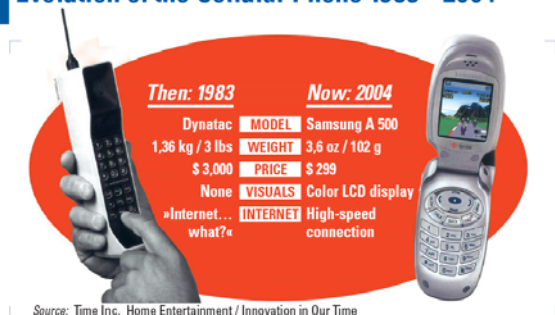


Figure 3. Evolution of the Cellular Phone 1983-2004

Evolution of the Aircraft Industry 1903-2005. Figure 4. Evolution of the Aircraft Industry comparing Wright's Flyer with today's Airbus A380 over the past 102 years. When Orville and Wilbur Wright left their plane after the first powered flight (lasting 57 seconds) in Kitty Hawk, North Carolina, December 17th, 1903, they would never imagine that only 100 years later there would be an aircraft built with a range of more than 8000 miles carrying 550 passengers in peace and comfort. Today's Hydrogen and Fuel Cell industry status compares with the time of the Wright Brothers. There are more dramatic developments coming than anyone can imagine, hopefully, in less than 100 years.

> Evolution in the Aircraft Industry 1903 – 2005



Figure 4. Evolution of the Aircraft Industry comparing Wright's Flyer with today's Airbus A380 over the past 102 years

FOUR STEPS TO AN ENERGY SUPPLY BASED ON HYDROGEN AND FUEL CELLS. Figure 5: Illustration of steps towards a cleaner, reliable, decentralised energy supply. In my opinion, cars could be the key for a new Energy Supply based on H₂/FC. All it takes is four steps. Step 1 – Renewable energies (like wind, solar, hydroelectric and/or biomass energy) produce Hydrogen. Step 2 – The cars drive on Hydrogen using Fuel Cells and electrical motors. (The first two steps are readily available worldwide. However, at this time, there's no public demand for use of these options. To get the repeatedly promised Hydrogen economy on its wheels, two more steps must follow.) Step 3 – While parked, these vehicles drive idle and supply electricity to the buildings where they are parked. Step 4 – Car owners earn money based on the electricity/heat supplied by their cars.

The incentive for car owners driving and using vehicles equipped with Hydrogen and Fuel Cells systems is twofold. They can either save or earn money while their cars are parked and plugged into buildings via a smart docking station. For example, your car parked at home in your garage will supply electricity to your home and additionally, replace the function of your existing boiler and even all air conditioning units, thus saving you money. You can earn money

by selling the electricity generated, but not used at home at that time, to the utilities and feed it into the existing electricity grid.



Figure 5. Illustration of steps towards a cleaner, reliable, decentralised energy supply

REVOLUTION IN THE GARAGE. Figure 6. Illustration of Personal Power Car taking over the role of the boiler & delivering electricity to house & electrical grid whereby creates a "revolution in the garage". Looking at today's so-called "western" countries, if all registered cars would be equipped with a Fuel Cell system, they could (all together) easily take over the function of today's existing stationary power plants. This is due to the fact that the total power installed in the cars' engines exceed the capacity of existing stationary power plants by 20-35 times.

In the first stage, the Hydrogen needed to power this system will come from natural gas which is presently and widely available. The individually produced Hydrogen will be stored in a personal tank inside the garage or the cellar. The Fuel Cell in the cars produces DC, which will be converted in the house into AC. DC can also be used directly with nearly all advanced appliances like computers, plasma screens, mobile phones. The heat generated by the fuel cell in the car will warm your home in winter, and in summer, the heat will be converted by means of special heat exchangers to eventually replace all residential air-conditioning units. This idea has many "fathers", Amory B. Lovins to mention one, and is just one example of where we could apply this technology.

> Revolution in the Garage

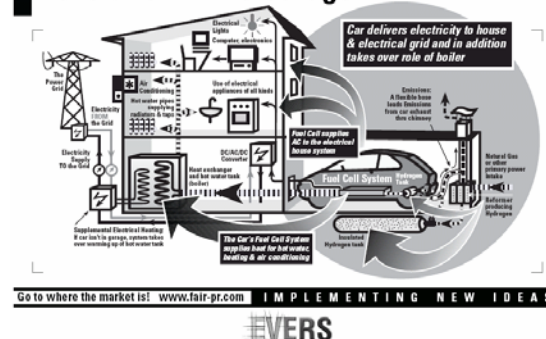


Figure 6. Illustration of Personal Power Car taking over the role of the boiler & delivering electricity to house & electrical grid whereby creates a "revolution in the garage".

NECESSARY CONDITIONS TO REACH THE FINAL GOAL: MASS DEMAND WILL DRIVE MASS PRODUCTION.

Figure 7. Illustration of Strategic Alliances and relationship to Mass Production. To achieve early market entry, it is first necessary to make the consumer excited and eager to use the new services provided by the H₂/FC technology. Nobody will ever buy a Fuel Cell just to have one. What the public will buy (and pay a lot of money for) are new services unknown today. All new inventions began as “luxury” goods. The consumer must be motivated and be given certain incentives: personal advantages, product reliability and usefulness. Only when these factors are guaranteed, will the price, at least in the beginning, play a less important role. This means the more expensive the product/service is, the more chances the early adopters will buy this “luxury”. In addition, entrepreneurs involved in R&D, production & marketing of H₂/FC services must also be motivated and stand firmly behind their vision. Commitment and belief in their technology will play a critical role in the early stages of fuel cell commercialisation. Strong efforts are needed in convincing the politicians, the media, and the involved companies that H₂/FC is a viable solution for the growing energy demand. Raising energy security concerns and the impact of global pollution will additionally support the implementation. These general conditions will lead to worldwide mass-production and make H₂/FC's appearance in the marketplace, sooner rather than later.

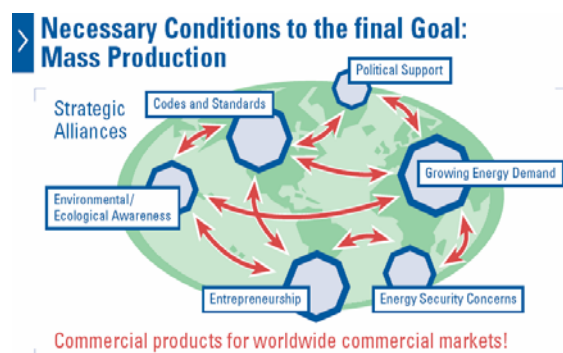


Figure 7. Illustration of Strategic Alliances and relationship to Mass Production

MARKET OUTLOOK: EUROPE AND CHINA

Europe.

Figure 8. Map of European Fuel Cell stationary units and buses including percentage share of Euro industry by country. In Europe, there are currently 81 Stationary H₂/FC units (power plants) in operation with a total capacity of 12 MW power. There are 27 H₂/FC buses planned by the EU-sponsored CUTE programme. Germany leads with a share of the European industry of 31% followed by UK with 19%, Italy with 7% and France, Spain with 6%.

Some recent EU policy actions: Action plans on energy efficiency include improving energy efficiency by +18% from 1995 to 2010 and increasing the share of co-generation to 12% of EU-15 (member countries) electricity by 2010. A white paper on renewable energies recommends doubling the share of renewable energies from now 6% to future 12% of final energy. There are active committees who analyse the communication on alternative fuels. They propose Hydrogen with a share of 5% of road transport fuel by 2020.

China.

The National Natural Scientific Foundation (NSFC) is responsible for Fundamental Research. Projects include: The “863 High Technology Research and Development” project deals with commercially potential ventures. Key projects include: Fuel Cell cars and buses with a allocated budget of 33 million EURO; Fuel Cell Key

Material Project concentrating on membrane and bi-polar development; Future Energy Project focusing on DMFC, MCFC, SOFC.

The “973 Project” is dedicated to high technology fundamental research on Hydrogen Energy (including Fuel Cells). The NSFC is looking at new material possibilities and new Fuel Cell concepts. The Chinese Academy of Sciences, Ministry of Education works on fundamental and applied fundamental research in Fuel Cell engines and Hydrogen Technology. The up-and-coming Chinese H₂/FC industry deals with applied fundamental research such as advances in Hydrogen production from Natural Gas, Methanol and Gasoline.

CONCLUSION

This industry overview shows that the demand of the consumer will play the critical role in the mass-market evolution of H₂/FC products and services. At first, H₂/FC powered products/services will be considered luxury items with only a handful of the population being able to afford to buy them. However, over time and as the technological awareness and knowledge about the advantages grows, the consumer will become better educated as to the many benefits offered by services powered by H₂/FC technologies. Increased convenience and awareness rather than the price of the merchandise, will have an enormous impact on the consumer and will compel them to buy H₂/FC powered goods, and furthermore, lead to the development of completely new H₂/FC products and services which are unobtainable today. The Personal Power Car as described is just one example. However, the current activities in Europe and China as presented are sure to further accelerate the trend towards the coming Hydrogen Economy. **Figure 10:** Diagram of growth and development - Hydrogen + Fuel Cells Group Exhibit

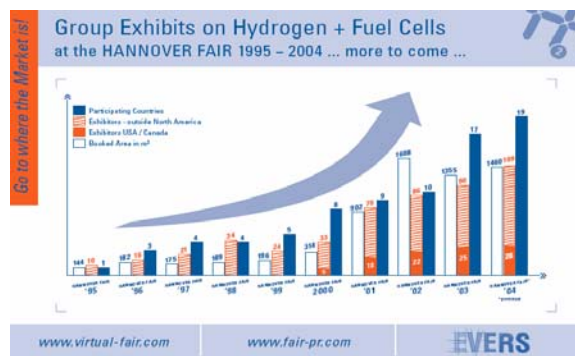


Figure 10. Diagram of growth and development - Hydrogen + Fuel Cells Group Exhibit

Seven Drivers to the Hydrogen Economy

Rahul Iyer

Intelligent Energy, Inc, 2955 Redondo Avenue, Long Beach, CA 90806.

The global demand for electric power is growing at an aggressive pace. An additional capacity of 183GW will be required from years 2000 and 2030. There are **seven** key distinctions between this growth and the previous 30 years of capacity growth. These distinctions will drive a dramatic paradigm shift from the homogenous and centralized energy systems of developed economies, to diversified and H₂ based micro-grid systems established first in developing economies. Contrary to the notion that environmental concern is the only driver to the hydrogen economy, the forces pushing us towards H₂ are diverse and numerous. The promise of the H₂ economy rests largely on the concept of hydrogen's use as an "energy-currency."

In this new energy economy, diverse primary energy sources compete to provide an appropriate cost effective blend of energy. Fuel cells provide highly efficient energy conversion near the point of use for any number of applications. With H₂ as the energy carrier, the delicate balance between scale, capital expenditure, and profitable plant operation becomes more robust. The rising marginal utility of increases in power/hydrogen generation capacity promotes more sustainable growth in infrastructure. Distributed H₂ generation will become a viable industry.

Renewable energy sources are currently plagued with availability issues. Renewable sources of any scale geared to produce hydrogen fuel whenever the primary renewable source is available increases the value of all renewable energy. Renewables and non-renewables compete to supply the demand of hydrogen fuel for vehicles, stationary, and other applications. Markets with a larger number and higher diversity of suppliers create a more stable and economical energy supply. As with all majoreconomic change, early stages are fraught with technological missteps. A fresh approach based on appropriate energy solutions will meet and exceed the world's demands not only for power, but quality of life.

1. Emerging Markets

The most dramatic growth in the energy industry will come from emerging markets and entirely new groups and types of customers. These new markets have demands and priorities which have not, and will not, be met by traditional energy market approaches. As developed economies are characterized as post industrial revolution economies, these emerging economies will be characterized as post information revolution economies. As such, these economies will rely heavily on high quality and high availability power, a requirement for high technology economies.

2. Sustainable Development

Focus on Sustainable Development and environmental concerns will take on new importance, driving certain technologies forward. New market vectors around these concepts will evolve and play a major role in future energy economics.

3. Deregulation

General global drift towards deregulation, and the fall of fully funded state and para-state energy regimes help foster entirely new types of organizations and businesses to meet energy needs of emerging markets.

4. Financial Markets

The financial world has evolved to embracing shorter time horizons, generally supporting smaller investments, and tolerating less risk. These market forces primarily impact the way energy programs and markets around the world will be structured, and secondarily impact technology choice.

5. Cognizant Consumption

The socioeconomic weight of the global energy market is undeniable. The geopolitical implications of installing low wattage lighting, and choosing to drive a hybrid vehicle, are fast becoming factors in consumptions patterns.

6. Market Convergence

As communications technology and use have converged by way of the internet, so too will energy technology and use converge by way of the hydrogen economy. Domestic power and motive power markets will experiences a convergence, resulting in new technologies and business constructs. These new concepts will be as numerous and diverse as were spawned by the recent and ongoing information economy transformation.

7. Flexibility

Flexibility and dynamism will become an important aspect of energy technologies, as infrastructure growth is increasingly required to be as dynamic as the populations which they serve. As populations, communities, families, and individuals have become more dynamic and diverse, the energy infrastructures (including transportation) will be called on to exhibit the same level of flexibility.

THE NATIONAL HYDROGEN STORAGE PROJECT

Antonio Bouza, John Petrovic¹, Carole Read, Sunita Satyapal, and JoAnn Milliken

U.S. Department of Energy
Office of Hydrogen, Fuel Cells and Infrastructure Technologies
1000 Independence Ave. SW
Washington DC 20585

Introduction

The transition to a hydrogen economy with fuel cell-powered vehicles over the next few decades is crucial to energy security and environmental quality in the United States and around the world. This energy vision was put forward by President Bush in his January 2003 State of the Union address.

A critical enabling technology for the development of hydrogen fuel cell-powered vehicles is the capability to have sufficient on-board hydrogen storage to enable greater than 300-mile driving range under the weight, volume, and cost constraints posed by customer expectations. Current vehicular hydrogen storage systems cannot meet this ultimate requirement. New materials and approaches are needed and that is why the U.S. Department of Energy (DOE) is proceeding with the implementation of a National Hydrogen Storage Project.

Requirements for On-Board Hydrogen Storage

Storing sufficient hydrogen on a vehicle to achieve a greater than 300-mile driving range is difficult. On a weight basis, hydrogen has nearly three times the energy content of gasoline (120 MJ/kg for hydrogen versus 44 MJ/kg for gasoline). However, on a volume basis the situation is reversed (8 MJ/L for liquid hydrogen versus 32 MJ/L for gasoline).

On-board hydrogen storage system performance targets have been developed through the FreedomCAR Partnership between DOE and the U.S. Council for Automotive Research (USCAR). These targets are system-driven and are based on achieving similar performance and cost levels as current gasoline fuel storage systems.

Current Status of On-Board Hydrogen Storage

Current on-board hydrogen storage approaches involve compressed hydrogen gas tanks, liquid hydrogen tanks, complex metal hydrides, chemical hydrogen materials such as chemical hydrides, and carbon-based materials. Carbon fiber-reinforced 5000-psi and 10,000-psi compressed hydrogen gas tanks are under development, as are liquid hydrogen tanks. Issues with compressed gas tanks include high pressure, volume and cost. Liquid hydrogen tanks have boil-off and liquefaction energy penalties and cost issues. Complex metal hydrides have low hydrogen capacity, unacceptable uptake and release kinetics and cost issues. Chemical hydrogen materials include key issues associated with regeneration energy requirements and cost. Carbon-based materials, which are at an earlier stage of development, are encountering hydrogen storage capacity, performance reproducibility issues and high cost.

The current status of on-board hydrogen storage systems are shown in Table 1 based upon estimates provided to DOE by program participants and available in the open literature.

Table 1. Current Status of On-Board Hydrogen Storage Systems

Storage Approach	Gravimetric Energy Density (kWh/kg)	Volumetric Energy Density (kWh/liter)	Storage System Cost (\$/kWh)
5000-psi gas tanks	2.1	0.8	\$12
10,000-psi gas tanks	1.9	1.3	\$16
Liquid H ₂ tanks	2.0	1.6	\$6
Metal hydrides	0.8	0.6	\$16
Chemical hydrides	1.6	1.4	\$8
2010 System Target	2.0	1.5	\$4
2015 System Target	3.0	2.7	\$2

At the present time, there is no on-board hydrogen storage technology that can meet the combined requirements of weight, volume, and cost that are necessary for implementation of hydrogen fuel on the full spectrum of light-duty vehicle platforms by the target year of 2020 put forward by President Bush. For example, the volumetric energy capacity required for full implementation in all light-duty vehicle platforms is greater than that of liquid hydrogen. The most promising technologies require using solid-state materials or liquids as storage media, but very little scientific work exists on these approaches. This is the main driver for DOE proceeding with the implementation of a National Hydrogen Storage Project.

The National Hydrogen Storage Project

The DOE in July 2003 issued a "Grand Challenge" for Basic and Applied Research in Hydrogen Storage. This Grand Challenge called for the establishment of hydrogen storage Centers of Excellence: Metal Hydrides, Chemical Hydrogen Storage, and Carbon-Based Materials, led by a DOE national laboratory and having a number of university, industry, and federal laboratory partners. In addition, independent projects are established with respect to new materials and concepts, off-board hydrogen storage systems, and analysis. The new Centers and independent projects, together with existing DOE hydrogen storage efforts, constitute the framework of the National Hydrogen Storage Project.

The structure of the National Hydrogen Storage Project is shown in Figure 1. On April 27, 2004 the Secretary of Energy Spencer Abraham announced the selections for the Hydrogen Storage Grand Challenge.

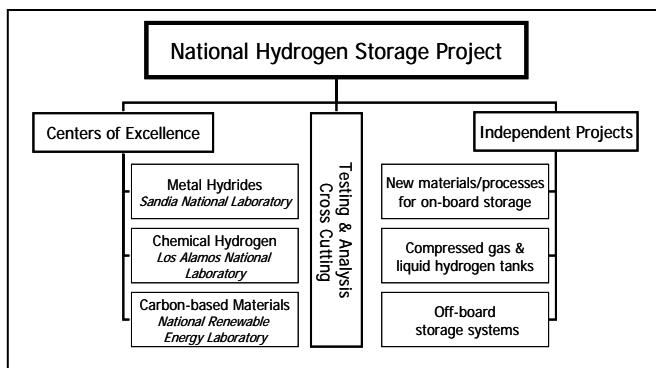


Figure 1. Structure of the National Hydrogen Storage Project

¹ Laboratory Fellow, Los Alamos National Laboratory, on assignment to DOE Headquarters.

The Metal Hydride Center is led by Sandia National Laboratories in Livermore, California. The Sandia Center will focus on the development of advanced metal hydride materials. The Metal Hydride Center includes 7 university partners, 3 industrial partners, and 5 federal laboratories.

The Chemical Hydrogen Storage Center is led by the Los Alamos National Laboratory in Los Alamos, New Mexico in partnership with Pacific Northwest National Laboratory in Richland, Washington. The Los Alamos Center will focus on three “tiers” of R&D for chemical hydrogen storage: borohydride-water, novel boron chemistry, and innovation beyond boron. The Chemical Hydrogen Storage Center includes 6 university partners, 3 industrial partners, and 2 federal laboratories.

The Carbon-Based Materials Center is led by the National Renewable Energy Laboratory (NREL) in Golden, Colorado. The NREL Center will focus on breakthrough concepts for storing hydrogen in carbon-based materials such as hybrid nanotubes, aerogels, and nanofibers, as well as novel materials such as metal-organic frameworks and conducting polymers. The Carbon Center includes 7 university partners, 1 industrial partner, and 4 federal laboratories.

The National Hydrogen Storage Project also involves independent projects that explore promising new hydrogen storage materials and concepts, off-board hydrogen storage needed for a hydrogen delivery infrastructure, standardized testing of hydrogen storage capacities, and analyses of life-cycle cost, energy efficiency, and environmental impact for materials-based hydrogen storage systems. Some of the new materials/concepts being studied include nanostructured materials, amine borane complexes, metal perhydrides, clathrates, lithium nitride, glass microspheres, and irradiation activation of materials.

A down-select process has been incorporated into all of the Grand Challenge projects, so that the most promising hydrogen storage approaches can be identified and focused on as quickly as possible. Starting in Fiscal Year 2005, the DOE will provide funding at a level of \$150 million over a five year period (subject to congressional appropriations) for the National Hydrogen Storage Project. The result of this R&D effort will be the development of hydrogen storage systems capable of meeting the 2015 DOE targets.

HIGH-TEMPERATURE OXYGEN SEPARATION MEMBRANES FOR USE IN THE SULFUR-IODIDE THERMOCHEMICAL CYCLE FOR HYDROGEN PRODUCTION

Andrea Ambrosini,¹ Terry Garino² and Tina Nenoff¹

¹ Chemical and Bio Technologies, Sandia National Laboratories, PO Box 5800, MS 0734, Albuquerque, NM 87185-0734

² Ceramic Materials, Sandia National Laboratories, PO Box 5800, MS 1411, Albuquerque, NM 87185-1411

Introduction

Efficient and environmentally sound methods of producing hydrogen are of great importance to the US as we progress toward the H₂ Economy. Current studies are investigating the use of high temperature systems driven by nuclear and/or solar energy to drive thermochemical cycles for H₂ production. These processes are advantageous since they do not produce greenhouse gas emissions that are a result of hydrogen production from electrolysis or hydrocarbon reformation. Earlier studies have identified over 100 possible reaction cycles that produce H₂ at high temperatures.¹ Of the cycles identified as the most promising, many require the removal of O₂ or H₂ to push reaction equilibria in favorable directions. Based on a previous extensive survey of over 100 thermochemical cycles, which took into account such metrics as efficiency, cost, number of steps, number and phases of reactants, among others, the Sulfur-Iodide (SI) cycle was deemed to be one of the most promising. As shown in Figure 1, the first step of the SI cycle involves the decomposition of H₂SO₄ into O₂, SO₂, and H₂O at temperatures around 850 °C. Removal of O₂ from this reaction pushes the equilibrium towards dissociation, thus increasing the overall efficiency. The membrane required for this step must withstand the high temperatures and corrosive conditions inherent in this process. Perovskites are promising materials for such membranes due to their robustness and mixed ionic/electronic conductivities. A mixed ionic-electronic conductor would benefit the process by alleviating the need for an applied electrode across the membrane to balance the oxygen ion flux. To this end, dense ceramic membranes based on the double-substituted perovskite, A_xSr_{1-x}B_yCo_{1-y}O_{3-δ} (A=La, Y; B=Cr, Mn, Fe, Ni) were synthesized by solid state methods and structurally characterized using powder x-ray diffraction. TGA vs. temperature and oxygen partial pressure was performed to test the oxygen absorption and desorption properties of the material, while conductivity and permeability measurements are in process.

Experimental

Synthesis. Perovskite oxides were synthesized by the nitrate-citrate method.² Metal nitrates were dissolved into 100 mL of deionized H₂O. Citric acid was added in a 1:1 citric acid:metal cation molar ratio and the solution was heated to 90 °C with stirring until water evaporated and then dried overnight in drying oven. Resulting powder was ignited at 350 °C to burn off nitrates and citrates, ground with a mortar and pestle, and sintered at 1250 °C for 24 hours.

Structural characterization. The materials were structurally characterized by powder x-ray diffraction (PXRD) on a Siemens D500 diffractometer (Cu K_α radiation, Bragg-Brentano geometry) and refined using the Jade 6.5+³ and FullProf⁴ Rietveld refinement software.

Thermal studies. Thermal studies on samples determined to be single-phase were performed using a TA Instruments STD 2960 DTA-TGA in order to obtain information on oxygen stability and oxygen adsorption/desorption. To estimate oxygen stoichiometry, samples were reduced under 5% H₂/N₂ at 1000°C until weight loss

stabilized, usually at about 14%. For absorption/desorption, multiple-cycle thermogravimetric analysis (TGA) was run on the single-phase samples. First the temperature was cycled three times between 50 - 850°C under an O₂ atmosphere. This was followed by cycling between O₂ (high pO₂) and Ar or He (low pO₂) atmospheres at a constant temperature of 850°C. PXRD studies were run before and after thermal study samples to confirm retention of the structure.

Results and Discussion

The double-substituted perovskites were indexed in the cubic Pm-3m (221) space group. Table 1 shows the compositions of the synthesized materials that were determined to be single phase, their lattice parameters, weight loss after reduction, and their average weight loss versus temperature and oxygen partial pressure. Yttria-stabilized zirconia (YSZ), a well-known ion conductor, is included in Table 1 for comparison purposes.

Figure 1 illustrates an example of a multiple-cycle TGA analysis. The first part of the graph shows the weight change as the temperature is cycled between 50-850 °C, under a constant flow of O₂ gas. This describes an easily reversible temperature-swing adsorption/desorption of oxygen. The second part of the graph illustrates the reversible weight change as a function of oxygen partial pressure, by cycling the gas between O₂ and Ar or He at a constant temperature of 850 °C. This implies that the material can transport oxygen across a membrane with an oxygen partial pressure differential. Post-TGA powder diffraction patterns reveal no structural changes after the temperature and gas treatments, demonstrating the robustness of the material. (Figure 2)

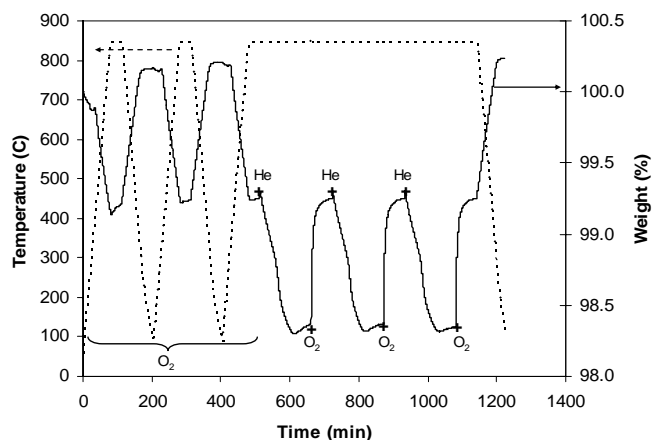


Figure 1. TGA of La_{0.1}Sr_{0.9}Co_{0.7}Mn_{0.3}O_{3-δ}. The crosses mark where the atmosphere was changed between O₂ and He.

The most promising material thus far is the La_{0.1}Sr_{0.9}Co_{1-x}Mn_xO_{3-δ} perovskite. As shown in Table 1, the oxygen sorption properties increase with increasing Mn doping. Studies are currently underway to determine the extent of this solid solution and the composition of greatest oxygen conductivity.

Ongoing work involves the determination of the conductivity and permeation of these materials. For conductivity purposes, a four-point conductivity test instrument has been designed and built. Measurements have begun on samples of synthesized materials as well as on standard materials (YSZ), for comparison. Pressed and heat-treated powder samples are machined into bars nominally 2mm x 2 mm x 20 mm. Platinum wires are then wrapped around the bars at four places, both ends and just inside each end. Conducting paint

Table 1. Composition, desorption properties, and lattice parameters of single-phase perovskites.

Nominal Composition	Avg. Weight Loss vs. T	Avg. Weight Loss vs. Atm	Weight loss upon reduction	Lattice Parameter (Å)
YSZ (3%)	0.470%	0.0955%	N/A	N/A
$\text{Y}_{0.1}\text{Sr}_{0.9}\text{Co}_{0.9}\text{Fe}_{0.1}\text{O}_{3-\delta}$ (YSCF1991)	1.38%	0.892%	13.66%	3.840
$\text{La}_{0.1}\text{Sr}_{0.9}\text{Co}_{0.9}\text{Ni}_{0.1}\text{O}_{3-\delta}$ (LSCN1991)	1.21%	0.624%	13.98%	3.847
$\text{La}_{0.1}\text{Sr}_{0.9}\text{Co}_{0.8}\text{Ni}_{0.2}\text{O}_{3-\delta}$ (LSCN1982)	1.37%	0.730%	14.16%	3.847
$\text{La}_{0.1}\text{Sr}_{0.9}\text{Co}_{0.9}\text{Mn}_{0.1}\text{O}_{3-\delta}$ (LSCM1991)	1.36%	0.707%	14.00	3.845
$\text{La}_{0.1}\text{Sr}_{0.9}\text{Co}_{0.8}\text{Mn}_{0.2}\text{O}_{3-\delta}$ (LSCM1982)	1.13%	0.780%	12.99%	3.844
$\text{La}_{0.1}\text{Sr}_{0.9}\text{Co}_{0.7}\text{Mn}_{0.3}\text{O}_{3-\delta}$ (LSCM1973)	0.949%	0.910%	10.40%	3.841
$\text{La}_{0.1}\text{Sr}_{0.9}\text{Co}_{0.9}\text{Cr}_{0.1}\text{O}_{3-\delta}$ (LSCCr1991)	1.15%	0.699%	12.99%	3.868
$\text{La}_{0.1}\text{Sr}_{0.9}\text{Co}_{0.9}\text{Fe}_{0.1}\text{O}_{3-\delta}$ (LSCF1991)	1.45%	0.624%	13.51%	3.852

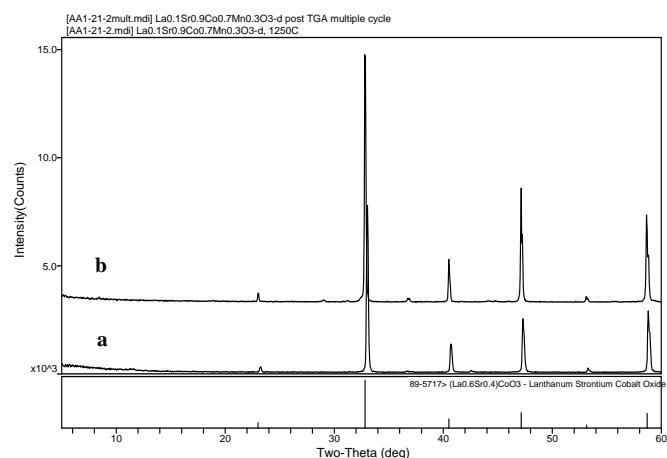


Figure 2. Powder x-ray diffraction pattern of $\text{La}_{0.1}\text{Sr}_{0.9}\text{Co}_{0.7}\text{Mn}_{0.3}\text{O}_{3-\delta}$ (a) after sintering at 1250 °C and (b) after multiple-cycle TGA. The bottom pattern is a reference of a perovskite with the space group Pm-3m.

(silver-palladium) is used to ensure good electrical contact between the wires and the sample. The samples are placed in a tube furnace under controlled temperature and atmosphere. Measurements are being made in the 400° to 800 °C range. A DC current source is connected to the wires at the ends of the sample and voltage drop across the other two wires is measured with a voltmeter. The conductivity is then simply determined from the current, voltage and the geometry. The initial measurements for each sample are done in air. Materials with high conductivity (comparable to that of the YSZ reference material) are measured in other pO_2 atmospheres (e.g., UHP Ar and 3% hydrogen in Ar) to determine whether the conductivity is ionic or electronic: ionic conductivity will be independent of the oxygen pressure while electronic conductivity will scale with it. For materials of interest, AC measurements (impedance spectroscopy) will also be performed to learn more details about the mechanism of conductivity. In addition, a high temperature permeation unit is under construction to test the oxygen permeation properties of these materials at 850 °C under an oxygen partial pressure differential. The unit will be connected to a residual gas analyzer (RGA) to monitor the permeate.

Conclusions

Double-substituted perovskites, $\text{A}_{1-x}\text{Sr}_x\text{Co}_{1-y}\text{B}_y\text{O}_{3-\delta}$ ($\text{A}=\text{Y}, \text{La}$; $\text{B}=\text{Fe}, \text{Ni}, \text{Cr}, \text{Mn}$) were synthesized for use as ceramic high-temperature oxygen separation membranes. Preliminary results show the materials have promising oxygen sorption properties and are structurally robust under varying temperatures and atmospheres. Continuing work will focus on conductivity and permeation measurements, as well as stability under reaction conditions of H_2SO_4 , SO_2 , and H_2O at high temperatures.

Acknowledgement. Sandia is a multiprogram laboratory operated by Sandia Corporation, a Lockheed Martin Company, for the US DOE's NNSA, contract DE-AC04-94-A185000. The authors would like to thank John Heald for the acquisition of the x-ray data and Dr. Fred Gelbard and Dr. Terry Guilinger for their helpful discussions.

References

- (1) Brown, L.; Besenbruch, G.; Lentsch, R.; Schultz, K.; Funk, J.; Pickard, P.; Marshall, A.; Showalter, S. *High Efficiency Generation Of Hydrogen Fuels Using Nuclear Power*; Grant No. DE-FG03-99SF21888; Technical Report prepared for the Nuclear Energy Research Initiative (NERI) Program: December 2003.
- (2) Yang, Z.; Lin, Y.; Zeng, Y., High-temperature sorption process for air separation and oxygen removal. *Ind. Eng. Chem. Res.* **2002**, 41, (11), 2775.
- (3) *Jade 6.5+*, 6.5+; Materials Data Inc.: Livermore, CA, 2002.
- (4) Rodriguez-Carvajal, J. *FullProf.2k*, 2.60; ILL: 2004.

INDUCED DEFECTS IN CARBONACEOUS MATERIALS FOR HYDROGEN STORAGE

Angela D. Lueking, Caroline E. Burgess Clifford,
Deepa L. Narayanan

Department of Energy & Geo-Environmental Engineering
The Energy Institute
The Pennsylvania State University
University Park, PA 16802

Introduction

The use of hydrogen as an energy carrier will require a means to transport and store hydrogen, yet no existing technology meets the performance requirements established by the U.S. Department of Energy. Carbon nanomaterials (SWNT, MWNT, GNF) have several properties favorable for adsorption—surface area, pore size, and electrical conductivity—and these properties can be tuned by judicious selection of the conditions by which the carbons are prepared. However, hydrogen storage claims in these carbon nanomaterials have been highly scattered, ranging from 0.4%–67%. The discrepancies in these reports are thought to be due to experimental artifacts, impurities, carbon properties, and assessment techniques.

There has been a recent resurgence in hydrogen storage claims for graphite nanofibers (GNF) and multi-wall nanotubes (MWNT), and the results have been reported by a number of research groups: 3.8% at 69 bar,¹ 6.5% at 120 bar for GNF²; and 1.97% at 40 bar³ to 6.3% at 148 bar⁴ for MWNT. These recent claims discuss how: (a) the nanotube structure and defects relate to hydrogen uptake,¹ (b) these defects can be formed during synthesis or subsequent pretreatment¹; (c) terminal carbon groups act to dissociate hydrogen,^{1, 2}; and (d) the carbon structure may become expanded after exposing the carbon to hydrogen.⁵ The ball-milling of graphite has been used to obtain a total hydrogen capacity of 7.4% with neutron diffraction evidence of chemisorbed hydrogen.⁶ Ball-milling of carbon nanotubes has also shown promise, as long as the graphitic nature of the nanotubes is partially retained.⁷ Additionally, graphitic carbon has shown a synergistic effect when ball-milled with magnesium.⁸ These reports suggest that defects within the graphitic structure lead to enhanced hydrogen storage and that this effect can be magnified through synthesis, pretreatment, and processing.

The goal of this project was to induce defects in carbonaceous materials through both ball-milling and/or carbon exfoliation; here, we report initial exfoliation results. This study serves to test the emerging hypothesis in the literature: carbon defects chemisorb hydrogen, with possible expansion of the graphite lattice. If the advantageous effect of carbon defects is confirmed and better understood, controlled introduction of defect may increase hydrogen storage by introducing new hydrogen storage sites.

Methods

Materials. Ultra-high purity hydrogen (99.999%) was used in adsorption experiments, and ultra high purity helium (99.999%) was used to determine the bulk density of the adsorbents for buoyancy corrections, both gases were pretreated with an in-line 3A molecular sieve zeolite column to eliminate possible moisture contamination. Graphite nanofibers were purchased from Catalytic Materials, Ltd. A powdered graphite sample was obtained from Carbone and used as received.

Introduction of Defects. Carbon exfoliation served as one means to impart defects and increase interlayer spacing between graphene sheets. Methods to exfoliate graphite are well known and were extended here to other graphitic carbons. The primary

exfoliation method used in this study was a mixture of nitric and sulfuric acids followed by thermal shocking at 700 °C.⁹

Materials were treated *in situ* on the IGA prior to adsorption measurements. The thermal treatments were chosen based on previous studies¹ and the thermal stability of the fibers.

Characterization. Standard physisorption methods, including surface area and pore size distribution, were determined *in situ* on the Hidden IGA-003 after thermal degassing and prior to adsorption measurements. Electron microscopy, including TEM and SEM (Philips XL20), was used to determine the morphology and diameter of the material, before and after treatments. The bulk density of the carbon materials was determined by helium isotherms on the IGA. Carbon materials were thermally decomposed on the IGA in 100 ml/min helium with a ramp rate of 4 °C/min. These thermal decomposition studies were used to determine applicable degas temperatures and to give an indication of the thermal stability of the fibers after the treatments.

Hydrogen Uptake. A high-pressure TGA (Hidden Isochema IGA-003) was used to evaluate hydrogen uptake at pressures up to 20 bar. The IGA provided a high sensitive measurement with precise temperature and pressure control for automated measurements of adsorption and desorption isotherms. In addition, the IGA enabled *in situ* treatment and characterization prior to hydrogen measurements; typical pretreatments consisted of inert thermal treatments with or without partial thermal degradation. All hydrogen uptake measurements are normalized to sample mass after pretreatment, with buoyancy corrections determined from bulk density measurements with helium.

Results and Discussion

Introduction of Defects and Exfoliation of Graphite Lattice.

The relatively mild sulfuric/nitric acid treatment successfully exfoliated graphite (Figure 1), in agreement with previous results.⁹ Preliminary results of GNF exfoliation with the same method illustrate definite differences in SEM micrographs (Figure 2): exfoliated GNF had ragged edges when compared to the untreated GNF. TEM analysis is underway to better analyze the effect of exfoliation and quantify the GNF diameter before and after exfoliation. There was some indication that a milder exfoliation method may be needed for GNF, as SEM indicated that some regions of the sample lost the fiber structure after exfoliation (data not shown). The bulk density of the GNF, as measured by helium buoyancy on the IGA, changed from 1.86 g/cc to 1.31 g/cc upon exfoliation.

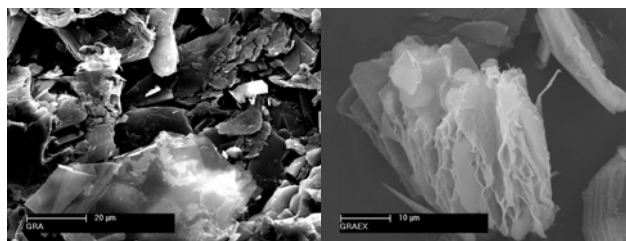


Figure 1. Exfoliation of powdered graphite in a mixture of nitric/sulfuric acid with thermal shocking at 700 °C (a) before exfoliation; (b) after exfoliation.

Thermal decomposition of the GNF before and after sulfuric/nitric acid exfoliation indicated a clear loss of thermal stability. Prior to exfoliation, the GNF showed no significant degradation in helium at temperatures up to 1000 °C; however, the onset of thermal degradation of the sulfuric/nitric acid exfoliated

GNF was at 100 °C with a maximum rate of mass loss at 120 °C (Figure 3). This thermal reactivity is an initial indication of both the increased reactivity and the decreased graphiticity of the GNF samples upon exfoliation. Comparison of the 70% mass loss to SEM visualization suggests that the increased reactivity occurs in both amorphitized GNF and exfoliated GNF, however further quantification of this is clearly needed.

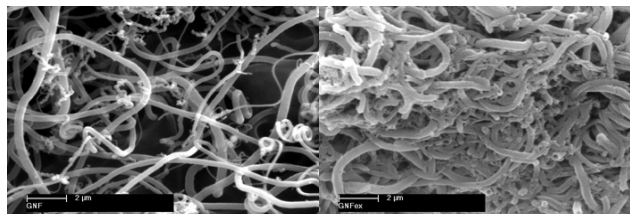


Figure 2. Exfoliation of GNF in a mixture of nitric/sulfuric acid with thermal shocking at 700 °C (a) before exfoliation; (b) after exfoliation.

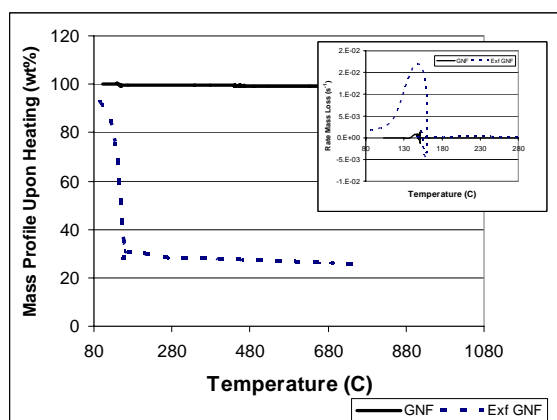


Figure 3. Exfoliation of the GNF in a mixture of nitric/sulfuric acid resulted in a loss of thermal stability of the materials, indicating a higher overall reactivity of the fibers caused by loss of graphitic structure and/or chemical defects. The inset shows the rate of mass loss for the fibers; the rate of thermal degradation was greatest at 120 °C.

Hydrogen Uptake. Prior to exfoliation, the GNF had 0.02% hydrogen uptake, with apparent saturation at 10 bar (Figure 4). Exfoliation of the GNF led to a slight increase in hydrogen uptake: 0.046 % after outgassing at 80 °C and 0.099% after outgassing at 100 °C. The two temperatures were chosen based on the thermal degradation discussion, with mass loss at 80 °C corresponding outgassing but little or no thermal degradation and 100 °C corresponding to partial gasification of the exfoliated GNF (Figure 3). It is expected that the amorphous carbon is more reactive than GNF, and decomposes before the GNF. Thus, the higher pretreatment temperature is intended to preferentially remove amorphous carbon leaving a higher purity of exfoliated GNF. Future studies will include characterization of the materials to quantify the GNF content.

Conclusions

GNF exfoliation enhanced the hydrogen uptake by a factor of five compared to the untreated GNF. Further studies will explore additional exfoliation methods and further characterize the sample to better quantify the degree of exfoliation. The nitric/sulfuric acid exfoliation method may have been too severe for GNF as evidenced

by the high thermal reactivity; our next attempt will be the milder nitric/formic acid exfoliation method, as described previously.^{10, 11} However, the overall degree of hydrogen uptake was low; we will explore additional carbon samples and verify the extent of exfoliation before addressing the expanded graphite lattice and/or defect hypothesis.

Acknowledgement. This work was funded through start-up funds proved by Pennsylvania State's Institute for the Environment, The Energy Institute, and The College of Earth & Mineral Sciences. Funding for exfoliation of carbon for hydrogen storage was provided, in part, by the H₂E Center at Penn State University.

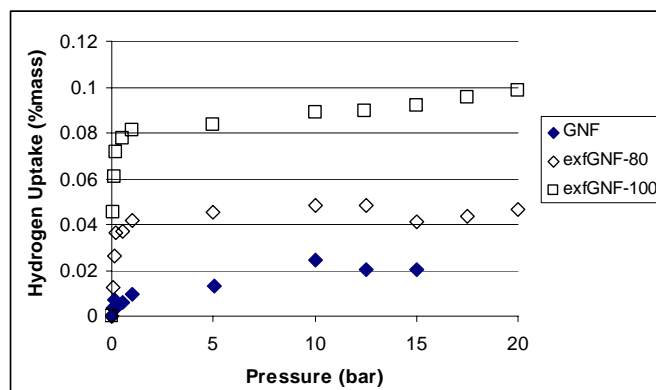


Figure 4. Hydrogen uptake of the GNF before (a) and after (b) exfoliation, followed by different degrees of thermal degradation. Hydrogen uptake is normalized per mass of carbon remaining after each pretreatment.

References

- Lueking, A. D.; Yang, R. T.; Rodriguez, N. M.; Baker, R. T. K., Hydrogen Storage in Graphite Nanofibers: Effect of Synthesis Catalyst and Pretreatment Conditions. *Langmuir* **2004**, 20, 714-721.
- Browning, D. J.; Gerrard, M. L.; Lakeman, J. B.; Mellor, I. M.; Mortimer, R. J.; Turpin, M. C., Studies into the storage of hydrogen in carbon nanofibers: Proposal of a possible reaction mechanism. *Nano Letters* **2002**, 2, (3), 201-205.
- Lee, S. M.; Park, K. S.; Choi, Y. C.; Park, Y. S.; Bok, J. M.; Bae, D. J.; Nahm, K. S.; Choi, Y. G.; Yu, S. C.; Kim, N. G.; Fraunheim, T.; Lee, Y. H., Hydrogen adsorption and storage in carbon nanotubes. *Synthetic Metals* **2000**, 113, (3), 209-216.
- Hou, P. X.; Yang, Q. H.; Bai, S.; Xu, S. T.; Liu, M.; Cheng, H. M., Bulk storage capacity of hydrogen in purified multiwalled carbon nanotubes. *Journal of Physical Chemistry B* **2002**, 106, (5), 963-966.
- Gupta, B. K.; Srivastava, O. N., Further studies on microstructural characterization and hydrogenation behaviour of graphitic nanofibers. *International Journal of Hydrogen Energy* **2001**, 26, (8), 857-862.
- Orimo, S. I.; Matsushima, T.; Fujii, H.; Fukunaga, T.; Majer, G.; Zuttel, A.; Schlapbach, L., Nanostructured graphite-hydrogen systems prepared by mechanical milling method. *Molecular Crystals and Liquid Crystals* **2002**, 386, 173-178.
- Hirscher, M.; Becher, M.; Haluska, M.; Quintel, A.; Skakalova, V.; Choi, Y. M.; Dettlaff-Weglikowska, U.; Roth, S.; Stepanek, I.; Bernier, P.; Leonhardt, A.; Fink, J., Hydrogen storage in carbon nanostructures. *Journal of Alloys and Compounds* **2002**, 330, 654-658.
- Imamura, H.; Tabata, S.; Shigetomi, N.; Takesue, Y.; Sakata, Y., Composites for hydrogen storage by mechanical grinding of graphite carbon and magnesium. *Journal of Alloys and Compounds* **2002**, 330, 579-583.
- Chung, D. D. L., Exfoliation of Graphite. *Journal of Materials Science* **1987**, 22, (12), 4190-4198.
- Toyoda, M.; Katoh, H.; Inagaki, M., Intercalation of nitric acid into carbon fibers. *Carbon* **2001**, 39, (14), 2231-2234.
- Toyoda, M.; Sedlacik, J.; Inagaki, M., *Synthetic Metals* **2002**, 130, 39-43.

PURE HYDROGEN FROM MULTIPLE FUELS IN MEMBRANE REFORMERS

A.S. Chellappa, T. R. Vencill, D. C. LaMont

MesoFuel, Inc. 1001 Menaul Boulevard NE, Albuquerque, NM 87107

Introduction

The ability to produce hydrogen from multiple fuels using the same hydrogen generator is desirable for a wide range of applications. Of greater impact for compact PEM fuel cell power systems, is the ability to produce pure hydrogen using membrane reformers. We have recently demonstrated "hot-swapping" of fuels with uninterrupted production of pure hydrogen. This paper will discuss performance metrics and challenges associated with using membrane steam reformers in fuel cell power systems.

MesoChannel™ Membrane Reformers

A schematic representation of a MesoChannel™ membrane reformer is shown in Figure 1. The system consists of 3 main components, namely: (1) a reactor, (2) a combustor, and (3) a hydrogen separation membrane. This membrane-based system therefore produces pure hydrogen for PEM fuel.

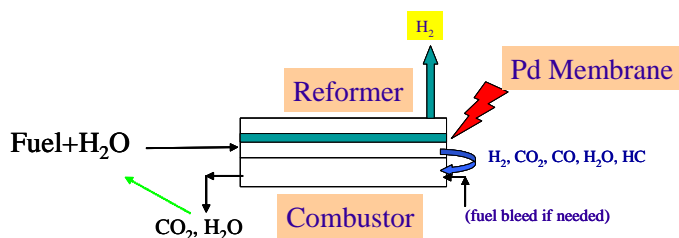


Figure 1. Membrane Reformer (Fuel = methane, propane, butane, ethanol etc).

cell applications in a single unit. These three components are integrated in an intimate fashion with each other to facilitate high heat and mass transfer rates, which in turn translate to higher processing rates per unit volume and subsequently to a compact and efficient fuel processor.

The fuel is mixed with water (steam) and is fed into the reactor where hydrogen is produced in the presence of a catalyst. In the absence of a hydrogen separation membrane, the product gas stream can consist of up to a maximum of 70% hydrogen on a dry basis, with the remaining constituents being CO, CO₂, and unreacted hydrocarbons. The integration of a separation membrane module with the reactor greatly facilitates the selective removal of the desired hydrogen from the reactor, as it is produced, to yield a very pure hydrogen stream (> 99.9%) which is then routed to the PEM fuel cell. The availability of this pure H₂ fuel leads to increased operating efficiencies of the PEM fuel cell. The reject gas is routed into the combustion chamber where it is combusted to supply the heat required for reforming.

Another advantage of a membrane reformer is that the *in-situ* removal of hydrogen allows higher hydrocarbon conversions at temperatures as low as 600°C to 650°C, relative to competing processes that use no hydrogen separation membrane. Operating at these lower temperatures permits the use of conventional materials of construction and machining/manufacturing practices

that lead to lower costs per unit. (In contrast, industrial reactors are operated at temperatures greater than 750°C, and require the use of specialty alloys and refractory materials).

This approach also obviates the conventional process train that contains water gas shift units, and CO polishing units such as preferential oxidation and /or pressure swing adsorption units that are both capital intensive and unsuitable for compact applications such as portable power systems, battery chargers, back-up power supplies and transportation applications.

Pure Hydrogen Production

Pure hydrogen was produced by steam reforming of several fuels while operating at 575 to 650 °C, 6 to 7 bar and S/C ratio of 2 to 4. The targeted hydrogen production rates were in the 300 to 500 sccm range - sufficient to power a 20 to 40 W PEM fuel cell suitable for compact power applications.

Figure 2 shows pure hydrogen production rates from a synthetic kerosene (C₁₂) fuel. As can be seen, about 300 sccm of hydrogen was produced in a stable manner for 1000 h confirming reliability of the reformer. The purity of hydrogen was assessed using helium ionization detectors and an FID was found to be > 99.96%.

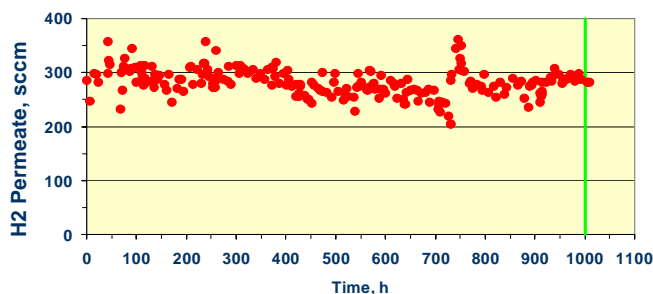


Figure 2. Pure hydrogen (> 99.96% purity) from kerosene: reliability test.

In a subsequent test, after establishing steady state operation under kerosene reforming, the kerosene fuel was replaced with propane (LPG) while the unit was at temperature. That is, the fuels were "hot swapped". The propane (or LPG) fuel was desulfurized prior to feeding into the reformer. The hydrogen production rates during this test are shown in Figure 3.

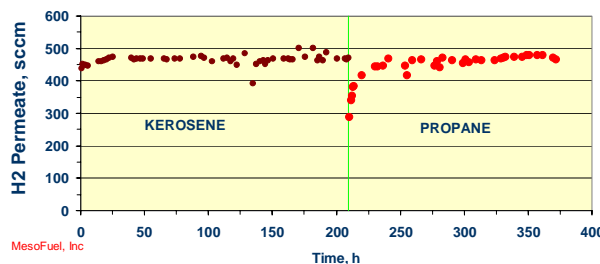


Figure 3. "Hot -swap" of fuels: hydrogen from kerosene and propane.

After demonstrating pure hydrogen production from kerosene for about 210 h, kerosene was cut-off and replaced with propane (LPG). Note that the targeted hydrogen production rate of about 450 sccm was maintained even after the fuel swap. This test demonstrates the robustness of our membrane reformers; a desired characteristic for portable power applications. Purity levels of the hydrogen product at three different run times are shown in Table 1.

Table 1. Purity levels of hydrogen during the hot-swapping from kerosene to propane.

Sample	Fuel	TOS (h)	CH ₄ (ppm)	CO ₂ (ppm)	CO (ppm)	H ₂ (purity, %)
1	Kerosene	43	3.58	9.98	2.71	99.998
2	Kerosene	113	5.99	22.31	3.06	99.997
3	Propane	279	15.05	30.23	5.72	99.995

At > 99.99% purity and with CO levels < 10 ppm, the hydrogen product is suitable for powering PEM fuel cells without any subsequent polishing steps. We have successfully powered PEM FCs of several vendors using the hydrogen that was produced, and have demonstrated that pure hydrogen (as opposed to a CO free reformat stream) affords ‘Plug ’N Play’ interaction between the hydrogen generator and the PEM FC.

Pure hydrogen production from renewable fuels such as ethanol has also been demonstrated. A reformer unit similar to that used for the hydrocarbon fuels was used for the ethanol reforming tests. The ethanol/water fuel feed was formulated using absolute ethanol (99.5% purity, Aldrich) and distilled water. The fuel was then routed into the membrane reformer. Hydrogen production was assessed while operating at 500°C to 650°C, and 6 bar while changing the space velocity and S/C ratio.

Figure 4 shows purity levels of the hydrogen product at 625 °C, 6 bar and at S/C ratios of 3 to 4. The hydrogen production rates were in the 350 to 400 sccm range. As can be seen, hydrogen at > 99.98% purity levels was produced during this test. The hydrogen product was also collected twice during the course of the test, and analyzed by a third party for validation of purity.

The hydrogen purity was unaffected by a change in operating parameters (Figure 4), but as expected, hydrogen production rates decreased while increasing the S/C ratio from 3.2 to 4.2 (dilution effects).

Carbon balance closures were within 10% and ethanol conversion was 100%. We did not observe any coke formation, nor did we detect any intermediate products such as ethylene and acetaldehyde.

During the course of the ethanol reforming test, ethanol was replaced by methanol – a “hot swap” of fuels. Uninterrupted hydrogen production was once again demonstrated using the hot swap of these oxygenated fuels. More details will be provided during the presentation.

Conclusions

Pure hydrogen (> 99.96% purity) was produced by steam reforming of multiple fuels using our MesoChannel™ membrane reformers while operating at 4 to 6 bar and 575 to 625 °C. Stable hydrogen production at rates of 300 to 500 sccm was achieved. The CO levels in the hydrogen product are below 10 ppm, and generally below 5 ppm. As a result, the hydrogen product can be used to power PEM fuel cells without any polishing. “Hot swapping” of fuels has been demonstrated. Packaging of the reformers to yield a compact hydrogen generator is in progress. These hydrogen

generators are potentially robust and can be used for a wide range of commercial and military applications.

Acknowledgments. This work was funded in part by the DARPA Palm Power program.

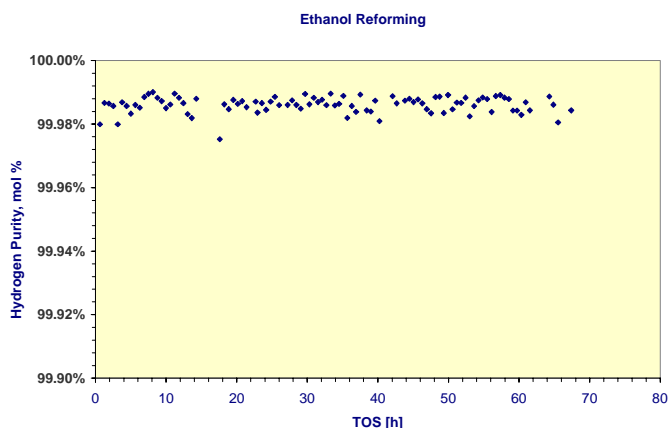


Figure 4. Purity of hydrogen produced by steam reforming of ethanol in a MesoChannel membrane reformer. P = 6 bar, T = 625 °C.

Hydrogen storage in chemical hydrides

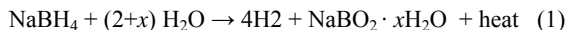
Michael, A. Matthews, Thomas A. Davis, and Eyma Y. Marrero-Alfonso

University of South Carolina
Department of Chemical Engineering
301 Main, Swearingen Engineering center
Columbia, SC 29208

Introduction

This is an investigation of a gas/solid chemical reaction between steam and chemical hydrides that liberates pure hydrogen gas. The aim is to obtain fundamental kinetic, chemical, catalytic, and thermodynamic data on the reaction so that sufficient information is known to evaluate this technology rigorously for its potential as a means of delivering hydrogen for fuel cells and internal combustion engines.

It is known that simple chemical hydrides (e.g. LiH, CaH₂) as well as complex hydrides (NaBH₄, LiBH₄, and others) react with liquid water to produce H₂. For example, NaBH₄ has been extensively studied:



In equation 1, x is the “excess hydration factor”, representing the fact that the solid byproduct can exist in varying degrees of hydration. This liquid reaction has some disadvantages. For example, in the case of NaBH₄, an acid catalyst is required to liberate 100% of the hydrogen, because dissolved NaBH₄ is stable in basic solution, and the byproducts (sodium borate and similar compounds) are basic in solution. In this reaction, the ideal case is where $x = 0$, in which case the mass yield is 10.3 kg H₂ per 100 kg of reactants. In practice, excess water is required ($x=2$ is more realistic) so that the NaBH₄ and byproducts remain completely dissolved. Excess water rapidly reduces the mass efficiency of the system.

A recent discovery shows that by vaporizing water prior to contact with the hydride, hydrogen yields in excess of 90% may be obtained without the need for a catalyst. Thermodynamic considerations show that, in principle, the heat liberated by the reaction is more than sufficient to vaporize the stoichiometric water required for the steam. Thus, there is the possibility of developing a hydrogen reactor/delivery system that is autothermal at steady state, that produces pure hydrogen in 100% yield, that requires no catalyst, that does not involve strongly caustic solutions, and that uses a minimum of water. Furthermore, the solid reaction products should be nearly free of water, which in the long term will facilitate recycling and regeneration to the hydride.

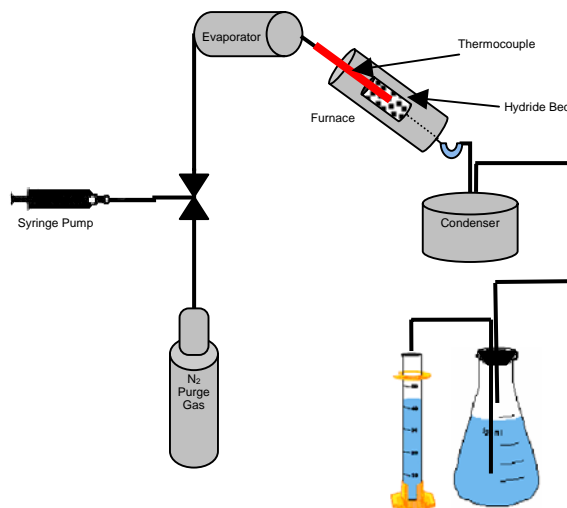
Experimental

Figure 1 shows a schematic representation of the NaBH₄ steam hydrolysis reactor system. The reactor itself is a cylindrical quartz reactor tube placed inside a Thermolyne Model 21100 tube furnace that controls the temperature. One thermocouple placed in the center of the reactor vessel monitors the reaction temperature.

The reaction temperature is also affected by the temperature of the incoming steam. Steam temperature is controlled by a three-stage heater. The first stage of the heater system preheats the steam to approximately 100°C. This preheated liquid/vapor mixture then enters the second and third stage, which superheats the water vapor to the desired reaction temperature. A KD Scientific

Model 200 Programmable Syringe Pump is used to pump the desired water flow to the evaporator.

Figure 1. Schematic of the steam hydrolysis reactor system



The volumetric flow rate and cumulative volume of hydrogen are measured as the volume of water displaced from the Erlenmeyer flask to the graduated cylinder. Condensable water is removed in a cold trap, leaving a stream of hydrogen with a trace amount of water. The gas product stream has a septum port (not shown) before the condenser for sampling the product gases. A gas-tight syringe is used to withdraw a small sample from the system for analysis.

All experiments were conducted with one gram of NaBH₄ mixed with glass beads packed into the reactor between glass-wool plugs in a glass reaction tube. After installation, the reactor is purged with a steady stream of nitrogen to ensure that the reactants are continuously under a blanket of inert gas until the hydrolysis begins.

Results and Discussion

Figure 2 shows the volume of hydrogen collected over the course of the experiments. The horizontal line labeled “Theoretical Yield” shows that theoretically 2,550 mL (0.106mol) of H₂ can be produced from 1 g of NaBH₄. The three lines labeled “Theoretical rates” were calculated based on the Equation (1), assuming that water is the limiting reactant and that the reaction is instantaneous. Calculations were done for $x=0$, 4 and 6. For example, if no excess water is added ($x=0$) and the water flow rate is 0.1 mL/min (0.0055 mol/min), the theoretical rate of hydrogen production is 0.011 mol/min, which is the slope of the line shown in the graph.

Figure 2. Experimental H₂ yield for 1 gram of NaBH₄.

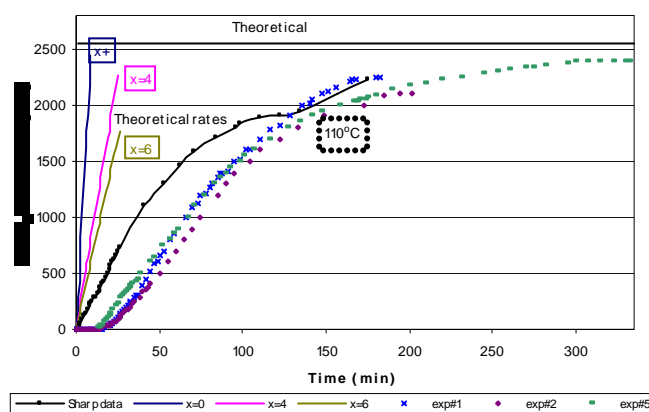


Figure 2 shows the experiments done with pure steam at 110°C. Experimental conditions are listed in Table 1. The data show good reproducibility and are in agreement with work done in the past.[1] Hydrogen yields from 82% to 94% of the maximum were obtained without the need of an additive. The curve labeled “Sharp data” is from past work with a different experimental apparatus. The Sharp data show a greater initial rate than the new experiments, but similar H₂ yield.[1] All the experimental rates are lower than the theoretical rates, because the excess water required moves the slope to the right decreasing the reaction rate. The 15-min. induction period seen in some of the curves was an artifact of the apparatus used at that time, and it disappeared when the design was modified (see Figure 3).

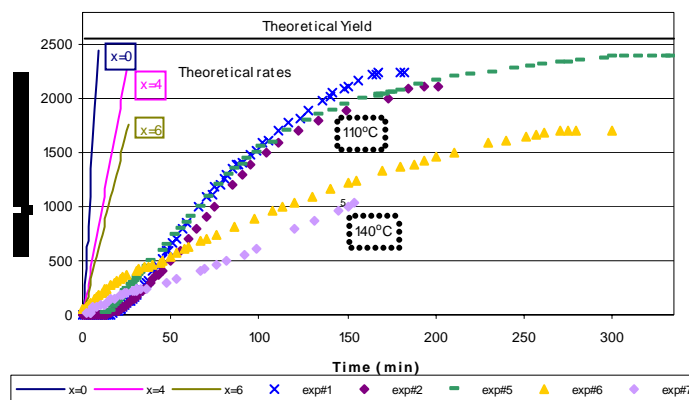
The initial rate of the reaction, expressed as moles of H₂ produced per minute per gram of NaBH₄, was determined for each experiment by measuring the slope of the curve after the induction period and is shown in Table 1. Additives, methanol and acetic acid, did not increase the initial rate, and raising the temperature to 140°C decreased the reaction rate. Experimental results of the past work [1] show that for the different hydrides used, higher yields of hydrogen were obtained at the lowest temperature (110°C).

Table 1. Initial Rates

Exp#	Description	T (°C)	Initial Slope (mol/g _{NaBH₄} *min)	% of Theo. H ₂ Yield	Time (min)
1	Old NaBH ₄	110	8.12E-04	88.2%	128
2	Old NaBH ₄	110	7.17E-04	82.7%	202
3	1% acetic acid	110	5.82E-04	101.4 %	228
4	1% methanol	110	7.15E-04	92.7%	250
5	New NaBH ₄	110	7.17E-04	94.0%	323
6	New NaBH ₄	140	3.49E-04	67.1%	296
7	New NaBH ₄	140	2.69E-04	40.8%	154
8	6.5% methanol	110	5.45E-04	68.5%	365
9	15% methanol	110	5.89E-04	82.0%	450
Sharp data	NaBH ₄	110	1.10E-03	87.4%	175
Theoretical Rates		x=0	1.11E-02	100%	-
		x=4	3.70E-03	100%	-
		x=6	2.78E-03	100%	-

Figure 3 shows hydrogen yield from the experiments done at 140°C and the experiments done at 110°C. Both the initial rates and the yields were lower at 140°C, consistent with earlier work. [1]

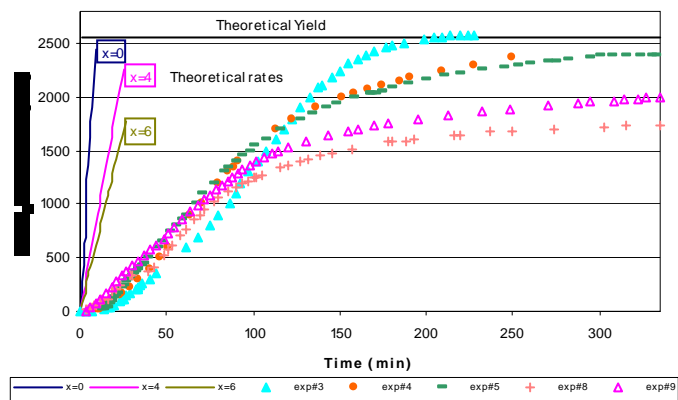
Figure 3. Experimental H₂ yield for 1 gram of NaBH₄ at 110°C & 140°C



The lower rates and yields at higher temperature are counterintuitive, but they might be attributable to mass transfer limitations in the particle. Observation of the reactor contents after the experiments indicates that the solid particles remain intact but agglomerated. The agglomerated material was soft and wet after the 110°C experiment and hard and dry after the 140°C experiment. Presumably the NaBH₄ on the surface of the particle reacts first and forms a layer of sodium borate (NaBO₂), which grows in thickness as the reaction proceeds. That NaBO₂ would be hydrated at lower temperatures but not at higher temperatures. The lower reaction rates at higher temperatures would be explained if the dehydration makes the NaBO₂ less permeable to water vapor. This theory remains to be proven.

Figure 4 shows the hydrogen yields for the experiments with additives. Separate aqueous solutions of 1mol%, 6.5mol% and 15 mol% of methanol and 1mol% of acetic acid were injected by the syringe with the same procedures used for the other experiments. The initial rate of the reaction was about the same regardless of the type or concentration of the additive, but different yields were obtained. Yields of 68% to 93% of the maximum were obtained with methanol, but no explanation is offered for the fact that the best yield occurred with the lowest concentration of methanol. The best yield with methanol is no better than yields with just steam (82% to 94%) as shown in Table 1. The use of acetic acid gave a yield of 100%. For safety reasons and to avoid any undesired byproduct the use of additives must be considered carefully.

Figure 4. Experimental H₂ yield for 1 gram of NaBH₄ using additives

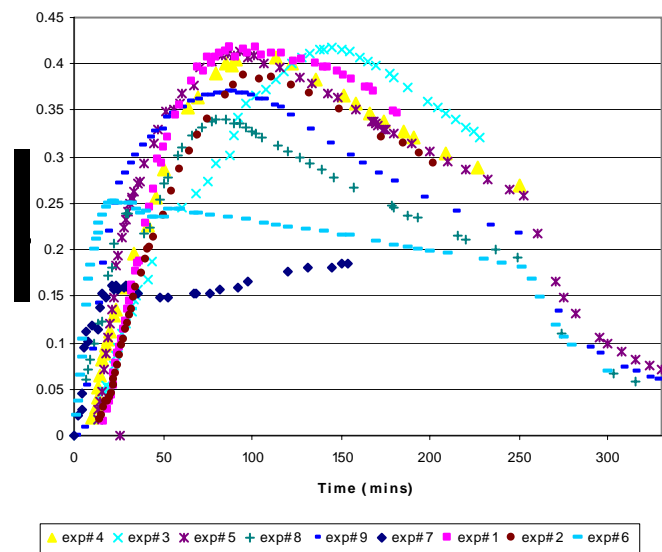


The Department of Energy (DOE) designs the FreedomCAR Technical Targets to promote scientific research in the area of hydrogen storage.[2] New technologies should meet these targets. One of the targets is the usable specific energy from hydrogen (net useful energy/max system mass) and is shown in Table 3. Values of kWh per mass of the reactants were calculated for each experiment to provide an indication of the mass available for a reactor to meet the target. Figure 6 shows the calculations of the energy as function of time. It was observed that the usable specific energy reaches a maximum. Subsequently, the specific energy decreases due to the excess water required.

Table 3. FreedomCAR Targets for Specific Energy [2]

Usable specific energy from Hydrogen			
Year	2005	2010	2015
Target (kWh/kg system)	1.5	2	3
Target (kg H ₂ /kg system)	0.045	0.060	0.090

Figure 6. Usable Specific Energy from H₂.



Conclusions

With the data collected it is shown that more than 80% yields of H₂ can be obtained without the need of any additive. The intrinsic reaction kinetics may be obscured because of impermeable byproducts. More knowledge in that area will help to approach an improvement in the rate of the reaction without the need of excess water. Using less water to obtain a high yield will make this technology viable as a medium for hydrogen storage.

Acknowledgement.

This work was carried out under Agreement No. DAAB07-03-3-K416 with the US Army Communications-Electronics Command (CECOM) for Hybrid Advanced Power Sources with guidance from the RDECOM / CERDEC Fuel Cell Technology Team at Fort Belvoir, VA.

References

- (1) Aiello R.; Sharp J.; Matthews M. *International Journal of Hydrogen Energy*; **1999**, 1123-1130.
- (2) www.eere.energy.gov/hydrogenandfuelcells/pdfs/freedomcar_targets_explanations.pdf

Water Gas Shift Catalysts for H₂ Production in Membrane Reactors

Thomas Henry Vanderspurt*, Rhonda R. Willigan, Rakesh Radhakrishnan, Caroline A. Newman, Susanne M. Opalka, Zissis Dardas, Mallika Gummalla, Fabienne Wijzen, Xia Tang, Harry Cordatos, Ying She and Fangxia Feng

United Technologies Research Center, 411 Silver Lane, East Hartford, CT 06108 USA

Polymer electrolyte fuel cells perform best on pure H₂. Low sulfur hydrocarbon fuels can be converted to PEM fuel grade H₂ using a compact membrane reactor architecture¹. Consequently United Technologies Research Center (UTRC) is developing integrated Pd Membrane reactors for H₂ production through reforming of fossil fuels and the subsequent conversion of the CO in the reformat to hydrogen through the Water Gas Shift (WGS) Reaction. This not only allows the shifting of the WGS equilibrium through H₂ removal but it greatly simplifies the system design by eliminating all the other reactors, as well as a major part of the multiple heat exchangers and the air mixers down stream of the reactor that they are integrated with in the traditional fuel processing system for H₂ generation.

Metal supported tubular Pd membranes have high modularity and thus can be easily scaled up to any system capacity while they do not employ components with low reliability like frequently actuated rotating valves. This approach results in significant system cost savings and controls simplicity (thus higher system reliability) due to system and system controls simplification through component elimination. These are significant advantages over the currently applied and more mature technology for H₂ production, the Pressure Swing Adsorption. However this approach requires cost effective, air tolerant catalysts with high volumetric activity and high stability for prolonged operation at ~ 400 °C. On the basis of Gorte's² studies noble metal on nano-crystalline ceria-mixed metal oxide catalysts were explored to provide such a catalyst. Eventually a high temperature metal alloy on ceria based mixed metal oxide catalyst was found that gave excellent performance during an 880 hr test with synthetic reformat. This test included 560 hrs at ~420 °C. Although projecting life and stability has to be done cautiously the projected activity of this catalyst after 10,000 hrs at 420 °C was 73% of its 100 hr lined out activity or a turn over frequency TOF of >2.4 CO/Pt-sec.

This catalyst was a member of a family of catalysts designed from the outset to have both high surface area and a network of pores sized to eliminate internal mass transfer. To this end a synthesis route to 2.5 to 3.5 nm doped ceria-zirconia or ceria hafnia oxide crystallites was devised. This route and its variants can accommodate a wide variety of both Ce/Zr or Ce/Hf ratios and dopants. The careful processing allows the recovery of a fractal structured material wherein the fundamental crystallites link through their high energy faces to form high porous ~100 nm particles. These particles link together forming even larger pores inside micro-sized aggregates. A typical Ce_(1-x)Zr_xO₂ with skeletal density of ~6 and a crystallite size of 3 nm by PXRD can be obtained with 270 m²/gm surface area. To put this in perspective this is about 70% of the theoretical surface area for the crystallite size. If the oxide had the same skeletal density as γ-Al₂O₃ then these catalysts would have a surface area of about 425 m²/gm. Surface area of ~ 200m²/gm are typical of oxides designed for long term ~ 310 °C operation.

Significantly, the nano-crystallites are primarily cubic (Fm3m) in structure as determined by a combination of PXRD and Raman spectroscopy even at oxide compositions that in

larger crystallites are tetragonal (P4₂/nmc) according to Kaspar³. Raman is critical for determining the structure of these nano-crystalline materials as broader peaks caused by the small crystallite size tends to preclude definitive PXRD determination. Ce_{0.50}Zr_{0.50}O₂ crystallites with an average size of 3.45 nm by PXRD exhibits a major, broad Raman peak at ~465 cm⁻¹ with a low shoulder extending beyond 650 cm⁻¹ ascribed to oxygen vacancies. This shoulder appears even at 10% Zr and grows with Zr concentration. The Raman spectra of the nano-crystalline Ce_{0.25}Zr_{0.75}O₂ is dominated by a broad 465 cm⁻¹ peak though with a weaker ~640 cm⁻¹ peak. Ce_{0.17}Zr_{0.83}O₂ on the other hand is tetragonal by PXRD and had Raman spectra indicative of a tetragonal structure.

These oxides were converted to WGS catalysts by loading with noble metals either alone, in combination or with transition metal promoters. Gorte⁴ has demonstrated the major impact that Fe can have on Pd/CeO₂ activity. For the Ce_(1-x)Zr_xO₂ and Ce_(1-x+y)Zr_xDp_yO₂ prepared by our techniques Pt seems superior to the other metals. As prepared these supported Pt catalysts have 100% dispersion by CO chemisorption. High resolution TEM investigation is consistent with the majority of the Pt forming small, ~1nm rafts. After loading with Pt these oxides are reducible at low temperatures by TPR. This is not a function of either Pt or oxide crystallite size. A Pt/ Ce_(1-x)Zr_xO₂ catalyst was calcined at 1000 °C in air and had a major reduction peak at ~130°C despite very large Pt crystallites and nil surface area.

These high surface area catalysts were first explored for their low temperature water gas shift activity. Besides automated micro-reactor screening and kinetics studies, VASP atomistic modeling of the Ce_(1-x+y)Zr_xDp_yO₂ system along with in-situ CIR-FTIR studies were initiated. A range of compositions were examined as 80-120 mesh granules diluted with 40 mesh α-alumina run at high space velocity. Typically between 210 and 240 °C the kinetic expression $r = A \exp(-E_a/RT) [\text{CO}]^a [\text{H}_2\text{O}]^{0.6} [\text{CO}_2]^{0.2} [\text{H}_2]^{-0.6}$ would fit the data with E_a values ranging from 66 to 73 kJ/mole. These results are consistent with a rate limiting step involving water. The modeling work predicted domination of the oxide surface by a formate like species, but that this domination could be lessened by doping the Ce-Zr oxide with any of several species, Mo among them. The in-situ FTIR spectra taken at low space velocity indeed indicated domination of the surface by a formate like species as well as carbonate for Pt/Ce_{0.65}Zr_{0.35}O₂. Doping with La apparently increased and changed the nature of the adsorbed CO while also enhancing peaks attributable to CO on Pt. Mo doping on the other hand decreased the apparent intensity of peaks attributed to CO and carbonate adsorbed on the oxide. These results were consistent with reactor studies where a Mo doped catalyst exhibited a lower apparent activation energy than the undoped material.

While Mo exhibited some low temperature promoting ability it did not increase high temperature activity. The catalysts suitable for long term <320 °C deactivated when exposed to high temperatures for hundreds of hours. Catalysts deactivated even with UHP feed gases passed through activated carbon, mole sieve and Oxisorb[™] traps as well as a heated ZnO bed. Analysis of these deactivated catalysts revealed only slight oxide crystallite growth or loss of surface area. Their PXRD patterns showed no evidence of severe Pt agglomeration and there were no drastic changes in their Raman spectra. Notably however the low temperature reduction peak so evident in the TPR of fresh catalysts was absent.

A promoter M was found for Pt / Ce_(1-x)Zr_xO₂. Kinetic studies were carried out and Athena software used to fit the data to $A \exp(-E_a/RT) [\text{CO}]^a [\text{H}_2\text{O}]^b [\text{CO}_2]^c [\text{H}_2\text{O}]^d (1-\beta)$ where β is the approach to equilibrium. At low temperatures, below 250 °C, E_a

was 71 kJ/mole and $\alpha = -0.2$, $b = 0.8$, $\gamma = -0.12$, $\delta = -0.4$, while at high temperatures the activation dropped to 46 kJ/mole and $\alpha = 0.2$, $b = 0.4$, $\gamma = -0.2$, $\delta = -0.4$. This promoted catalyst still lacked the requisite high temperature stability. A Pt-M/Ce_{1-(x+y)}Hf_xDp_yO₂ catalyst with a skeletal density >8.0 and a surface area of 146 m²/gm and a crystallite size of 3.3 nm was synthesized. On a skeletal density adjusted basis its surface area was equivalent to about 190 m²/gram for a 60% cerium, 40% zirconium oxide. This catalyst was tested for 880 hrs at 740,000 hr⁻¹ space velocity under a variety of conditions. Its activity retention was excellent. Under 7.5% CO, 5.5% CO₂, 27.6% H₂O, 28.9% H₂, bal. N₂ at 740,000 hr⁻¹ after ~560 hours at 420 °C this catalyst's TOF was 3.0 CO/Pt-sec.

On the basis of an activity versus log of time plot its projected activity at 10,000 hrs was > 2.4 CO/Pt-sec suggesting that it might retain 73% of its 100 hr activity at 10,000 hrs. United Technologies Research Center is working with HydrogenSource LLC and their suppliers to commercialise this catalyst technology for hydrogen production. Extended monolith tests are planned.

References

1. Gummalla, M.; Olsommer, B.; Dardas, Z.; She, Y.; Vanderspurt, T.H. "On-Board Cost Effective Hydrogen Enhancement Technology for Transportation PEM Fuel Cells" DOE Merit Review, Berkeley CA May 19, 2003
2. Bunluesin, T.; Gorte, R.J.; Graham, G.W. Applied Catalysis B: Environ. **1998**, *15* (1-2), 107-114.
3. Kaspar, J. and Fornasiero, P. in *Catalysis by Ceria and Related Materials*; Trovarelli, A. Ed. Imperial College Press, London 2002 pp. 217-241.
4. Wang, X.; Gorte, R.J. Applied Catalysis, A: General **2003**, *247* (1), 157-162.

START-UP OF AN AUTOTHERMAL REFORMER

S. Ahmed, R. Ahluwalia, S. Lee, S. Calderone, T. Harvey, K. Liao

Argonne National Laboratory, 9700 S. Cass Ave., Argonne, IL 60439

Abstract

The question of whether the hydrogen infrastructure or the fuel cell vehicle should come first has been debated for over a decade. This chicken-or-egg dilemma can be resolved with on-board fuel processors that can convert gasoline to hydrogen on demand. These on-board fuel processors have to meet many criteria for success in a demanding automotive application – a key requirement being the ability to start-up rapidly.

Argonne National Laboratory has been studying the feasibility of a fast-starting fuel processor (FP) by designing and testing an autothermal reformer (ATR) based fuel processor. The first step in this start-up process requires readying the ATR. With the FP start-up times targeted at 30 seconds, the constraints on the ATR for a smooth start-up transition are quite rigorous. This paper presents the experimental data of start-up protocols that begin the reactions in the partial oxidation mode and then switch to the autothermal reaction mode.

Introduction

The strategy for mass commercialization of fuel cell vehicles invariably brings up the question of whether the fuel cell vehicle or the hydrogen refueling infrastructure should come first. One solution around this dilemma is to use on-board fuel processors which can convert currently available fuels such as gasoline to hydrogen on demand. For commercial success of these vehicles, the revolutionary change in the power source should be transparent to the consumer, one element of which is that the fuel processor does not adversely contribute to the driving experience. One of those features is its ability to start-up rapidly.

The autothermal reforming process is recognized for its ability to reach operating temperatures quickly. However, the transition of a cold catalytic reactor to operating temperatures greater than 650°C within a few seconds requires synchronization of the balance of plant and careful control of the reaction parameters. A myriad of combinations are possible, each set introducing its own advantages and limitations, some of which are delineated in this paper. The experiments were conducted in the autothermal reaction zone of an integrated fuel processor [1].

Initiating the Catalytic Reactions

The catalytic autothermal reforming reaction is typically started in the partial oxidation mode (POX) by contacting the oxygen (air) and the fuel over the heated catalyst bed. Then as the exothermic reaction further heats up the catalyst bed, the reaction is switched to the autothermal mode by introducing water.

The start-up of our ATR catalyst consisted of the following steps, programmed as a sequence of logical steps using the LabView software. The fuel pump and the water pump were started to establish pressurized recirculation loops for each. The flows to each of their respective vaporizers were controlled to the desired setting with a pneumatic valve, a mass flow controller, and a PID control loop. A 3-way solenoid valve directed the flow from the vaporizer to either the ATR or back to their respective tank. The air flow was simpler (a compressor start-up was not necessary since our apparatus was connected to the house compressed air line) and consisted of a mass flow controller that directed the air through the nozzle into the ATR. Electrical heater coils placed above the catalyst bed were powered up

to allow the catalyst bed to heat up, by a combination of radiation heat transfer and sensible heat transferred via the air stream that flowed past it and through the catalyst. Figure 1 shows the temperature rise measured on a heater coil and on the front face of the ATR catalyst. The test was performed with the heaters powered at 1.2 kW, while 5 L/min of air flowed past the heaters and into the catalyst structure.

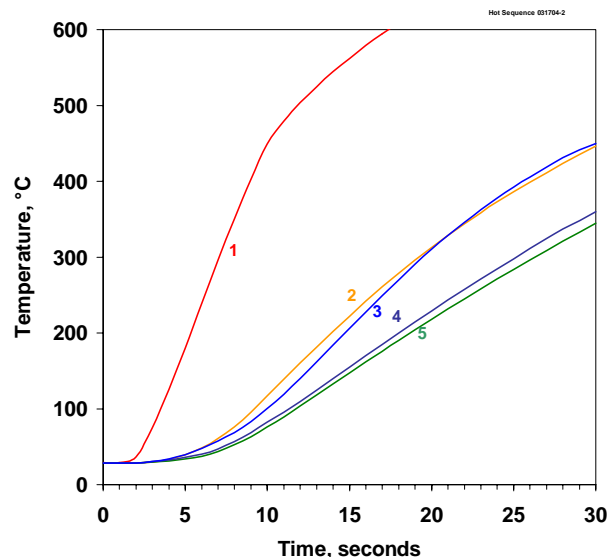


Figure 1. Temperature rise on a heater rod (1) and the ATR catalyst surface (2-5).

Ignition on the ATR catalyst depends on many conditions such as the catalyst formulation, structure, the composition, phase, and temperature of the fuel, and the air/fuel ratio, etc. Experiments were conducted to start the ATR operations using four different feed combinations. These were (1) vaporized fuel and air; (2) liquid fuel and air, followed by liquid water; (3) vaporized fuel and air, followed by steam; and (4) vaporized fuel and air, followed by liquid water. In all cases the fuel feed rate was maintained at 40 g/min. Liquid injections were achieved through a nozzle that delivered a fine spray over a catalyst bed with a diameter of 9.7 cm. The catalyst bed was 3.2-cm deep.

Results and Discussion

Figure 2 plots the feed rates of vaporized fuel, air, and water into the reactor as a function of time. The initial air flow rate corresponded to an O/C ratio of 0.56. Water was injected 40 seconds after the fuel to allow a sufficient depth of the catalyst zone to warm up such that the introduction of water would not quench the reactions entirely. Since water has a significant cooling effect, the air flow rate was increased to an O/C ratio of 0.92 and eventually to 1.07. The final steam-to-carbon (S/C) ratio was 1.28.

Figure 3 shows the temperatures of the catalyst at depths of 6-mm and 18-mm from the front face of the catalyst. The delay in temperature rise at the two locations is representative of the thermal mass of the catalyst and support that separates the two thermocouples. In 40 seconds the temperatures at the 6-mm and 18-mm locations had reached 856°C and 610°C, respectively. Introducing the water spray and the higher air flow rate brought the temperatures down to between 650-750°C. The effects of the air flow increases were more prominent on the downstream thermocouple.

Figure 4 shows the concentration of hydrogen and carbon monoxide measured by on-line analyzers. The introduction of water increases the hydrogen concentration to above 30%, while the CO

concentration drops below 4%. The presence of water has the desired effect of promoting the endothermic steam reforming reaction ($C_nH_m + H_2O \rightarrow CO + H_2$) and the mildly exothermic water gas shift reaction ($CO + H_2O = CO_2 + H_2$). The heat effects are reflected in the temperature responses seen in Figure 3.

Conclusions

Initiation of reforming reactions in a catalytic autothermal reforming reactor was conducted in a partial oxidation mode. It requires a combination of a heated catalyst surface and an appropriate air-to-fuel ratio. Introduction of water into the process has the desired effects of increasing the H_2 yield, reducing the CO yield, lowering the peak temperature, and reducing the potential for coke formation. The timing of the water injection (without quenching the catalyst bed) depends on the combination of feed proportions (O/C and S/C), the bed temperature profile, and the size and distribution of the liquid particles.

Acknowledgement. This work was supported by the Hydrogen, Fuel Cells, and Infrastructure Technologies Program of the U.S. Department of Energy, Office of Energy Efficiency and Renewable Energy, under Contract W-31-109-ENG-38.

Reference

1. Ahmed, S.; Ahluwalia, R.; and Lee, S.H.D., "Experimental Study to Determine Fast-Start Capability of On-Board Fuel Processors," 2003 Fuel Cell Seminar Abstracts, Miami Beach, FL, Nov. 2003.

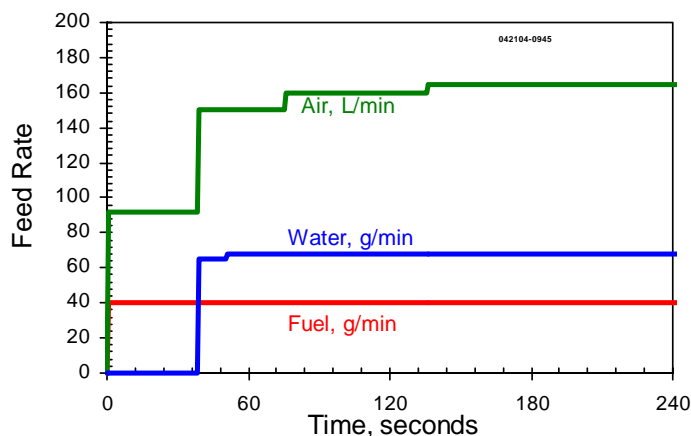


Figure 2. Feed rates into the autothermal reactor.

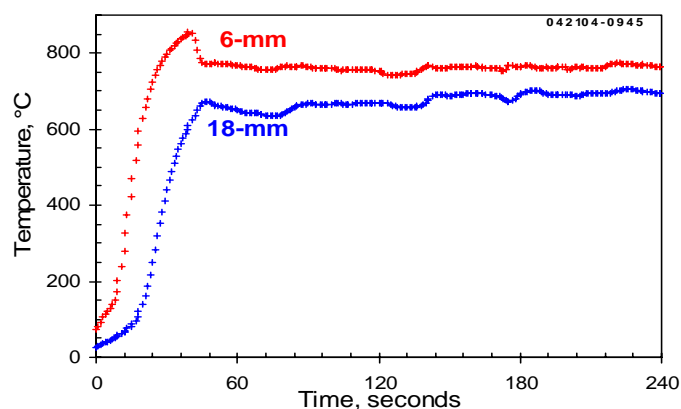


Figure 3. Temperature history in the ATR catalyst bed.

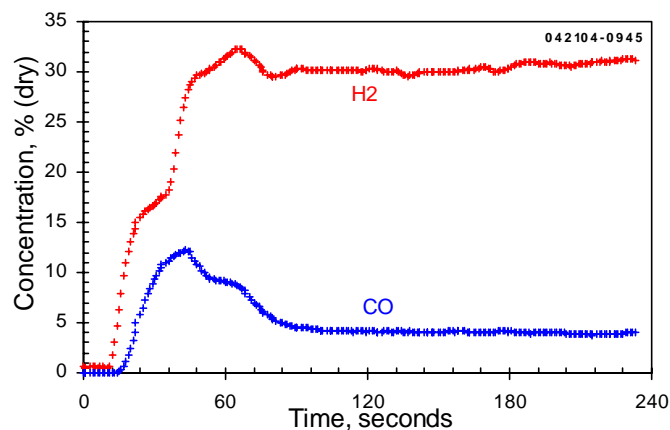


Figure 4. History of the hydrogen and carbon monoxide concentrations in the reformat from the ATR.

LIQUID HYDROGEN PRODUCTION VIA HYDROGEN SULFIDE METHANE REFORMATION

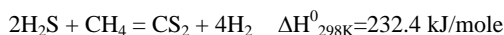
Cunping Huang and Ali T-Raissi

Florida Solar Energy Center
University of Central Florida
1679 Clearlake Road
Cocoa, FL 32922

Introduction

Hydrogen sulfide is a common contaminant in many of the world's natural gas (NG) wells. Approximately one-third of U.S. NG resources can be considered low or sub-quality gas not suited for pipeline shipment.¹ Hydrogen sulfide concentration in NG varies from traces to 90% by volume.² In natural gas processing hydrogen sulfide is viewed as a pollutant requiring treatment and removal. Presently, hydrogen sulfide is separated from hydrocarbon gases by amine adsorption and regeneration, producing acid gas containing 10-90% by volume hydrogen sulfide. When hydrogen sulfide concentration exceeds 40% the natural gas must be treated in the Claus plant, where a portion of hydrogen sulfide is burned to form sulfur dioxide. The gas then reacts with the main hydrogen sulfide stream to produce elemental sulfur and water. In this process, hydrogen in the hydrogen sulfide is converted into water vapor and wasted instead of being extracted as a clean energy source.

As an alternative to the Claus process, hydrogen sulfide can be removed by methods that produce elemental sulfur and hydrogen instead. For example, pyrolysis, thermochemical cycles, electrochemical and photochemical methods can be used to decompose H₂S directly. However, there are two drawbacks to direct decomposition of hydrogen sulfide for hydrogen production. Firstly, in the case of a hydrogen sulfide contaminated NG, the treatment process requires that H₂S be recovered from the sub-quality gas prior to its decomposition. In many cases, H₂S separation process requires considerable energy input, making utilization of the "sour" gas economically unfavorable. Secondly, H₂S decomposition produces only one mole of hydrogen per mole of H₂S reacted. A better approach is to reform H₂S and CH₄ already present in natural gas in a process analogous to steam reformation of methane as follows:



Hydrogen sulfide reformation of methane (HSRM) can generate two moles of hydrogen per mole of H₂S reacted. The main objective of this paper is to assess the merits of HSRM process with respect to the thermodynamics and chemical equilibrium considerations. Prior to the development of flowsheets, pinch point analyses are conducted to determine the necessary process conditions for zero carbon lay down based on the underlying HSRM chemistry. In addition, certain aspects of the process relevant to the liquid hydrogen production by cryogenic separation of constituent gases are discussed and compared to hydrogen membrane separation processes. The process energy requirements and efficiencies are also calculated using Aspen Technologies HYSYSTM chemical process simulator.

Thermodynamics of hydrogen sulfide reforming of methane

The thermodynamic analyses were carried out using Aspen Technologies HYSYSTM chemical process simulator. Since methane decomposition can result in carbon lay down that deactivates catalyst used for HSRM process, the analyses intended to find conditions that minimize carbon formation. This is done by pinch-point analyses. The yield of carbon, carbon disulfide and hydrogen are defined as the moles of product divided by the moles of methane input. The yield

of carbon and carbon disulfide as a function of temperature during HSRM process are given in Figure 1 and 2.

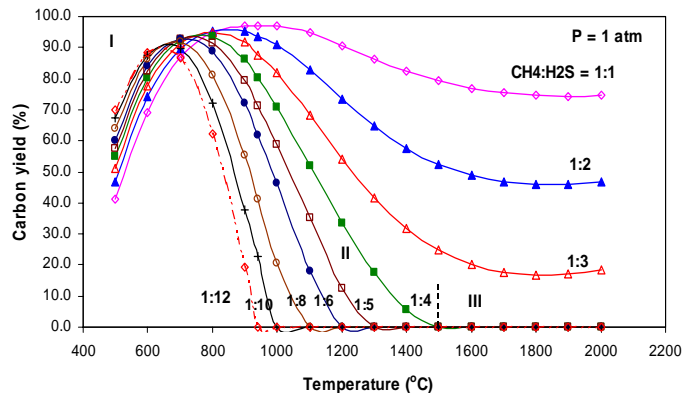


Figure 1. Carbon yields at various temperatures and CH₄ to H₂S molar feed ratios (Region I - CH₄ pyrolysis; Region II - excess CH₄ pyrolysis and HSRM zone; Region III - purely HSRM process).

In region III (HSRM), the hydrogen sulfide to methane feed ratio (x) does not have appreciable effect on the extent of CH₄ conversion. The major factor affecting methane conversion is temperature. When reaction temperatures exceed 800°C, methane conversion is practically 100% at all x values. The amount of carbon formed increases with increasing temperatures and has maxima as depicted in Figure 1. The temperature at which pinch-point occurs decreases with the increasing feed ratio x . For example, when $x = 4$, pinch point temperature is 1500°C, while it is 1000°C at $x = 10$. Carbon lay down can't be avoided if the hydrogen sulfide to methane feed ratio is lower than 4.

Total enthalpy (ΔH) change of HSRM process is calculated based on the enthalpy differences of products and reactants shown in Figure 2 for one mole methane system.

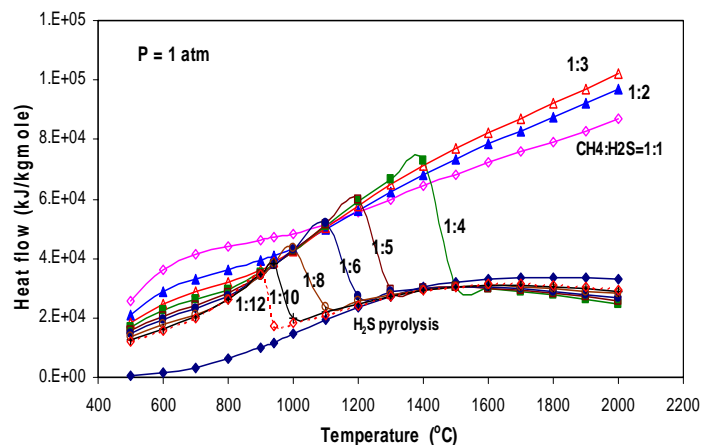


Figure 2. Total heat flow for HSRM process as a function of temperature and CH₄ to H₂S molar feed ratios.

It can be seen that ΔH is strongly dependent on both the temperature and hydrogen sulfide to methane feed ratio x . The required energies can be separated into two categories. Process energies required to carry out HSRM are much higher than those needed for hydrogen sulfide decomposition. At pinch-point temperature, the required energy drops from that for HSRM to a much lower value associated with the H₂S pyrolysis. As Figure 2 indicates, HSRM is a highly

endothermic process and as such can be employed for storing energy in the form of chemical energy (*e.g.* hydrogen) from high temperature sources such as solar resource. The pinch-point temperatures and energy requirements for HSRM process are depicted in **Figure 3**. Increasing the hydrogen sulfide to methane ratio, x , reduces the pinch-point temperature, as does the total energy required for the HSRM process

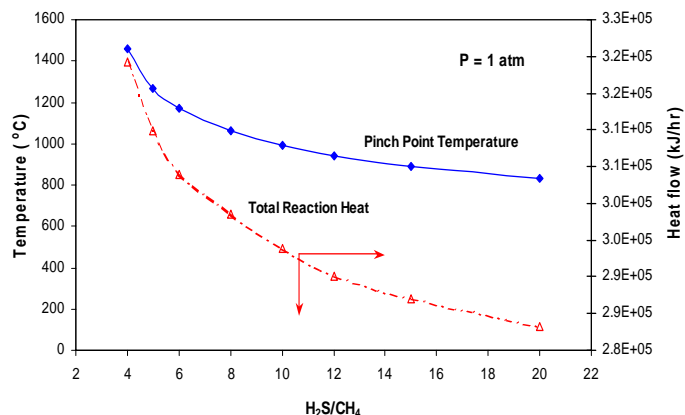


Figure 3. Pinch points temperature and total heat flow at various CH_4 to H_2S molar feed ratios.

Process flowsheet and efficiency calculations

Based on the thermodynamic analyses discussed above, three flowsheets based on cryogenic and membrane separation techniques were established for producing both liquid and gaseous hydrogen via HSRM process. All three flowsheets were set up at the pinch-point conditions for the HSRM process.

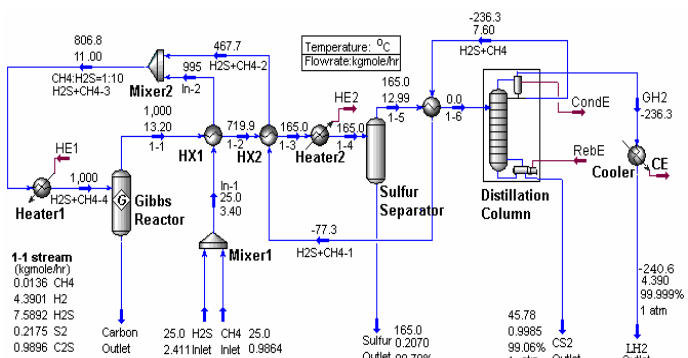


Figure 4. Process flowsheet for liquid hydrogen production via HSRM process.

A HYSYSTM-based process flowsheet for liquid hydrogen production by cryogenic separation is shown in **Figure 4**. Hydrogen, sulfur diatomic gas and carbon disulfide are produced in a Gibbs reactor that operates under no carbon lay down condition. The gaseous mixture at the outlet of the Gibbs reactor is cooled to separate out sulfur, and the remaining gases are sent to a cryogenic distillation tower to recover hydrogen and carbon disulfide from the unreacted hydrogen sulfide and methane. The unreacted hydrogen sulfide and methane are mixed with fresh feed in a manner to maintain the initial H_2S to CH_4 feed ratio x and subsequently heated and sent back to the Gibbs reactor. Low temperature (-236.3°C) gaseous hydrogen that exists distillation tower can be liquefied to by adding a small amount of cryogenic energy to reduce its temperature to -240.6°C . One important advantage of the process is that

hydrogen sulfide serves as both a reactant and as a working fluid for the cryogenic separation process. With H_2S recirculation, no other working fluid, such as nitrogen or helium, is necessary.

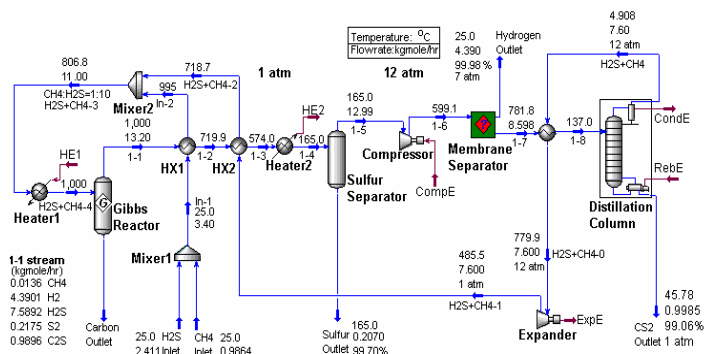


Figure 5. Gaseous hydrogen production via HSRM process paired with a membrane separation.

The HSRM process can be combined with a membrane separation technology for gaseous hydrogen production. Two types of membrane separation processes are developed based on the sequences of carbon disulfide and hydrogen separation. In one version depicted by the flowsheet of **Figure 5**, hydrogen separation occurs before that of carbon disulfide. After quenching the gas mixture exiting the Gibbs reactor, sulfur separates out of the main stream and the remaining gas mixture compressed to 12 atm (necessary for hydrogen separation through the membrane). The membrane separation efficiency assumed to be 100%. After hydrogen separation, the remaining gas mixture, consisting of hydrogen sulfide, methane and carbon disulfide, is sent to a distillation tower to separate the carbon disulfide from the mixture. The gas mixture is then expanded to 1 atm, mixed with fresh feed and sent back to the Gibbs reactor. The total required energy for both the cryogenic and membrane systems portions of the process are show in **Figure 6**.

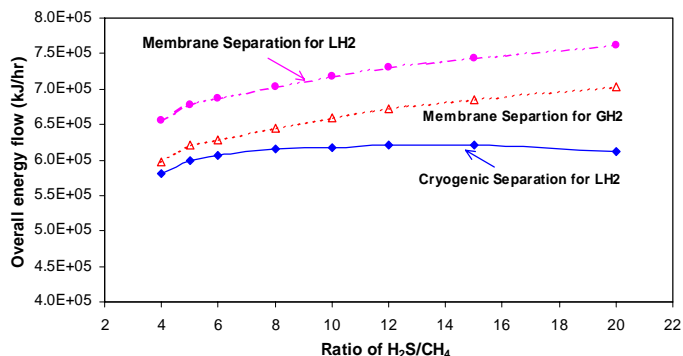


Figure 6. Overall energy requirements for hydrogen production via HSRM process

Acknowledgments. The authors are grateful for the financial support provided by the U.S. Department of Energy and NASA Glenn Research Center.

References

- Hugman, R.H., Vida, E.H., Springer, P.S., Chemical composition of discovered and undiscovered natural gas in the United States. 1993 update. *GRI-93/0456* **1993**.
- T-Raissi, A., Technoeconomic analysis of area II hydrogen production – Part 1. Final report fro DOE, **2002**.

HYDROGEN PRODUCTION BY STEAM REFORMING OF HYDROCARBONS

Niels R. Udengaard

Haldor Topsoe Inc.
17629 El Camino Real, Suite 300
Houston, Texas 77058

Introduction

The use of hydrogen for petrochemicals, fertilizers and as energy carrier in connection with renewable energy production will increase substantially in the next 5-10 years as even more stringent environmental legislation is enforced. Low sulfur gasoline and diesel fuels will become mandatory and harmful emissions will be reduced drastically. Hydrogen will be required by refiners and specialty chemical manufacturers to meet the global need for cleaner products. The growing fuel cell market will be dependant on hydrogen as a primary fuel source.

Hydrogen requirements vary widely. For small capacities below 0.1 MM SCFD, supply in cylinders or production by electrolysis may be preferable. Hydrogen production from methanol or ammonia cracking is suitable for small, constant or intermittent requirements as used in the food, electronics and pharmaceutical industries. For larger capacities hydrocarbons are used primarily as feedstock in the steam reforming process for production of hydrogen and synthesis gas.

The current production of hydrogen in North America is about 6000 MM SCFD, and the annual growth is expected to be above 4%. Most of this growth is for refineries for their production of ultra-low sulfur diesel and gasoline.

In spite of efforts to produce hydrogen by processes involving solar energy, wind energy, nuclear energy and biofuels, fossil fuels remain the most feasible feedstock in the near term, and for commercial scale production of pure hydrogen, steam reforming remains the most economic and efficient technology for a wide range of hydrocarbon feedstocks.

Steam Reforming Technologies

A typical layout of a hydrogen plant based on steam reforming includes the following steps:

Natural gas feed is preheated in coils in the waste heat section of the reformer, and sulfur is removed over a zinc oxide catalyst. Process steam is added, and the mixture of natural gas and steam is further preheated before entering the tubular reformer. Here, conversion to equilibrium of hydrocarbons to hydrogen, carbon monoxide and carbon dioxide takes place over a nickel based reforming catalyst.

The gas exits the reformer and is cooled by steam production before entering the shift converter, typically a medium temperature shift. Over the shift catalyst more hydrogen is produced by converting carbon monoxide and steam to carbon dioxide and hydrogen. The shifted gas is cooled further to ambient temperature before entering the PSA unit. High purity hydrogen product is obtained, and the off-gas from the PSA unit is used in the reformer as fuel supplemented with natural gas fuel.

Combustion air for the tubular reformer burners can be preheated in coils in the reformer waste heat section. Part of the steam produced in the hydrogen plant is used as process steam, the excess steam is exported.

In many situations when natural gas is not available, higher hydrocarbons become the preferred feedstock for the reforming process. Many refineries also can benefit from flexibility in

feedstock, taking advantage of the surplus of various hydrocarbon streams in the refinery.

Fired tubular reforming is generally the most competitive technology for capacities of up to more than 100 MM SCFD hydrogen.

Topsoe's latest development in steam reforming process technology is the advanced steam reforming process. The characteristics of this process are:

- High reformer outlet temperature
- Low steam to carbon ratio.
- High combustion air preheat (optional).
- Adiabatic prereforming (optional).
- High heat flux reformer.

Low steam to carbon ratios, typically 2.5, in hydrogen plants, reduce the mass flow through the plant and thus the size of equipment. The lowest investment is therefore generally obtained for plants designed for low steam to carbon ratios. However, a low steam to carbon ratio also increases the methane leakage from the reformer. This can be compensated for by increasing the reformer outlet temperature to typically 1690° F in hydrogen plants. Furthermore, operating at a low ratio requires the use of non-iron containing catalyst i.e. a copper-based medium temperature shift catalyst in order to eliminate production of by-products in the shift section.

The installation of an adiabatic prereformer upstream of a tubular reformer has been found to be very advantageous in naphtha based plants and plant operating on fuel gases with higher concentrations of higher hydrocarbons. Since all higher hydrocarbons are converted over the prereformer catalyst, the inlet temperature of the gas inlet in the reformer can be increased to 1200° and the reformer can be designed for higher heat fluxes. This reduces the size of the tubular reformer, resulting in direct capital cost reduction.

High combustion air preheat temperatures results in reduced fuel consumption and reduced steam production. The combustion air temperature can be used to adjust the steam export to a desired level. Temperatures of up to 1020° F are industrially proven in a radiant wall reformer.

The Topsoe convection reformer (HTCR) is a new concept which combines the radiant and waste heat section of the conventional reformer in one relatively small piece of equipment, thereby optimizing heat transfer to the steam reforming reaction and avoiding the surplus energy (often seen as steam export) inherent in conventional plants.

HTCR based layout is an attractive option for smaller sized hydrogen plants.

Efficiency and Production Costs

With no steam export the theoretical energy consumption is 300 BTU/scf H₂ on LHV (lower heating value) basis. The industrial value for natural gas based plants is about 320 BTU/scf H₂ corresponding to 94% of the theoretical efficiency. At locations with high natural gas prices, the energy efficiency becomes critical. For a natural gas price of 4 USD/MM BTU, the feedstock and utility costs makes about 65% of total operating costs.

Catalysts and the Mechanism of Steam Reforming

The steam reforming process may appear straightforward from an overall consideration as the product composition is determined

by simple thermodynamics, but in reality it is a complex coupling of catalysis, heat transfer and mechanical design.

In recent years, there has been progress in steam reforming technology resulting in less costly and more efficient plants, in part because of better materials for reformer tubes, better control and understanding of carbon limits, and better catalysts and process concepts with high feedstock flexibility. This progress has been accompanied by a better understanding of the reaction mechanism.

The typical steam reforming catalyst contains nickel. The catalyst properties are dictated by the severe operating conditions in the reformer with high temperatures and steam partial pressures. Sintering is an important cause of deactivation of nickel-containing steam reforming catalysts. The most important parameters are the temperature and the atmosphere in contact with the catalyst. The catalyst support can affect the sintering in various ways by loss of surface area. The sintering ceases when the nickel particle size exceeds a given size. The maximum size increases with temperature.

The catalyst activity is rarely a limiting factor. The catalyst volume (space velocity) is fixed from the tubular reformer design. The equilibrium conversion at high reforming temperatures is achieved at even very high space velocities when extrapolating the intrinsic rates. In practice, however, the utilization of the activity (as expressed through the effectiveness factor) is smaller than 10% because of transport restrictions. It can be shown by computer simulations that the catalyst is not the limiting factor for the design of a tubular reformer. An increase of the heat flux and the load at a given exit temperature by a factor of two results in an increase in methane leakage by only 10%.

Recent studies of the fundamentals of the steam reforming reactions have lead to a more consistent understanding of the mechanism of the main reactions and the competing reactions for carbon formation. The dissociation of methane on nickel surfaces has been investigated extensively, and several details of the reaction pathway are known from fundamental studies, in-situ high resolution electron microscopy and theoretical calculations.

In-situ high resolution electron microscopy has provided new information on sintering mechanisms and for the importance of steps in nucleation of whisker carbon. Density Functional Theory calculations have quantified the energetics of methane activation and shown that activation barriers are smaller on surface steps where also carbon is the most stable surface species.

Conclusions

The demand for hydrogen is growing in many industries, particularly in the chemical and refining industries. Topsoe has been active in this field for more than 50 years and offers a wide range of advanced technologies for small and large capacities meeting the demand for low operating and investment costs.

For small plants, convection reforming in the form of compact, skid-mounted plants is available. This is a low investment alternative to conventional concepts using tubular reforming.

For medium and large-scale plants the predominant technology is steam methane reforming of hydrocarbons. Advanced steam reformer design allows high temperatures and low steam to carbon ratios for hydrogen production resulting in high energy efficiency and lower cost plants.

For very large hydrogen and syngas plants the oxygen reforming technology may be applied, such as autothermal reforming and oxygen fired secondary reforming. These technologies are especially attractive when cheap oxygen is available.

References

- (1) Rostrup-Nielsen, J.R.; Sehested, J.; Norskov, J.K.; Hydrogen and Syngas by Steam Reforming, Academic Press, 2002.
- (2) Dybkjaer, I.; Winter Madsen, S., Hydrocarbon Engineering, December/January 1997/98.

Logistic Reformation of Hydrocarbon Mixtures and Jet Fuels

Ivan C. Lee¹, Jakob J. Krummenacher², Brady Dreyer²,
and Lanny D. Schmidt²

¹ AMSRD-ARL-SE-DC
US Army Research Laboratory
2800 Powder Mill Road
Adelphi, MD 20904

And

²Department of Chemical Engineering and Materials Science
University of Minnesota
412 Washington Ave SE
Minneapolis, MN 55455

Abstract

Reformation of logistic fuels (diesel and jet fuel) has attracted a lot of attentions recently, mainly because a reformer can be integrated with fuel cells or internal combustion engines for power generation and/or emission control. Previous work in this group focused on the catalytic partial oxidation (CPOX) of a variety of heavy hydrocarbon including C8-C16. Here we will reformation results with both air and steam addition. This paper will focus on jet fuel, decane, and a binary mixture. All experiments are performed in a short contact time adiabatic reactor with a rhodium-coated monolithic catalyst. The addition of steam lowers the reformation temperature and reduces the undesired carbon deposition, while the fuel conversion remains above 90% in low fuel-to-air-ratio (i.e. syngas production regime).

Introduction

An integrated system of a fuel reformer and a fuel cell can provide portable and mobile power for battery chargers and scout vehicle silent watch. However, one of the key challenges is the hydrogen source.

The catalytic partial oxidation of heavy alkanes (C8 to C16) can produce H₂ and CO with >80% selectivities on Rh-based catalyst at short contact times operating autothermally⁽¹⁾⁻⁽³⁾. Previously, all these experiments considered reformation in dry conditions. This paper focuses on jet fuel and hydrocarbon mixtures with steam addition. Steam addition with water-to-carbon ratio (H₂O/C) of 1 simulates the condition at which the reformer utilizes the recycle steam from solid oxide fuel cells.

Experimental

Material Synthesis. The catalyst sample were Rh/alumina on ceramic alumina monolith foams. The foams (1 cm thick) were coated with 5wt% γ -Al₂O₃ to roughen the catalyst surface and increase the surface area. The monolith with wash-coats were then coated with 5wt% Rh by soaking them in Rh(NO₃)₃ solution and by calcination.

Fuel Characterization. The jet fuel sample is a military JP-8. Sulfur Analysis of the jet fuel is performed on a Agilent gas chromatography (GC) with a Ionic/ Sievers sulfur chemiluminescence detector (SCD). The total sulfur content was determined by peak area summation on the SCD chromatogram.

Catalysis and Carbon Burn-off. Since JP-8 is a hydrocarbon mixture, the conversion of JP-8 was estimated by assuming that all molecules > C8 were jet fuel reactants. This gives a lower bound to the conversion, and the actual conversion is higher than the value

reported here. Similar experiments on decane and decane-naphthalene mixture were also performed. The product gas analysis was performed with a GC.

Carbon burn-off experiment was performed after each CPOX experiment by feeding oxygen and nitrogen while the fuel and H₂O feed was shut off. The exothermic nature of the carbon burn off was recorded by changes in the catalyst bed face temperatures.

Results and Discussion

Figure 1 shows the chromatograms of a military JP-8. Area summation of sulfur peak in sulfur chromatogram indicates that the sulfur content of this jet fuel is 310ppmw.

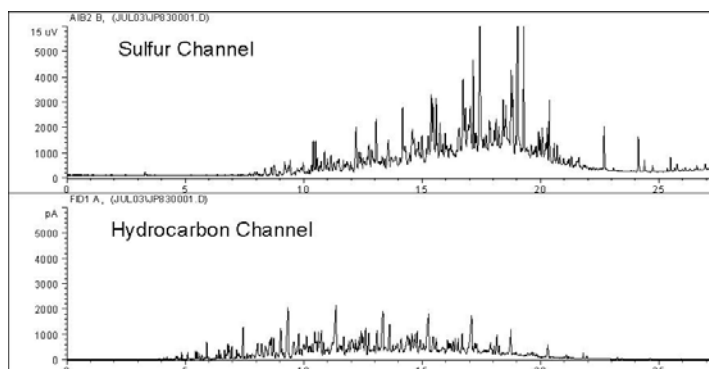


Figure 1. Analysis of a jet fuel that is being reformed in this study.

Figure 2 shows the jet fuel conversion and corresponding catalyst back face temperature at various C/O ratios. The conversion remains high at any C/O ratio when the reformer runs dry. The results also indicate that the steam addition (H₂O/C=1) lowers the catalyst back face temperature by 50 to 100 oC. At C/O = 1.3 and H₂O/C = 1.0, the catalyst back-face temperature is 770 °C and the conversion is 90%; at C/O = 1.5 and H₂O/C =1.0, the catalyst back-face temperature is 752 °C and the conversion is 65%. Apparently, catalyst temperature (as a result of steam addition) of 752°C is too low to sustain high fuel conversion.

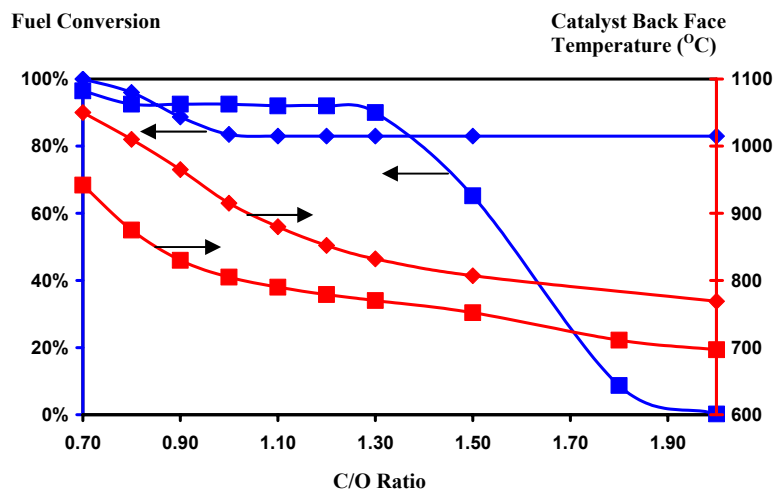


Figure 2. Fuel conversion and catalyst back face temperature of JP-8 catalytic partial oxidation. ∇ represents H₂O/C = 0, and \circ represents H₂O/C = 1.

Figure 3 shows the selectivities to syngas (H_2 & CO), combustion products (H_2O & CO_2) and olefins for the JP-8 reformation at $H_2O/C=0$. The major products at low C/O ratio are H_2 and CO . When $C/O > 1.0$, the major products are olefins. Since the preferable products for solid oxide fuel cells are H_2 and CO , one would like to run C/O of 0.7 or 0.8 for fuel cell applications.

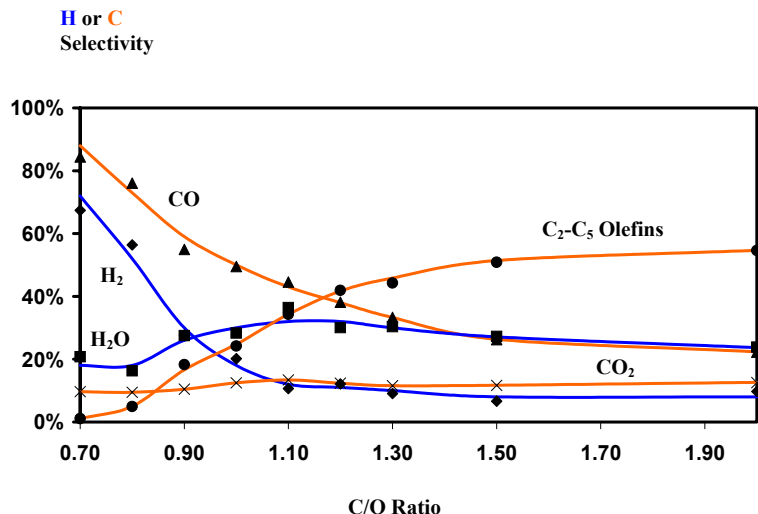


Figure 3. Product selectivities for catalytic partial oxidation of JP-8.

As aforementioned, one key benefit of steam addition is the reduction of reaction temperature. Another potential benefit is the reduction of carbon formation. Carbon burn-off results are shown in Figure 4. Smaller peak area for steam addition reformation implies less carbon formation.

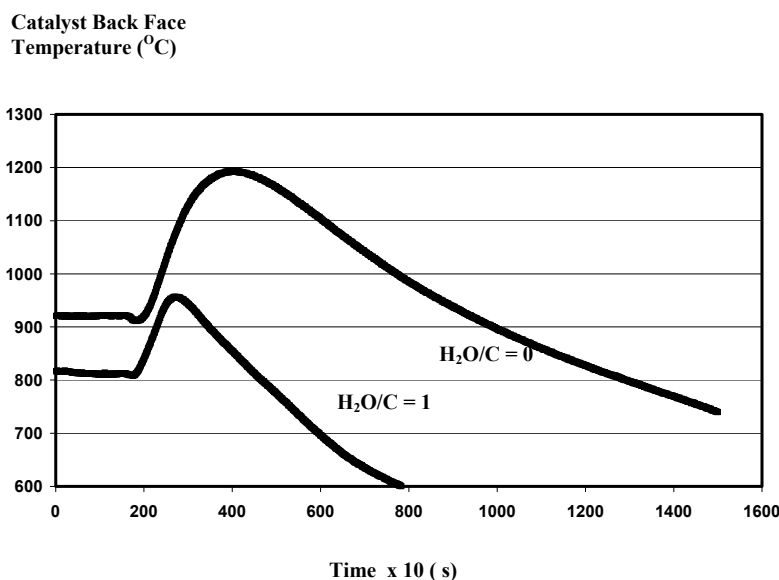


Figure 4. Carbon burn off curves (Exotherms) for JP-8 reformation at C/O ratio = 1.

Recently, Krummenacher and Schmidt have demonstrated that the selectivities of CO and H_2 formation are both above 80% ^{(1),(2)}. Here Figure 5 indicates that there is some extra hydrogen being stripped off from H_2O , which results in the hydrogen selectivity above 100%. Moreover, the CO selectivity is suppressed to 60%. This suggests that the steam addition also enhance the water-gas shift reaction.

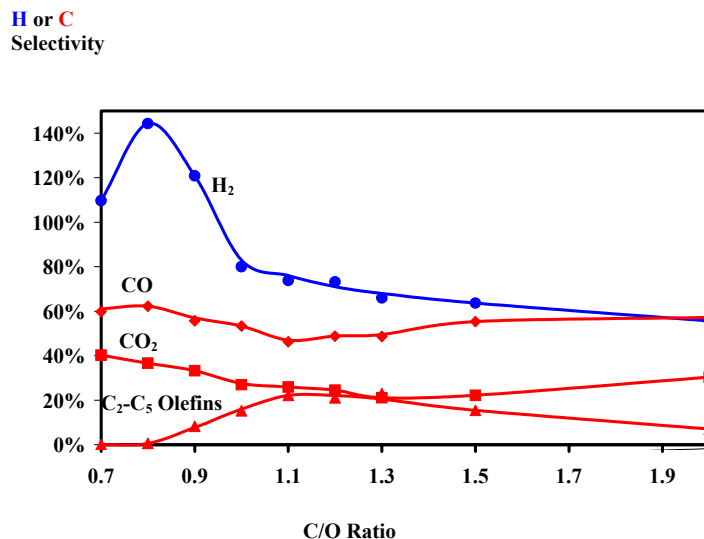


Figure 5. Product selectivities for decane reformation with steam addition ($H_2O/C=1.0$)

Additional steam addition experiments on binary mixtures such as decane-naphthalene were performed. The data analysis is underway.

Conclusions

These experiments demonstrate that a single monolithic reactor with Rh/alumina catalyst can operate under dry or steam condition. Steam addition lowers the reforming temperature and reduces the carbon formation. Low C/O ratio (0.7-0.8) favors hydrogen and carbon monoxide production. Steam addition also promotes the hydrogen production for decane reformation by stripping off hydrogen from water or by high temperature shift reaction.

Acknowledgement. This work was sponsored by the Army Research Laboratory Collaborative Technology Alliance in Power and Energy.

References

- (1) Krummenacher, J. J., West, K. N. and Schmidt, L. D., *J. Catalysis* **2003**, 215, 332.
- (2) Krummenacher, J. J. and Schmidt, L. D., *J. Catalysis*, accepted.
- (3) Subramanian, R., Panuccio, G.J., Krummenacher, J. J., Lee, I. C. and Schmidt, L.D., *Chem. Eng. Sci.*, accepted

LOGISTIC FUEL TO HYDROGEN - FUEL PROCESSING USING MICROFIBROUS ENTRAPPED CATALYSTS AND SORBENTS FOR PEM FUEL CELL

Mukund Karanjikar, Bong-Kyu Chang, Yong Lu, Bruce Tatarchuk

Department of Chemical Engineering
Auburn University
Auburn, AL 36849

Introduction

Fuel cells offer a unique way to convert chemical energy of a fuel directly into electrical energy and is a renewable resource. Unlike most other fuel cell types, Polymer Electrolyte Membrane Fuel Cells (PEMFC) are suitable for small, low power applications. These can be scaled down to small size without sacrificing performance and are suitable for applications ranging from microwatts to hundreds of kilowatts. Other advantages are low noise signature, pure water as by-product and the ability to refuel rather than recharge or discard. PEMFC are preferred in many applications like mobile power generation units, man-portable power generators and on-board power generation for automotive propulsion.

The bandwidth requirement for new electronic appliances demands more energy density than the existing batteries can offer (1). Due to the high cost of primary batteries and the large weight of rechargeable batteries, fuel cell technology is being developed to provide a power source for the individual soldier, sensors, communication equipment and other various applications in the United States army (2).

PEMFC require hydrogen as a fuel to generate electricity. Hydrocarbon reforming is widely regarded as the best means of hydrogen generation for PEM Fuel Cells.

Various fuels such as methane, methanol, ethanol, gasoline, diesel and JP8 are being considered for fuel cell applications. Diesel and JP8 have salient advantages over other fuels mainly high energy density, safe handling and logistics (3).

Present work deals with development of a bread-board fuel processor for JP8 fuel. The fuel processor has its main components to be reformer, post-reformer, H_2S removal, water gas shift, carbon dioxide removal, preferential oxidation and fuel filter units. Most of these units contain microfibrous entrapped catalysts and sorbents. Microfibrous materials is a new class of proprietary materials that offer advantages such as high contacting efficiency, very low pressure drop and efficient thermal management over conventional packed bed approach thereby making the whole processor very compact (4).

Experimental

Experimental Set-up. Figure 1 shows the schematic process flow diagram of the fuel processor. First reactor is steam reformer for JP8 fuel the outlet of which flows into post-former followed by H_2S removal reactor through intermediate gas storage tank by means of a compressor. After H_2S removal the reformat flows into high temperature water gas shift and low temperature water gas shift reactors followed by preferential oxidation of CO reactor. The reformat then flow through carbon dioxide removal absorption tower that has continuous circulation of alkaline absorbent. The reformat finally flows through fuel filter unit to remove trace quantities of all gases other than hydrogen before entering fuel cell.

Catalysts and Sorbents. Catalysts for reformer, post-former (precious metal) and water gas shift reaction (Fe-Cr and Cu-Zn) were obtained commercially from Sud-chemie Inc. Sorbent used for H_2S removal was a microfibrous entrapped ZnO sorbent. The liquid sorbent used for CO_2 removal was alkaline solution. The solid sorbent in the fuel filter for CO_2 removal was microfibrous entrapped lime based sorbent. The PROX catalyst was a microfibrous entrapped metaloxide promoted precious metal catalyst (5). The fuel filter had microfibrous entrapped sorbents for CO, CO_2 , NH_3 and H_2S .

Preparation of Catalysts and Sorbents. The microfibrous entrapped catalysts and sorbents are prepared by wet-lay process followed by sintering at high temperature in presence of hydrogen. D. Cahela and B. Tatarchuk (6) discuss the process in details. This gives the support material for the catalyst /sorbent. The final catalysts/sorbents were prepared using conventional incipient wetness method followed by calcination in air. Figures 2 shows SEM image of microfibrous entrapped PROX catalyst.

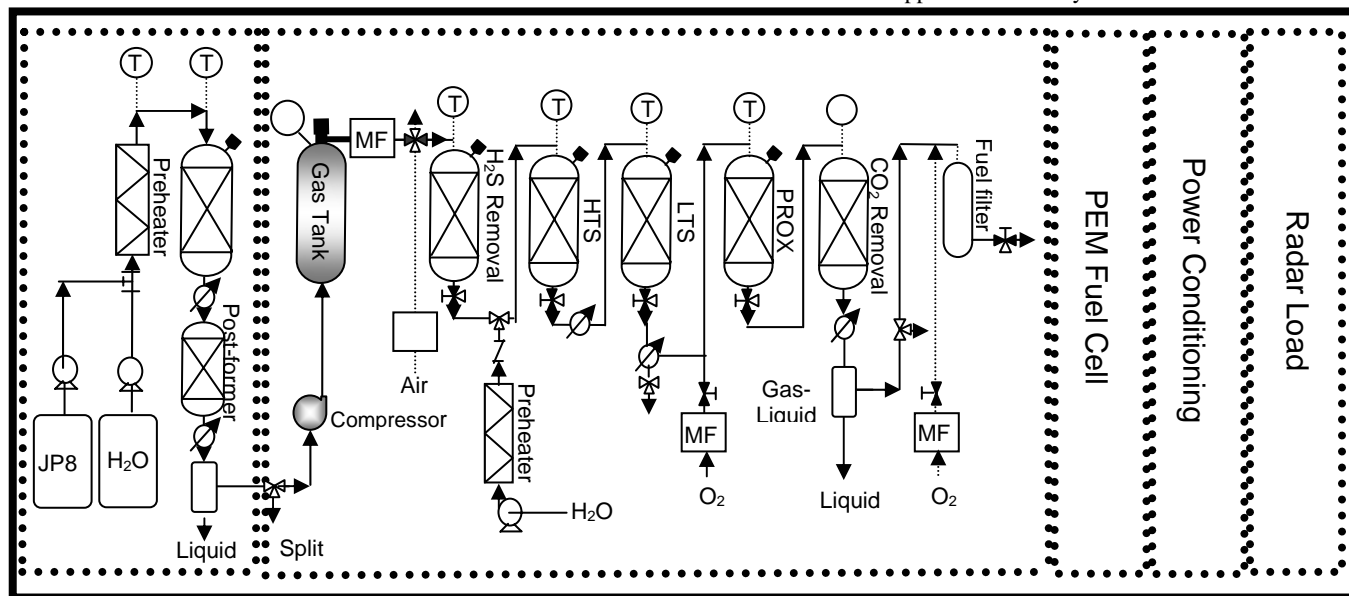


Figure 1. Process Flow Diagram of Fuel Processor Unit

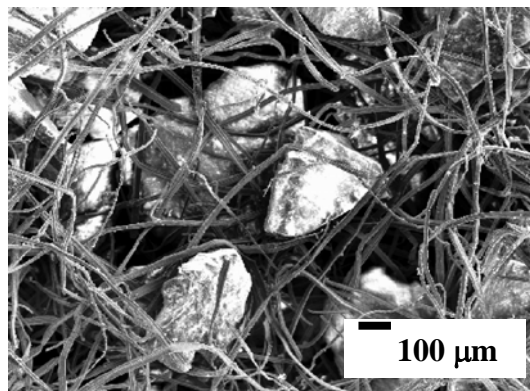


Figure 2. SEM of PROX catalyst support

Results and Discussion

Reformer and Post-former. The steam reforming of JP8 at 900°C and atmospheric pressure over the commercial catalyst gives reformat with composition 60 – 65% H₂, 18-22% CO₂, 8-12% CO, 5 – 12% C₁-C₃ and around 60 ppm H₂S. Post-former reduces the light hydrocarbons to below detection limits. The reforming and post-forming catalyst is sulfur tolerant hence the sulfur removal phase was employed after these stages.

Hydrogen Sulfide Removal. This section of the processor implements polishing sorbent concept. A composite bed consisting of the packed bed of 1-2mm Sud-Chemie ZnO extrudates followed by the above mentioned microfibrous entrapped ZnO/SiO₂ sorbent particulates has been demonstrated for H₂S removal from H₂ fuel stream. Figure 3 shows the breakthrough curves for 2vol% H₂S challenge in H₂ in single and composite beds at 400°C and a face velocity of 1.2cm/s (30mL(STP)/min dry gas flow rate). Two single beds, 7mm(dia.)×3mm(thick) microfibrous entrapped ZnO/SiO₂ (A) and 7mm(dia.)×7mm(high) packed bed of 1-2mm Sud-Chemie ZnO sorbent extrudates (B), provided breakthrough times (@ 1ppmv H₂S detection limit) of 5min and 28min, respectively. The breakthrough curve with small particulates (ZnO/SiO₂) alone is very sharp. But the breakthrough curve in packed bed with large particulates (B) is very sigmoidal. When the polishing sorbent was placed behind the packed bed (B+A), the outlet from the packed bed B, where the H₂S concentrations increased very slowly with the time on stream after the breakthrough point in bed B, was encountered immediately with the high contacting efficiency polishing sorbent A. As a result, a very large extension in gas life was obtained due to high contacting efficiency, compared to that either the polishing sorbent or the packed bed alone will do.

For this demonstration, 60 ppm H₂S in real reformat is reduced to less than 0.6 ppm at the outlet at 400°C and 30% water content.

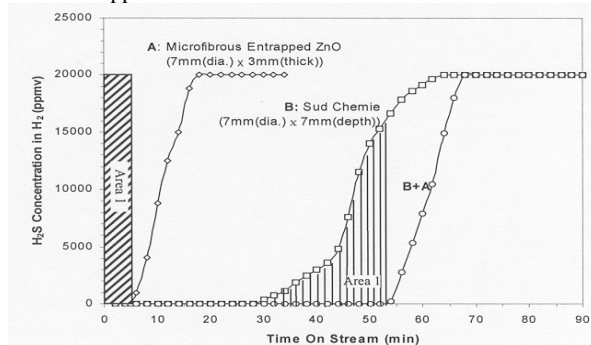


Figure 3. H₂S Adsorbent performance

Water Gas Shift Reactions. High temperature and low temperature water gas shift reactions operate respectively at 350 -400 and 180 -200 °C and atmospheric pressure. The inlet CO concentration of 10 -15% is reduced to around 0.75 - 1% in presence of microfibrous entrapped catalysts.

PROX Stage. The PROX reactor operates at 180 – 200 °C and atmospheric pressure. The carbon monoxide content is reduced to less than 10 ppm at the exit of the reactor.

Figure 4 compares the performance of microfibrous entrapped catalyst with pellets of the size 1.5 – 2.5 mm.

CO₂ Removal Section. The absorption in alkaline solution reduces the CO₂ content from 35% to about 200 ppm at the outlet. The absorption unit is operated in a continuous circulating fashion.

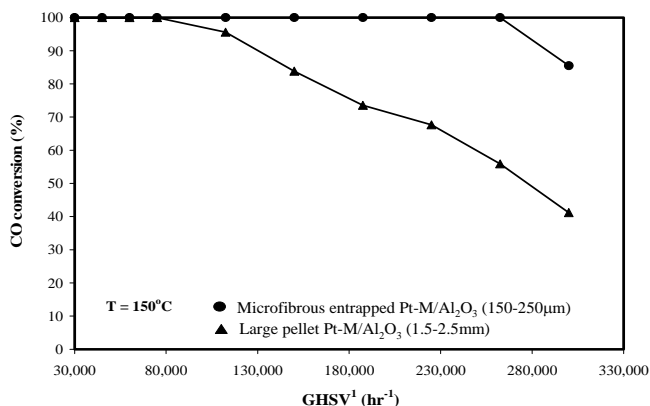


Figure 4. Comparison of microfibrous entrapped PROX catalyst with pellets

Fuel Filter Section. All the ppm level gases such as H₂S CO, CO₂, NH₃ and organic vapors are removed by means of various microfibrous entrapped sorbents. This unit operates at room temperature and atmospheric pressure.

Conclusion

1. Logistical fuel to radar power is possible by means of a fuel processor followed by PEM fuel cell.
2. Traditional processes are applicable for reformat clean-up processing technologies can be reduced in weight and volume by means of new materials such as microfibrous entrapped sorbents and catalysts and regenerable continuous – batch operation.
3. With additional process integration, mainly energy, the fuel processor can become an attractive means of hydrogen generation.

Acknowledgment. The financial support of SMDC – SMDTC is gratefully acknowledged.

References

1. C.K.Dyer, *J Power Sources*, 4675 (2000), 1-4
2. A.S. Patil, *Proceedings of 32nd Intersociety Energy Conversion Engineering Conference*, (1997) 793-795
3. C. Pereira, J-M. Bae, S. Ahmed, M. Krumpelt, *DOE Hydrogen Program Annual Review*, May 9, 2000, San Ramon CA
4. D Harris, D Cahela, B Tatarchuk, *Composites Part A*, 32, (2001)1117-1126
5. B.K. Chang, B. J. Tatarchuk, *Prepr. Pap. – Am. Chem. Soc., Div. Fuel. Chem*
6. D. Cahela and B. Tatarchuk, *Catalysis Today*, 69(2001) 33-39

HYDROGEN PRODUCTION FROM BIOMASS FEEDSTOCKS

Hyun-Seog Roh, David L. King, and Yong Wang*

Pacific Northwest National Laboratory, P.O. Box 999, Richland, WA 99352, USA

Introduction

Hydrogen attracts significant research interests because it is a clean fuel emitting only water without formation of greenhouse gases. Commercially, hydrogen has been produced from catalytic steam reforming of fossil fuels, for example, methane.¹ To reduce greenhouse gas emissions, the hydrogen should be derived from renewable energy sources such as bio-ethanol.²⁻⁴ As a consequence, ethanol steam reforming has been studied, which gives potential alternative to hydrogen production.^{4,5} For the purpose of H₂ production as a fuel in molten carbonate fuel cell (MCFC), ethanol steam reforming has been studied at the temperature range of 600 – 700°C, which is the operating temperature of anode in MCFC.⁶⁻⁸ As for a steam/ethanol ratio, most researchers employ more than 8 to avoid carbon formation.⁷⁻⁹

In this paper, we have tested various supported Rh catalysts and the effects of metal composition, promoter, and support on the selectivity to intermediates, hydrogen, and CO/CO₂ were evaluated. For comparison, micro-channel reactor was employed at low temperatures (350 – 500°C) with a stoichiometric feed ratio (H₂O/EtOH = 3.0) to examine the benefits of efficient heat and mass transport comparing with conventional quartz tube reactor.

Experimental

Support materials employed in this study were γ -Al₂O₃ (99%, SASOL), ZrO₂ (99%, MEL Chemicals), and CeO₂-ZrO₂ (CeO₂: 17.5%, MEL Chemicals). The supports were pre-calcined at 800°C for 6 h in air. Supported Rh catalysts were prepared by the incipient wetness method using its nitrate source. In some cases, Pt was co-impregnated with Rh. The catalyst samples were calcined at 600°C for 6 h in air.

Catalytic activity measurements were conducted in a fixed-bed micro-tubular quartz reactor with an inner diameter of 4 mm at atmospheric pressure. Special cares were taken to eliminate the potential mass and transport limitations. SiC was employed as a diluent in a micro-tubular quartz reactor, otherwise stated. For comparison, catalytic performance was also tested in a micro-channel single reactor having a gap of 0.75 mm, which is a much shorter transport distance as compared to that in a micro-tubular reactor. Thermocouples were placed strategically throughout the reformer system. Prior to each catalytic measurement, the catalyst was reduced in H₂/N₂ (10% H₂ in vol.) at 350°C for 1 h. A stoichiometric steam to ethanol ratio of 3 and a weight hourly space velocity (WHSV) of 75,660 cm³/g cat/hr were used in all experiments. The mixture of ethanol and water was fed using a syringe pump and was vaporized at 250°C in the vaporizer.¹⁰ The reformat was chilled, passed through a ice-trap to condensate residual water and ethanol, and then flowed to the on-line gas chromatograph (GC) for analysis. The GC was a micro-GC (Agilent) and GC columns used in this study were Molesieve 5A and Poraplot Q.

Results and Discussion

A thorough literature search on ethanol steam reforming indicates that the Rh based catalysts are most active, and ethanol steam reforming mechanisms are complex.^{4,5,7-9} Cavallaro assumes

that the ethanol is converted during the first stage into ethylene by dehydration or into acetaldehyde by dehydrogenation.¹¹ The acetaldehyde easily undergoes decarbonylation to form CH₄ and CO.

First, we studied the effect of support on product distribution. Ethanol conversion is relatively independent on Rh loading (over 3wt%) while methane selectivity increases with Rh loading. It is most likely that acidic supports favor the ethylene formation over methane formation. The ethylene selectivity over Rh/Al₂O₃ catalysts with various Rh loading is summarized in Table 1.

Table 1. Ethylene Selectivity with Temperature over Rh/Al₂O₃ Catalysts

Temp. (°C)	1%Rh	3%Rh	6%Rh	10%Rh
500	0.73	0.69	0.59	0.46
550	0.46	0.45	0.34	0.22
600	0.14	0.12	0.00	0.00
650	0.00	0.00	0.00	0.00

1%Rh catalyst showed higher than 70% ethylene selectivity at 500°C. The ethylene selectivity decreases with reaction temperature due to the fact that ethylene steam reforming is favorable at higher temperatures. It is also clear that the ethylene selectivity decreases with Rh loading. This is possibly due to the fact that the portion of Al₂O₃ in the catalyst decreases with Rh loading. In addition, the effects of support were also studied. 10%Rh/ZrO₂ showed 12% ethylene selectivity at 500°C, while 10%Rh/CeO₂-ZrO₂ exhibited no ethylene formation at the same condition. Instead, 10%Rh/CeO₂-ZrO₂ showed 43% CH₄ selectivity. Under the same condition, the selectivities to CH₄ over 10%Rh/ZrO₂ and 10% Rh/Al₂O₃ were 15% and 3%, respectively.

Table 2 summarizes the effect of Pt promotion on 3%Rh/CeO₂-ZrO₂ catalyst at 450°C.

Table 2. Promotion Effect of Pt on 3%Rh/CeO₂-ZrO₂ Catalyst at 450°C

Catalyst	X _{EtOH}	S _{CO}	S _{CO2}	S _{CH4}
3%Rh3%Pt	1.00	0.08	0.38	0.53
3%Rh	0.74	0.57	0.12	0.30

The addition of Pt to Rh based catalysts results in enhanced ethanol conversion. In addition, Pt plays a role in decreasing CO selectivity and enhancing both the formation of CH₄ and CO₂. The increased CH₄ selectivity is possibly due to the enhanced decarbonylation of CH₃CHO.¹¹ The increase of CO₂ selectivity is mainly due to the beneficial effect of CeO₂ to increase water gas shift reaction.

In order to demonstrate the potential advantages of microchannel reactors, a 3%Rh3%Pt/CeO₂-ZrO₂ catalyst was compared in both a micro-channel reactor and a conventional micro-tubular reactor. Here, micro-channel reactor has a gap of 0.75 mm, which is a much shorter transport distance as compared to that in a micro-tubular reactor with an inner diameter of 4 mm. To demonstrate the benefits of micro-channel reactor, the catalyst packed in the micro-channel reactor was not diluted with inert materials. In the case of micro-tubular quartz reactor, catalyst tests were executed both with and without catalyst dilution. The comparison of reaction results at 400°C are summarized in Table 3. Comparing the results of diluted quartz reactor with undiluted one, the former exhibited higher ethanol conversion than the latter. This is due to the enhanced heat transfer in the presence of SiC as diluents. The product distribution is similar to each other. As a result, the

* Corresponding author: yongwang@pnl.gov

hydrogen produced per ethanol fed of diluted quartz reactor is higher than that of undiluted one. At the same temperature, the ethanol conversion was 99% using micro-channel reactor but less than 80% with the undiluted quartz reactor. This clearly shows the benefit of micro-channel reactor in ethanol steam reforming. In another word, similar hydrogen productivity can be achieved in a microchannel reactor at a lower temperature. Lower temperature operations can directly translate into potential energy savings. In addition, the CO selectivity was decreased by employing micro-channel reactor resulting in high CO₂ selectivity.

Table 3. Comparison of Reaction Results on 3%Rh3%Pt/CeO₂-ZrO₂ Catalyst at 400°C

Reactor	X _{EtOH}	S _{CO}	S _{CO2}	S _{CH4}	H ₂ /EtOH
Micro-channel	0.99	0.33	0.25	0.40	2.10
Quartz (diluted)	0.97	0.44	0.11	0.44	1.65
Quartz (undiluted)	0.76	0.45	0.10	0.43	1.31

The CH₄ selectivity of micro-channel reactor was also slightly lower than those of quartz reactor with or without diluents. The reduced heat transfer distance was anticipated to be beneficial to the endothermic ethanol steam reforming.¹⁰ Therefore, it is not surprising to see that the micro-channel reactor outperforms the micro-tubular reactor in terms of hydrogen productivity under the identical reaction conditions.

Table 4 shows the hydrogen produced per mole ethanol fed which are dependent on the reactor-type and reaction temperature.

Table 4. H₂/EtOH Depending on Reactor-Type with Reaction Temperature over 3%Rh3%Pt/CeO₂-ZrO₂ Catalyst

Reactor	350°C	400°C	450°C	500°C
Micro-channel	1.25	2.10	2.64	2.64
Quartz (diluted)	0.92	1.65	1.86	2.32
Quartz (undiluted)	0.79	1.31	1.73	2.29

The H₂/EtOH typically increases with reaction temperature because ethanol steam reforming is thermodynamically favorable at higher temperatures. However, it is clear that the productivity of H₂ is strongly dependent upon the reactor-type within the temperature range tested in this study. It should be noted that the productivity of H₂ at 450°C in the micro-channel reactor is even higher than that of 500°C with the quartz reactor regardless of the presence of diluents.

Conclusions

Ethanol steam reforming follows either dehydration to form ethylene or dehydrogenation to form CH₃CHO resulting in decarbonylation to form methane pathways. Acidic supports favor the ethylene formation over methane formation. Ethanol conversion is relatively independent on Rh loading (over 3wt%) while methane selectivity increases with Rh loading. Non acidic supports, such as CeO₂-ZrO₂, favors methane formation. Addition of Pt to Rh based catalysts increases both the formation of methane and CO₂ via water gas shift reaction. The micro-channel reactor outperforms the micro-tubular reactor in terms of hydrogen productivity under identical

reaction conditions over 3%Rh3%Pt/CeO₂-ZrO₂ catalyst due to the reduced heat transfer distance, which is beneficial to the endothermic ethanol steam reforming.

Acknowledgement. This work was supported by Department of Energy's Office of Hydrogen, Fuel Cells, and Infrastructure Technologies. Most of work was performed in the Environmental Molecular Science Laboratory, a national scientific user facility sponsored by the U.S. Department of Energy's Office of Biological and Environmental Research and located at Pacific Northwest National Laboratory in Richland, WA.

References

- (1) Rostrup-Nielsen, J. R. In *Catalysis, Science and Technology*; Anderson, J. R, Boudart, M., Eds; Springer: Berlin, 1984; Vol. 5.
- (2) Huber, G. W.; Shabaker, J. W.; Dumesic, J. A. *Science* **2003**, *300*, 2075.
- (3) Cortright, R. D.; Davda, R. R.; Dumesic, J. A. *Nature* **2002**, *418*, 964.
- (4) Deluga, G. A.; Salge, J. R.; Schmidt, L. D.; Verykios, X. E. *Science* **2004**, *303*, 993.
- (5) Liguras, D. K.; Kondarides, D. I.; Verykios, X. E. *Appl. Catal. B* **2003**, *43*, 345.
- (6) Cavallaro, S.; Freni, S. *Int. J. Hydrogen Energy* **1996**, *21*, 465.
- (7) Freni, S. *J. Power Sources* **2001**, *94*, 14.
- (8) Cavallaro, S.; Chiodo, V.; Freni, S.; Mondello, N.; Frusteri, F. *Appl. Catal. A* **2003**, *249*, 119.
- (9) Diagne, C.; Idriss, H.; Kiennemann, A. *Catal. Commun.* **2002**, *3*, 565.
- (10) Palo, D. R.; Holladay, J. D.; Rozmiarek, R. T.; Guzman-Leong, C. E.; Wang, Y.; Hu, J.; Chin, Y.-H.; Dagle, R. A.; Baker, E. G. *J. Power Sources* **2002**, *108*, 28.
- (11) Cavallaro, S. *Energy and Fuels* **2000**, *14*, 1195.

Hydrogen Production from Ethanol Using Low Energy Pulse Discharge at Ambient Temperature

Y. Sekine, M. Matsukata, E. Kikuchi, S. Kado*, F. Haga**

Department of Applied Chemistry, School of Engineering and Science, Waseda University, Tokyo, Japan

*Department of Mechanical Engineering and science, Tokyo Institute of Technology, Tokyo, Japan

**Nissan, Yokosuka, Kanagawa, Japan

Introduction

Recently fuel cell is attracting attention. Especially, Polymer Electrolyte Membrane Fuel Cell (PEMFC) is one of the candidates. Because it is operated lower temperature than that of other fuel cell, and it has high performance in energy efficiency. Other reasons, clean exhaust gases, small size, light weight, fast start-up, rapid response and so on are also worthy of remark. So PEMFC is expected to serve as a fuel cell vehicle (FCV) and a home cogeneration system. But recent considerable Hydrogen production and transportation processes have many problems with the present technology (for example, The transportation and storage of Hydrogen), so it is need to research innovative technological methods to produce Hydrogen. So, we applied low energy pulse (LEP) discharge for this purpose. If LEP discharge used for reforming, reactions can be achieved at room temperature and atmospheric pressure. On the other hand, ethanol has a potential for being an alternative fuel replacing fossil fuels because ethanol can be produced from various renewable sources. So we tried to unify a supply and storage system with using liquid fuel (ethanol and water solution) and LEP discharge. And it was also attempted to design much smaller reformer, and improve energy efficiency.

Experimental

Figure 1-(a) shows our previous fuel delivery system. No catalyst was used, and argon was used as carrier gas. Gap distance of electrodes was fixed at 2.1 mm. Our previous reformer was flow type reactor, and the mixture of ethanol and water was supplied by chemical pump, and evaporated at 413 K. The reaction temperature was set at 393 K to prevent condensation into liquid.

On the other side, Figure 1-(b) shows our novel system. The bottom of carbon fiber bundle was soaked in ethanol solution contained in a small bottle. Present reformer was so attractive, because it was no need of heaters or pumps at all. This reformer used carbon fiber bundle as electrode. The solution could be pumped up to the top of the carbon fiber bundle by capillary action and supplied into discharge region. And, liquid fuel was evaporated by Joule heat which generate from internal resistance of electrode. The supplied fuel amount was controlled by the length and number of carbon fibers. The amount became larger in proportion to fiber length and fiber number. And the supplying fuel amount into the discharge region was about 30 cc min⁻¹, when the length was 7 cm and the number of carbon fiber was 84,000.

And a DC power supply (Matsusada precision inc. HARB-40R30) was used to produce the non-equilibrium pulsed discharge. All products were analyzed using a gas chromatography equipped with FID and TCD (Shimadzu GC14-B). The waveforms of current and voltage were observed by a digital signal oscilloscope (DSO):(Lecroy 9314C).

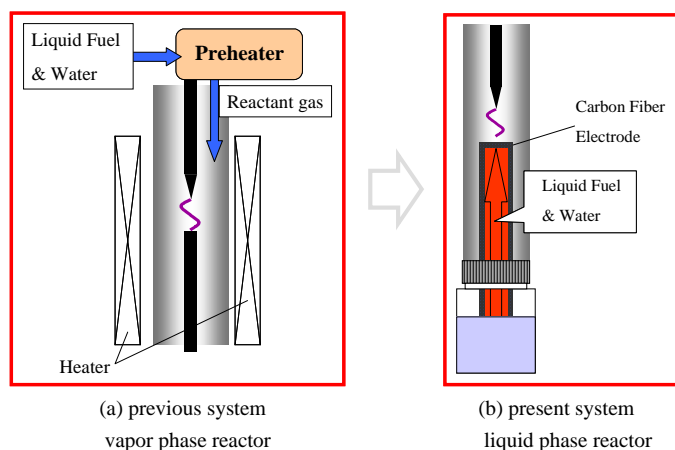


Figure 1. Schematic diagram of previous and present fuel delivery system to discharge region.

Results and Discussion

1) **Comparison of the vapor phase reaction and the liquid phase reaction.** Here, steam reforming of ethanol proceeded and hydrogen obtained as a main product. In addition to hydrogen, gases such as carbon monoxide, carbon dioxide, C₂ compounds (mainly acetylene) and methane were produced. And the amount of produced gas increased in proportion to the increase of the gap distance of electrodes. But there is no influence of the gap distance of electrodes on the selectivity to product. So we discussed difference of H₂ formation rate before and after improvement. It was shown in Figure 2. They showed almost same trends. So the discharge energy loss in case of vapor phase reactor was partly utilized to vaporize ethanol solution in the case of liquid phase reactor. Moreover, it was possible to lessen the size of the reformer compact, and make the process more efficient, because of the needless to install such equipments as heaters to evaporate liquid fuel.

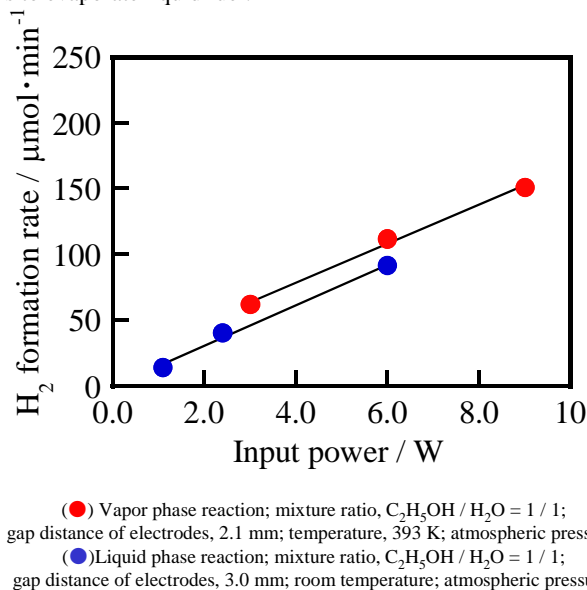
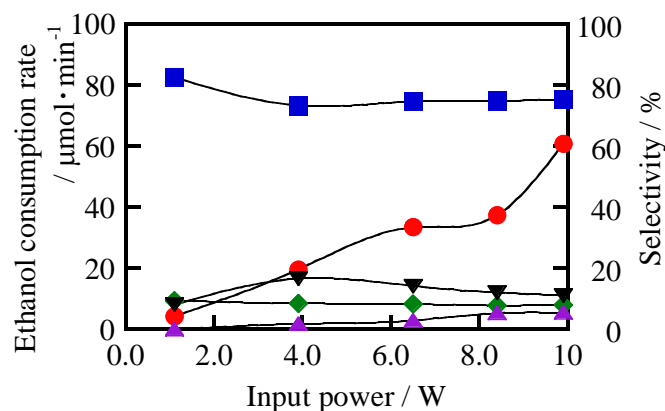


Figure 2. Comparison of previous and present reaction system

2) **Effect of input power.** In this section, we investigated effect of input power on ethanol consumption rate and carbon selectivity. The results of ethanol consumption rate and carbon selectivity are plotted against the input power in Figure 3. As shown in Figure 3, carbon selectivity was almost stable under any conditions.



(●) ethanol consumption rate, (■) CO Sel., (◆) CH₄ Sel., (▲) CO₂ Sel., (▼) C₂ Sel.
Conditions; mixture ratio, C₂H₅OH / H₂O = 1 / 1;
gap distance of electrodes, 3.0 mm; room temperature; atmospheric pressure.

Figure 3. Effect of input power on ethanol consumption rate and on Carbon selectivity.

3) Effect of concentration of C₂H₅OH and H₂O. In this section, we investigated effect of concentration of ethanol and water. At first, H₂ and O₂ were not generated when H₂O concentration was 100 %. So the reaction of water electrolysis did not advance. Next, at the decomposition reaction of ethanol 100 %, small amount of carbon deposition were gradually formed, and it caused destabilization to stop the discharge. So the discharge couldn't be kept stable for a long time. On the other hand, when the reaction was handled in the case of steam reforming (0 < ethanol concentration < 100), the discharge could be stabilized for a long time and could be continued in steam reforming without stopping the reaction.

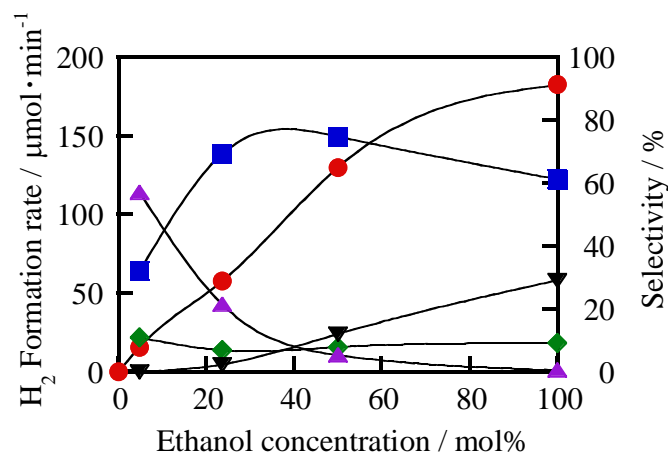
Figure 4 showed the results. The larger ethanol concentration is, the more produced H₂. And higher ethanol concentration field, C₂ selectivity was rather high (it was about 30 %), compared to that of lower ethanol concentration field. So it seems to say that the reaction of which ethanol concentration is from 20 to 50 mol % is the highest efficiency at a present stage. Because C₂ selectivity was not high, and carbon deposition was not observed.

4) Calculating result of Energy efficiency. Input power was regarded as the power consumption in the discharging space. And it was calculated from integration value which is current multiply by voltage, picked up from the waveforms of the oscilloscope. Here, input power (E_i) was calculated based on the following formula.

$$E_i = \sum_i \left\{ (v_i + v_{i+1}) / 2 \right\} \times \left\{ (c_i + c_{i+1}) / 2 \right\} \times (t_{i+1} - t) \times f \quad (1)$$

On the other hand, output power was regarded as the difference of the standard enthalpy of formation between the amount of liquid fuel converted and the amount of compounds formed. Finally energy efficiency was calculated by making output power into the numerator and by making input power into the denominator.

And, if it's supposed that input and output power were calculated such way, energy efficiency was 41.7 % at the ethanol concentration of 50 %, the gap distance of electrode 3.0 mm. The efficiency in this experiment was exceeding that of the former way. Furthermore, this reformer has a potential to improve the efficiency by controlling Voltage and Current system.



(●) ethanol consumption rate, (■) CO Sel., (◆) CH₄ Sel., (▲) CO₂ Sel., (▼) C₂ Sel.
Conditions; input current 7.0 mA, gap distance of electrodes,
3.0 mm; room temperature; atmospheric pressure.

Figure 4. Effect of ethanol concentration on H₂ formation rate and on Carbon selectivity.

Conclusions

We succeeded in improving the energy efficiency because the liquid phase reactor does not require a heater which is needed to vaporize the mixture of water and ethanol. Moreover any pump supplying the liquid into the reactor was not required. So the liquid phase reactor made the process scale reduced, and also made the device size compact without spoiling its function. Therefore, if the controlling Voltage and Current system makes more progress, we consider that this process would be very useful for room temperature hydrogen formation system.

References

- (1) Kado, S., Y. Sekine and K. Fujimoto, ; "Direct synthesis of acetylene from methane by direct current pulse discharge" Chem Commun., 1999, 24 2485.
- (2) Kado, S., K. Urasaki, Y. Sekine and K. Fujimoto, ; " Low temperature reforming of methane to synthesis gas with direct current pulse discharge method" Chem. Commun., 2001, 5 415.
- (3) Martin K., B. Eliasson, U. Kogelschatz and A. Wokaun,; " CO₂ reforming of methane by the combination of dielectric-barrier discharge and catalysis," Phys. Chem. Chem. Phys., 2001, 3, 294-300.
- (4) Nozaki, T., Y. Miyazaki, Y. Unno and K. Okazaki, ; "Energy distribution and heat transfer mechanisms in atmospheric pressure non-equilibrium plasmas" J. Phys. D: Appl. Phys. 34 (2001) 3383-3390.
- (5) Nozaki, T., Y. Unno and K. Okazaki, ; "Thermal structure of atmospheric pressure non-equilibrium Plasmas" Plasma Source Sci. Technol. 11 (2002) 431-438.
- (6) Sekine, Y., K. Urasaki, S. Kado, M. Matsukata, and E. kikuchi, ; " Nonequilibrium Pulsed Discharge: A Novel Method for Steam Reforming of Hydrocarbons or Alcohols" Energy Fuels, 2004, 18, 455-459.
- (7) S.L. Yao, M. Okumoto, A.Nakayakma and E. Suzuki, ; " Influence of Rise Time of Pulse Voltage on the Pulsed Plasma Conversion of Methane," Energy Fuels, 2001,15,1295.
- (8) Wonihl C., Y. beak, S. Moon, Y. C. Kim, ; "Oxidative coupling of methane with microwave and RF plasma catalytic reaction over transitional metals loaded on ZSM-5," Catal. Today 74 (2002) 207-223.

SOLID OXIDE FUEL CELL COMBUSTIBLE BY PLASMA SPOUTED BED GASIFICATION OF GRANULATED BIOMASS

Jerzy W. Jurewicz, Alan Lemoine

CREPE – Centre de Recherche en Énergie, Plasma et Électrochimie
Université de Sherbrooke,
Sherbrooke, Québec, Canada J1K 2R1

Introduction

In the search for both the most suitable and efficient methods of biomass gasification, the plasma spouted bed reactor, already tested^(1,2) in this application exhibits, among other benefits, high transformation rates for solids to gases and the absence of tarry by products. This short report is a statement on our continuing research program and describes the most recent results where the research effort has been concentrated on process efficiency issues, including determining mass and energy balances.

Experimental

Raw Materials. The properties of the canola used as the raw material, were as follows: average grain size ≈ 1.5 mm, the moisture content of ≈ 8 %, ultimate analysis: mass composition of 56.43 ! 1 % carbon, 8.76 ! 0.2 % hydrogen, 23.43 ! 0.5 % oxygen, 7.34 ! 0.15 % nitrogen, 3.75 ! 0.1 % ash and traces of sulphur < 0.3 % and chlorine < 0.1 %. The heating value using the Dulong formula amounts to 28.23 MJ/kg.

Apparatus. The pyrolytic gasification tests were performed in an atmospheric-pressure bench scale plasma spouted bed apparatus (Fig. 1).

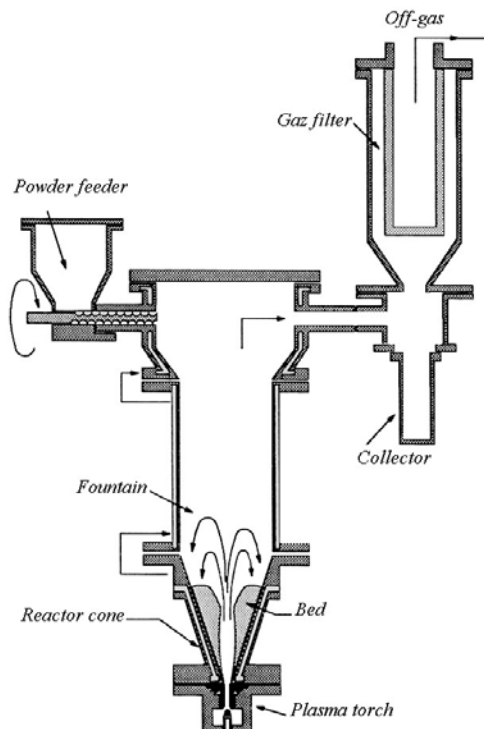


Figure 1. The schematic of the plasma spouted bed apparatus used in this study.

The stainless steel reactor, comprised a 150 mm cylindrical chamber part fitted to a conical (40°) base, protected with a thermal barrier ZrO_2 coating on the inside, and coupled with a standard DC plasma torch. The carbon dioxide was injected through three orifices at the periphery of the 4 mm torch nozzle. The seeds material was screw fed into the reactor from the sealed top.

Results and Discussion

Series of tests were performed to determine the effect of plasma power and injected carbon dioxide flow rate on product gas yield, its composition and overall energetic efficiency of the process.

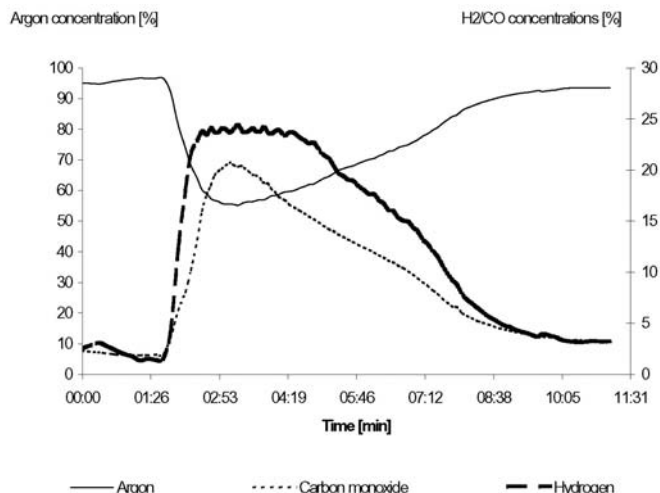


Figure 2. The variation of the off-gas composition during experiment for non-reactive plasma (without carbon dioxide).

Table 1. The Distribution of Solids (By Size Fraction) Remaining After the Run for Injected Power of 4,69 kW (% of Initial Load).

Size fraction ③m	Reactor		Collector	Filter	Total
	Bottom	Walls			
$d_p > 425$	4,59	1,51	1,00	0,87	7,97
$425 > d_p > 212$	0,79	1,21	1,70	2,94	6,64
$212 > d_p > 150$	0,23	0,70	0,39	1,64	2,97
$150 > d_p > 125$	0,14	0,71	0,21	1,84	2,89
$125 > d_p > 90$	0,12	1,28	0,25	0,82	2,47
$90 > d_p > 45$	0,09	2,11	0,25	0,37	2,82
$45 > d_p$	0,00	1,50	0,08	0,00	1,59
Total	5,96	9,03	3,88	8,49	27,35

Due to the appreciable variation in off-gas composition for various applied plasma powers related to the different rate of pyrolysis for the input volatile matter (Fig.2), the total volume of gases produced for each pyrolytic gasification run was chosen as the mean for making comparison between the different runs (Table 2a,b,c). Time period of each experiment: 450 seconds.

Table 2a. Total Volume of Gas Produced per Gram of Canola Consumed During Complete Run for Injected Power of 3,58 kW.

Gas	Volume of gas produced per gram of canola consumed (L/g)			
	Spouting gas composition			
	Ar (plasma gas)	CO ₂ Flowrate (Lpm)		
	30 Lpm	2,5	5	10
H ₂	0.33	0.28	0.24	0.19
CO	0.16	0.26	0.37	0.46
CH ₄	0.02	0.15	0.017	0.016
CO ₂	0.03	-	-	-
C ₂ H ₄	0.03	0.03	0.03	0.03
C ₂ H ₂	0.13	0.08	0.08	0.06
Total	0.7	0.8	0.74	0.76

Table 2b. Total Volume of Gas Produced per Gram of Canola Consumed During Complete Run for Injected Power of 4,69 kW.

Gas	Volume of gas produced per gram of canola consumed (L/g)			
	Spouting gas composition			
	Ar (plasma gas)	CO ₂ Flowrate (Lpm)		
	30 Lpm	2,5	5	10
H ₂	0.33	0.39	0.38	0.31
CO	0.16	0.20	0.36	0.48
CH ₄	0.02	0.02	0.02	0.02
CO ₂	0.03	0.04	-	-
C ₂ H ₄	0.03	0.03	0.03	0.03
C ₂ H ₂	0.13	0.14	0.17	0.09
Total	0.7	0.82	0.96	0.93

Table 2c. Total Volume of Gas Produced per Gram of Canola Consumed During Complete Run for Injected Power of 5,88 kW.

Gas	Volume of gas produced per gram of canola consumed (L/g)			
	Spouting gas composition			
	Ar (plasma gas)	CO ₂ Flowrate (Lpm)		
	30 Lpm	2,5	5	10
H ₂	0.33	0.42	0.38	0.34
CO	0.16	0.21	0.33	0.43
CH ₄	0.02	0.02	0.02	0.02
CO ₂	0.03	0.04	-	-
C ₂ H ₄	0.03	0.03	0.03	0.03
C ₂ H ₂	0.13	0.13	0.11	0.09
Total	0.7	0.85	0.87	0.91

As seen from table 1a,b,c the increase in the plasma power and the introduction of carbon dioxide corresponds to the increased volume of gases produced during the same time period. The input seeds are exposed to higher temperatures resulting in liberation of more volatile matter and its increased decomposition rate, in addition to increased formation of carbon monoxide through char oxidation by carbon dioxide.

Analysis of the overall energy efficiency values, which can reach 60% for the medium value plasma power of 9.4 kW and decrease for the highest plasma power value employed, indicates the necessity for further process optimization especially in respect of the reactor design (its volume versus the plasma jet length).

Table 2. Overall Energy Efficiency of the Process

Plasma power		CO ₂ Flow rates			
Electric	Effective injected	0 lpm	2.5 lpm	5 lpm	10 lpm
[kW]	[kW]	[%]	[%]	[%]	[%]
6.5	3.58	58	53	59	56
9.4	4.69	54	59	57	60
12	5.88	48	51	50	52

Conclusions

The plasma spouted bed gasification of canola seeds is characterized by following advantages:

- Process is very fast – comparable with flash pyrolysis;
- Absence of tarry by products – at least at the process scale investigated;
- Very high overall energy efficiencies – up to 60 %, it is expected, that for continuous operation of such reactor the efficiency will increase further;
- High hydrogen and carbon monoxide contents in the gas product accompanied only by light hydrocarbons: methane, ethylene and acetylene with absence of sulphur;
- The possibility of employing medium temperature SOFC off-gas recycling into a plasma spouted bed gasifier is a very interesting option to consider for achieving future balanced energy needs.

Acknowledgement. The financial support of Natural Sciences and Engineering Research Council of Canada (NSERC) is gratefully acknowledged.

References

- (1) Lemoine, A., - *MscA Thesis.*, **2001**, Université de Sherbrooke.
- (2) Lemoine, A., Jurewicz J.W., *Proc. of International Symposium on Plasma Chemistry ISPC-15*, **2001**, pp. 2873-8.

H₂ SEPARATION THROUGH ZEOLITE THIN FILM MEMBRANES

Margaret E. Welk, Tina M. Nenoff

Sandia National Laboratories, PO Box 5800, MS 0734, Albuquerque, NM 87185-0734
mewelk@sandia.gov

Introduction

The synthesis and testing of inorganic zeolite membranes has been intensely studied because of their potential applications in the domains of gas separation, pervaporation, reverse osmosis and in the development of chemical sensors and catalytic membranes.^{1,2,3,4,5} Specifically, development of new technologies, such as zeolite membranes, for H₂ separation and purification has a high priority for the future of H₂ as a fuel source. H₂ is commonly produced by the reformation of hydrocarbons, creating CO₂, CO, CH₄ and H₂O as by-products. A successful membrane for the separation of H₂ from other reformat gases must have both high flux and high selectivity for H₂ in the presence of these other gas species. Inorganic membranes, which have good thermal stability and chemical inertness, are highly attractive. Distinctively, zeolite membranes combine pore size and shape tunability with the inherent mechanical, thermal, and chemical stability necessary for long term separations. The effective pore size distribution, and hence the separation performance, of a defect free zeolite membrane is intrinsically governed by the choice of the zeolitic phase.^{6,7,8,9}

Numerous pure gas permeation studies have been performed on MFI-type zeolite membranes that allow ideal selectivities to be calculated.^{10,11,12,13,14,15,16,17,18,19,20,21} Typical literature selectivity values of H₂ from CO₂, CH₄ and CO range from 2 to 8, below the values necessary for successful industry integration. It is well recognized that gas mixtures flowing through separation membranes will behave differently than pure gases owing to adsorption effects and other phenomena. We report here the study of the permeance and selectivity of both ZSM-5 and silicalite-1 zeolite membranes under the flow of three gas mixtures, two chosen as benchmarks (50/50 mol% H₂/CH₄ and 50/50 mol% H₂/CO₂) and one chosen to emulate an industrial methane reformat stream. The H₂ selectivities for both membranes outstrip the calculated ideal selectivity values from pure gas data by eight times or more.

Experimental

Gases. Reagent grade pure gases were purchased from Matheson Trigas. H₂, CO₂, O₂, CH₄, N₂, CO were used to test the permeability of the membranes. SF₆ was used to assess membrane quality, He was used to clean and purge the unit, shown in Figure 1. Three reagent grade gas mixtures pre-mixed by Matheson Trigas were also tested: 50/50 mol% H₂/CH₄, 50/50 mol% H₂/CO₂, and a four gas component mixture that approximates a methane steam reformat stream, excluding the water vapor (will be referred to as the reformat mixture): 76.2% H₂, 13.6% CO₂, 6.8% CO, and 3.4% CH₄.

Membrane Synthesis. A thorough description of the silicalite membrane growth has been published elsewhere.²² The support cleaning, seed synthesis,^{12,22} and seeding methodology for the ZSM-5 membranes are identical to the steps for silicalite also can be found in the same reference. A description of the ZSM-5 gel and hydrothermal synthesis of the ZSM-5 membranes is presented here.

In the gel used for the hydrothermal synthesis, the silicon source for the membrane synthesis was colloidal silica Ludox SM-30; the source of aluminum was Al₂(SO₄)₃·18H₂O, and NaOH is the alkalinity source. Ludox SM-30 was filtered prior to use to remove

any SiO₂ flakes; all other reagents were used as received. 2.14 g of NaOH, and 0.832 g of Al₂(SO₄)₃·18H₂O were added to 68.4 g of H₂O, and stirred until dissolved. 20 g of Ludox SM-30 was added drop-wise to the mixture while stirring. Each gel was then aged for 24 hours while being stirred at room temperature. Gels that were not aged under agitation did not result in selective membranes. The aged gels in this work were homogeneous and no precipitate had formed prior to the reactions.

The alpha-alumina substrates supplied by Inocermin GmbH have a 1.8 μm average pore size, a diameter of 13 mm and a thickness of 1 mm. Their high density ensures good mechanical properties and robustness. MFI zeolite seeds were rubbed onto both sides of the cleaned substrates; the seed synthesis and application has been described elsewhere.²³ The seeded substrates were held vertically in the Teflon lined Parr reactor using Teflon holders to prevent sedimentation on top of the membrane. The homogeneous gel was then poured in the reactor until the membrane was fully immersed. The hydrothermal syntheses were carried out in Parr reactors with a 23 ml Teflon liner at 170°C for 12 hours under autogenous pressure.

After the hydrothermal synthesis, the two-sided membrane was removed from autoclave, washed with DI water and dried in air at 50°C for few hours. A permeation test on the as-synthesized, uncalcined membrane allows the rapid assessment of its quality before the time-consuming calcination step. At this stage, a good quality membrane should be impermeable for SF₆. The SF₆ kinetic diameter of 5.5 Å is similar to the pore dimensions of the calcined ZSM-5 zeolite (diameter range 5.1 – 5.6 Å). Substantial SF₆ diffusion through the uncalcined membrane indicates the presence of detrimental membrane defects larger than the zeolite pores which will be opened during calcination.²³ Any existing large defects (partial coverage of the substrate and micro-cracks) may be repaired by a second hydrothermal synthesis step, using a shorter reaction time and more diluted starting gel.

Once the quality of the membrane was established, the water was removed from the membrane pores by calcination in air. A calcination temperature of 600°C led to cracks in the membrane and drastic reduction in permeation performance unless a slow temperature ramp rate was used. The stress at the interface between the zeolitic layer and the alumina substrate due to thermal expansion mismatch has to be minimized by using slow heating rates,²⁴ below 1°C/min. A typical successful temperature profile for the calcination is a heating and cooling rate of 0.5°C/min with a maximum temperature of 600°C maintained for 6 hours. This ensures the removal of water from the pores without creating detrimental defects within the membranes.

Characterization Techniques. The zeolite membranes were characterized by X-ray diffraction (Siemens D500 diffractometer, Cu Kα radiation, Bragg-Brentano geometry) and by Scanning Electron Microscopy (JEOL-6300V equipped with a Link Gem Oxford 6699 EDAX attachment).

Permeation Measurements. The membrane permeations were measured at room temperature using pure and mixed gases and a constant trans-membrane pressure of 16 PSI controlled by a backpressure regulator (see Figure 1). The membrane was sealed in a Swagelok fitting using Viton O-rings. The gas flow through the membrane was measured using an acoustic displacement flowmeter (ADM 2000 from J&W) and a digital bubble flowmeter (HP-9301). Between permeation measurements with different pure (SF₆, H₂, CO₂, O₂, CH₄, N₂, CO) and mixed (50/50 H₂/CO₂, 50/50 H₂/CH₄, and the reformat mixture) gases, the whole system was purged, flushed with He and evacuated several times. For the pure gases, the ideal gas selectivity was calculated as the ratio of the permeances in the steady regime.

Residual Gas Analyzer. For the mixed gas studies, an RGA (Stanford Research Systems QMS 200 Residual Gas Analyzer) in Pressure vs. Time graphing mode was attached to the permeate side of the membrane. The RGA tracks the partial pressure of each gas species over time using an internal mass spectrometer. Data points are taken once per second. Before each run, both sides of the membrane were evacuated and flushed with He three times. The permeate side of the membrane was then filled with He to atmospheric pressure, and the retentate side was evacuated just prior to the initiation of mixed gas flow. A constant trans-membrane pressure of 16 PSI was controlled by the back pressure regulator. Selectivities were calculated as the ratio of the partial pressures of the gas species of interest.

Results and Discussion

The mixed gas permeance and selectivity results have been presented elsewhere.²⁵ Table 1 below includes the selectivity data, where $\text{selectivity} = [y_i/(1-y_i)]_{\text{permeate}}/[y_i/(1-y_i)]_{\text{inlet}}$. Please see reference 25 for graphs and additional details.

Table 1. H₂ Selectivity Through ZSM-5 and Silicalite Membranes Using Gas Mixtures

	Reformate Mix	50/50 H ₂ /CO ₂	50/50 H ₂ /CH ₄
ZSM-5 H ₂ Selectivity	58.8	60.1	39.4
Silicalite-1 H ₂ Selectivity	21.5	22.9	16.9

According to the pure gas data, the ZSM-5 membrane was calculated to have an ideal selectivity for H₂ from the other reformat gases around 4 to 10, depending on the gas species.²⁵ In both 50/50 gas mixtures, the actual selectivities jumped almost 8-fold to 39.4 and 60.1. The selectivity for H₂ in the reformat mixture jumped to 58.8, a value more than six times that of the pure gas approximation.

Both ZSM-5 and Silicalite-1 are MFI type zeolites. Although they have identical structures, the pore chemistry differs owing to the presence of even a small amount of aluminum replacement of the silicon atoms in the ZSM-5 compound. The pore chemistry directly impacts adsorption and therefore, the permeation characteristics of the membranes, particularly the pure gas permeation results. Silicalite-1 membranes have a higher permeance for pure CO₂ than for pure H₂ because of the adsorption of CO₂ to the all-silica pore surfaces, while the ZSM-5 membranes show a strong preference for H₂, even though the percentage of aluminum substituting for silicon is very small – 0.25%. With gas mixtures, the silicalite membranes are selective for H₂, having lower H₂/CO₂ selectivities as compared with the ZSM-5 membranes for the 50/50 H₂/CO₂, the 50/50 H₂/CH₄ and the reformat gas mixtures.

Conclusions

The testing of the permeation of mixed gases through both ZSM-5 and Silicalite-1 zeolite membranes has revealed the extraordinary selectivities of these membranes for H₂. The ZSM-5 membrane had the following H₂ selectivities for the 50/50 H₂/CH₄ mixture, the 50/50 H₂/CO₂ mixture and the reformat mixture respectively: 39.4, 60.1, and 58.8, respectively. The silicalite membrane had lower H₂ selectivities for the same gas mixtures, 16.95, 22.9 and 21.73. The high permeances and extremely high selectivities of these membranes make them viable choices for H₂ gas separation applications.

Further studies on these MFI-type membranes continue, and include elevated temperatures, increased lifetime studies, pressure

variations, and additional gas mixtures. We will also investigate different microporous materials as well as b-axis oriented MFI type zeolite membranes. The effects of different support materials on membrane performance are also under investigation.

Acknowledgement. Sandia is a multiprogram laboratory operated by Sandia Corporation, a Lockheed Martin Company, for the United States Department of Energy under contract DE-AC04-94-AL85000. We thank the DOE/Hydrogen, Fuel Cells, and Infrastructure Technologies Program for continued funding. We also wish to acknowledge MesoFuel, Inc. for constructive discussions, collaborations, and industrial perspective.

References

- 1 Armor, J. N. *J. Membr. Sci.* **1998**, 147, 217.
- 2 Caro, J.; Noack, M.; Kolsch, P.; Schafer, R. *Microp. Mesop. Mat.* **2000**, 38, 3.
- 3 Chiang, A. S. T.; Chao, K.-J. *J. Phys. Chem. Solids* **2001**, 62, 1899.
- 4 Noack, M.; Kolsch, P.; Schafer, R.; Toussaint, P.; Caro, J. *Chem. Eng. Technol.* **2002**, 25, 221.
- 5 Thoma, S. G.; Trudell, D. E.; Bonhomme, F.; Nenoff, T. M. *Microp. Mesop. Mat.* **2001**, 50, 33.
- 6 Vroon, Z. A. E. P.; Keizer, K.; Gilde, M. J.; Verweij, H. Burggraaf, A. J. *J. Membr. Sci.* **1996**, 113, 293.
- 7 Geus, E. R.; DenExter, M. J.; van Bakkum, H. *J. Chem. Soc. Faraday Trans.* **1992**, 88, 3101.
- 8 Bakker, W. J. W.; Kapteijn, F.; Poppe, J.; Moulijn, J. A. *J. Membr. Sci.* **1996**, 117, 57.
- 9 Bai, C.; Jia, M.-D.; Falconer, J. L.; Noble, R. D. *J. Membr. Sci.* **1995**, 105, 79.
- 10 Lai, R.; Gavalas, G. R. *Ind. Eng. Chem. Res.* **1998**, 37, 4275.
- 11 Hedlund, J.; Noack, M.; Kolsch, P.; Creaser, D.; Caro, J.; Sterte, J. *J. Membr. Sci.* **1999**, 159, 263.
- 12 Tuan, V. A.; Falconer, J. L.; Noble, R. D. *Ind. Eng. Chem. Res.* **1999**, 38, 3635.
- 13 Lai, R.; Gavalas, R. *Microp. Mesop. Mat.* **2002**, 38, 239.
- 14 Xomeritakis, G.; Nair, S.; Tsapatsis, M. *Microp. Mesop. Mat.* **2000**, 38, 61.
- 15 Hedlund, J.; Sterte, J.; Anthonis, M.; Bons, A. J.; Carstensen, B.; Corcoran, N.; Cox, D.; Deckman, H.; De Gijnst, W.; de Moor, P.-P.; Lai, F.; McHenry, J.; Mortier, W.; Reinoso, J.; Peters, J. *Microp. Mesop. Mat.* **2002**, 52, 179.
- 16 Noack, M.; Kolsch, P.; Schafer, R.; Toussaint, P.; Sieber, I.; Caro, J. *Microp. Mesop. Mat.* **2002**, 49, 25.
- 17 Lai, Z. P.; Bonilla, G.; Diaz, I.; Nery, J. G.; Sujatoti, K.; Amat, M. A.; Kokkoli, E.; Terasaki, O.; Thompson, R. W.; Tsapatsis, M.; Vlachos, D. G. *Science*, **2003**, 300, 456.
- 18 Xomeritakis, G.; Lai, Z.P.; Tsapatsis, M. *Ind. Eng. Chem. Res.* **2001**, 40, 544.
- 19 Lovallo, M. C.; Tsapatsis, M. *AIChE Journal* **1996**, 42, 3020.
- 20 Lovallo, M. C.; Gouzinis, A.; Tsapatsis, M. *AIChE Journal* **1998**, 44, 1903.
- 21 Poshusta, J. C.; Noble, R. D.; Falconer, J. L. *J. Membr. Sci.* **1999**, 160, 115.
- 22 Bonhomme, F.; Welk, M. E.; Nenoff, T. M.; *Microp. Mesop. Mat.* **2003**, 66, 181.
- 23 Breck, D.W. *Zeolite Molecular Sieves*, (John Wiley and Sons, New York 1997).
- 24 Dong, J.; Lin, Y. S.; Hu, M. Z. C.; Peascoe, R. A.; Payzant, E. A. *Microp. Mesop. Mat.* **2000**, 34, 241.
- 25 Welk, M. E.; Nenoff, T. M. *J. Membr. Sci.* **2004** submitted.

HYDROGEN GAS SEPARATIONS USING A HIGHLY MICROPOROUS POLYMER

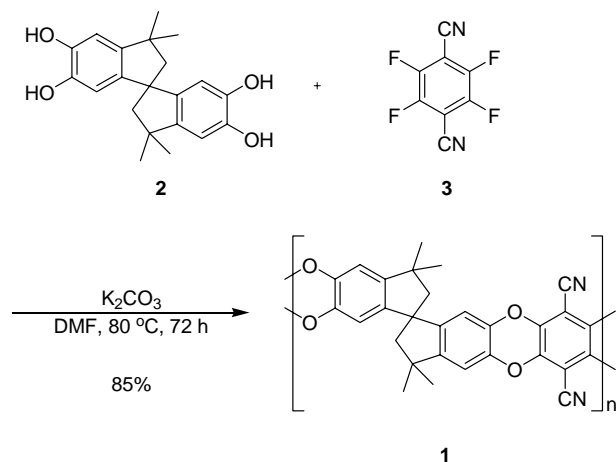
Chad L. Staiger, Chris J. Cornelius & David R. Wheeler

Chem & Biotechnologies/Micro Analytical Systems Departments
Sandia National Laboratories, PO Box 5800, MS 0888
Albuquerque, NM 87185-0888 e-mail: clstaig@sandia.gov

Introduction

Increasing interest by governmental entities to realize a future in which hydrogen is a dominating fuel source has spurred great interest in all aspects of hydrogen production, storage and utilization. Currently, hydrogen is produced by reforming fossil fuels (natural gas, oil, and coal). The capital and energy intensive reforming step does not produce pure hydrogen, but a mixture of light gases (syngas). Current methods for hydrogen purification/separation include pressure swing adsorption or cryogenic technologies. While these technologies work well, membranes for hydrogen separation represent an attractive alternative to further lower the costs of hydrogen production. Recently, McKeown *et al* reported a series of highly porous polymers (**1**) which have good thermal and mechanical stability.¹⁻³ The bispiroindane ring system induces an extreme amount of contortion into the polymer backbone. Rotational freedom in the polymer backbone is limited because of the ladder structure. The contortion and rigidity allow a high degree of void volume to exist. High polymer void volumes typically lead to increased gas throughput (permeability), however selectivity can be negatively affected.^{4,5} We have prepared one of these microporous polymers and evaluated its permeability and selectivity for use in hydrogen and other light gas separations.

Scheme 1. Preparation of spiro polymer 1.



Experimental

All solution NMR spectra were recorded on a Bruker Avance DRX spectrometer. Proton spectra were obtained at an operating frequency of 400 MHz. Infrared spectra (FTIR) were obtained using a Perkin Elmer Model 1600 FTIR spectrometer. Thermal analyses were performed on a Perkin Elmer TGA 7 and a TA 2010 DSC. Size exclusion chromatography was performed using a Polymer Labs PL-GPC210 operating at 40 °C equipped with RI detection. The mobile phase was THF at a flow rate of 1.00 mL/min. Separation was affected using two 300 × 7.5 mm PLgel 5

μm mixed-C columns. Calibration curves were generated using polystyrene standards. Surface area and pore analysis obtained by N_2 adsorption at 77 K using a Quantachrome Autosorb 6B. Membrane permeabilities were obtained using a home made permeation apparatus described elsewhere.⁶ Reagents and anhydrous grade solvents (Aldrich or Acros) were used as received unless otherwise stated.

Poly(3,3,3',3'-tetramethyl-1,1'-spirobisindane-5,5',6,6'-tetrol-co-2,3,5,6-tetrafluorophthalonitrile) (1). A mixture of K_2CO_3 (6.91 g, 50.0 mmol), 3,3,3',3'-tetramethyl-1,1'-spirobisindane-5,5',6,6'-tetrol (3.40 g, 10.0 mmol) and 2,3,5,6-tetrafluorophthalonitrile (2.00 g, 10.0 mmol) were stirred in DMF (50 mL) at 80 °C for 72 h. The heterogeneous solution was cooled to room temperature and then poured into rapidly stirred H_2O (300 mL). The solid was collected by vacuum filtration and washed with MeOH (2×100 mL). The bright yellow solid was taken up in a minimum amount of THF (~25 mL) and precipitated into rapidly stirring MeOH (400 mL). The polymer was collected by vacuum filtration and dried under vacuum (0.1 mm Hg @ 50 °C) to give 4.07 g (88%) of a bright yellow solid. 1H NMR (400 MHz, $CDCl_3$) δ 6.90-6.70 (br s, 2H), 6.60-6.30 (br s, 2H), 2.70-1.90 (br m, 4H), 1.70-0.80 (br m, 12H). IR (KBr) ν 2959, 2235, 1452, 1314, 1011 cm^{-1} . GPC: M_w =90,010; M_n =30,800; PDI = 2.92. BET surface area = 818 m^2/g .

Film preparation of spiro polymer 1. Spiro polymer **1** (550 mg) was dissolved in CH_2Cl_2 (15 mL) and filtered (2 μm glass microfiber). The filtered solution was pouring into a flat Petri dish (12 cm dia.) and then placed in a vacuum desiccator with the gas inlet open to the atmosphere. The solution was allowed to evaporate for 4 days. The dish was removed and the clear yellow film released from the glass using H_2O .

Results and Discussion

A prototypical microporous polymer **1** was prepared by heating a DMF solution of 3,3,3',3'-tetramethyl-1,1'-spirobisindane-5,5',6,6'-tetrol and 2,3,5,6-tetrafluorophthalonitrile at 80 °C for 72 h in the presence of K_2CO_3 (Scheme 1). After cooling the solution, polymer **3** was precipitated by pouring into water. The bright yellow polymer was further purified by dissolving in THF and reprecipitated by pouring into methanol. Yields of the polymer **1** after drying under vacuum were generally in excess of 85%. Size exclusion chromatography revealed a molecular weights typically greater than 100,000 (M_w) with a PDI's of 3 to 3.5.

The thermal stability of polymer **1** was investigated using DSC and TGA under an atmosphere of nitrogen. The DSC was unremarkable with the exception of a decomposition event with an onset of 395 °C. There was no discernable glass transition (T_g) present. The TGA showed the onset of weight loss at 484 °C and by 800 °C had only lost 55% of the original mass. The high thermal stability of spiro polymer **1** can be attributed to its ladder structure, since two bonds must be broken to cleave the polymer backbone.

Surface area analysis of spiro polymer **1** by N_2 adsorption/desorption revealed a highly porous structure. The surface area, calculated from BET, was 818 m^2/g . The pore volume at 0.99 relative pressure (P/P_0) was 1.06 cc/g. The pore size distribution (BJH Desorption) suggested a significant number of pores between 20 and 30 Å. The microporosity of the material (pore size < 20 Å) is currently being evaluated.

Spiro polymer **1** films were cast into free standing films (~60 μm thick) from CH_2Cl_2 and then subjected to gas permeability

measurements. Single gas permeabilities were measured for helium, hydrogen, carbon dioxide, oxygen, nitrogen and methane at 35 °C using the time lag method (Table 1). Spiro polymer **1** showed high permeability for each gas, with H₂ having the highest permeability of 1763 Barrers. In addition, permselectivities were particularly good for O₂/N₂, H₂/CH₄ and CO₂/CH₄ with respect to there permeabilities.⁷

Table 1. Single gas permeabilities and ideal permselectivities of spiro polymer 1. Permeabilities are the average of two different films.

Permeability at 35 °C (Barrers)											
He		H ₂		CO ₂		O ₂		N ₂		CH ₄	
877		1763		1590		496		135		157	
Ideal Permselectivity											
He/H ₂	0.5	H ₂ /CO ₂	1.1	CO ₂ /O ₂	3.2	O ₂ /N ₂	3.7				
He/CO ₂	0.6	H ₂ /O ₂	3.6	CO ₂ /N ₂	11.8	O ₂ /CH ₄	3.2				
He/O ₂	1.8	H ₂ /N ₂	13.1	CO ₂ /CH ₄	10.1						
He/N ₂	6.5	H ₂ /CH ₄	11.2					N ₂ /CH ₄	0.9		
He/CH ₄	5.6										

Conclusion

A highly contorted ladder polymer was prepared and evaluated for gas transport. The membrane permeabilities were consistent with those of a polymer containing large amount of free volume. While permeabilities were high, permselectivities were also good, particularly for O₂/N₂, H₂/CH₄ and CO₂/CH₄ separations. Manipulating polymer functionality or structure in this class of polymers may allow for increased permeabilities and permselectivities.

Acknowledgement. Sandia is a multiprogram laboratory operated by Sandia Corporation, a Lockheed Martin Company, for the United States Department of Energy's National Nuclear Security Administration under contract DE-AC04-94AL85000. We would like to thank Margaret Welk for her assistance with some of the gas permeability measurements.

References

- (1) Budd, P. M.; Elabas, E. S.; Ghanem, B. S.; Makhseed, S.; McKeown, N. B.; Msayib, K. J.; Tattershall, C. E.; Wang, D. *Adv. Matls.* **2004**, *16*, 456-459.
- (2) Budd, P. M.; Ghanem, B. S.; Makhseed, S.; McKeown, N. B.; Msayib, K. J.; Tattershall, C. E. *Chem. Commun.* **2004**, 230-231.
- (3) Budd, P. M.; Makhseed, S.; Elabas, E. S.; Ghanem, B. S.; Msayib, K. J.; Tattershall, C. E.; McKeown, N. B. *Mater. Today* **2004**, *7*, 40-46.
- (4) Masuda, T.; Isobe, E.; Higashimura, T. *Macromolecules* **1985**, *18*, 841-5.
- (5) Merkel, T. C.; Bondar, V.; Nagai, K.; Freeman, B. D. *J. Polym. Sci., Part B: Polym. Phys.* **2000**, *38*, 273-296.
- (6) Cornelius, C. J. PhD Thesis, Virginia Polytechnic Institute and State University, 2000.
- (7) Robeson, L. M. *J. Membr. Sci.* **1991**, *62*, 165-185.

REMOVING HYDROGEN SULFIDE FROM HYDROGEN-RICH GAS STREAMS BY SELECTIVE CATALYTIC OXIDATION

Xianxian Wu, Andrew K. Kercher, Viviane Schwartz,
Steven H. Overbury and Timothy R. Armstrong

Oak Ridge National Laboratory (ORNL)
Oak Ridge, TN 37831

Introduction

As the ideal fuel for proton-exchange membrane (PEM) fuel cells, hydrogen will mainly be generated from fossil fuels by steam reforming or partial oxidation before a long term energy solution is developed. One main problem associated with hydrogen production from fossil fuels is sulfur which is commonly in the form of hydrogen sulfide (or is chemically combined with hydrocarbons and can be converted into hydrogen sulfide during fuel processing). Hydrogen sulfide (H_2S) is a strong poison for fuel processing catalysts and PEM fuel cells, thus it must be removed at the early stages.

Among the available techniques for sulfur removal, direct oxidation of H_2S to elemental sulfur by the use of a special, highly selective oxidation catalyst and moderate temperatures is the preferred approach for dilute H_2S -containing gas streams.¹ The selective oxidation of H_2S has the thermodynamic potential to remove H_2S to the parts-per-billion level at low temperature.² This technology can be easily integrated into the current fuel processing plants,³ it can be used with diverse gas streams, and it does not consume H_2 or other useful gas components.⁴ As for the catalysts, activated carbons have been shown to be the most suitable candidates.⁵ Their use in partial oxidation of H_2S has been identified as a highly promising approach for removing sulfur content in fuel cell feedstocks.³ Experimental investigations showed that the by-products like SO_2 and COS are a potential problem associated with the use of commercial activated carbons.³ There is, then, a need to develop optimized catalysts. In this study, we report the test results of an activated carbon made at ORNL, and compare them with those of selected commercial carbons using reformat as the model gas stream.

Experimental

Three commercial activated carbons were used for this study: Centaur (Calgon Carbon, bituminous coal-based, physical activation), WV-B (Westvaco, wood-based, chemical activation), VA-507 (PICA, coconut shell-based, physical activation). The laboratory-made activated carbon (ORNLB) used cellulosic material as the precursor. Carbonization was conducted in a Kiln furnace at 850°C (6 h dwell) in the presence of 9.4 L/min N_2 flow. The activation was carried out in a Lindberg tube furnace (model 59754-A) at 875-975°C with a CO_2 flow of 0.5 L/min. Inert gas was used during heating to the designed temperature and cooling down to room temperature.

The nitrogen adsorption/desorption isotherms of these samples were determined at 77 K using an AUTOSORB-1 (Quantichrome Corporation). The outgas temperature was 300°C. Characteristic data derived from the isotherms are listed in Table 1.

Table 1. Properties of Activated Carbon Samples

Sample	BET surface area (m^2/g)	V_t (cm^3/g)	D-R micropore volume (cm^3/g)	D-A avg. pore diameter (\AA)
Centaur	817	0.465	0.344	15.6
WV-B	1840	1.49	0.957	19.2
VA-507	1022	0.545	0.414	15.6
ORNLB	579	0.341	0.245	13.6

Catalytic experiments were conducted in a laboratory-scale, fix-bed reactor system. The gas flow rates were controlled by a mass flow controller system (Omega, Model FMA-700 series controllers coupled with FMA-78P4 readout/power supply). The glass reactor tube used was 49.5 cm long with an I.D. of 1.25 cm. It is vertically positioned in an ATS single zone split tube furnace (Series 3210) in the down flow mode. Approximately 7.8 cm carbon sample is loaded in its center region. The reaction temperature is controlled by a K-type thermocouple in the furnace and monitored by another K-type thermocouple axially centered in the reactor tube. The concentrations of the exhaust gases from the reactor are monitored by a Gas Chromatography (GC) and a FTIR Spectrometer (MIDAC). The GC (Model 910, Buck Scientific, Inc.) has a 30 meter metal column (Q-Plot, Restek Corporation) and a FPD detector which can detect sulfur compounds down to about 200 ppb.

Results and discussion

The ORNL laboratory-made activated carbons have showed excellent activity (complete conversion of H_2S) and selectivity (100% to elemental sulfur) in H_2 stream.⁶ Generally, the processing gases in H_2 production processes are only hydrogen-rich streams which contain a large amount of H_2O , CO , CO_2 and other components. When selective oxidation is used for sulfur removal from these streams, COS and SO_2 formation becomes a problem.³ In this study, the catalytic behaviors of activated carbons were tested in a model reformat: 50% H_2 , 15% CO_2 , 9% CO , 1% N_2 , ~24% balance H_2O with 1000 ppm input H_2S . Air was introduced at the inlet according to an $O_2:H_2S$ ratio of 2:1. The experiments were conducted at 150°C at atmospheric pressure with a space velocity of 3100 h^{-1} (GHSV).

The measured catalytic activities for the four activated carbons are shown in Figure 1. The Centaur sample, WV-B sample and ORNLB-1 Sample showed 100% conversion of H_2S over an almost 9 h test, while the VA-507 sample showed a breakthrough of H_2S after being on stream for about 4 h and only about 70% H_2S conversion afterwards. The catalytic selectivity (to elemental S, calculated from the

equation: $sulfur\ yield = \frac{C_{H_2S,in} - C_{H_2S,out} - C_{SO_2,out} - C_{COS,out}}{C_{H_2S,in} - C_{H_2S,out}}$) of the samples

is shown in Figure 2. It is seen that only the laboratory-made sample (ORNLB) showed 100% selectivity in the whole test. Neither COS nor SO_2 was detected for this sample. The measured COS concentrations at the reactor exit for different catalysts are shown in Figure 3. The emission of COS was detected right after the introduction of H_2S and air when the Centaur sample or the WV-B sample was used, while COS was measured after about 3 h and SO_2 was measured after about 5 h (as shown in Figure 3) when the VA-507 sample was used. The VA-507 sample displays the worst selectivity after being on stream for about 5 h.

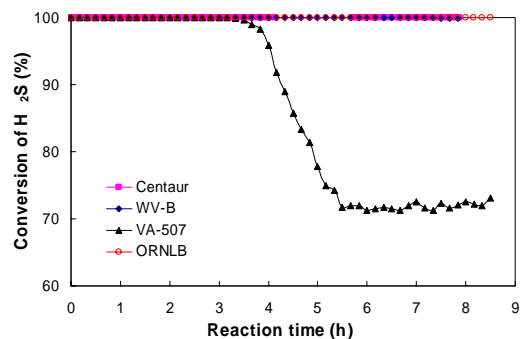


Figure 1. Conversion of H_2S versus time on stream.

The Centaur sample had relatively low specific surface area, pore volume and contained about 5% ash. According to the manufacturer, although it is not impregnated with metals or alkali, it displays the catalytic function of these materials. Our test showed this activated carbon is a strong catalyst which intends to over-oxidize the sulfur to undesired by-products. A better selectivity was observed for the WV-B sample than for the Centaur sample, but the immediate emission of a small amount of COS also is a problem for this sample. In the first 3 h, the VA-507 sample converted all H_2S to elemental sulfur, but both activity and selectivity became progressively worse afterwards. The observed diverse behaviors emphasize the importance of determining the factors responsible for the catalytic effects of activated carbons. On-going analysis and testing are aimed at understanding these factors and determining why the laboratory-made sample behaviors better than commercial samples.

Conclusions

The formation of COS is a problem for the use of commercial activated carbons as the oxidation catalysts of H_2S in reformat. The activated carbon synthesized at ORNL has the ability to selectively oxidize H_2S down to ppb level without detectable occurrence of unwanted side-reactions.

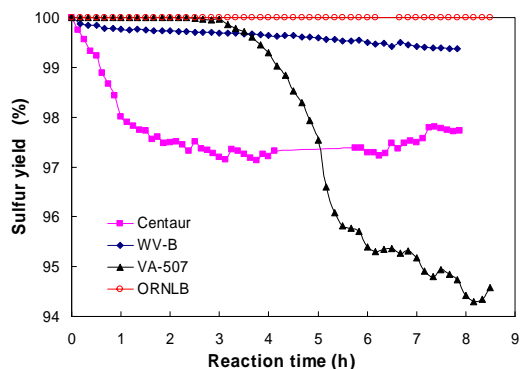


Figure 2. Selectivity (to S) versus time on stream.

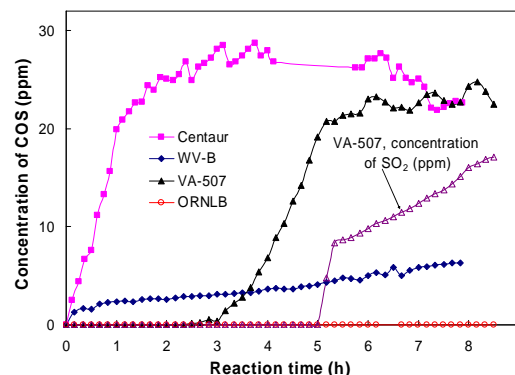


Figure 3. Exit concentration of COS versus time on stream.

Acknowledgements. This research was sponsored by the U.S. Department of Energy, Office of Hydrogen, Fuel Cells and Infrastructure Technologies under contract DE-AC05-00OR22725 with UT-Battelle, LLC, at Oak Ridge National Laboratory. The research was supported in part by an appointment to the Oak Ridge National Laboratory Postdoctoral Research Associates Program administered jointly by the Oak Ridge Institute for Science and Education and Oak Ridge National Laboratory.

References

- (1) Kohl, A. L.; Nielsen, R. *Gas Purification*, 5th ed.; Gulf Professional Publishing Company: Houston, 1997.
- (2) Gamson, B. W.; Elkins, R. H. *Chemical Engineering Progress* **1953**, 49, 203.
- (3) Gardner, T. H.; Berry, D. A.; Lyons, K. D.; Beer, S. K.; Freed, A. D. *Fuel* **2002**, 81, 2157.
- (4) Lagas, J. A.; Borsboom, J.; Berben, P. H. *Oil & Gas Journal* **1988**, 86, 68.
- (5) Steijns, M.; Mars, P. *Industrial and Engineering Chemistry Product Research and Development* **1977**, 16, 35.
- (6) Wu, X. X.; Kercher, A. K.; Schwartz, V.; Gallego, N. C.; Overbury, S. H.; Armstrong, T. R. "Activated carbons as catalyst for selective partial oxidation of hydrogen sulfide"; Carbon2004, July 11-16, 2004, Providence, RI.

KINETICS AND MICROSTRUCTURE OF Cu DEPOSITS FROM ELECTROLESS PLATING BATHS

Federico Guazzone, Erik E. Engwall, Ivan P. Mardilovich
and Yi Hua Ma

Center for Inorganic Membrane Studies
Department of Chemical Engineering
Worcester Polytechnic Institute
100 Institute Road
Worcester, Massachusetts 01609 USA

Introduction

One method for hydrogen production is to use metal supported Pd or Pd-alloy membranes in steam reforming reactors. The resistance to sulfur poisoning of the Pd₆₀Cu₄₀ alloy may make it suitable for the reforming of hydrocarbons with high sulfur content¹. Pd-Cu membranes have already been prepared by Ma et al², yet they showed low hydrogen permeability mainly due to a Cu wt% far from the optimum 40wt%. A better understanding of Cu plating baths is actually needed to reach the optimal Cu content. The objective of this work was to investigate the effects of pH and Cu concentration on the Cu deposition kinetics and the structure, including microstructure, of Cu deposits by electroless deposition. Non porous stainless steel plates were used as the surrogate for the porous support for the investigation.

Experimental

Non-porous stainless steel (316L) plates, 1cm², were cleaned with high alkaline solution for grease removal, oxidized at 400°C and activated following the procedure described Ma et al.³. Copper was deposited using the electroless deposition method. Table 1 shows the typical bath chemistry for Cu deposition and includes: Cu₂SO₄·5H₂O as copper ion source, HCHO as reducing agent and EDTA (or Rochelle salt) as complexing agent. The pH was adjusted with 10M NaOH and varied between 10 and 13.5. The temperature was set at 60°C

Table 1. Copper bath chemistry used for copper electroless deposition on non-porous stainless steel plates

CuSO ₄ ·5H ₂ O (g/l)	3-20
Na ₂ EDTA 2H ₂ O (g/l)	30
HCHO (37 %) (ml/l)	14
pH	10-13.5
Temperature (°C)	60

The thickness of Copper deposits was determined by gravimetric methods. The microstructure was characterized by Scanning Electron Microscope (SEM) (Amray 1600 Turbo) and X-Ray Diffraction (XRD) (Rigaku Geigerflex, Cu Kα (λ=1.5418Å) radiation source and monochromator) for grain size measurements.

Results and Discussion

The behavior of an EDTA based copper plating bath has been studied and the copper deposition rate are listed in Table 2 as a function of pH and Cu₂SO₄·5H₂O concentration. EDTA concentration was 30g/l and the formaldehyde concentration was 14ml/l. The deposition rate was measured within an accuracy of 0.5μm/hour.

Three important observations can be made from Table 2. The first one is that copper deposited very slowly when pH was below 12.

The second important result is that the Cu deposition rate increased when the concentration of Cu(II) ions was increased at a given pH. The copper deposition rate should have increased if the pH was increased according to the results reported by Ohno et al.⁴. However, for Cu₂SO₄·5H₂O concentrations of 6 and 9g/l listed in Table 2, the copper deposition rate appeared to decrease when the pH was increased. This might be due to an increase in the viscosity of the solution.

Table 2. Copper deposition rate (μm/hour) as a function of pH and Cu₂SO₄·5H₂O (g/l)concentration

	pH			
	10	12	≈13	≈13.5
3	≈0	≈0	1.7, 1.8	2.3, 2.4
6	-	-	8.0, 8.5	7.2, 7.9
9	≈0	≈0	10.4	8.2, 9.9
12	≈0	≈0	-	-
20	≈0	≈0	13.6	-

The deposited Cu was dull and lacked brightness when its deposition rate was fast. Using 3g/l Cu₂SO₄·5H₂O concentration led to better deposits, which appeared brighter. The same experiment was carried out for that specific Cu₂SO₄·5H₂O concentration (3g/l) but changing the complexing agent to Rochelle salt (NaKC₄H₄O₆). Again, no Cu could be deposited at pH below 12. On the other hand, the deposition rate at a pH of 12.5 was measured to be 1.5μm/hour. Since NaKC₄H₄O₆ is a weaker complexing agent than EDTA the deposition rate of EDTA based baths should be lower than the deposition rate of NaKC₄H₄O₆ based bath. However, the value of 1.5μm/hour at pH 12.5 of the NaKC₄H₄O₆ based bath is very closed to the deposition rate that an EDTA based bath at pH 12.5 would have, see Table 2.

The XRD pattern of a 1.5μm Cu deposit from the Rochelle salt based bath is shown in Figure 1. Cu peaks appear as shoulders since reflections of Cu and substrate (316L) are very close. The overlapping of the two patterns is due to the thinness of the Cu layer.

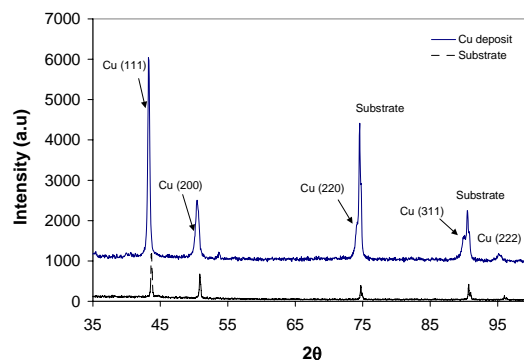


Figure 1. XRD pattern of a thin (1.5μm) Cu layer on stainless steel. Reflections from Cu are so close to stainless-steel peaks that Cu peaks appear as shoulders on the left side of the substrate peaks

In order to measure Cu grain size, thicker Cu substrates were needed in order to avoid peak broadening from the overlapping of the patterns. Figure 2 shows the XRD pattern of a 9μm thick copper deposit obtained from a high Cu(II) ion concentration (9g/l) and high pH (13). The patterns from the substrate and from the thin Cu layer

of Figure 1 are also included for comparison purposes. It is clearly seen in Figure 2 that all diffracted rays come from the copper layer since the intensity ratios of all peaks are equivalent to the intensity ratio of a Cu polycrystalline sample. For example, the intensity of peak (220) is similar to the intensity of peak (311) which is not the case in Figure 1 due to the presence of the substrate peak.

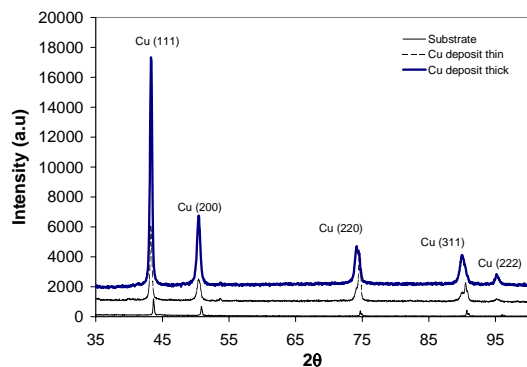


Figure 2. XRD pattern of a thick (9µm) Cu deposit obtained from a 9g/l Cu(II) bath at pH 13. Patterns from Figure 1 are also shown for intensity comparison

Copper crystallites using Scherrer equation after machine broadening correction ranged between 5-15 nm. This result is in good agreement with the results reported by Lin et al.⁵ and Xu et al.⁶

SEM micrographs of Cu deposits from Rochelle salt based bath showed uniform layers composed of 0.3-1µm clusters in diameter. In fact, such clusters, seen in Figure 3, are agglomerates of Cu grains with dimensions smaller than 20nm as stated above.

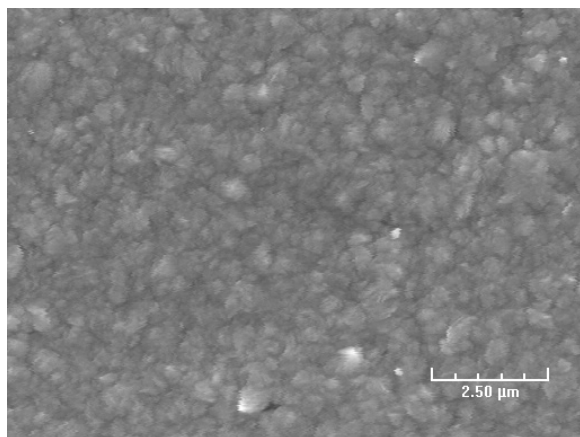


Figure 3. Copper deposit on oxidized stainless steel plates. Cu deposits as spherical clusters including nano-crystallites.

Conclusion

Copper deposited very slowly when pH was below 12. The Cu deposition rate increased when the concentration of Cu(II) ions was

increased. At high Cu concentrations The Cu deposition rate decreased when pH was increased which might have been due to an increase in viscosity. The Cu was dull in appearance when the deposition rate was fast (above 10µm/hour). Cu deposited very uniformly on oxidized non-porous stainless steel. The deposits were characterized by clusters as large as 1µm including crystallites smaller than 20 nm.

Acknowledgement. The authors gratefully acknowledge the financial support provided by Shell Hydrogen and Shell International Exploration and Production, Inc.

References

- McKinley, D.L. & W. Va. Nitro. 1969. U.S. Patent 3,350,845
- Ma, Y. H.; Mardilovich, I. P.; Engwall E. E. *Advanced Membrane Technology* 984 (2003) 346-360
- Mardilovich, P. P.; She, Y.; Ma, Y. H. and Rei M. H. *AIChE journal*, Vol. 44, No. 2, (1998) 310-322
- Ohno I., Wakabayashih O. and Haruyama S. *J. Electrochem. Soc.: ELECTROCHEMICAL SCIENCE AND TECHNOLOGY*, Vol. 132, No. 10, (1985) pp 2323-2330
- Lin, W. H. and Chang, H. F. *Surface and coatings Technology* 107 (1998) 47-54
- Xu L., Zhou K., Xu H., Zhang H., Huang L., Liao J., Xu A., Gu N., Shen H, Liu J. *Applied surface science*, 183 (2001) 58-61

A NOVEL LOW-COST HEATED Pd MEMBRANE SEPARATOR FOR HYDROGEN RECOVERY FROM REFORMATES

P. Bossard, J. Mettes

Power & Energy, 106 Railroad Dr., Ivyland, PA 18974 USA

Abstract

Thinner membranes not only reduce the amount of costly palladium needed but also produce higher hydrogen throughput per surface area. These two effects combine to reduce the amount of palladium needed by the square of the reduction ratio of the Pd membrane thickness which is the motivation behind a number of current state of the art studies. Thinner membranes need to be supported by a rigid hydrogen permeable substrate which can be made either from porous metal or from ceramic material. Power and Energy, Inc. has identified the main technical bottlenecks associated with the first approach and has generated corresponding novel solutions. A mathematical model of the physics involved in a practical separator has been developed. This model enables the calculation of membrane performance for a given set of design and operational parameters. Preliminary data showing the performance of this novel permeable membrane support structure is also presented.

Keywords: hydrogen, separation, purification

Introduction

Palladium membrane based devices have the potential to provide low cost separation and purification of Hydrogen in a single step; however, due to the relatively high cost of palladium, fabrication and lack of reliability, practical applications using palladium membranes have been limited. Separation is needed to extract hydrogen from reformed fuel sources ranging from fossil fuels to renewable biomass. Purification of the extracted hydrogen is required to remove deleterious impurities that can reduce the lifetime of a proton exchange membrane (PEM) fuel cell. The PEM fuel cell is the device of greatest practical interest in realizing the benefits of distributed electrochemical power generation. The separation is typically done in a centralized fashion in which leading to significant challenges related to the problematic transport and storage of hydrogen. Given a low cost efficient separation technology, hydrogen separation can also be done at the point of use. Point of use hydrogen generation has distinct advantages which include avoiding the need to develop a hydrogen distribution infrastructure and also allowing the storage of liquid precursor fuels that are easily stored in traditional storage tanks.

Supported Thin Pd-alloy Membrane

Thinner membranes not only reduce the amount of costly palladium needed but also produce higher hydrogen throughput per surface area. These two effects combine to reduce the amount of palladium needed per unit of hydrogen flux by the square of the reduction ratio of the Pd membrane thickness which is the motivation behind a number of current state of the art studies. Thinner membranes need to be supported by a rigid hydrogen permeable substrate which can be made either from porous metal or from ceramic material.

Performance impacted by the presence of the membrane substrate

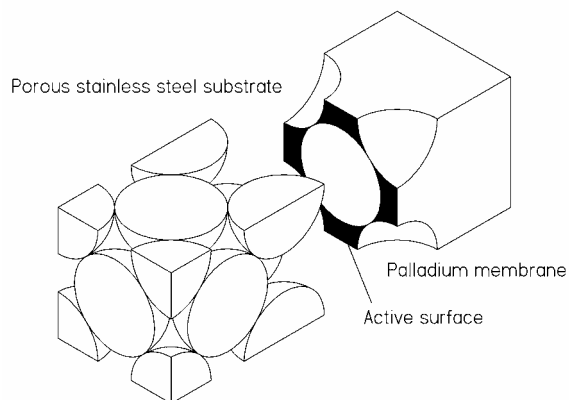


Figure 1. State of the Art substrate showing significantly reduced useful membrane area due to substrate blocking

The presence of a substrate, supporting a thin membrane, introduces a performance reducing factor for the composite structure. This is illustrated in figure 1 showing large part of a state of the art membrane surface being physically blocked by the substrate which reduces the area available for hydrogen transport. Figure 2 illustrates P&E's patent pending solution that provides a strongly supported membrane without obstructing significant parts of the surface area for hydrogen permeation. These features are obtained by placing a porous layer of palladium nanospheres in between the porous substrate and the solid palladium membrane. As becomes apparent in figure 2 the top layer of interconnected palladium spheres becomes an integral part of the solid membrane layer. Depending on the lattice structure of the substrate, the difference in transport capability ranges from a factor 20 to 40 for respectively a loosely packed cubic to dense hexagonal packed lattice. In reality the spheres will be compressed into each other, reducing the membrane area available for hydrogen transport even further.

It should be emphasized that P&E's solution avoids the introduction of new problems related to intermetallic diffusion and thermal expansion because the solid palladium alloy layer and the porous palladium alloy layer can be made of the same material. Also, differences in thermal expansion between the non-palladium substrate material and the porous palladium layer will be buffered because of the relative loose bond between these layers.

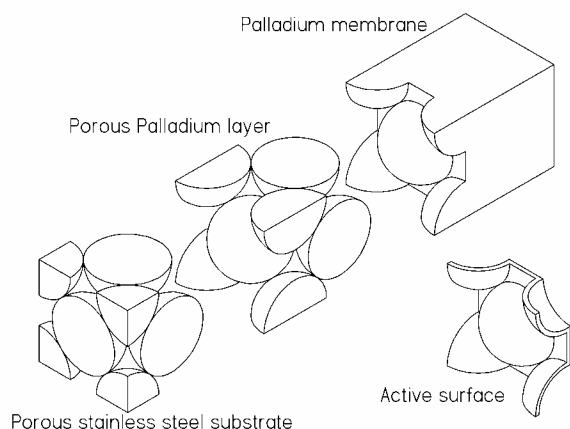


Figure 2. P&E structured composite membrane showing significantly increased useful membrane.

The interface between substrate and membrane is potentially problematic for a number of technical reasons, other than substrate blocking, such as:

- Bonding mechanism, inter-metallic diffusion, and robustness of adhesion strength
- Structural component differences in the coefficient of thermal expansion (without hydrogen)
- Hydrogen solubility, embrittlement, and coefficient of thermal expansion with hydrogen
- Pressure and thermal cycling behavior of permeability

Membrane test results using free-standing and supported membranes

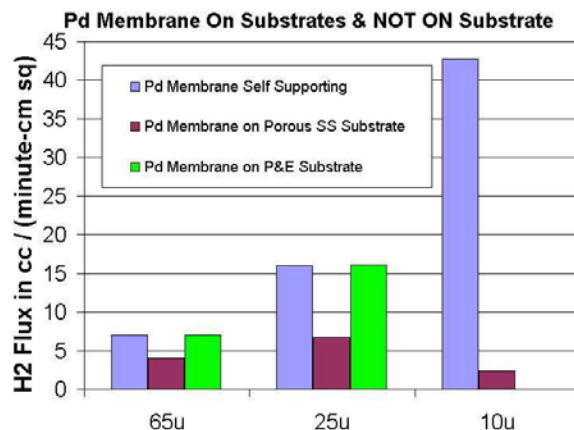


Figure 3. Data comparing H₂ flux rates for membranes of three different thicknesses. The left bar at each thickness represents the flux rate of a free-standing membrane (10 μ data is calculated). The center bar represents the typical flux reduction which results from employing a porous SS support substrate. The right bars are flux rates measured for membranes supported with the subject novel nano-structured membrane support.

PATHWAYS TO BUILD A HYDROGEN ECONOMY INFRASTRUCTURE

V. Raman, Consultant

Allentown, PA

Building the infrastructure to support a fully developed hydrogen economy is an undertaking of massive proportions. However it does not need to be done all at once.

This build-out could be accomplished starting from the current relatively modest base infrastructure that supplies hydrogen for industrial applications today.

In the long term the production can transition from the fossil-based technologies of today to renewable energy based technologies thus eliminating greenhouse gas emissions.

Over the last 150 years or so ago the world's energy needs were met by transitioning from solid fuels like wood and coal to liquid fuels. Currently liquid fuels exceed the amount of solid fuels in use. This was followed by the introduction of gaseous fuels in the early 20th century. Gaseous fuels have been gradually increasing at the expense of both solid and liquid fuels. The primary gaseous fuel we use today is natural gas. Looking into the future, predictions are for the use of gaseous fuels to increase even more and for solid and liquid fuels to disappear over the next 150 years or so. Also the gaseous fuel of choice is expected to gradually change from natural gas to hydrogen.

This shift from solid to liquid to gaseous fuels also represents a shift to increasing hydrogen content or decreasing carbon. With increasing hydrogen content these fuels are more energetic and also burn cleaner releasing less carbon dioxide and other pollutants into the atmosphere. The use of hydrogen as a fuel will be the cleanest as it has no carbon. It simply produces water on combustion. The hydrogen economy or the use of hydrogen fuel is considered by many to be the next transition of global energy use.

Hydrogen can be produced using electrochemical, thermochemical, bacterial fermentation, thermolysis and photolysis of water. However many of these processes require further development to make them competitive.

Today hydrogen is produced most economically via steam reforming of natural gas in large plants. The majority of the hydrogen produced today is transported in dedicated pipelines to large refining and chemical manufacturers.

Hydrogen is used daily by many industries, including the petroleum industry and in manufacturing processes for producing chemicals, foods and electronics.

Today the only significant fuel use of hydrogen is for the NASA space shuttle.

Efforts underway now on fuel cells should lead to a variety of special niche applications where hydrogen fuel cells provide unique advantages in portable and stationary power needs as well as in This presentation will address the issues and challenges in building an infrastructure to support a hydrogen economy. The challenge in developing a hydrogen infrastructure to support these needs include:

- How best to leverage the existing industrial infrastructure to support the introduction of hydrogen and fuel cell products?

- Developing new products to meet the emerging demands of the fuel cell market. Since distribution costs play a dominant role in hydrogen prices today, new models for the production and delivery may be warranted in the emergence of a hydrogen economy.
- How to introduce renewable hydrogen into the expanding hydrogen infrastructure as the market develops and the economics warrant?

There are currently about 20 demonstration fueling stations in operation in the US to support testing and development. Various low cost innovative solutions are being developed such as the mobile fueler, which is modeled after the industrial tube trailer high pressure gas delivery system. This is proving to be very popular with the various car manufacturers who want low cost solutions to placing a limited number of vehicles in various diverse locations.

This presentation will shed some light on these issues. Pathways to leverage the current infrastructure with distributed production and fueling will be discussed. Capital utilization, safety, codes and standards, and consumer acceptance are critical components to achieving a success. These will be discussed in some depth as well.

METAL-ORGANIC FRAMEWORKS (MOFs): NEW MATERIALS DESIGNED FOR H₂ STORAGE

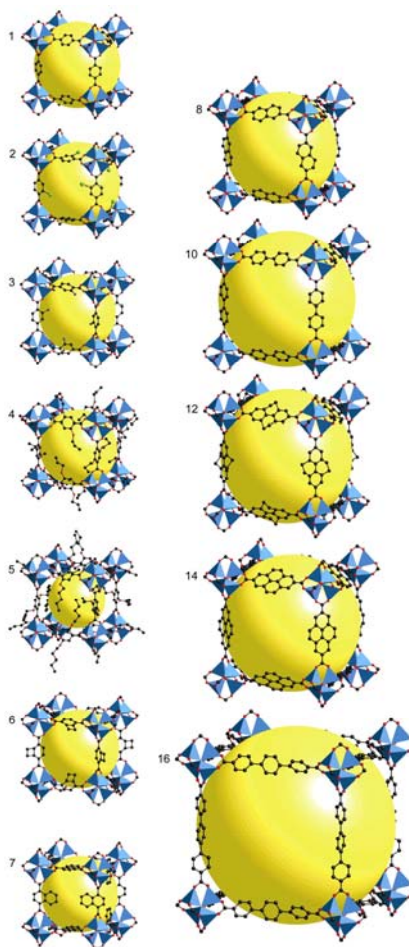
Omar M. Yaghi

Department of Chemistry, University of Michigan, Ann Arbor, MI 48103, USA

An outstanding challenge in the synthesis of crystalline solid-state materials is to alter chemical composition, functionality, and molecular dimensions systematically, that is, without changing the underlying topology. The insolubility of extended solids necessitates that their assembly be accomplished in only a single step. Thus, in order to design a target extended structure with the same precision practiced in organic synthesis, (i) the starting building blocks should have the relevant attributes necessary to assemble into the skeleton of the desired structure, (ii) the synthesis has to be adaptable to using derivatives of those building blocks to produce structures with the same skeleton but different functionalities and dimensions, and (iii) the products should be highly crystalline to facilitate their characterization by X-ray diffraction (XRD) techniques.

We have pursued the assembly of extended structures of metal-organic frameworks (MOFs) from molecular building blocks. In particular, in MOF-5, octahedral Zn-O-C clusters are linked by benzene struts to reticulate a primitive cubic structure (**1** in Fig.) and produce an exceptionally rigid and highly porous structure. Now we report the systematic design and construction of a series of frameworks having structures based on the skeleton of MOF-5, wherein the pore functionality and size have been varied without changing the original cubic topology. Several members of this series have pore sizes in the mesoporous range (>20 Å), and the lowest crystal density of any material reported to date.

The exceptionally high surface area and pore volumes observed for **6** coupled with its appropriately designed aperture made it an ideal candidate for methane and hydrogen storage. Indeed, the methane sorption isotherm was measured in the pressure range 0 to 45 atm and room temperature, and found to have an uptake of 240 cm³ (STP)/g (155 cm³/cm³) at 36 atm. The H₂ isotherm showed that up to 4.5 % wt/wt could be stored at 78 K, and up to 2 % wt/wt at room temperature and 10 bar. The presentation will discuss synthesis of these compounds and their use for separation of large organics, and gas storage including the use of H₂ for fueling of cellular phones, laptops, and potentially automobiles.



Chemical Systems for Hydrogen Storage

G. J. Thomas, *Consultant*

Sandia National Laboratories

Hydrogen storage systems for use in hydrogen-fueled vehicles will require high energy density and high specific energy in order to achieve comparable performance to conventional gasoline-fueled vehicles. It is believed that this issue remains as one of the critical barriers to the development of fuel cell powered vehicles. With the president's initiative and increased funding levels in hydrogen and fuel cell development, there are a number of new and exciting areas of research which have emerged aimed at developing high density hydrogen storage media.

At the present time, essentially all hydrogen-fueled vehicles use either compressed gas or liquid hydrogen tanks for onboard storage. Both of these technologies are straightforward, relatively mature and are commercially available. Compressed gas systems have progressed rapidly over the last few years. These cylindrical tanks, constructed with high strength carbon fiber composite materials, are robust, lightweight and have been demonstrated at hydrogen pressures up to 700 bar. However, even at this pressure at ambient temperature, the volumetric density of the hydrogen is insufficient for long-term use. Liquid hydrogen storage has been advocated mainly by BMW and a number of their demonstration vehicles have employed tanks which were developed by Linde. The high energy cost of liquefying hydrogen has been stated as a key issue in its utilization as a fuel.

This presentation will focus on chemistry-based hydrogen storage methods, that is, hydrogen storage materials. Storage materials can be broadly classified as having reversible or non-reversible hydrogen behavior. Reversible materials absorb and desorb hydrogen from the gas phase based on the hydrogen gas overpressure and temperature. These materials can therefore be recharged *in-situ* onboard the vehicle by supplying hydrogen at the appropriate pressure. On the other hand, non-reversible systems require chemical processing, perhaps including intermediate phases and additional materials, to be recharged. In this case, the spent material (depleted of hydrogen) which could be in liquid or solid form, must be removed from the vehicle and reprocessed elsewhere. These materials are generally referred to as chemical hydrides. Although reversible systems would be the preferred method, both options are currently under consideration.

There are many materials which have reversible hydrogen properties. These include materials where the hydrogen is adsorbed to the surface and those where the material is absorbed into the bulk. Single wall carbon nanotubes and other nanostructured materials, such as metal organic frameworks (MOFs), are examples of adsorbed hydrogen systems being studied. Critical issues which must be answered with adsorbed systems are hydrogen capacity, volumetric density and hydrogen binding energies.

Materials where hydrogen is absorbed and chemically bound in the bulk offer the potential of having the highest volumetric density of hydrogen, surpassing even that of liquid hydrogen. Metal hydrides are the best known class of materials with this property and these have been extensively studied for more than 30 years. Although they exhibit good capacities and good kinetic properties, they are generally too heavy. Lighter weight hydrides typically have stronger covalent or ionic hydrogen bonds and hence

require high temperatures for hydrogen release. Emphasis in this area of research has shifted in recent years to other materials. Complex hydrides, particularly those formed with Al-H or B-H complexes, offer higher hydrogen capacities, lighter weight over intermetallic hydrides and reduced hydrogen binding energies over covalent or ionic hydrides. However, only NaAlH_4 , doped with Ti, has been demonstrated to be reversible at this time. Work on this and other complex hydrides, as well as effective dopant materials and processes to achieve reversible behavior and the desired kinetic and thermodynamic properties, is currently being pursued. A number of other alternative materials have also shown promising early results and are being proposed for further study, including imide-amides and amine borane systems.

In this overview presentation we will discuss inherent limitations of hydrogen storage concepts and briefly describe some of the specific chemical systems mentioned above. Emphasis will be on material performance relative to that required in storage applications.